

DEVELOPMENT AND MECHANISTIC STUDY OF PHOTOREDOX SYSTEMS

Cole Cruz

A dissertation submitted to the faculty at the University of North Carolina at Chapel Hill in partial fulfillment of the requirements for the degree of Doctor of Philosophy in the Department of Chemistry

Chapel Hill
2018

Approved by:

David A. Nicewicz

Michael T. Crimmins

Simon J. Meek

Eric M. Brustad

Alexander J. M. Miller

© 2018
Cole Cruz
ALL RIGHTS RESERVED

ABSTRACT

Cole Cruz: Development and Mechanistic Studies of Photoredox Systems
(Under the direction of David A. Nicewicz)

Herein is described the development of a novel methodology utilizing photoredox catalysis along with a corresponding mechanistic analysis of this method. Additionally, the results of a mechanistic study of a separate methodology are also reported, revealing important details about the design and stability of photoredox dyes.

The development of a photoredox-mediated Newman-Kwart rearrangement is first described. This work was conducted jointly with Dr. Andrew Perkowski. The Newman-Kwart Rearrangement is a reliable methodology for the synthesis of aryl thiols. However, the extreme thermal energy required for the reaction presents a challenge for heavily modified substrates. The development of a mild set of reaction conditions represents an advancement in this field and allows for the facile synthesis of previously difficult to access substrates.

Following the development of the methodology, an investigation into the factors affecting reactivity was achieved. Through a combination of spectroscopic and kinetic analyses the photoredox Newman-Kwart rearrangement was found to strongly couple reactivity with substrate electronics. Furthermore, the reactive intermediate was characterized as a thione cation-radical which is best described as a thiyl-radical. Using thermochemical data, a predictive model for successful rearrangement was developed and displays excellent agreement with experimental results.

Finally, the elucidation of key reaction dynamics for an arene C-H functionalization reaction mediated by photoredox catalysis is described. Importantly, both the reaction mechanism as well as important factors governing catalyst efficiency were discovered. The understanding of this reaction manifold could allow for the development of other methodologies that access additional important structural motifs. More broadly, the results concerning acridinium stability and efficiency could be used to improve reactivity in a number of photoredox systems, not just those related to oxidative arene functionalizations.

ACKNOWLEDGEMENTS

First, I would like to thank Dave for allowing me to join his lab. I greatly value the experience of joining a group working in an exciting new field like photoredox catalysis. The projects that I worked on provided numerous opportunities for me to learn about new areas of chemistry and I am grateful that Dave had the patience to let me explore these areas, including photophysical measurements, at my own pace. I'm also extremely grateful for the opportunity to become involved in the UNC curriculum by developing a CURE program in the undergraduate organic labs, and thank Dr. Nita Eskew for her patience and enthusiasm in working with me to get these experiments up and running. I'm also very excited to see how "Rad" Natalie Holmberg-Douglas and "Slick" Nick Onuska continue to improve upon this program.

To all members of the Nicewicz lab, past and present, I'd like to thank you for providing an amazing atmosphere to do chemistry. I appreciate everyone's willingness to chat about chemistry and help each other under the glow of our blue lights. I'm also glad that we successfully embodied our lab's unofficial motto ("Work hard, Play hard"). I'd specifically like to thank Andrew Perkowski and Nathan Romero for their willingness to work with me and for their sage advice. I'd especially like to thank Cortney Cavanaugh and Jeremy Griffin. I can't imagine how much more difficult the graduate experience would have been without all of us helping to keep each other sane (while also trying to annoy each other into insanity). If all of our career plans fall through, I'm still prepared to start a radio talk show with you guys if you're willing.

I don't think it's possible to thank my family enough for all of their love and support. I would never have been able to even think about obtaining a graduate degree without the influence of my family. Thank you all for always encouraging me to pursue my intellectual pursuits and for providing me with everything I needed for academic success.

Finally, and certainly not least, I thank my fiancée Indalina. I cannot put into words all of the ways in which you have helped me along the way and I'm sure you helped me in ways that I'm not even aware of. Through all of the good times and bad times of graduate school I always knew that I could lean on you. I am eternally grateful for your love and support and promise to do the same for you.

TABLE OF CONTENTS

List of Figures.....	xi
List of Tables	xii
List of Abbreviations	xiii
CHAPTER 1: Overview of Photoredox Catalysis and Relevant Photophysical Properties.....	1
1.1 Photophysical and Electrochemical Terms Important in Photoredox Catalysis	1
1.2 Background of Photoredox Catalysis in the Nicewicz Lab.....	6
References	11
CHAPTER 2: Development of a Photoredox-mediated Newman-Kwart Rearrangement	15
2.1 The Importance of Aryl Sulfides in Bioactive Molecules and Their Synthesis.....	15
2.2 The Newman-Kwart Rearrangement: A Brief History	17
2.3 A Proposed Photoredox-Mediated Pathway	23
2.4 Initial Studies of a Photoredox Newman-Kwart Rearrangement.....	24
2.5 Substrate Scope of a Photoredox Newman-Kwart Rearrangement	26
2.6 Cyclic Voltammetry of O- and S-aryl Carbamothioates.....	32
2.7 Stern-Volmer Quenching Analysis of O-aryl Carbamothioates	34
2.8 Carbamothioate-Mediated Olefin Isomerization Promoted by Photoredox Catalysis...	37

2.9	Kinetic Studies of Photoredox Newman-Kwart Rearrangement	41
2.10	An Adjusted Mechanism for Photoredox Newman-Kwart Rearrangement.....	48
2.11	A Thermodynamic Cycle to Predict Photoredox Newman-Kwart Rearrangement	50
2.12	Final Conclusions.....	54
	References	56
CHAPTER 3: Mechanistic Investigations of a Photoredox-Mediated Arene C-H Amination ...		60
3.1	Introduction.....	60
3.2	Initial Proposed Mechanism.....	63
3.3	Antioxidant Studies.....	66
3.4	Catalyst Degradation Studies	75
3.5	Ground State or Excited State Decomposition?.....	84
3.6	TEMPO ⁺ : Alternative Reaction Pathways	89
3.7	Development of New Anaerobic Conditions	93
3.8	Elucidating the Origin of Regioselectivity.....	96
3.9	Clarifying the Mechanism.....	100
3.10	Conclusions.....	102
	References	104
Appendix A: Supporting Information for Chapter 2.....		109
A.1	General Information.....	109
A.2	Synthesis and Characterization of Catalyst and Substrates.....	109

A.3	Methods and Analytical Data for Rearranged Products.....	118
A.4	Large Scale Flow Synthesis: <i>S</i> -(2,4,6-trimethylphenyl)dimethylcarbamothioate.....	124
A.5	Measurement of Redox Potentials via Cyclic Voltammetry.....	125
A.6	Photophysical Measurements.....	130
A.7	Aminium Cation-Radical Reactions.....	136
A.8	Olefin Isomerization Studies.....	137
A.9	Reaction Monitoring using <i>in situ</i> IR Spectroscopy	142
	References	145
Appendix B: Supporting Information for Chapter 3.....		146
B.1	General Information.....	146
B.2	Synthesis and Characterization of Catalysts and Substrates	146
B.3	Measurement of Redox Potentials via Cyclic Voltammetry.....	155
B.4	Initial-Rates Kinetic Analyses.....	156
B.5	Photophysical Measurements.....	159
B.6	Ground-State Pyrazole-Acrinium Complex Investigation.....	160
B.7	Stern-Volmer Quenching Experiments.....	161
B.8	Monitoring Reaction Mixtures via UV-Vis and LC-HRMS.....	172
B.9	Observation of TEMPO ⁺ BF ₄ ⁻ Charge Transfer by UV-Vis.....	173
B.10	TEMPO ⁺ BF ₄ ⁻ Mediated Arene C-H Amination.....	175
B.11	Development of New Anaerobic Conditions.....	176

B.12	KIE Experiments.....	177
B.13	Added Acid Studies.....	181
	References	184

LIST OF FIGURES

Figure 1.1: Examples of organometallic and organic photoredox dyes with relevant electrochemical and photophysical data	2
Figure 1.2: Reduction potentials of various organic compounds and common photoredox catalysts.....	5
Figure 1.3: Examples of anti-Markovnikov hydrofunctionalization reactions developed in the Nicewicz lab.....	6
Figure 1.4: Proposed catalytic cycle for the acridinium-mediated anti-Markovnikov hydrofunctionalization of olefins.....	8
Figure 1.5: Examples of PRCC reactions developed in the Nicewicz lab.....	9
Figure 1.6: Photoredox-catalyzed arene C-H amination developed in the Nicewicz lab.	10
Figure 2.1: Examples of bioactive molecules containing an aryl-thiol linkage.....	16
Figure 2.2: Representative synthetic sequence for thiophenols utilizing Newman-Kwart Rearrangement.	17
Figure 2.3: Selected substrate scope of Newman's initial report	18
Figure 2.4: Results of Mechanistic Analysis of Newman-Kwart Rearrangement.....	20
Figure 2.5: Selected examples of NKR achieved through microwave heating	22
Figure 2.6: A Palladium-catalyzed NKR	23
Figure 2.7: Proposed sequence for cation-radical accelerated NKR	24
Figure 2.8: Unique reactivity of photoredox NKR	29
Figure 2.9: Limitations of cation-radical NKR.....	31
Figure 2.10: Initial proposed mechanism for cation-radical NKR	32
Figure 2.11: CV Traces of relevant carbamothioates	33
Figure 2.12: Hammett plot vs. σ^+ for the series of carbamothioates tested from table 1.....	36
Figure 2.13: Cation-radical NKR initiated by a ground-state oxidant.....	37
Figure 2.14: Experiments investigating olefin isomerizations during cation-radical NKR.....	38

Figure 2.15: Reactivity of aryl carbamothioate radical	40
Figure 2.16: Kinetic traces of cation-radical NKR of 2a obtained using in-situ FTIR.....	42
Figure 2.17: Kinetic traces showing lack of product-inhibition in cation-radical NKR.....	43
Figure 2.18: Relationship between quantum yield and substrate concentration.....	44
Figure 2.19: Possible modes of substrate inhibition	45
Figure 2.20: Hammett-type analysis of cation-radical NKR	47
Figure 2.21: Amended catalytic cycle for NKR along with description of intermediate 5	49
Figure 2.22: Thermodynamic cycle for the cation-radical NKR	51
Figure 3.1: Methods for the installation of arene-amine linkage.....	60
Figure 3.2: Photoredox-mediated arene C-H functionalization reactions developed in the Nicewicz group	62
Figure 3.3: Working mechanistic proposal for acridinium-mediated arene C-H amination	65
Figure 3.4: Observation of substrate decomposition during initial optimization of the reaction .	66
Figure 3.5: Spectroscopic evidence confirming turnover of acridine radical by oxygen.	68
Figure 3.6: Reactivity of TEMPO and related species under aerobic photoredox conditions.....	70
Figure 3.7: Initial rates analysis of TEMPO loading on rate of anisole - pyrazole photoredox coupling.....	71
Figure 3.8: Stern-Volmer quenching analysis of TEMPO and proposed SET products	72
Figure 3.9: Investigations of alternative antioxidants for arene C-H functionalizations	74
Figure 3.10: Dependence of substituent size on catalyst efficiency	76
Figure 3.11: Proposed pathways for covalent catalyst modification	77
Figure 3.12: Analysis of reaction mixture with Mes-NPA via UV-Vis	79
Figure 3.13: Analysis of reaction mixture with Xyl-NPA via UV-Vis	80
Figure 3.14: Analysis of reaction mixture with tBu-Mes-NPA via UV-Vis	82

Figure 3.15: Comparison of the absorptivity of the acridiniums shown.....	84
Figure 3.16: Reaction efficiency and catalyst stability observed using 2,7-tBu-Mes-NPA	88
Figure 3.17: Reactivity of TEMPO ⁺ BF ₄ with various arenes	91
Figure 3.18: Demonstration of scope for "second-generation" anaerobic conditions using tert butyl hydroperoxide as terminal oxidant	94
Figure 3.19: Kinetic isotope effect experiments with anisole.....	96
Figure 3.20: Exploring the effect of solution acidity on regioselectivity in addition of pyrazole to anisole	99
Figure 3.21: Outline of the elementary steps responsible for regioselectivity and the influence of acid on the equilibria	100
Figure 3.22: Revised mechanism for the photoredox arene C-H amination system and the catalytic effect of TEMPO	102

LIST OF TABLES

Table 2.1: Initial optimization of photoredox NKR.....	26
Table 2.2: Substrate scope of cation-radical accelerated NKR.....	28
Table 2.3 : Results of pyrylium fluorescence quenching by various O-aryl carbamothioates	35
Table 3.1: Stern-Volmer quenching data of a combination of acridiniums and quenchers.....	86

LIST OF ABBREVIATIONS

$*E_{1/2}$ and $E_{1/2}^*$	Excited state half wave reduction potential
$^{\circ}\text{C}$	Degrees Celsius
$+e^-$	Single electron reduction
$\pm\text{H}^+$	Protonation/deprotonation
$-e^-$	Single electron oxidation
^{13}C NMR	Carbon nuclear magnetic resonance spectroscopy
^{19}F NMR	Fluorine nuclear magnetic resonance spectroscopy
^1H NMR	Proton nuclear magnetic resonance spectroscopy
4-MeO-TPT	2,4,6-tris(4-methoxyphenyl)pyrylium tetrafluoroborate
A	Acceptor
Ac	Acetyl
Acr	Acridinium
AcO $-$	Acetate
AcOH	Acetic acid

b.p.	Boiling point
BDE	Bond Dissociation Energy
BDFE	Bond Dissociation Free Energy
BET	Back Electron Transfer
BF ₃ •OEt ₂	Boron trifluoride diethyl etherate
BF ₄	Tetrafluoroborate
Bn	Benzyl
Boc	<i>tert</i> -Butoxycarbonyl
bpy	2,2'-bipyridine
bpz	2,2'-bipyrazine
br s	broad singlet
Bz	Benzoyl
cat.	Catalytic
Cbz	Carboxybenzoyl
CDCl ₃	CDCl ₃ Chloroform- <i>d</i> ₁
CHCl ₃	Chloroform
cis	on the same side
cm	centimeter
D	Donor
d.r.	Diastereomeric ratio
DCE	1,2-dichloroethane
DCM	Dichloromethane
d	doublet

DMF	<i>N,N</i> -Dimethylformamide
DMSO	Methylsulfoxide
<i>E</i>	Energy
$E_{0,0}$	Excited state energy
$E_{1/2}^{\text{ox}}$	Oxidation potential
$E_{1/2}^{\text{red}}$	Reduction potential
Equiv.	Equivalent
ESI	Electrospray Ionization
Et	Ethyl
Et ₂ O	Diethyl ether
Et ₃ N / TEA	Triethylamine
EtOAc	Ethyl Acetate
EtOH	Ethanol
<i>F</i>	Faraday Constant
GC-MS	Gas chromatography – Mass spectrometry
HMDS	Hexamethyldisilazane
HMDSO	Hexamethyldisiloxane
HAT	Hydrogen atom transfer
Hz	Hertz
<i>i</i> Pr	isopropyl
IR	Infrared
Kcal	kilocalorie
Kcal/mol	kilocalorie per mole

KIE	Kinetic Isotope Effect
L	Liter
LED	Light-emitting diode
M	Molarity
Me	Methyl
MeCN	Acetonitrile
MeNO ₂	Nitromethane
MeO	Methoxy
MeOH	Methanol
Mes	Mesityl
MHz	Megahertz
Min	Minute
mL	Milliliter
mmol	Millimole
mol	Mole
MS	Mass spectroscopy
<i>n</i>	Moles
<i>n</i> Bu	Normal-butyl
nm	Nanometer
NMR	Nuclear Magnetic Resonance
NO ₂	Nitro
NO ₃	Nitrate
Nu / NuH	Nucleophile

<i>o</i>	ortho
O ₂	Molecular oxygen
<i>p</i>	Para
<i>p</i> -TsOH	P-toluenesulfonic acid
PC	Photocatalyst
pdt	Product
PET	Photoinduced Electron Transfer
PF ₆	Hexafluorophosphate
Ph	Phenyl
PhMe	Toluene
<i>pK</i> _a	Acid dissociation constant
PPh ₃	Triphenylphosphine
ppm	Parts per million
PRCC	Polar Radical Crossover Cycloaddition
PTFE	Poly-tetrafluoroethylene
q	Quartet
quant.	Quantitative
R	Arbitrary group
rt	Room temperature
s	Second
SCE	Saturated Calomel Electrode
SET	Single Electron Transfer
SHE	Standard Hydrogen Electrode

SM	Starting Material
T	Temperature
t-Butyl	Tertiary-butyl
Tf	Triflate
TFA	Trifluoroacetic acid
THF	Tetrahydrofuran
TLC	Thin Layer Chromatography
TMS	Trimethylsilyl
TPT	Triphenylpyrylium tetrafluoroborate
<i>Trans</i>	On the opposite side
Ts	Tosyl
TsO	Tosylate
TBS	Tert-butyldimethylsilyl
TEMPO	(2,2,6,6-Tetramethylpiperidin-1-yl)oxyl
TEMPOH	2,2,6,6-Tetramethylpiperidin-1-ol
TEMPO ⁺ ium	2,2,6,6-Tetramethyl-1-oxopiperidin-1-ium
V	Volt

CHAPTER 1: OVERVIEW OF PHOTOREDOX CATALYSIS AND RELEVANT PHOTOPHYSICAL PROPERTIES

1.1 Photophysical and Electrochemical Terms Important in Photoredox Catalysis

1.1.1 Photoredox Catalysis

In recent years there has been renewed interest in studying the chemistry of highly reactive odd-electron intermediates.¹⁻³ A number of methodologies, taking advantage of highly active radical species, have been utilized towards developing powerful C-H functionalization systems. Concurrently, the field of photoredox catalysis has seen a surge in activity due to the ability to access reactive odd-electron species.⁴⁻⁷ While these intermediates are derived from high-energy pathways their reactivity has shown a remarkable ability to be predicted and controlled to afford novel transformations. As a result of this surge in discovery a plethora of new transformations have been discovered that have already shown utility in industrial processes.⁸

Common catalysts used for photoredox catalysis include polypyridyl ruthenium and iridium-based catalysts due to their high reactivity at low loadings (**Figure 1.1**).⁵ Low cost alternatives have been developed due to the high cost of these metals.^{9,10} Considerable efforts have been made to synthesize and characterize organic analogues that display similar photophysical and electrochemical properties. However, many of these substitutes, as well as the ruthenium and iridium complexes they are based on, are unsuitable to use for a wide range of organic compounds. This is due to an energetic mismatch between photoredox catalysts electrochemical potentials ($E_{1/2}^*$) and organic compounds reduction potential ($E_{1/2}$).¹¹

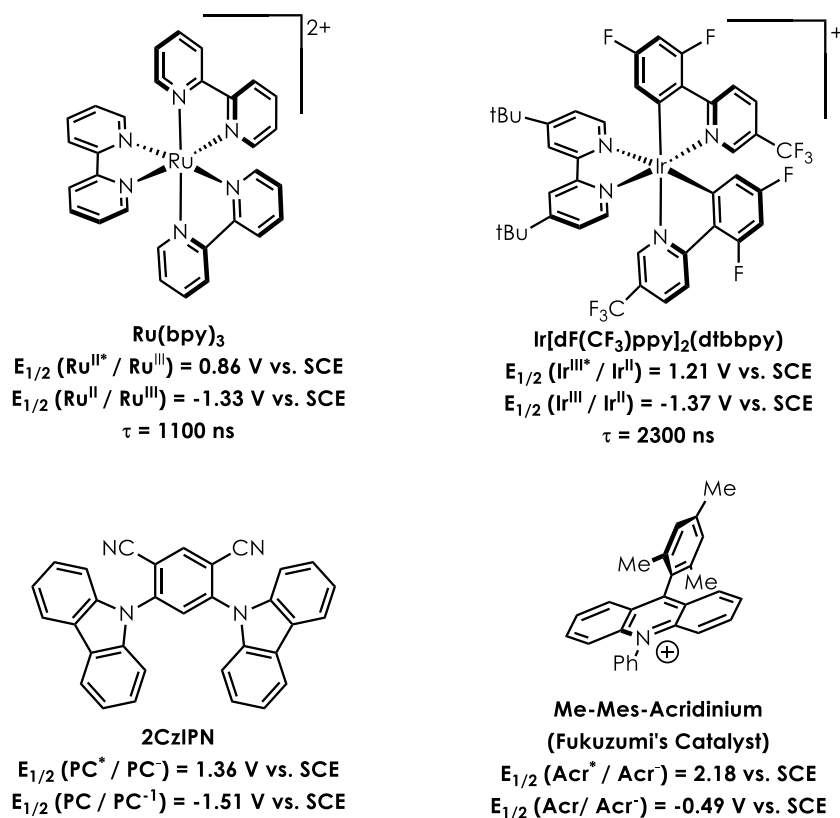


Figure 1.1. Examples of organometallic and organic photoredox dyes with relevant electrochemical and photophysical data, when available. All potentials were obtained in MeCN solutions.

1.1.2 Background of Electron Transfer and Photoinduced Electron Transfer

In the most general sense a photoredox catalyzed reaction is characterized by a redox reaction that is driven, or facilitated by, the absorption of a photon. As a result, any discussion of photoredox catalysis should include the relevant electrochemical values for reduction and oxidation of the catalyst and substrate.⁴ The free energy change for single electron transfer is given by **Equation 1.1.**, where \mathcal{F} is the Faraday constant (23.06 kcal mol⁻¹ V⁻¹) and $E_{1/2}(\text{A}/\text{A}^{\bullet-})$ corresponds to the reduction potential for single electron reduction (E_{red}) of a generic acceptor molecule **A**. $E_{1/2}(\text{D}^{\bullet+}/\text{D})$ corresponds to the reduction potential for single electron oxidation of a generic donor molecule **D**. As this value corresponds to an oxidation event, it is commonly referred to as an oxidation potential (E_{ox}) however the two terms are often used interchangeably.

Equation 1.1

$$\Delta G_{ET} = -\mathcal{F}(\Delta E) = -\mathcal{F}(E_{red} - E_{ox}) = -\mathcal{F}(E_{1/2}(A/A^{\bullet-}) - E_{1/2}(D^{\bullet+}/D))$$

Equation 1.1 outlines the thermodynamics for an electron transfer between two ground state molecules. However, as the name implies, photoredox catalysis characteristically involves an electron transfer event between two molecules, one of which in an electronically excited state in a process known as photoinduced electron transfer (PET). As a result of the extra energy gained from absorption of a photon, a compounds reduction potential is enhanced^{12,13} according to

Equation 1.2.

Equation 1.2

$$\Delta G_{PET} = -\mathcal{F}(E_{ox}(D^{\bullet+}/D) - E_{red}(A/A^{\bullet-})) - \omega - E_{0,0}$$

The excited state energy, $E_{0,0}$, accounts for the energy gained by a species when it enters an electronically excited state. The term ω is a term account for the electrostatic energy associated with charge separation that is induced from Coulombic interactions during the PET event. This term is often ignored as it has been shown to be highly variant but generally has a small impact on the overall thermodynamic calculation. Consequently, **Equation 1.2** can be simplified and is routinely used to determine if PET is favorable for a given photoredox process.

For a generic photoredox catalyst, **PC**, the excited state reduction potential ($E_{1/2}^*$) for single electron reduction of **PC** is given by **Equation 1.3**. These values can be easily determined for any **PC** through cyclic voltammetry^{11,14} ($E_{1/2}(PC/PC^{\bullet-})$) and absorption / emission spectroscopy ($E_{0,0}$). When characterizing **PC** via emission spectroscopy it is also necessary to consider from which excited state (singlet, **PC**¹ or triplet, **PC**³) the emission is occurring. In general, triplet states will have lower $E_{0,0}$, limiting their redox potentials however other considerations are needed when evaluating singlet vs. triplet systems.¹³ Once the desired **PC** has been identified and characterized

in this way, its likelihood to undergo PET with a suitable donor molecule **D** can be assessed using **Equation 1.4**.

Along the reaction coordinate for a photoredox-catalyzed mechanism, after PET a number of pathways become operative. The desired transformation can take place, if energetically favorable, however a number of deleterious pathways also become possible. Given the highly reactive nature of many of the odd-electron species generated from PET, degradation pathways are important to consider and try to limit. Most importantly, using **Equation 1.1** it also becomes obvious that after PET, the resulting $\text{PC}^{\bullet-}$ and $\text{D}^{\bullet+}$ can undergo back-electron transfer (BET) to afford the starting species. BET is found to be exergonic for any PET-initiated process and in many cases to a larger degree.¹³

This process is ultimately a non-productive pathway and serves to “waste” an absorbed photon of light, lowering the efficiency of a given photoredox transformation. It is important to consider that the presence of a thermodynamically favored PET is not indicative of a successful photoredox transformation. The various reaction dynamics of the generated odd-electron species, such as BET and other degradative pathways, ultimately determine if a desired transformation will take place. As a result, great care should be taken when analyzing photoredox mechanisms and efforts should be directed towards characterizing these “down-stream” pathways, as opposed to focusing solely on the feasibility of a proposed PET.

Equation 1.3

$$E^*_{1/2}(\text{PC}^*/\text{PC}^{\bullet-}) = E_{1/2}(\text{PC}/\text{PC}^{\bullet-}) + E_{0,0}$$

Equation 1.4

$$\Delta G_{\text{PET}} = -\mathcal{F}(E^*_{1/2}(\text{PC}^*/\text{PC}^{\bullet-}) - E_{\text{ox}}(\text{D}^{\bullet+}/\text{D}))$$

Along with $E^*_{1/2}(\text{PC}^*/\text{PC}^{\bullet-})$ it is also important to consider the lifetime (τ) of the excited state catalyst. While this property does not have any effect on the energetic favorability of PET it is

important when qualifying the relative kinetics between PET and relaxation of \mathbf{PC}^* . For example, singlet excited state species (\mathbf{PC}^1) typically have lifetimes on the order of 1 – 20 ns. As a result, PET is effectively competing with other non-productive pathways like fluorescence (τ_f) and non-radiative decay. Given the short lifetimes of singlet state \mathbf{PC}^* 's PET generally needs to be extremely rapid ($k_{\text{PET}} \sim 10^8 - 10^9 \text{ s}^{-1}$) in order to effectively compete with these pathways. Following this trend it is generally considered desirable to have a \mathbf{PC}^1 with a long singlet lifetime, as well as a high ϕ_f in order to maximize the likelihood of PET.

In contrast, triplet excited state species (\mathbf{PC}^3) tend to have much longer lifetimes (20 ns – 1000 ns are typical for organic molecules) as a result of the spin-forbidden nature of relaxation from these states. As a result, \mathbf{PC}^3 typically undergo more efficient PET despite their lower thermodynamic drive forces. Similarly, BET from \mathbf{PC}^3 -mediated PET is also typically slower due to the same electron-spin constraints.

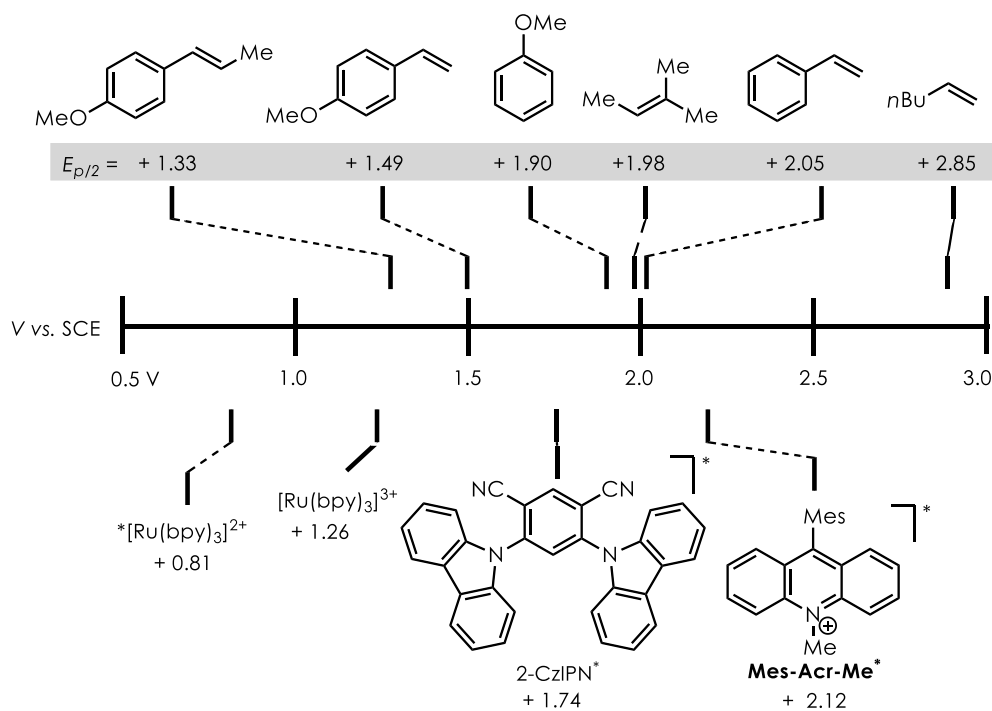


Figure 1.2. Reduction potentials of various organic compounds and common photoredox catalysts.

These factors can partially be attributed to the high reactivity and efficacy of ruthenium and iridium-based photoredox catalysts as they operate almost exclusively from triplet states.

1.2 Background of Organic Photoredox Catalysis in the Nicewicz Lab

Among organic photoredox catalysts, acridinium-based catalysts represent an attractive alternative to the metal-based compounds discussed above. Specifically, dyes derived from Fukuzumi's catalyst^{15–22} have been used in a number of systems to great effect in a number of oxidative processes. These dyes generally feature high $E^*_{1/2}$ values (~ 2.20 V vs. SCE) which renders them uniquely effective at oxidizing a wide range of organic molecules. Indeed, most common olefins and arenes possess $E_{1/2}(\text{D}^{\bullet+}/\text{D})$ values > 1.5 V vs. SCE¹¹, rendering them incompatible with many photoredox catalysts.

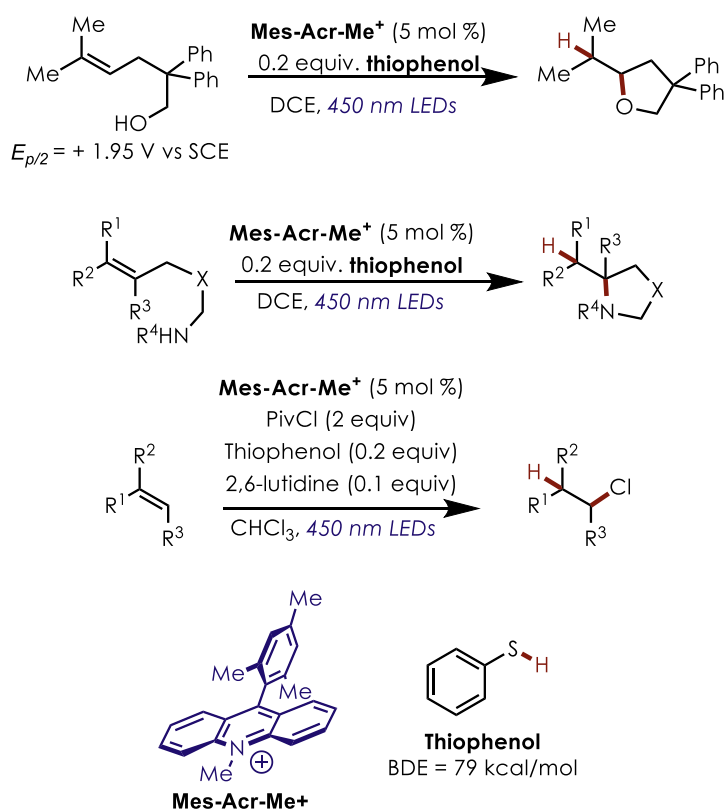


Figure 1.3. Examples of anti-Markovnikov hydrofunctionalization reactions developed in the Nicewicz lab.

The work of the Nicewicz lab^{11,23–25} has focused almost exclusively on developing new transformations using these powerful dyes. The anti-Markovnikov functionalization of olefins using a number of nucleophiles has been shown.^{26–29} This reaction manifold features the use of two different catalytic systems: a photoredox-pathway initiated via an acridinium dye and a hydrogen atom transfer (HAT) process utilizing an aryl thiol. A general mechanism is given in **Figure 1.3** and is presumed to be shared amongst all anti-Markovnikov hydrofunctionalization reactions using polar nucleophiles.³⁰

As a result of the high oxidizing potential of acridiniums, the olefin substrates can undergo exergonic PET with **Acr*** to afford the corresponding olefin cation-radical and acridine radical **Acr•**. These intermediates are rendered highly electrophilic due to the open-shell π system and undergo nucleophilic capture rapidly.³¹ This event furnishes, after deprotonation, a radical species. The regioselectivity of this process is determined by the relative stabilities of the radicals derived from the olefin. In the presence of a suitable HAT donor, such as thiophenol, this radical can be captured to furnish the anti-Markovnikov adduct. Turnover of both the acridinium catalyst as well as the thiol co-catalyst is achieved via electron transfer from **Acr•** and the thiyl radical.

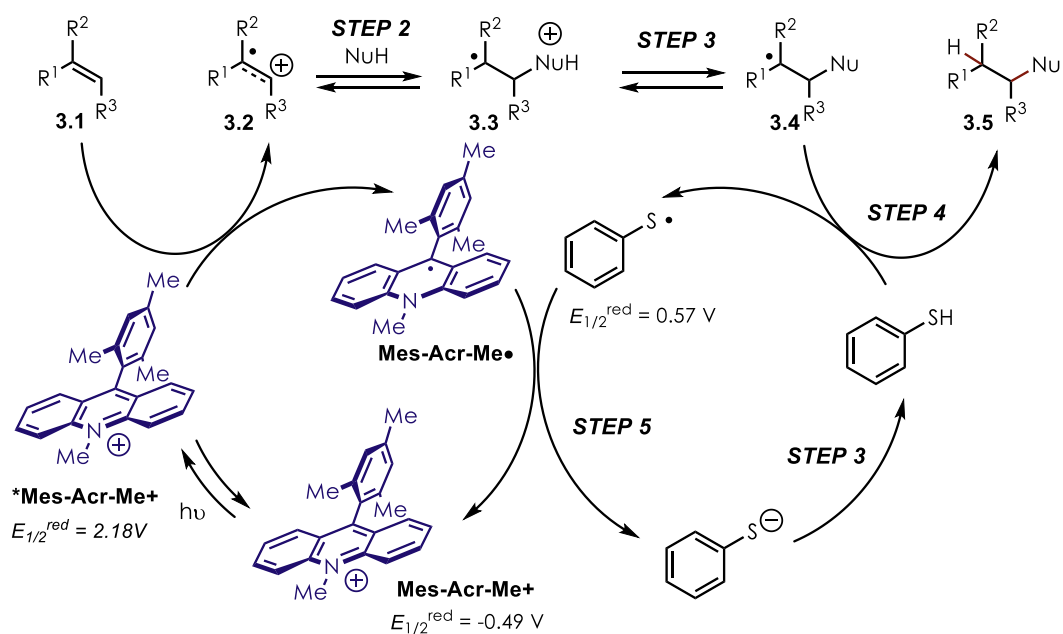


Figure 1.4. Proposed catalytic cycle for the acridinium-mediated anti-Markovnikov hydrofunctionalization of olefins. Steps 2, 4 and 5 have been observed spectroscopically³⁰.

A wide range of olefin substrates are compatible in this system from simple aliphatic tri-substituted olefins to electron-rich styrene derivatives. A range of halide, oxygen and nitrogen-containing nucleophiles have been shown to be competent coupling partners in these systems, offering access to valuable derivatives in a single, efficient step. Additionally, this reaction manifold can be modified to afford heterocycles via a polar-radical crossover cycloaddition (PRCC).^{32–34} Under these processes, a nucleophile containing a pendant π -system, generally an olefin, can undergo an intramolecular radical cyclization following nucleophilic capture (but prior to the HAT step). This cyclization affords the heterocyclic skeleton and, following HAT, furnishes the desired products. Using this methodology, a number of heterocycles, including lactones and lactams, can be synthesized rapidly in a convergent fashion from easily obtained precursors.

These reactions are known as redox-neutral transformations as there is no net change in the oxidation state of the molecule. We have also developed net-oxidation reactions using acridinium dyes in the development of various arene C-H functionalization reactions.^{35–37} These systems,

along with previous examples from Fukuzumi^{18,19}, have shown that appropriately electron-rich arenes can undergo coupling reactions with a number of nucleophiles. These transformations have allowed for the rapid synthesis of useful aryl frameworks that are commonly featured in pharmaceuticals.

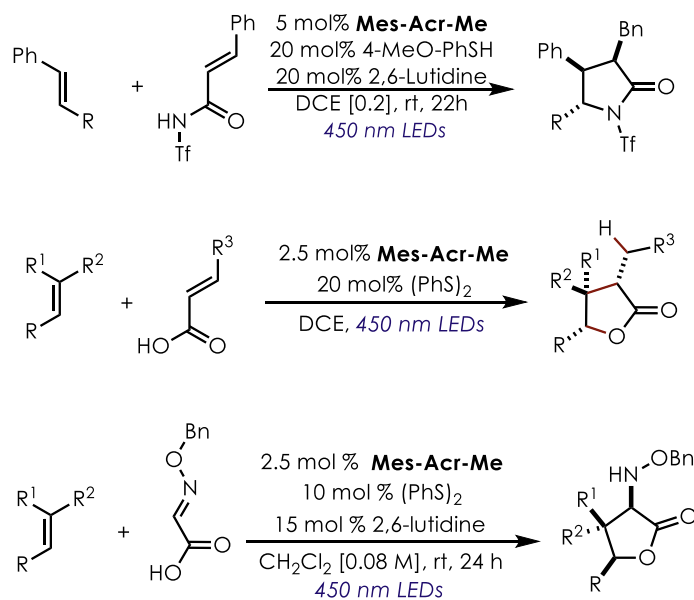


Figure 1.5. Examples of PRCC reactions developed in the Nicewicz lab.

In a similar process to the anti-Markovnikov hydrofunctionalization, the reactions are proposed to proceed via PET from the arene substrate to **Acr*** to furnish the arene cation-radical (**Figure 1.5**). This intermediate can then be captured by an appropriate nucleophile to furnish a cyclohexadienyl radical intermediate. In the presence of a suitable oxidant, O₂ in almost all cases thus far, this species can undergo a formal oxidation to afford the rearomatized coupled product³⁸. The acridinium catalyst can then be regenerated via electron transfer from **Acr•** to O₂. Consequently, this transformation represents a net two electron oxidation of the arene substrate and reduction of O₂ to formally produce HOOH. The study of this mechanism will form the basis of one chapter of the present work.

Romero *et. al.*, *Science* **2015**, *349*, 1326 - 1330

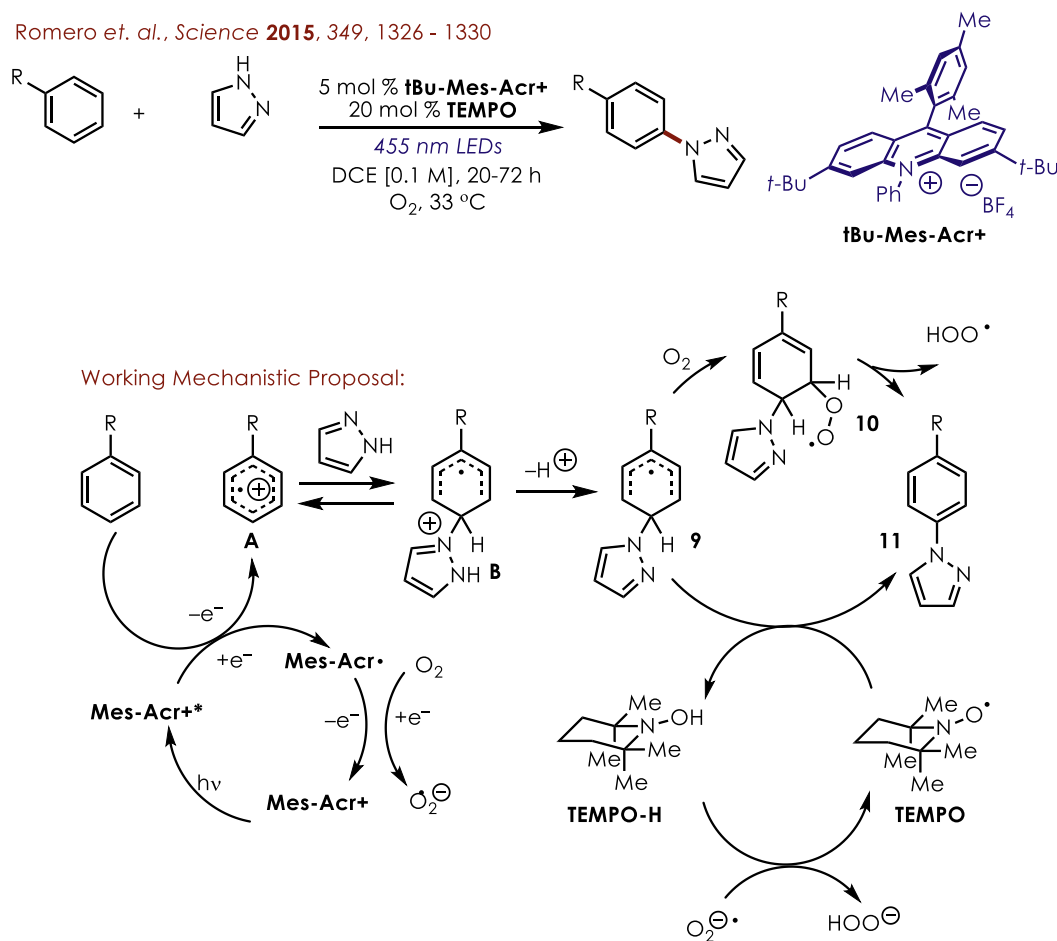


Figure 1.6. Photoredox-catalyzed arene C-H amination developed in the Nicewicz lab.

In order to better design photoredox catalyzed systems it has become necessary to undertake studies of the elementary steps of these processes. Importantly, throughout the development of acridinium-mediated systems it has been observed that the structure of the acridinium dye has a large impact on reaction efficiency. Specifically, for the transformation displayed in **Figure 1.5**, the tert-butyl acridinium catalyst displays drastically higher yields than the unsubstituted derivative **Mes-Acr-Me**. Obtaining a better understanding of the effect that catalyst structure has on reaction efficiency could allow for the development of transformations that would otherwise be unlikely. Our efforts towards this goal are reported in the following chapters.

REFERENCES

- (1) Studer, A.; Curran, D. P. Catalysis of Radical Reactions: A Radical Chemistry Perspective. *Angew. Chem. Int. Ed.* **2016**, *55* (1), 58–102.
- (2) Sibi, M. P.; Manyem, S.; Zimmerman, J. Enantioselective Radical Processes. *Chem. Rev.* **2003**, *103* (8), 3263–3296.
- (3) Yan, M.; Lo, J. C.; Edwards, J. T.; Baran, P. S. Radicals: Reactive Intermediates with Translational Potential. *J. Am. Chem. Soc.* **2016**, *138* (39), 12692–12714.
- (4) Romero, N. A.; Nicewicz, D. A. Organic Photoredox Catalysis. *Chem. Rev.* **2016**, *116* (17), 10075–10166.
- (5) Prier, C. K.; Rankic, D. A.; MacMillan, D. W. C. Visible Light Photoredox Catalysis with Transition Metal Complexes: Applications in Organic Synthesis. *Chem. Rev.* **2013**, *113* (7), 5322–5363.
- (6) Shaw, M. H.; Twilton, J.; MacMillan, D. W. C. Photoredox Catalysis in Organic Chemistry. *J. Org. Chem.* **2016**, *81* (16), 6898–6926.
- (7) Twilton, J.; Le, C. (Chip); Zhang, P.; Shaw, M. H.; Evans, R. W.; MacMillan, D. W. C. The Merger of Transition Metal and Photocatalysis. *Nat. Rev. Chem.* **2017**, *1* (7), 0052.
- (8) Douglas, J. J.; Sevrin, M. J.; Stephenson, C. R. J. Visible Light Photocatalysis: Applications and New Disconnections in the Synthesis of Pharmaceutical Agents. *Org. Process Res. Dev.* **2016**, *20* (7), 1134–1147.
- (9) Joshi-Pangu, A.; Lévesque, F.; Roth, H. G.; Oliver, S. F.; Campeau, L.-C.; Nicewicz, D.; DiRocco, D. A. Acridinium-Based Photocatalysts: A Sustainable Option in Photoredox Catalysis. *J. Org. Chem.* **2016**, *81* (16), 7244–7249.
- (10) Luo, J.; Zhang, J. Donor–Acceptor Fluorophores for Visible-Light-Promoted Organic Synthesis: Photoredox/Ni Dual Catalytic C(Sp³)–C(Sp²) Cross-Coupling. *ACS Catal.* **2016**, *6* (2), 873–877.
- (11) Roth, H.; Romero, N.; Nicewicz, D. Experimental and Calculated Electrochemical Potentials of Common Organic Molecules for Applications to Single-Electron Redox Chemistry. *Synlett* **2015**, *27* (05), 714–723.
- (12) Lakowicz, J. R. *Principles of Fluorescence Spectroscopy*, 3rd ed.; Springer: New York, 2006.
- (13) Turro, N. J.; Scaiano, J. C.; Ramamurth, V. *Modern Molecular Photochemistry of Organic Molecules*; University Science Books: California, 2010.

- (14) Elgrishi, N.; Rountree, K. J.; McCarthy, B. D.; Rountree, E. S.; Eisenhart, T. T.; Dempsey, J. L. A Practical Beginner's Guide to Cyclic Voltammetry. *J. Chem. Educ.* **2018**, *95* (2), 197–206.
- (15) Ohkubo, K.; Fujimoto, A.; Fukuzumi, S. Visible-Light-Induced Oxygenation of Benzene by the Triplet Excited State of 2,3-Dichloro-5,6-Dicyano- *p* -Benzoquinone. *J. Am. Chem. Soc.* **2013**, *135* (14), 5368–5371.
- (16) Kotani, H.; Ohkubo, K.; Fukuzumi, S. Photocatalytic Oxygenation of Anthracenes and Olefins with Dioxygen via Selective Radical Coupling Using 9-Mesityl-10-Methylacridinium Ion as an Effective Electron-Transfer Photocatalyst. *J. Am. Chem. Soc.* **2004**, *126* (49), 15999–16006.
- (17) Ohkubo, K.; Mizushima, K.; Iwata, R.; Souma, K.; Suzuki, N.; Fukuzumi, S. Simultaneous Production of *p*-Tolualdehyde and Hydrogen Peroxide in Photocatalytic Oxygenation of *p*-Xylene and Reduction of Oxygen with 9-Mesityl-10-Methylacridinium Ion Derivatives. *Chem Commun* **2010**, *46* (4), 601–603.
- (18) Ohkubo, K.; Mizushima, K.; Iwata, R.; Fukuzumi, S. Selective Photocatalytic Aerobic Bromination with Hydrogen Bromide via an Electron-Transfer State of 9-Mesityl-10-Methylacridinium Ion. *Chem. Sci.* **2011**, *2* (4), 715.
- (19) Ohkubo, K.; Fujimoto, A.; Fukuzumi, S. Photocatalytic Monofluorination of Benzene by Fluoride via Photoinduced Electron Transfer with 3-Cyano-1-Methylquinolinium. *J. Phys. Chem. A* **2013**, *117* (41), 10719–10725.
- (20) Ohkubo, K.; Mizushima, K.; Iwata, R.; Souma, K.; Suzuki, N.; Fukuzumi, S. Simultaneous Production of *p*-Tolualdehyde and Hydrogen Peroxide in Photocatalytic Oxygenation of *p*-Xylene and Reduction of Oxygen with 9-Mesityl-10-Methylacridinium Ion Derivatives. *Chem Commun* **2010**, *46* (4), 601–603.
- (21) Jonker, S. A.; Ariese, F.; Verhoeven, J. W. Cation Complexation with Functionalized 9-Arylacridinium Ions: Possible Applications in the Development of Cation-Selective Optical Probes. *Recl. Trav. Chim. Pays-Bas* **2010**, *108* (3), 109–115.
- (22) Benniston, A. C.; Harriman, A.; Verhoeven, J. W. Comment: Electron-Transfer Reactions in the 9-Mesityl-10-Methylacridinium Ion: Impurities, Triplet States and Infinitely Long Lived Charge-Shift States? *Phys. Chem. Chem. Phys.* **2008**, *10* (33), 5156.
- (23) Riener, M.; Nicewicz, D. A. Synthesis of Cyclobutane Lignans via an Organic Single Electron Oxidant–Electron Relay System. *Chem. Sci.* **2013**, *4* (6), 2625.
- (24) Perkowski, A. J.; Cruz, C. L.; Nicewicz, D. A. Ambient-Temperature Newman–Kwart Rearrangement Mediated by Organic Photoredox Catalysis. *J. Am. Chem. Soc.* **2015**, *137* (50), 15684–15687.

- (25) Morse, P. D.; Nicewicz, D. A. Divergent Regioselectivity in Photoredox-Catalyzed Hydrofunctionalization Reactions of Unsaturated Amides and Thioamides. *Chem. Sci.* **2015**, *6* (1), 270–274.
- (26) Griffin, J. D.; Cavanaugh, C. L.; Nicewicz, D. A. Reversing the Regioselectivity of Halofunctionalization Reactions through Cooperative Photoredox and Copper Catalysis. *Angew. Chem. Int. Ed.* **2017**, *56* (8), 2097–2100.
- (27) Nguyen, T. M.; Nicewicz, D. A. Anti-Markovnikov Hydroamination of Alkenes Catalyzed by an Organic Photoredox System. *J. Am. Chem. Soc.* **2013**, *135* (26), 9588–9591.
- (28) Wilger, D. J.; Grandjean, J.-M. M.; Lammert, T. R.; Nicewicz, D. A. The Direct Anti Markovnikov Addition of Mineral Acids to Styrenes. *Nat. Chem.* **2014**, *6* (8), 720–726.
- (29) Hamilton, D. S.; Nicewicz, D. A. Direct Catalytic Anti-Markovnikov Hydroetherification of Alkenols. *J. Am. Chem. Soc.* **2012**, *134* (45), 18577–18580.
- (30) Romero, N. A.; Nicewicz, D. A. Mechanistic Insight into the Photoredox Catalysis of Anti-Markovnikov Alkene Hydrofunctionalization Reactions. *J. Am. Chem. Soc.* **2014**, *136* (49), 17024–17035.
- (31) Mangion, D.; Arnold, D. R. Photochemical Nucleophile–Olefin Combination, Aromatic Substitution Reaction. Its Synthetic Development and Mechanistic Exploration. *Acc. Chem. Res.* **2002**, *35* (5), 297–304.
- (32) Cavanaugh, C. L.; Nicewicz, D. A. Synthesis of α -Benzyloxyamino- γ -Butyrolactones via a Polar Radical Crossover Cycloaddition Reaction. *Org. Lett.* **2015**, *17* (24), 6082–6085.
- (33) Gesmundo, N. J.; Grandjean, J.-M. M.; Nicewicz, D. A. Amide and Amine Nucleophiles in Polar Radical Crossover Cycloadditions: Synthesis of γ -Lactams and Pyrrolidines. *Org. Lett.* **2015**, *17* (5), 1316–1319.
- (34) Grandjean, J.-M. M.; Nicewicz, D. A. Synthesis of Highly Substituted Tetrahydrofurans by Catalytic Polar-Radical-Crossover Cycloadditions of Alkenes and Alkenols. *Angew. Chem. Int. Ed.* **2013**, *52* (14), 3967–3971.
- (35) McManus, J. B.; Nicewicz, D. A. Direct C–H Cyanation of Arenes via Organic Photoredox Catalysis. *J. Am. Chem. Soc.* **2017**, *139* (8), 2880–2883.
- (36) Romero, N. A.; Margrey, K. A.; Tay, N. E.; Nicewicz, D. A. Site-Selective Arene C Amination via Photoredox Catalysis. *Science* **2015**, *349* (6254), 1326–1330.
- (37) Margrey, K. A.; Levens, A.; Nicewicz, D. A. Direct Aryl C–H Amination with Primary Amines Using Organic Photoredox Catalysis. *Angew. Chem. Int. Ed.* **2017**, *56* (49), 15644–15648.

- (38) Fang, X.; Pan, X.; Rahmann, A.; Schuchmann, H.-P.; von Sonntag, C. Reversibility in the Reaction of Cyclohexadienyl Radicals with Oxygen in Aqueous Solution. *Chem. - Eur. J.* **1995**, *1* (7), 423–429.

CHAPTER 2: DEVELOPMENT OF A PHOTOREDOX-MEDIATED NEWMAN-KWART REARRANGEMENT

Reproduced in part with permission from Perkowski, A. J.; Cruz, C. L.; Nicewicz, D. A. *J. Am.*

Chem. Soc. **2015**, *137*, 15684–15687. Copyright 2015 American Chemical Society

2.1 The Importance of Aryl Sulfides in Bioactive Molecules and Their Synthesis

The aryl sulfide moiety is a common motif in naturally occurring bioactive compounds as well as pharmaceutical and agrochemical agents (**Figure 2.1**). A variety of chemical tools have been developed as a means of establishing this important functionality. These methodologies include simple alkylation reactions of aryl thiolates¹, trapping of organometallic reagents with electrophilic sulfur sources², cross-coupling manifolds³, and rearrangement reactions like the Smiles or Newman-Kwart rearrangements. The formation of aryl sulfides from thiophenol derivatives and alkylating agents is perhaps the simplest method however suffers from a low availability of chemically diverse thiophenol derivatives.

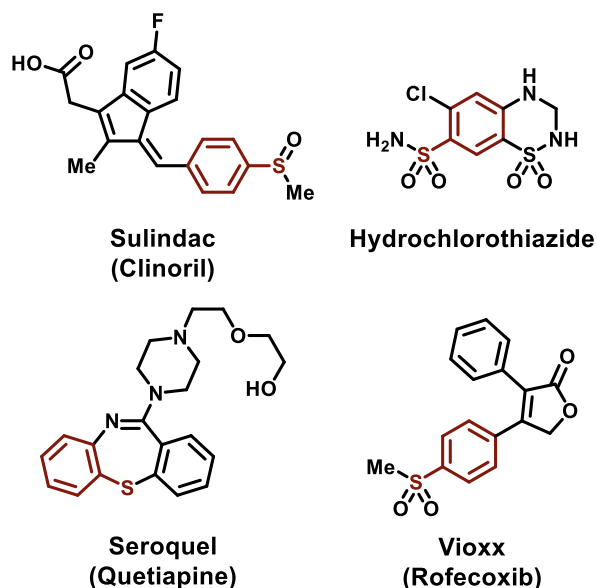


Figure 2.1. Examples of bioactive molecules containing an aryl-thiol linkage.

Instead, organometallic cross-coupling reactions between an aryl halide and thiol nucleophile represent an attractive alternative to rapidly construction aryl sulfides with diverse structures.

Despite the similarity to other cross-coupling methodologies, *e.g.* the Buchwald-Hartwig amination, thiol cross-couplings have not been explored as extensively. One possible reason for this lack of chemical investigation is due to a lack of suitable catalytic systems. Common cross-coupling systems include late-transition metal catalysts featuring phosphine-ligated Pd, Cu or Ni complexes. These metal-ligand combinations have shown to be extremely effective for cross-coupling reactions, however, thiols are known to form unfavorable complexes with these metals.

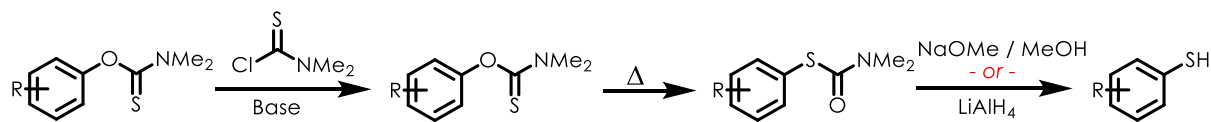
Thiols, or thiolates, can displace dative phosphine ligands, critical for cross-coupling activity, to form metal-thiolate complexes that show drastically reduced activity or are simply inactive. Thus, suitable catalytic systems for aryl-thiol cross-couplings require suitably strong ligands that cannot be displaced by the thiol substrates. An early example demonstrating the success of this strategy employed small loadings of Pd with a bulky, electron rich phosphine ligand (JosiPhos)³. Using this catalytic system, it was shown that a variety of alkyl and aryl thiols could be cleanly

coupled to aryl halides, or pseudohalides, in good to excellent yields. Importantly, a hydrogen sulfide equivalent, TIPS-SH, was shown to be a competent nucleophile under these reaction conditions. Use of this reagent would allow for the straightforward synthesis of aryl sulfides for which either the appropriate electrophilic or nucleophilic coupling partner could not be easily obtained.

2.2 The Newman-Kwart Rearrangement: A Brief History

An attractive alternative to cross-coupling methodologies for the synthesis of aryl thiols is the Newman-Kwart rearrangement (NKR).^{4,5} This transformation can formally be described as the synthesis of a thiophenol derivative from the corresponding phenol (**Figure 2.2**). Phenols are common chemical feedstocks and as a result more derivatives exist for purchase. Consequently, syntheses of aryl alcohols, for which there exist more methods for construction, constitute formal syntheses of aryl thiophenols through the NKR.

Figure 2.2. Representative synthetic sequence for thiophenols utilizing Newman-Kwart Rearrangement.



A typical reaction sequence for the overall transformation begins with thiocarbamylation of the phenol with *N,N*-thiocarbonyl chloride, a commercially available solid, in the presence of a base and heating in aprotic media. This generally high-yielding step affords the *O*-aryl carbamothioate, generally crystalline solids, which can then be subjected to NKR to form the desired *S*-aryl carbamothioate. The thiophenol can then be liberated via methanolysis or reductive conditions in generally good-to-excellent yields. Alternatively, the disulfide can be obtained via methanolysis under an O₂ atmosphere. The NKR overall represents a three-step

synthetic sequence, however, the thiocarbamoylation and cleavage steps are generally high and thus synthetically useful.⁶

First reported in 1966 by Kwart⁵, the vapor phase rearrangement of *O*-aryl carbamothioates was achieved via flash vacuum pyrolysis (FVP). While this represented the first report of the transformation it was not immediately useful to the synthetic chemist. The apparatus needed for FVP required specialized glassware and throughput of material in this method was slow. A more synthetically useful protocol was published the same year by Newman⁴ wherein the rearrangement could be achieved via batch heating on the benchtop (**Figure 2.3**). Excellent yields of the *S*-aryl carbamothioates could be achieved by heating the *O*-aryl carbamothioate either as the bulk solid or in a high boiling solvent like diphenyl ether. Due to the extreme temperatures, reaction mixtures must be rigorously degassed in order to avoid undesired oxidation products. However, the utility of the products and the ease of execution makes the NKR an attractive protocol for the synthesis of thiophenol derivatives.

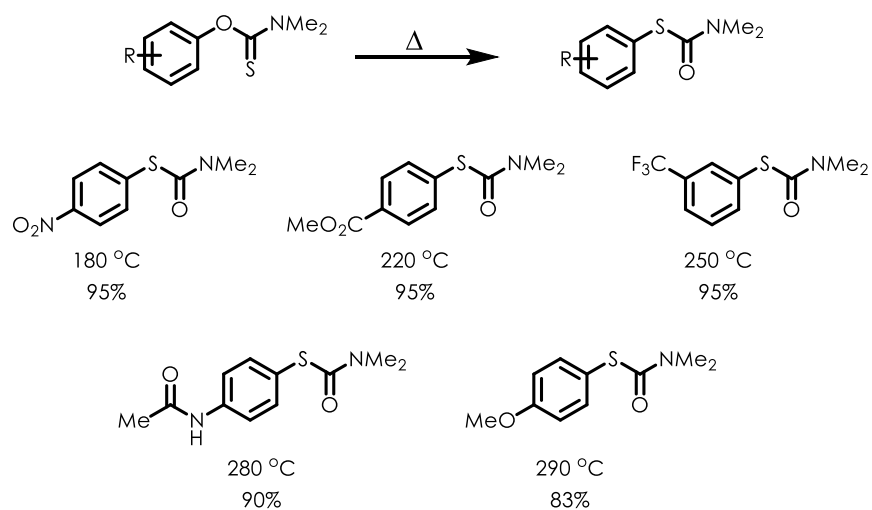


Figure 2.3. Selected substrate scope of Newman's initial report.

The original report from Newman showed an excellent substrate scope, tolerating both electron-rich and electron-poor arene substrates (**Figure 2.3**). One important feature of the

substrate scope that Kwart reported was a distinct temperature dependence for the rearrangement. For example, 4-nitro *O*-aryl carbamothioate **X** underwent smooth NKR at 180 °C while the 4-methoxy derivative required prolonged heating at 290 °C. This trend was reliably observed across electronically-differentiated substrates, with more electron-deficient substrates requiring substantially lower temperatures for rearrangement. Moreover, substrates with Lewis basic functional groups could be activated for rearrangement at drastically lower temperatures. For example, 2 and 4-pyridyl substrates could be acetylated, affording the acyl-pyridinium species *in-situ*, and undergo NKR at room temperature. Simple hydrolytic workup afforded the cleaved pyridine products. Similarly, carbonyl-containing arenes could be activated using boron trifluoride as a Lewis acid and undergo NKR at much lower temperatures.

These observations, also qualitatively comparable to those made by Kwart, supported the mechanism shown below (**Figure 2.4A**). Partially inspired by the structurally-related Schonberg⁷ and Chapman⁸ rearrangements, the *O*-aryl carbamothioate was proposed to undergo an intramolecular nucleophilic capture through the carbamothioate moiety. The resulting Meisenheimer complex, a spirocyclic thiotane, can undergo C-O cleavage to afford the rearranged *S*-aryl carbamothioate. The overall transformation has been shown to be favorable due to the formation of the more thermodynamically stable carbonyl complex from the thione. The extreme temperatures required for rearrangement can be rationalized due to the enthalpic penalty of breaking aromaticity as well as the ring-strain induced during formation of the spirocyclic transition state.

Shortly after the initial publication of the transformation two groups undertook more detailed mechanistic studies of the NKR. Pizzolato⁸ *et al.* confirmed initial reports from Newman that the reaction proceeded via a unimolecular mechanism; kinetic monitoring of the reaction showed

excellent fitting to a first-order exponential decay. Moreover, Pizzolato undertook Hammett and Arrhenius analyses of the rearrangement to confirm other features of the reaction. The Arrhenius analysis suggested that the NKR proceeds through a very high energy transition state ($\Delta H^\ddagger = 39.5 \pm 1.5$ kcal / mol for the parent substrate) as well as a moderately ordered transition state. It was also noted that including substitution at the 2 and 6 positions of the arene tended to decrease ΔS^\ddagger (Figure 2.4B), suggesting that the molecular geometry for these substrates was preorganized in the conformation required for the proposed ipso-nucleophilic capture. These data, combined with the Hammett analysis affording $\rho = 1.62$ vs. σ^- , offer excellent support for the spirocyclic transition state proposed by Newman. These results were also supported by a corresponding study published by Miyazaki⁹, who also reported a negative crossover experiment which supports the unimolecularity of the rearrangement.

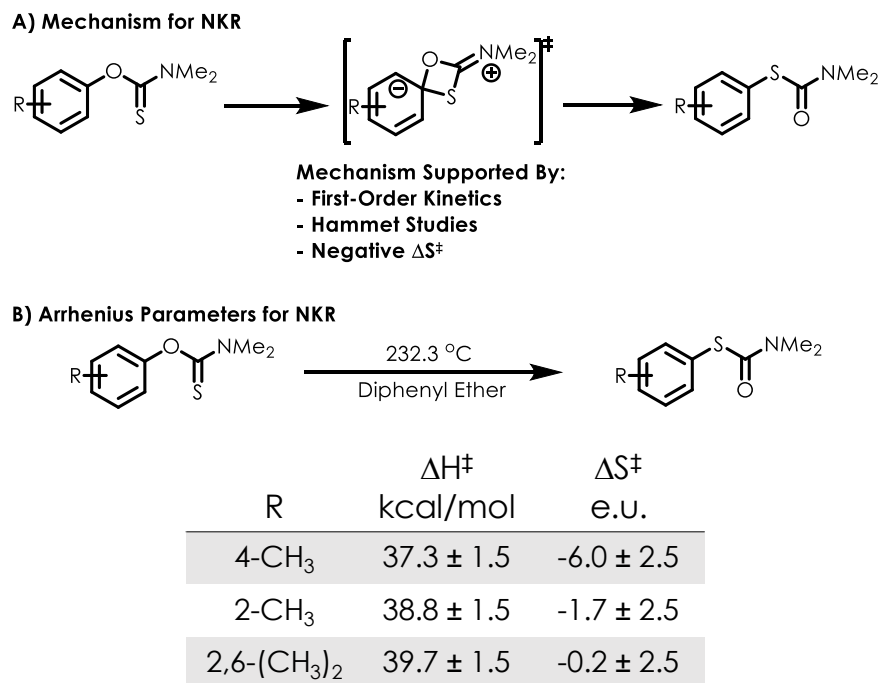


Figure 2.4. A) Experimentally supported mechanism for NKR and B) Relevant thermochemical data for NKR.

Given the utility of the NKR in generating novel aryl thiols a variety of modifications to the original procedure have been developed in the literature¹⁰⁻¹². Most efforts have, as their main goal, attempted to either make the extreme temperatures required for NKR more practically amenable via microwave heating or reducing the temperature altogether via catalytic methods. Microwave heating has emerged as an attractive method to achieve high reaction temperatures under very controlled conditions. Heating via microwave allows for a more even thermal distribution throughout a reaction solution ensuring that there is not a large temperature gradient throughout a reaction.

A major decomposition pathway observed during NKR is charring of reaction material due to insufficient heat transfer from the outer edges of a reaction container to the inner volume of material. As a result, a number of microwave heated NKR systems have been reported in the literature. These systems^{10,11} feature excellent tolerance of a variety of functional groups for NKR and have demonstrated better impurity profiles over traditional batch-heating (**Figure 2.5**). One system has also been reported using water as a solvent which is a large improvement over the traditional solvents used (*e.g.* NMP and dichlorobenzene) in terms of waste generation.

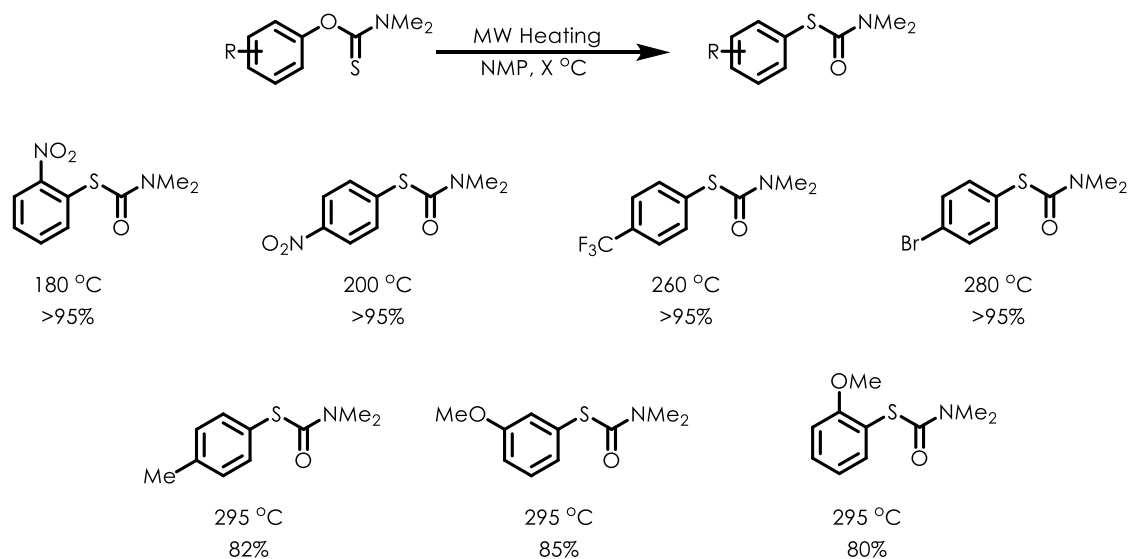


Figure 2.5. Selected examples of NKR achieved through microwave heating.

Alternatively, methods towards lowering the reaction temperatures for NKR have been investigated. Newman initially reported Lewis and Bronsted acid catalyzed systems in his initial report, *vide supra*, however these methods are specific to substrates bearing Lewis or Bronsted basic functional groups in conjugation with the aryl π system. A more general catalytic method was reported recently by Lloyd-Jones¹² utilizing a Pd-based catalytic system (**Figure 2.6**).

Using a simple phosphine ligand and low loadings of Pd the NKR could be affected at lower temperatures. For example, an arene bearing a single nitro group undergoes thermal NKR at 180 °C while in the Pd-catalyzed system quantitative NKR was observed at 100 °C. These conditions represent a dramatic decrease in reaction temperature especially for electron-rich substrates, which undergoes NKR at 295 °C through batch heating. However, this example also required a much larger Pd loading (8 mol% vs 2 mol%). Mechanistic experiments supported a catalytic cycle initiated via oxidative addition into the aryl-O bond followed by reductive elimination to form the aryl-S bonded product.

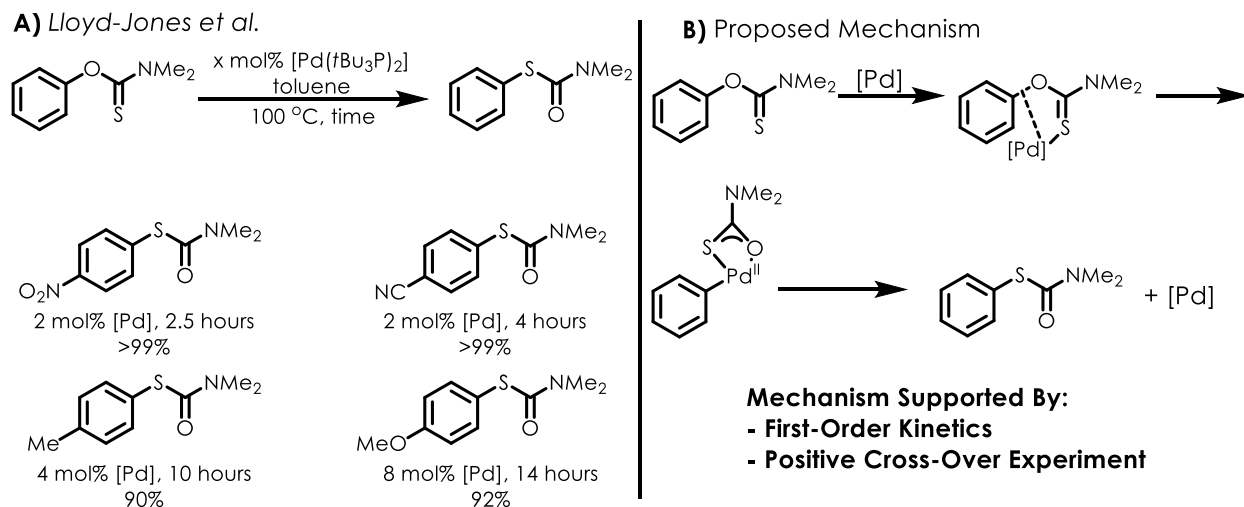


Figure 2.6. A) Palladium-catalyzed NKR reported by Lloyd-Jones B) Proposed mechanism

2.3 A Proposed Photoredox-Mediated Pathway

We became interested in developing an alternative catalytic method for NKR as a result of our groups desire to synthesize thiophenol derivatives. During our analysis of the NKR literature we concluded that while there were numerous methods to effect the NKR, there was no general method that favored arenes bearing electron-donating groups. The system developed by Lloyd-Jones was compatible with this substrate class however featured much higher Pd loading which makes this process unattractive due to the cost of Pd. We became curious if a catalytic method could be developed that was more amenable to electron-rich arene substrates.

We postulated that a photoredox-mediated NKR might be possible via single electron oxidation of an *O*-aryl carbamothioate using a suitable organic photocatalyst (**Figure 2.7**). This would furnish the corresponding cation-radical, *a priori* designated as an arene-centered cation-radical, which we believed might lower the barrier for the required intramolecular nucleophilic capture. This would furnish the *S*-aryl carbamothioate cation radical at reduced temperatures,

relative to the traditional conditions, which could undergo single electron reduction by the reduced form of the photocatalyst, furnishing the product.

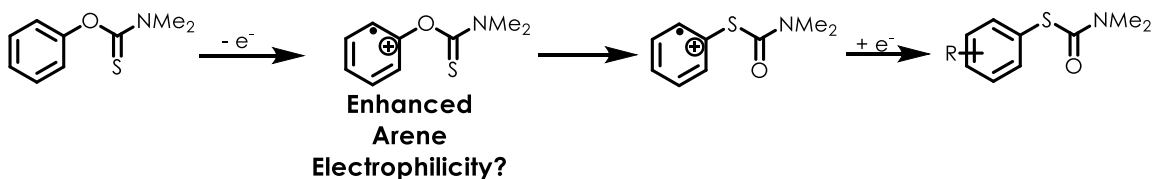


Figure 2.7. Proposed sequence for cation-radical accelerated NKR.

The proposed mechanism for a cation-radical mediated NKR was initially supported by a report from Prabhakar¹³ detailing a study of *O*-aryl carbamothioates via GC-MS. It was found that both isocyanate and isothiocyanate fragmentation patterns, respectively generated from *S*-aryl and *O*-aryl carbamothioates, could be observed in the mass spectra for *O*-aryl species. A thermal rearrangement process was ruled out by varying the injection and column temperatures of the GC, strongly suggesting that the *S*-aryl carbamothioate fragmentation species were being generated during ionization in the MS. It was proposed that this ionization produced the *O*-aryl carbamothioate cation radical and that rearrangement occurred to generate the *S*-aryl carbamothioate cation radical, both of which could then undergo the required fragmentation processes. Importantly, they noted that when synthesized samples of *S*-aryl carbamothioates were analyzed in this method no isothiocyanate fragmentation species were observed, suggesting that the rearrangement was irreversible. Given these results we became confident that a solution-phase, synthetically useful photoredox NKR could be developed.

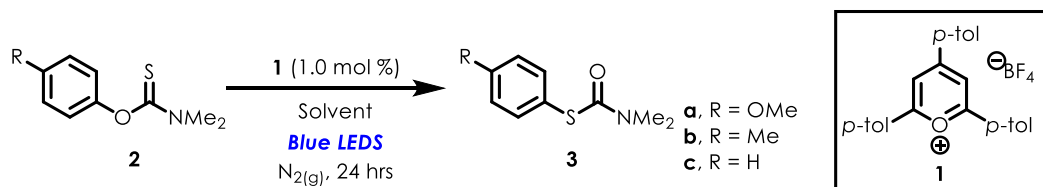
2.4 Initial Studies of a Photoredox Newman-Kwart Rearrangement

In order to begin investigating a photo-redox NKR we identified a model substrate and photoredox catalyst that we believed would be most suitable for reactivity under our proposed mechanism. We began our studies by irradiating solutions of *O*-(4-methoxyphenyl) dimethylcarbamothioate (**2a**) with 1.0 mol % **1** using blue light emitting diodes (LEDs). It was

decided that the methoxy group present in **2a** should render the substrate sufficiently oxidizable by the catalyst **1** based on the high redox potential of **1*** ($E_{1/2}^* = 2.30$ V vs. SCE) and the ease of oxidation of methoxy-substituted arenes (as a reference, $E_{1/2}(\text{anisole}) = 1.90$ V vs. SCE).

After 24 hours, formation of *S*-(4-methoxyphenyl) dimethylcarbamothioate **3a** was evident via ^1H NMR analysis, though appreciable amounts of **2a** remained (Table 2.1, entry 1). The more polar solvents dichloromethane and acetonitrile were tested (entries 2 and 3, respectively), and complete conversion of **2a** was observed after 24 hours. Ease of work-up and purification lead us to choose acetonitrile as the optimal solvent. No appreciable side products were observed by ^1H NMR analysis of the crude reaction mixture, and a silica plug eluted with 19:1 hexanes/ethyl acetate was sufficient to provide pure **3a**. The reaction was initially found to be relatively tolerant of ambient oxygen, though further studies were done under anaerobic conditions due to the propensity of oxygen to react with radical-cation intermediates.

After discovering this initial result additional substrates were synthesized and tested in this new system. The less-electron rich 4-methyl substituted **2b** failed to give detectable levels of conversion in the system as first tested. It was initially hypothesized that this lack of reactivity was due to a more difficult oxidation step, as a methoxy-bearing arene is generally more readily oxidizable than a methyl-bearing arene (*e.g.* the $E_{p/2}$ of oxidation for anisole and toluene are ~ 1.9 V and 2.3 V, respectively, vs. SCE). Consequently, initial optimization attempts focused on screening different photooxidants that might improve the efficiency of substrate oxidation. In all cases no increase in reactivity was observed, suggesting that the lack of reactivity was not due to inefficient electron transfer.

Table 2.1. Initial optimization of photoredox NKR.

Entry	Substrate	Solvent	Conc. [M]	3 : 2
1	2a	CHCl ₃	[0.5]	1 : 2
2	2a	DCM	[0.5]	> 19 : 1
3	2a	MeCN	[0.5]	> 19 : 1
4	2b	MeCN	[0.5]	1 : 9
5	2b	MeCN	[0.12]	1 : 3
6	2b	MeCN	[0.06]	> 19 : 1
7	2c	MeCN	[0.03]	1 : 1

It was eventually found through additional optimization for **2b** that more dilute conditions resulted in dramatic rate increases. Dilution of the reaction solution from [0.5 M] to [0.06 M] afforded the rearranged product now in acceptable yields. It was observed that the level of dilution could be increased to give faster reactivity for **2a**, suggesting that substrate concentration might play an important role for rearrangement of all substrates. The parent *O*-phenyl dimethylcarbamothioate **2c**, which features no electron-releasing substituents, reacted poorly even at more drastically dilute conditions ([0.03 M]) (entry 7).

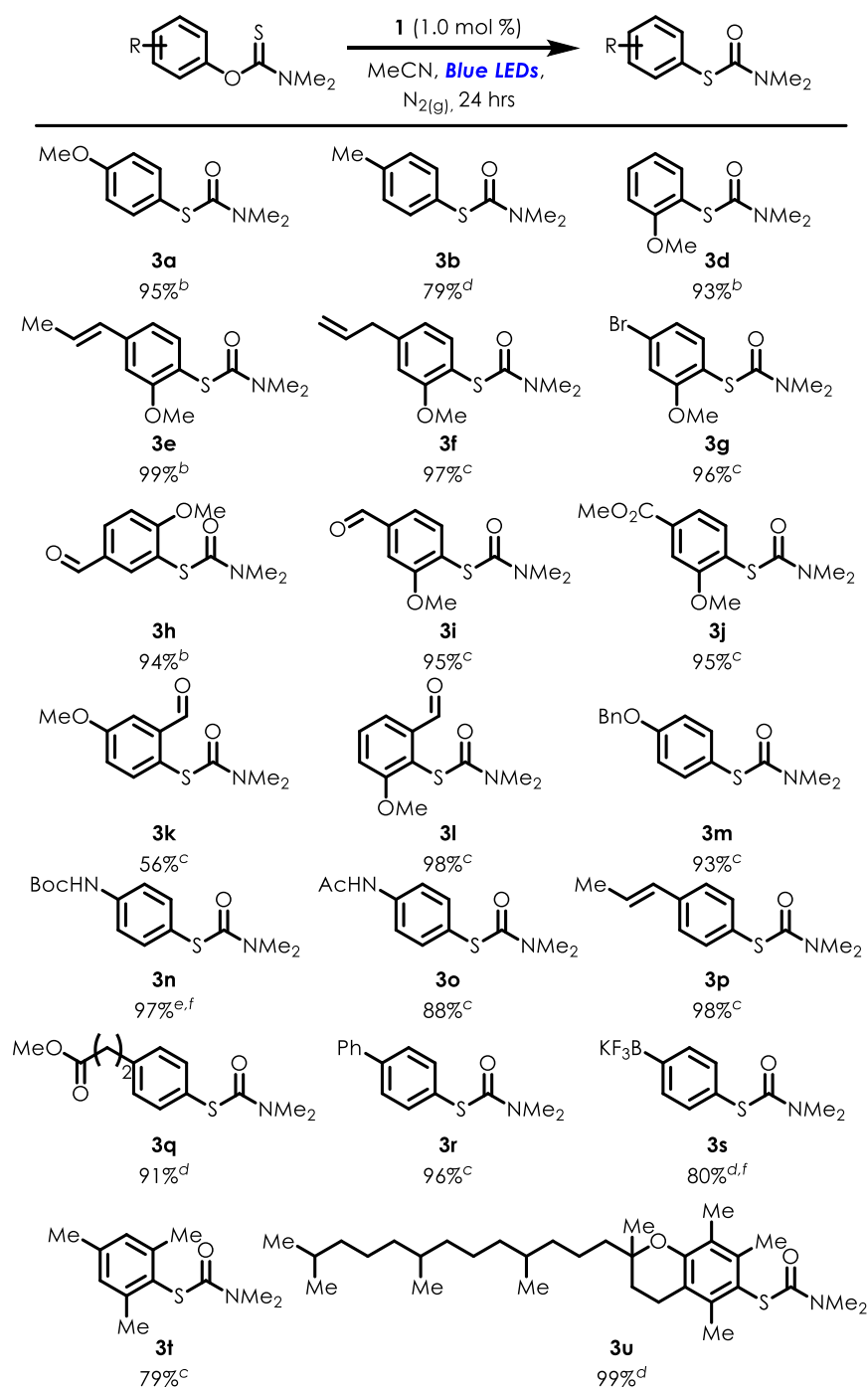
2.5 Substrate Scope of Photoredox Newman-Kwart Rearrangement

Next, the scope of the reaction was investigated (Table 2.2). Given the observed concentration dependence, an optimum concentration was identified that would afford 100% conversion within 24 h. In general, more dilute conditions were observed to accelerate rearrangement of all the

substrates under examination. The *O*-(2-methoxyphenyl) dimethylcarbamothioate reacted competently to afford **3d** in excellent yield. Additional 2-methoxy substituted substrates underwent smooth rearrangement providing the propenyl-substituted **3e**, allyl substituted **3f**, bromo-substituted **3g**, *meta* and *para* formyl substituted **3h** and **3i**, respectively, and the 4-methylester substituted **3j**, all in nearly quantitative yields. The *O*-(2-formyl-4-methoxyphenyl) dimethylcarbamothioate also rearranges smoothly to give **3k** in good isolated yield as does the *O*-(2-formyl-6-methoxyphenyl) dimethylcarbamothioate **3l**. Benzyl protecting groups are also tolerated (**3m**) in good yield as well as thermally-sensitive Boc groups (**3n**).

The corresponding dimethylcarbamothioate of acetaminophen readily undergoes the *O*–*S* rearrangement, giving the corresponding *S*-aryl dimethylcarbamothioate **3o** in excellent yield. Less electron-rich groups can also be present, as evidenced by 4-propenyl substituted **3p**, dihydrocinnamyl methyl ester derivative **3q**, and biphenyl **3r** which all underwent rearrangement in good to excellent yields (88-98%). It is worthy of note that **3p** is produced as >19:1 ratio of *E* to *Z* isomers, despite beginning with a 1:9 *E*:*Z* ratio of the propenyl carbamothioate. Given this, it is notable that the allyl group of **3f** does not undergo any detectable isomerization to the propenyl product **3e**. We were also pleased to find that a potassium trifluoroborate salt substrate is also capable of undergoing the photoredox mediated NKR (**3s**), providing a handle for further elaboration using cross coupling techniques. Finally, sterically-hindered substrates derived from mesitol and (\pm)-alpha tocopherol also reacted efficiently, giving **3t** and **3u**, respectively.

Table 2.2. Substrate scope of cation-radical accelerated NKR.^a



^aIsolated yields, the average of two reactions at 100 mg scale of substrate. ^b[0.5 M] substrate concentration, ^c[0.12 M] substrate concentration, ^d[0.06 M] substrate concentration, ^e[0.03 M] substrate concentration with 48 h irradiation, ^f5 mol% **1**

Unfortunately, *O*-(2-naphthyl) dimethylcarbamothioate failed to give appreciable rearrangement, while the regioisomeric *O*-(1-naphthyl) dimethylcarbamothioate (**2v**) was a competent candidate providing **3v** in excellent yield (**Figure 2.8A**). Intriguingly, the propensity towards rearrangement under thermal NKR conditions is reversed, with *O*-(2-naphthyl) dimethylcarbamothioate undergoing *O* to *S* aryl migration at 285 °C, while **2v** does not undergo rearrangement under thermal conditions.¹⁴

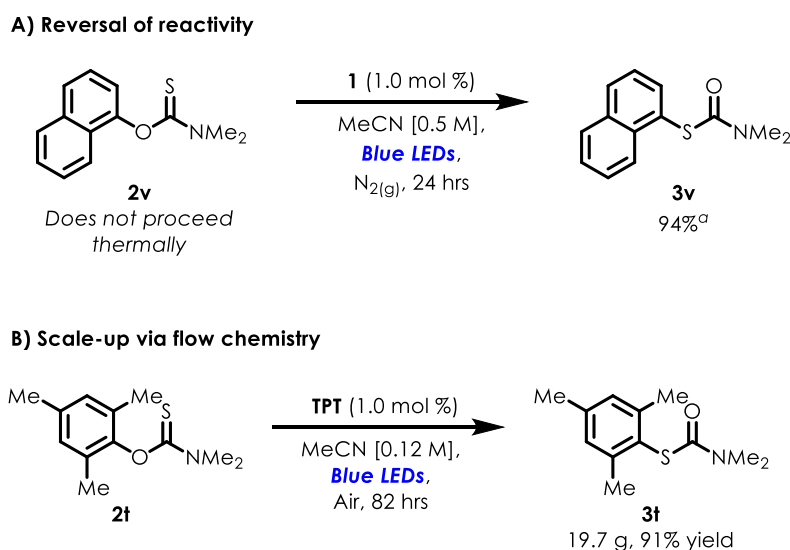


Figure 2.8. A) Evidence for complementary reactivity of naphthyl substrates between thermal and cation-radical NKR. B) Example of multi-gram scale cation-radical NKR.

The broad substrate scope and practical execution of the photoredox NKR prompted us to explore simple methods for scale-up. A common obstacle in scaling photochemical reactions is the development of experimental setups that provide sufficient photon flux to allow for reactivity. On small scales (typically ~100 mg or 0.5 mmol scale in 2 dram vials as reaction vessels), irradiation by high-powered LED flood lamps provides sufficient photon flux to achieve high reactivity. At larger scales (> 1g in round bottom flasks), photon flux becomes severely limiting for reactivity. In our hands we found that the photoredox NKR afforded inconsistent results on gram-scale reactions run in round-bottom flasks when irradiated with flood lamps. We attribute this to poor

light penetration due to the curvature of the glassware and the increased photon flux requirement due to the increase in reaction volume.

Consequently, we became interested in developing a flow apparatus to overcome this practical barrier to large scale reactivity. Adopting photochemical reactions to flow processes is inherently beneficial, due to the increased surface area afforded by flow setups, which would allow for better light penetration without the need for developing more powerful LEDs. We chose *O*-(2,4,6-trimethylphenyl) dimethylcarbamothioate (**2t**) as a representative substrate to assess the suitability of this protocol using a flow apparatus (**Figure 2.8B**). No precautions were taken to exclude moisture or oxygen and we employed commercially-available triphenylpyrylium tetrafluoroborate (**TPT**) as catalyst. Using the optimized conditions, 21.5 grams of **2t** underwent smooth rearrangement to **3t** after 82 hours. After chromatography, the desired product was isolated in a 91% yield providing 19.7 grams of **3t**.

Despite the success of this system, there are substitution patterns for which rearrangement was not observed (**Figure 2.9**). Weakly deactivating groups like a boronate ester (**4a**) showed diminished reactivity as well as *meta*-substituted methoxy substrate (**4b**), a drastic difference in comparison to the *ortho* and *para*-isomers (vide supra). Monosubstituted haloarenes gave little to no rearrangement, regardless of halide identity or position. Substrates bearing alkenyl or aryl substitution *ortho* to the *O*-carbamothioate moiety also proved recalcitrant. Additionally, substrates containing only a single *meta* substituent showed reduced or no reactivity. As a rough generalization it appeared that in order to achieve appreciable conversion in the photoredox NKR a substrate must possess an activating group in either the *ortho* or *para* positions.

Having demonstrated the utility and scope of the photoredox NKR we became interested in further elucidating the mechanism of the transformation. Our working mechanism throughout the

initial development of the cation-radical NKR is in **Figure 2.10**. Excitation of **1** by visible light results in the formation of the highly oxidizing **1*** which can feasibly undergo SET upon encountering the substrate **2**, furnishing an arene cation-radical species **5**. Rearrangement from this intermediate affords the *S*-aryl carbamothioate cation-radical **6** which can undergo reduction to afford **3**. This can occur via SET from either the reduced form of **1** to regenerate the catalyst or from another equivalent of **2** in a chain-transfer process.

A few key features prompted us to reconsider our initial mechanistic proposal. First, a

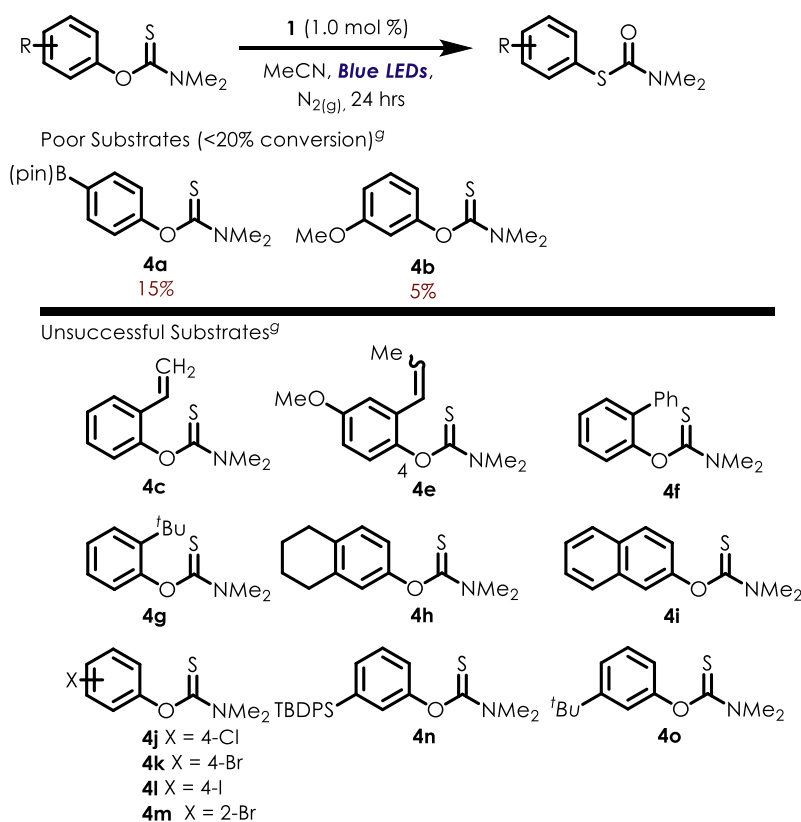


Figure 2.9. Limitations of cation-radical NKR.

definitive explanation for why certain substrates display excellent reactivity in the present system while others show none. The drastic concentration dependence on reactivity could not be explained by a simple oxidation – rearrangement – reduction sequence of events. In order to account for concentration dependence, we believed that there may exist off-cycle reactivity of one or more

intermediates. Moreover, this concentration dependence was apparently closely coupled to the electronic nature of the arene substrate. Under our initial mechanistic proposal, we believed that more electrophilic arene cation-radicals would undergo rearrangement more easily. Consequently, substrates bearing less-activating substituents were expected to react more favorably. The observed reactivity trends suggested that these substrates were in fact the most recalcitrant. These questions prompted us to re-evaluate our mechanistic proposal through a more thorough mechanistic study.

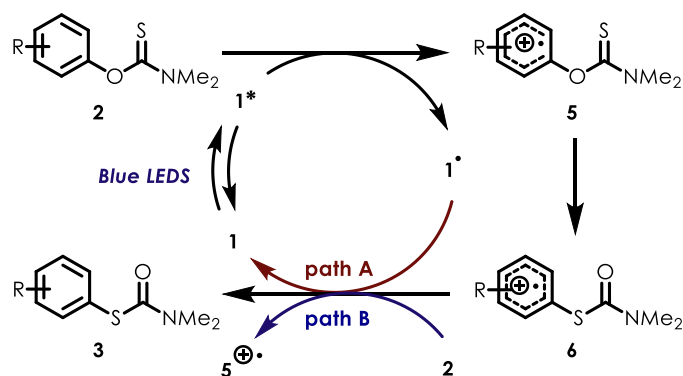


Figure 2.10. Initial proposed mechanism for cation-radical NKR.

2.6 Cyclic Voltammetry of S-aryl Carbamothioates

Initial efforts towards studying the mechanism of the photoredox NKR focused on electrochemical studies of the *O*-aryl and the corresponding *S*-aryl carbamothioate substrates via Cyclic Voltammetry (CV). Analysis of **2a** and **3a** gave several irreversible oxidation waves (Figure 2.11). Qualitatively, the traces for **2a** and **3a** appear similar except for an irreversible oxidation wave with $E_{p/2} = +1.1$ V vs SCE present in the CV trace for **2a** but absent for **3a**. This irreversible oxidation wave proved to be diagnostic of an *O*-aryl carbamothioate. A number of substrates were analyzed by CV and in all cases, even for *O*-aryl carbamothioates that

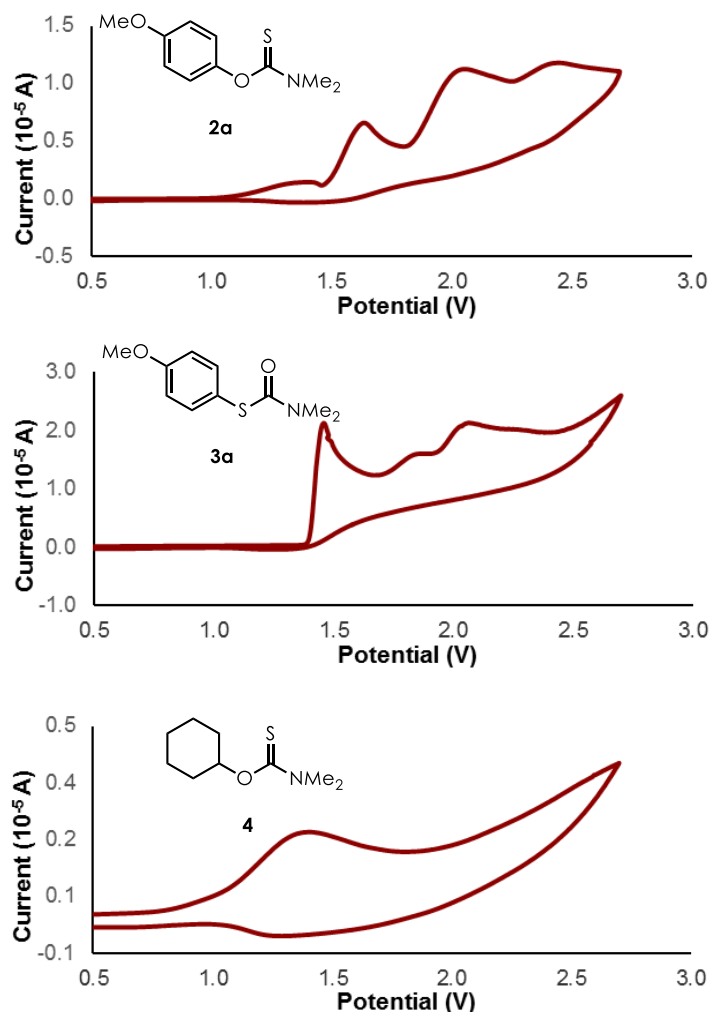


Figure 2.11. CV Traces of relevant carbamothioates. All potentials are recorded vs. Ag/AgCl in a MeCN solution containing 0.1 M NBu₄PF₆.

do not undergo photoredox NKR, an irreversible oxidation wave was observed at potentials around +1.1 V vs SCE. Moreover, substrate **4** which cannot undergo rearrangement and lacks any other π -containing moiety, exhibits an oxidation wave at +1.1 V vs. SCE nearly identical to the *O*-aryl substrates tested. This data suggests that oxidation of the thiocarbonyl moiety, rather than the arene, is likely involved in the rearrangement. This is in agreement with previous work¹⁵ carried out in our laboratory into the cyclization of thioamides onto pendant alkenes. It was found that thioamides, bearing unoxidizable pendant olefins, still afforded the cyclized products. To account for this reactivity, it was proposed that reactivity for these substrates was the result of

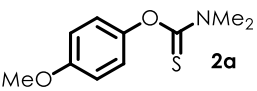
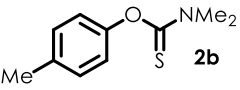
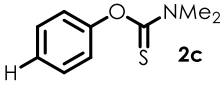
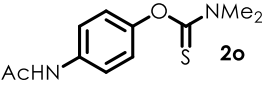
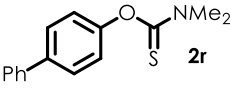
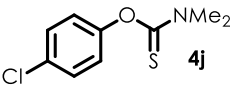
thioamide oxidation as opposed to olefin oxidation. It seemed reasonable that a similar conclusion, given our CV data, could be drawn in the photoredox NKR.

2.7 Stern-Volmer Quenching Analysis of *O*-aryl Carbamothioates

Having shown that oxidation of all *O*-aryl carbamothioate substrates should be feasible by the photooxidant **1** based on electrochemical considerations, we became curious if reactivity in this system was dominated by quenching interactions with the photocatalyst. While the electrochemical data would suggest facile PET, observing dynamic quenching of the excited state catalyst, **1**^{*}, would provide strong evidence for the intermediacy of a cation-radical intermediate.¹⁶ Moreover, we were curious if there existed a difference between the quenching characteristics of successful and unsuccessful substrates. If unsuccessful substrates were found to quench **1**^{*} less efficiently then this would suggest that efforts to expand the substrate scope should be directed towards maximizing catalyst – substrate interactions.

A series of *O*-aryl carbamothioates were tested as potential quenchers of the pyrylium photocatalyst (**Table 2.3**). All substrates tested were found to be effective quenchers of pyrylium fluorescence. The quenching constants, k_q , for all *O*-aryl carbamothioate substrates tested were found to be within the same order of magnitude, near the diffusion limit in acetonitrile, though did vary by 15% depending on the identity of the R-group in the 4-position. This variation, however, was not found to fit well with any linear free energy relationship.

Table 2.3. Results of pyrylium fluorescence quenching by various O-aryl carbamothioates.

	K_{SV} (M^{-1})	k_q ($M^{-1} s^{-1}$)	$E_{p/2}$ (V vs. SCE)
 2a	77.8	1.68×10^{10}	1.20
 2b	70.6	1.59×10^{10}	1.18
 2c	63.4	1.50×10^{10}	1.21
 2o	58.0	1.30×10^{10}	1.15
 2r	74.9	1.68×10^{10}	1.09
 4j	76.7	1.72×10^{10}	1.21

A poor correlation between the electronic nature of R group and k_{SV} could be observed through a Hammett-type analysis against σ values, and no correlation could be observed when plotted against σ^+ (**Figure 2.12**).^{17,18} These findings suggest that the electronic identity of the aryl component of the carbamothioate does not have a significant impact in the quenching event between substrate and photocatalyst. Moreover, given that all quenching rates were found to be within the diffusion limited region, quenching of the photocatalyst is unlikely to be the limiting factor in predicting successful reactivity.

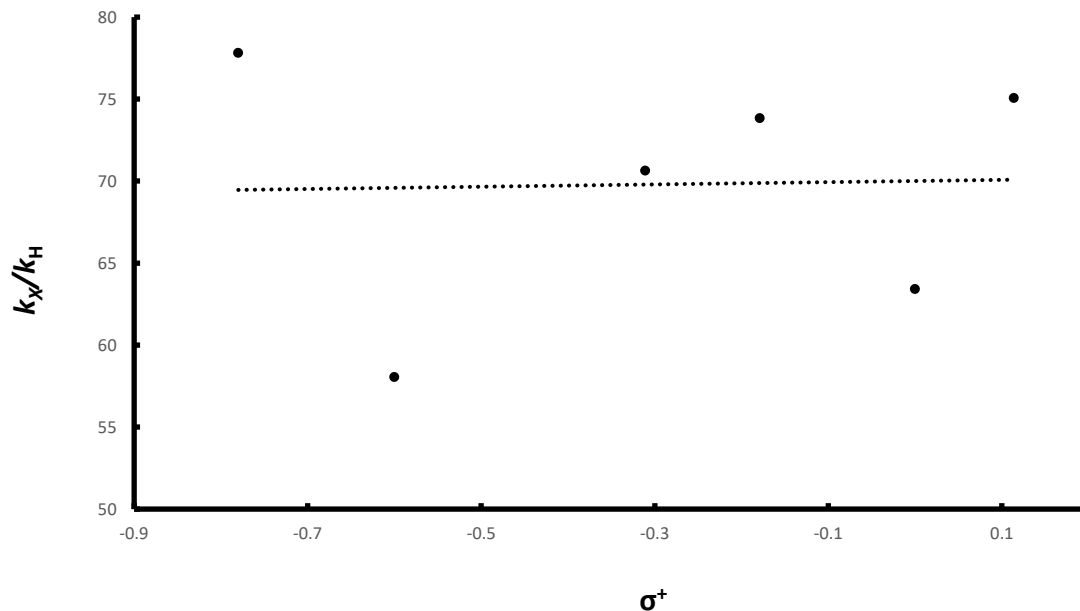


Figure 2.12. Hammett plot vs. σ^+ for the series of carbamothioates tested from table 1. The dotted line represents an attempted linear fit ($R^2 = 0.0034$)

Two mechanistic possibilities, among others, that account for dynamic quenching of the photocatalyst fluorescence are electron transfer or energy transfer events and both pathways might be responsible, a priori, for the photochemical rearrangement.¹⁹ In order to confirm that oxidation of aryl carbamothioates in solution phase¹³ leads to productive rearrangement we turned to potent, ground state oxidants. An attractive oxidant for this is the stable aminium cation-radical salt, which possesses a reduction potential similar to that of the aryl carbamothioates.²⁰ Thus, treatment of carbamothioates **2d** or **2f** with a catalytic amount of **aminium** results in productive formation of the S-aryl carbamothioate, albeit in low conversions (**Figure 2.13**). As **aminium** is a ground state oxidant, rearrangement through an excited state can be excluded.

Given this data we believe that quenching of the chromophore by the carbamothioate substrate occurs through an SET process and generates a cation-radical intermediate that undergoes rearrangement. The SET event occurs mainly from the thione moiety, with minimal involvement of the arene system, resulting in a cation-radical species with charge and spin density localized in

the thione moiety. We then became curious about how best to characterize this cation-radical species and if its characterization could help explain some of the features of the cation-radical NKR.

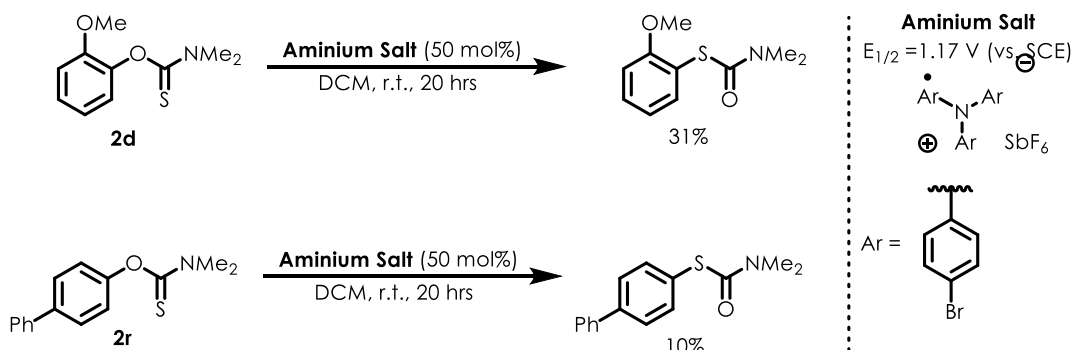


Figure 2.13. Cation-radical NKR initiated by a ground-state oxidant.

2.8 Carbamothioate-Mediated Olefin Isomerization Promoted by Photoredox Catalysis

In our initial communication we reported that an aryl carbamothioate **2p** underwent NKR under photoredox conditions.²¹ We also noted that the olefin in **2p** underwent isomerization during the course of the reaction. Substrate **2p** was synthesized as a 9 : 1 *Z* : *E* mixture of isomers, however the NKR product was obtained as a 1 : 19 *Z* : *E* mixture. We were curious to discern the pathway through which this isomerization takes place during the reaction and if this pathway could offer evidence concerning the reactivity of the thione cation-radical intermediate.

Control experiments confirmed that no isomerization occurred during irradiation without the pyrylium chromophore, ruling out a direct sensitization mechanism of isomerization. Monitoring the olefin isomer ratio during the course of the reaction (**Figure 2.14A**) revealed that isomerization had occurred prior to significant product formation and the geometric isomers reached equilibrium (i.e. 1 : 19 *Z* : *E*) after only ~10% conversion. Thus, the isomerization process occurs after quenching the excited chromophore but prior to the O-S aryl migration event and is evidently much faster than the re-arrangement process.

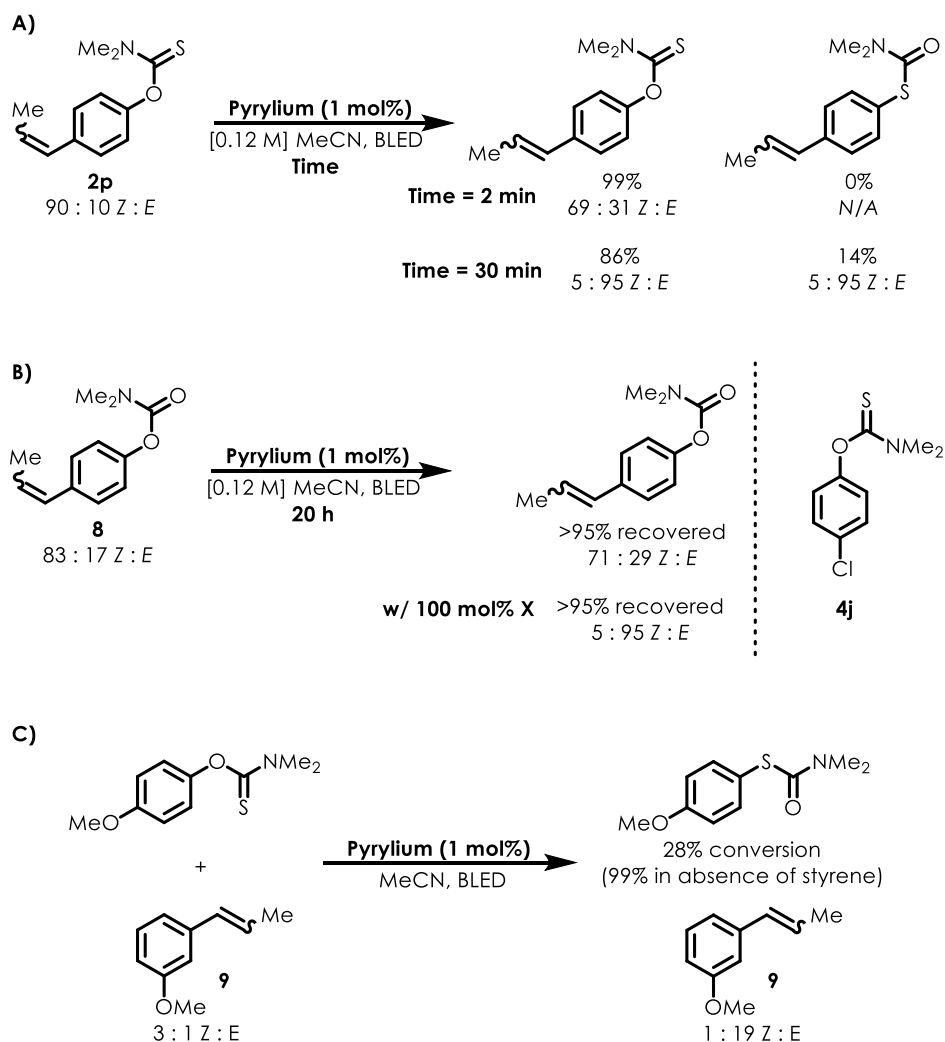


Figure 2.14. Experiments investigating olefin isomerizations during cation-radical NKR. All reactions run with 1.0 mol% pyrylium (1) loading. A) Time-course profile of olefin isomerization during cation-radical NKR. B) Isomerization of a carbamate under cation-radical NKR conditions. C) Inhibition of NKR by added olefin.

Pyryliums have been shown to affect the isomerization of olefins via both electron transfer and energy transfer pathways.^{22–25} However, given our CV and quenching data we believed that buildup of charge and spin density in, and weakening of, the olefin moiety to be unlikely. Also, energy transfer from either singlet or triplet excited states of $\mathbf{1}^*$ should be unfavorable, as the singlet and triplet energies of styrenes are much greater than that of $\mathbf{1}^*$. Moreover, irradiation of carbamate derivative **8** in the presence of **pyrylium** showed a small degree of isomerization, though never

reached the ratio observed for the carbamothioate analog (**Figure 2.14B**). However, the carbamate substrate was observed to undergo complete isomerization when a stoichiometric amount of thiocarbamate **4j**, which does not undergo rearrangement under the reaction conditions, was added to the solution. We reason that while SET or sensitization of a styrene may result, in some cases, in olefin isomerization, it is not the operative mechanism for isomerization observed for **8** or **2p**. Furthermore, isomerization must be an intermolecular process and is dependent on the presence of an *O*-bound carbamothioate, suggesting a bimolecular reaction with the thione cation-radical.

We were curious if this *O*-aryl carbamothioate mediated olefin isomerization process could be a general process. This could represent a catalytic isomerization of olefins when such substrates are synthesized in an unselective fashion. We subjected styrene derivative **9** to irradiation in the presence of the pyrylium and found the isomer ratio essentially unchanged. When the carbamothioate substrate **2a** was added, isomerization of the styrene was again observed with no other styrene-derived species having been formed (**Figure 2.14C**).²⁶ The carbamothioate was also found to have rearranged to the *S*-aryl product in 28% conversion. These equilibrations did not occur when the pyrylium or blue light were omitted from these mixtures.

The lack of olefin isomerization in both **8** and **9** when irradiated in the presence of **pyrylium** suggests that oxidation does not result in stereomutation for β -alkyl styrenes.²⁷ The equilibration observed only in the presence of carbamothioates suggests the formation of a reactive intermediate by SET between the pyrylium and **1**. We believe this species to be the thione-centered cation-radical **1**⁺, which in light of these results can best be described through the resonance shown²⁸, with significant spin density on the sulfur-atom (**Figure 2.15A**).

Thiyl radicals are known to induce isomerization in lipids and have been shown to give thermodynamic ratios of olefins.^{29–31} We observe the same stereomutation when **9** is irradiated in

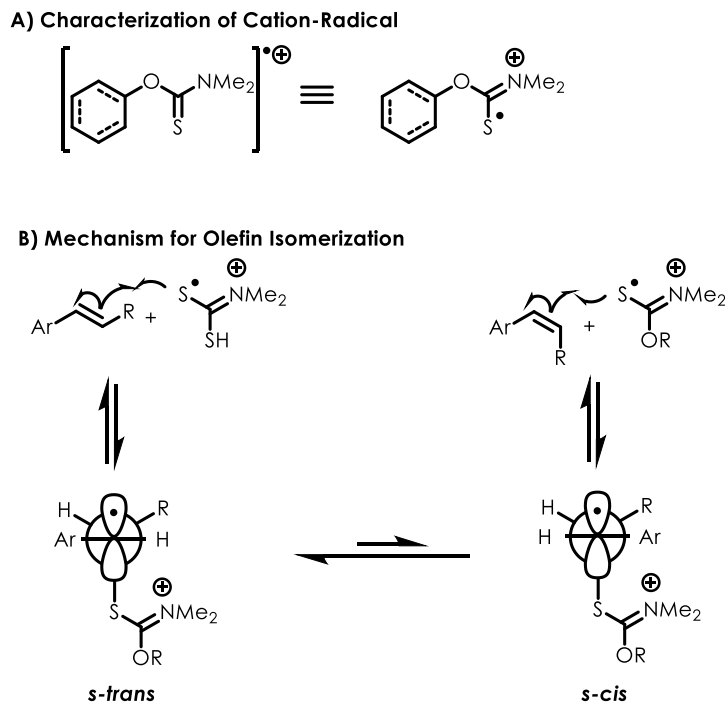


Figure 2.15. Reactivity of aryl carbamothioate radical. A) Classification of *O*-aryl carbamothioates as thione-centered cation radicals with thiyl radical character. B) Proposed mechanism for *O*-aryl carbamothioate cation-radical mediated olefin isomerization.

the presence of phenyl disulfide (see supporting information). We have shown previously²⁷ that irradiation of phenyl disulfide with blue LEDs results in homolytic cleavage of the disulfide bond, forming thiyl radicals. Consequently, the stereomutations observed in reactions with thiocarbamates can best be explained by the significant thiyl-radical character of **1**⁺. Similar intermediates have been proposed in oxidations of thioamides.^{32,33} Moreover, we believe characterizing thione radical cation adducts in this fashion may lead to its use in other transformations and have implications in other systems such as RAFT-type photopolymerizations developed by Fors.³⁴⁻³⁶

A mechanism to rationalize the isomerization is shown in **Figure 2.15B**.³¹ Upon formation of **1**⁺, radical addition from the sulfur center onto the styrene results in the formation of a benzylic radical species. This species now allows for rotation around the alpha and beta positions, forming

conformers *s-trans* and *s-cis*. Collapse from either of these benzylic radicals reforms the styrene and **1**⁺. The trans-styrene is formed from collapse of *s-trans* and the cis-styrene is formed from collapse of *s-cis*. The isomer distribution reflects the relative stabilities of each species as a result of the differing steric environments.

During the isomerization of **9** in the presence of **2a**, the carbamothioate was found to rearrange in 28% conversion. In the absence of the styrene, under similar conditions, **2a** proceeds cleanly to the NKR product **3a** in quantitative yield. From this we conclude that the olefin inhibits the cation-radical NKR from proceeding, however this may simply be due to competitive quenching of the photocatalyst.

2.9 Kinetic Studies of Photoredox Newman-Kwart Rearrangement

In our initial report we found that lower concentrations favored higher conversions for a number of substrates. We found that this concentration dependence was especially pronounced for arenes that lacked strong electron-donating groups. Moreover, we found that in all cases faster conversions could be achieved at lower concentrations for a given substrate.

For example, methoxy-substituted carbamothioate **2a** underwent rearrangement at >95% conversion in 16 hrs when irradiated at a concentration of 0.5 M but only 10 minutes when diluted to 0.06 M (**Figure 2.16**). Conversely, methyl-substituted **2b** afforded trace conversion at 0.5 M but could undergo 76% rearrangement in 24 hours at 0.06 M. In order to probe this concentration dependence, we performed a series of in-situ IR experiments.

Monitoring the conversion of **2a** at a range of concentrations revealed a dramatic rate enhancement. Indeed, at [0.06 M] the reaction is complete in under 20 minutes, while at [0.25 M] the reaction took over two hours to complete. To rule-out product-inhibition, the reaction was

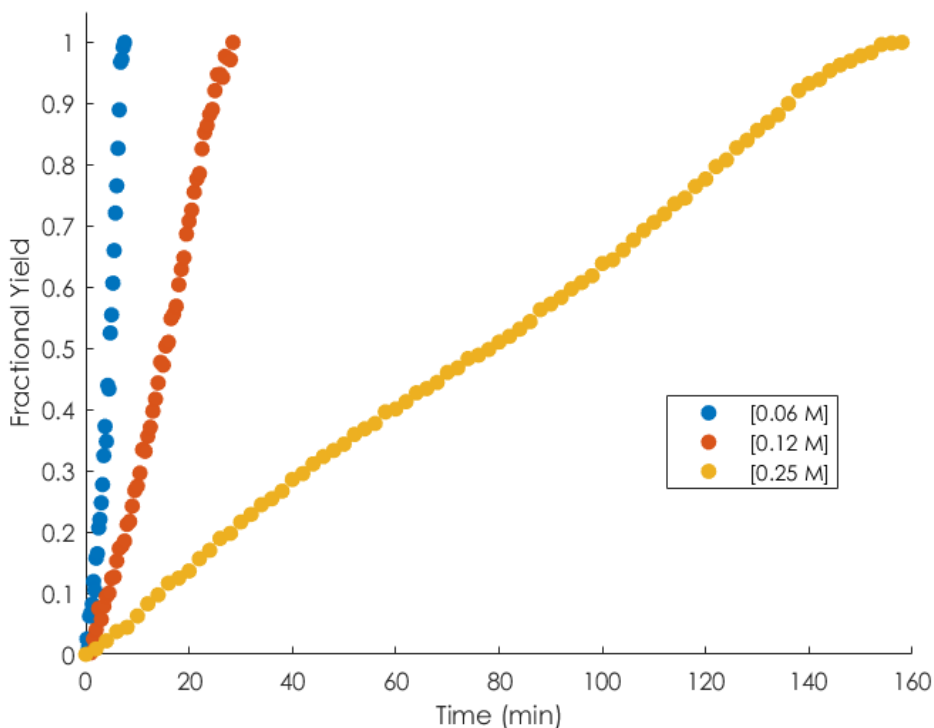


Figure 2.16. Kinetic traces of cation-radical NKR of 2a obtained using in-situ FTIR.

monitored at [0.06 M] with varying amounts of the product added at the beginning of the reaction. Overlap was good up to a full equivalent of product added (**Figure 2.17**).

In accordance with the observed rate enhancement, the quantum yield of the rearrangement was also found to increase at higher dilutions. The increase in quantum yield was found to be nonlinear, suggesting that the reaction efficiency is impacted by multiple chain-terminating pathways initiated by substrate (**Figure 2.18**). This is an important distinction to make in photoredox-catalyzed processes. While the elementary step for PET is not reversible itself, due to extremely high barrier of molecular excitation, the overall electron transfer process is reversible. The reduced catalyst and the cation-radical intermediate can react and undergo BET. This is a chain-terminating process, effectively wasting a photon used to initiate the reaction and lengthening the time required to achieve full conversion. Efforts to increase photoredox-catalyzed processes can thus increase

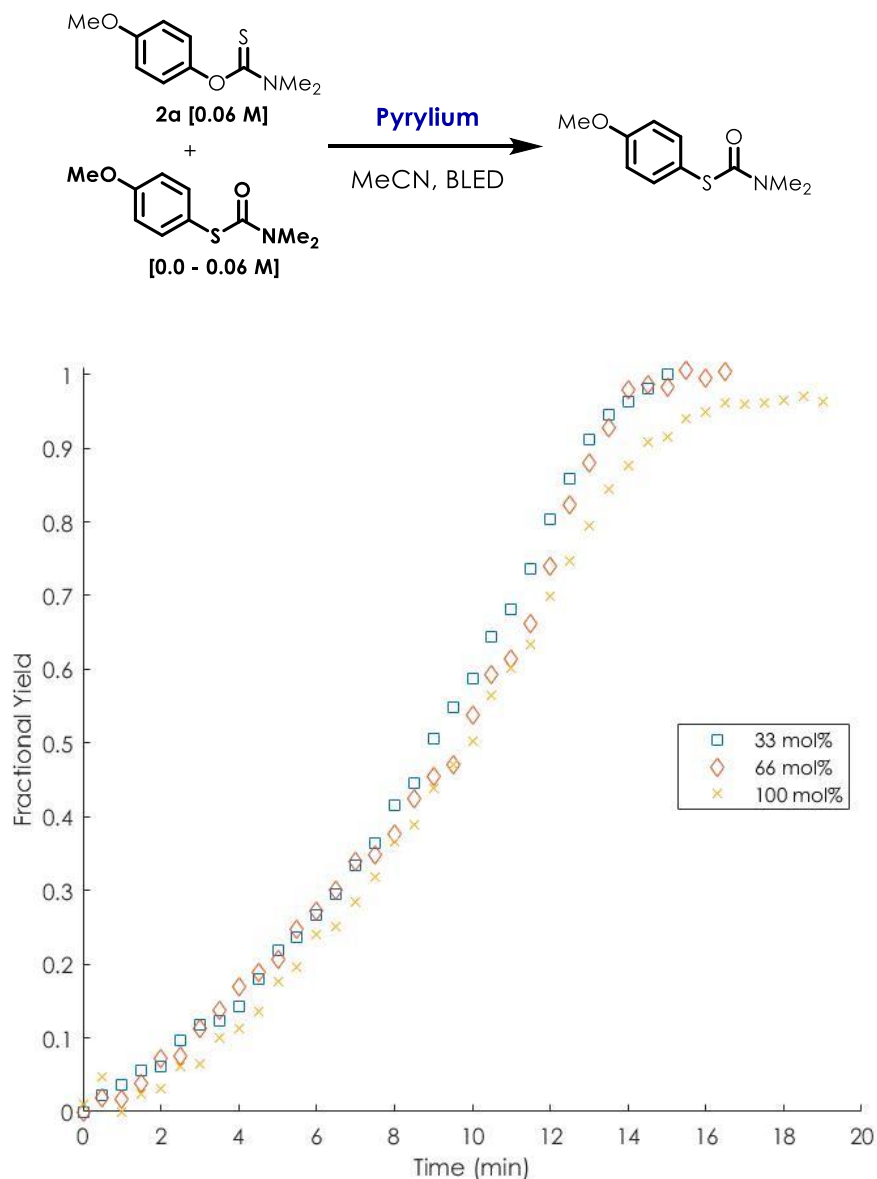


Figure 2.17. Kinetic traces showing lack of product-inhibition in cation-radical NKR. Traces obtained via in-situ FTIR.

efficiency by either limiting unproductive BET or determining what factors govern the rate of the productive elementary steps.

Rate enhancement upon dilution would suggest, mechanistically, either substrate or product inhibition. Reactions with added product show good overlap under these conditions, suggesting that product inhibition can be ruled out. Catalyst deactivation may play a role at late stages of the

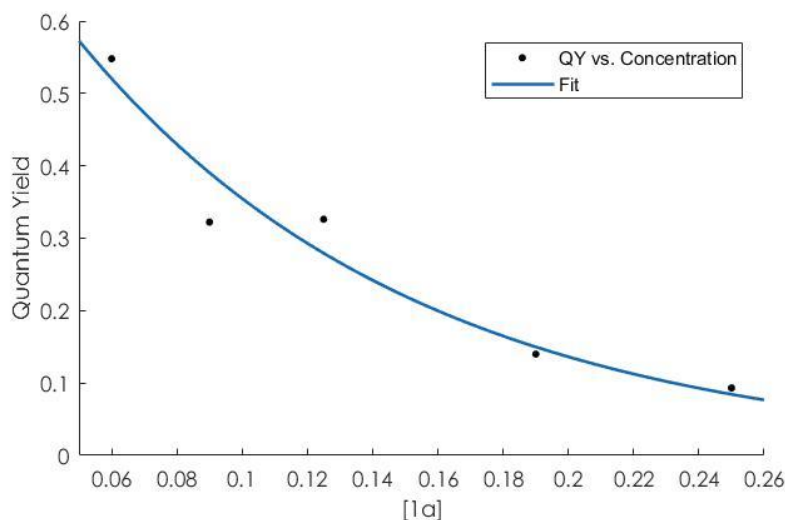


Figure 2.18. Relationship between quantum yield and substrate concentration. Quantum yields determined by calculating yields from crude NMR of reaction mixtures. Fit was determined via MATLAB curve fitting toolbox with $R^2 = 0.942$.

reaction, as time-adjusted overlays of the [0.12 M] and [0.25 M] data sets show poor overlap (see SI). However, at all time points a large divergence in rate is observed suggesting that substrate inhibition plays a role in this mechanism.

One possible mode of substrate inhibition would involve static quenching of the chromophore by the substrate. This quenching interaction would lead to inactivation of the catalyst. Steady-state fluorescence quenching experiments showed a linear quenching profile, suggesting that dynamic quenching is the only operative mechanism of chromophore quenching (*vide infra*).¹⁶ Thus, the concentration dependence is instead the result of post-quenching interactions which could be explained in two ways.

First, lower concentrations of **1** would disfavor back electron transfer from the reduced photocatalyst to **1**⁺ by increasing the likelihood of cage-escape of the reduced pyrylium species and **1**⁺. This would increase the lifetime of the reactive intermediate and allow it to undergo rearrangement (**Figure 2.19A**). Additionally, the formation of an off-cycle intermediate with

neutral **1** and cation-radical **1**⁺, would account for substrate inhibition if this adduct can also undergo back-

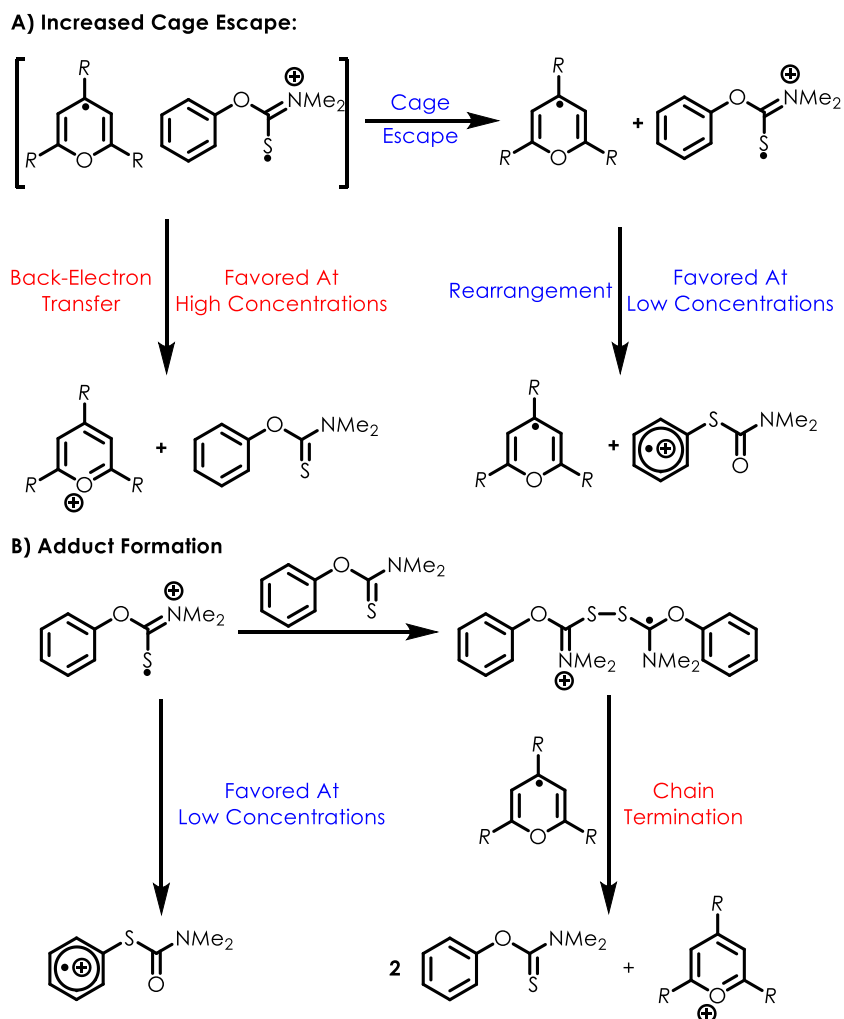


Figure 2.19. Possible modes of substrate inhibition. Counterions omitted for clarity.

electron transfer to furnish (Figure 1.19B). Given the thiyl-radical nature of the cation-radical intermediate, it is possible that this intermediate takes the form of a disulfide-type adduct. The formation of sulfur-sulfur adducts between thiyl radicals and thiones has been shown in Barton-type deoxygenation systems.³⁷ Lower substrate concentrations would disfavor formation of this off-cycle intermediate and allow the rearrangement to proceed. It is also possible that this

intermediate can undergo reduction by the reduced catalyst, which would presumably cause it to fragment to give two equivalents of the neutral *O*-aryl carbamothioate.

Since it has now been shown that substrate concentration plays a role in preventing the formation of chain-terminating intermediates, we also became curious about factors influence the rate of rearrangement. An interesting corollary to the observed concentration dependence is that this trend was also seemingly coupled to the electronic nature of the arene. In our initial report, substrates bearing less activated arenes required more dilute conditions to achieve high conversions. For example, substrate **2b** bearing only a methyl substrate proceeded in only <5% conversion at [0.5 M], however upon dilution to [0.06 M] 71% conversion could be achieved. This is in contrast to the more electron-rich **2a** bearing 4-OMe which successfully undergoes rearrangement at both concentrations, albeit at different reaction rates.

Having established a mechanistic explanation for substrate concentration dependence, we wondered if the dependence of the reaction on arene electron-density could be explained. We decided to observe the rates of rearrangement for different aryl carbamothioates (**Figure 2.20**). These reactions were run at the same concentration of the different carbamothioates so as to allow for a qualitative comparison of their rates. The acetamido and methoxy substituted arenes proceed in roughly the same rates, however drastically longer reaction times are observed for the less activated phenyl and methyl substituted arenes.

Under a Hammett³⁸ analysis using σ^+ as a reference system, it would be expected that the methyl-substituted arene would react faster ($\sigma^+ = -0.311$) than the phenyl-substituted arene ($\sigma^+ = -0.179$).³⁹ Instead, the opposite trend is observed in the kinetic traces. A suitable explanation for this reactivity trend can be found instead in the ionization potentials of the arenes. The relevant parent systems to compare for these two substrates would be toluene and biphenyl. As measured

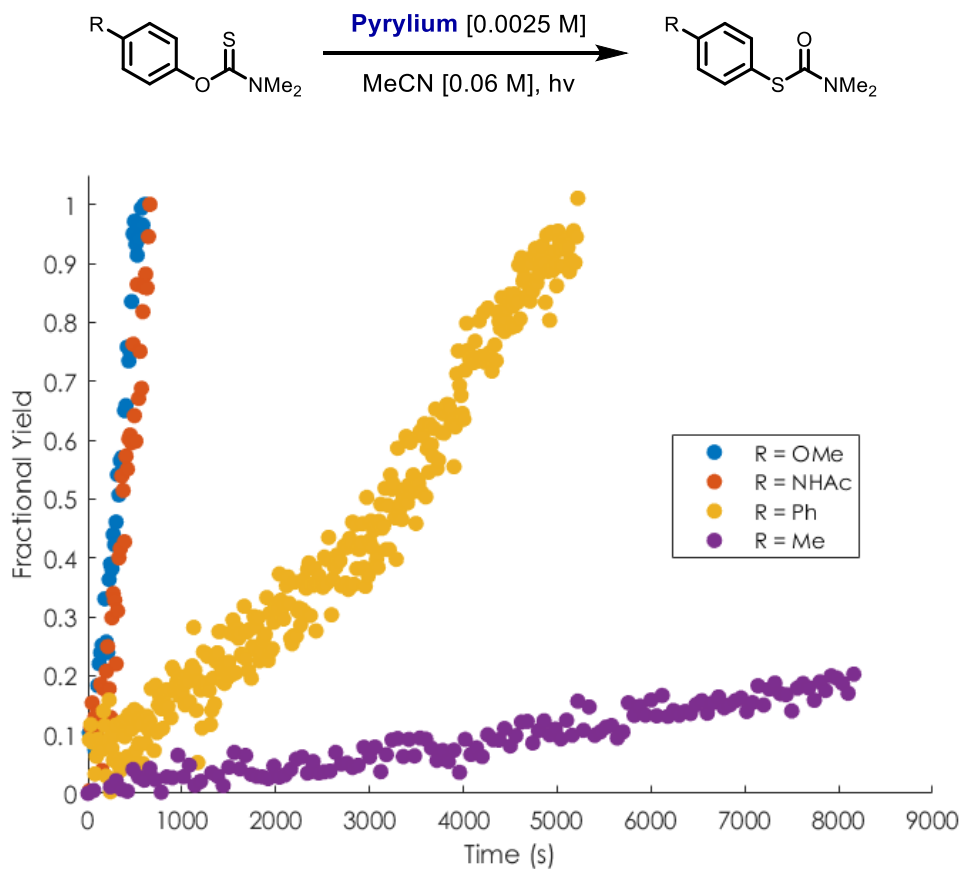


Figure 2.20. Hammett-type analysis of cation-radical NKR. Kinetic traces obtained via in-situ FTIR.

previously by our lab, $E_{p/2}$ (in V vs. SCE) is 1.90 V for biphenyl⁴⁰ and 2.30 V for toluene.⁴¹ Thus, biphenyl is more readily ionizable than is toluene. This ionizability may be critical in the transition state for the *O*-to-*S* aryl migration event, suggesting that significant charge density is building up in the arene system. This charge buildup is better described as cation-radical formation rather than carbocation formation, as the σ^+ values do not accurately reflect the relative reaction rates.

Under our first mechanistic proposal we believed this electronic dependence to be the result of a more feasible oxidation for more electron-rich arenes. However, as a result of the quenching studies, we believe this to be an insufficient explanation for the observed reactivity. Instead, we believe that the electronic-dependence is partially the result of a rate-determining intramolecular cyclization of the phenyl ring onto the thiyl-radical moiety of the cation-radical intermediate. In

order to observe such a high dependence of rate on the electronics of the arene, this transition state must feature a highly polarized arene system. This suggests that the intermediate after cyclization features charge-density centered in the arene and that during the transition state there is significant charge transfer⁴² from the arene to the thione moiety, ultimately resulting in heterolytic cleavage of the aryl-O bond. This step becomes slow for less activated arenes due to their lowered ionizability, allowing for competitive back-electron transfer to become more dominant and decreasing reaction efficiency.

2.10 An Adjusted Mechanism for Photoredox Newman-Kwart Rearrangement

In the previous sections we provided evidence supporting the formation of a thione-centered cation radical upon SET from the O-aryl carbamothioate substrates to the pyrylium chromophore. These results showed that formation of this species is both required for rearrangement and for off-cycle interactions. Quenching studies and olefin isomerization suggested that the species can be characterized in part as a thiyl radical. Consequently, we favored amending our mechanistic representation of the reaction to that shown in **Figure 2.21**.

Excitation of the **pyrylium** results in a potent excited-state oxidant and quenching of the chromophore by **2** results in formation of intermediate **5** and the pyranyl radical. The rearrangement proceeds from intermediate **5** involving an O-S migration event. This activated complex shares characteristics of the classical NKR transition state, namely, the disruption of aromaticity and the formation of a spirocyclic thiotane ring. However, given the electron deficient nature of the thiyl radical intermediate and the results of the Hammett experiments it seems more likely that this migration would be analogous to an S_EAr event, in contrast to the S_NAr character of the thermal NKR. Heterolytic scission of the O-aryl bond in the activated complex gives rise to intermediate X which has cation-radical character localized in the arene. Subsequent reduction

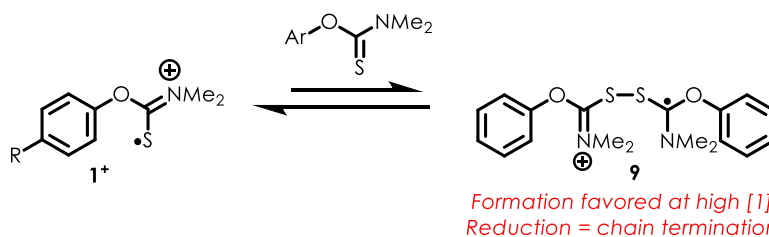
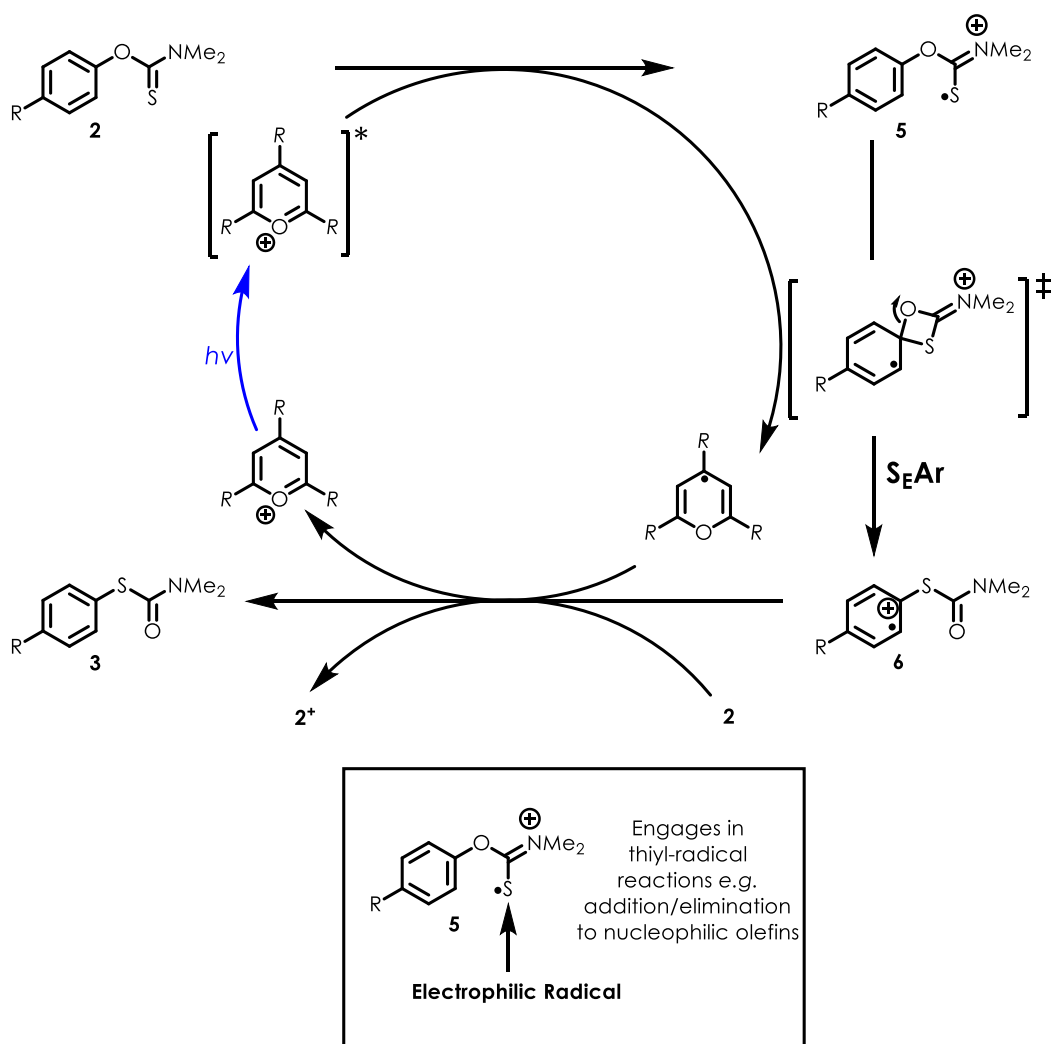


Figure 2.21. Amended catalytic cycle for NKR along with description of intermediate 5. furnishes the desired S-aryl product. Reduction can be achieved via SET from the pyranonium radical or another equivalent of substrate.⁴³ In light of the lack of a significant product inhibition, despite its capability of quenching the photocatalyst, we believe that chain propagation must be a possible propagation pathway.

The formation of off-cycle intermediates is supported by the concentration dependence studies. These intermediates serve to decrease the concentration of active chains at any given point during the reaction. Moreover, these intermediates must also be capable of oxidizing the pyranyl radical. This terminates the chain, returning the system to the beginning of the catalytic cycle and results in a wasted photon, thus lowering reaction quantum yield. This effect becomes more pronounced as the rate of rearrangement becomes increasingly slow for substrates bearing less activated arenes. Thus, in these cases, there is a larger proportion of chains that end in termination prior to rearrangement.

2.11 A Thermodynamic Cycle to Predict Photoredox Newman-Kwart Rearrangement

Under our first proposed mechanism we believed this system to be limited to electron-rich substrates due to the ease of oxidation of the arene. Consequently, we initially believed that exergonic electron transfer was the most important criterion for a successful reaction. Having shown that electron transfer is capable for substrates that do not undergo rearrangement, a new method to predict if a given substrate will undergo rearrangement became desirable.

Given the distinct electronic effect on the rate of rearrangement, we believe that an arene needs to be sufficiently electron rich to undergo rearrangement. This can be most generally predicted with mono-substituted arenes as electron-donating groups enhance reactivity while electron-withdrawing do not. However, the position of the electron-donating group can have a major effect on the success of the reaction. A 3-methoxy arene does not undergo cation-radical NKR to an appreciable degree, while the 4-methoxy analogue proceeds in excellent conversion.

In general, it appears that successful rearrangement can be predicted for mono-substituted arenes using similar guidelines as for standard S_EAr reactions: electron-donating groups, situated at para and ortho positions, accelerate the rearrangement while electron-withdrawing groups

deaccelerate. Substituents that activate arenes toward S_EAr via electron-releasing resonance forms, such as an alkoxy moiety, react smoothly when in the ortho or para position, but act as inductively electron-withdrawing groups when placed in the meta position. However, when both donating and withdrawing groups are present it can be difficult to determine if the reaction will proceed. We were curious if a thermochemical parameter could be used to predict if a given arene was sufficiently activated for cation-radical NKR.

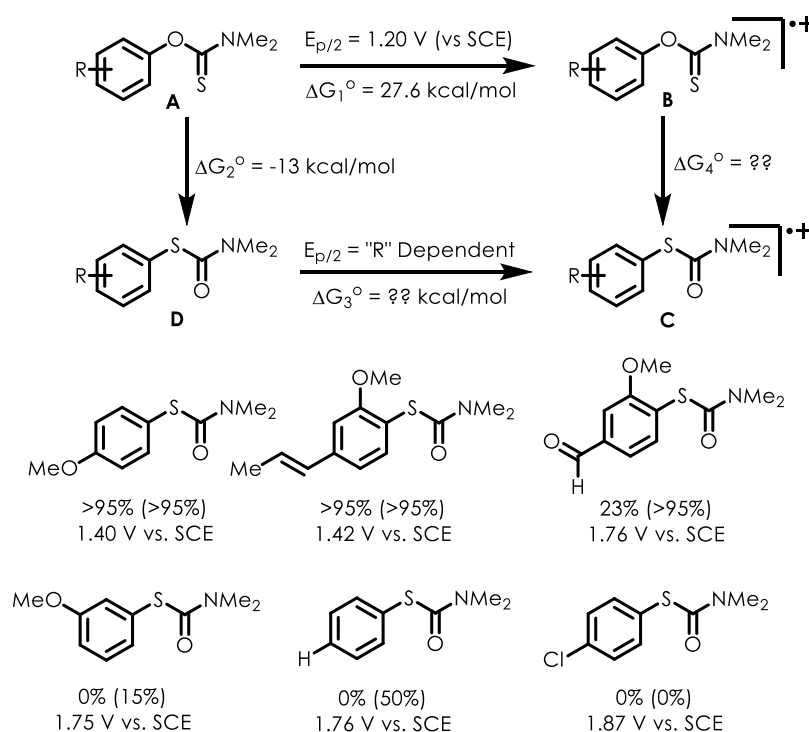


Figure 2.22. Thermodynamic cycle for the cation-radical NKR. Yields for substrates are for reactions performed at 0.5 M substrate concentration. Yields in parantheses refer to yields at lower concentrations (0.12 M or less).

In order to predict when rearrangement would be favorable we considered a thermodynamic cycle as in figure 2.22.⁴⁴⁻⁴⁸ As the overall transformation is thermodynamically favorable for all substitution patterns, we postulated that the success of the rearrangement might be kinetically dependent on the relative energies of the O- and S-aryl cation-radicals. As these intermediates are fleeting and thermochemical measurements of the rearrangement would be difficult, we sought to

utilize the more easily obtained parameters of the rest of the elementary steps. We reasoned that the energetics of the rearrangement step could be estimated by the more easily obtained thermo- and electrochemical values for the given elementary steps.

The conversion of the neutral O- and S-aryl carbamothioates to the corresponding cation-radicals can be easily estimated via CV. The $E_{p/2}$ values obtained from these experiments offer a reasonable estimation of the ΔG for electron transfer. In almost all cases reported thus far, the S-aryl carbamothioate possess a more positive $E_{p/2}$ for oxidation (**Figure 2.22**) than does the O-aryl carbamothioate (**Table 2.3**). Moreover, the O-aryl carbamothioates all possess $E_{p/2}$ around 1.15 V vs. SCE, while the S-aryl carbamothioates vary more predictably with the identity of the substituent. In order to complete the thermodynamic picture for conversion from O-aryl to S-aryl carbamothioate cation-radical, we must also take into account the energetics for the bonds being broken and formed. Previous reports on the thermal NKR have shown that ΔG for the overall transformation from O- to S-aryl carbamothioate is exergonic by ~ 13 kcal/mol.⁴⁹

Combining the thermochemical data for the “electronic” portion of rearrangement (represented by the $E_{p/2}$ values) with that of the “bonding” component (the exchange of a thione for a carbonyl, mainly) offers an approximation when rearrangement of the cation-radical species is thermodynamically favorable. Given that the overall exergonicity is relatively constant (~ 13 kcal/mol for the conversion of a thione to a carbonyl) as well as the initial oxidation ($E_{p/2} \sim 1.15$ V vs. SCE, 26.3 kcal/mol), the exergonicity of the rearrangement of cation-radicals can be determined by combining these two terms and subtracting them from the $E_{p/2}$ for oxidation of the S-aryl carbamothioate as in **Equation 2.1**.

Equation 2.1

$$\Delta G_1 + \Delta G_4 = \Delta G_3 + \Delta G_2$$

$$\Delta G_4 = \Delta G_3 + \Delta G_2 - \Delta G_1$$

$$\Delta G_4 = E_{p/2}(\mathbf{D}) - \left(13 \frac{\text{kcal}}{\text{mol}} + 26.3 \frac{\text{kcal}}{\text{mol}}\right)$$

$$\Delta G_4 = E_{p/2}(\mathbf{D}) - (1.71 \text{ V vs SCE})$$

These two terms combined account for 39.3 kcal/mol and the rearrangement of the cation-radicals will be exergonic only when $E_{p/2}(\text{S-aryl carbamothioate}) \leq 1.71 \text{ V vs. SCE}$ holds true. As a result, as the oxidation of the S-aryl carbamothioate becomes more unfavorable, the barrier for rearrangement from O-aryl to S-aryl cation-radical becomes higher. We stress that this calculation is not a measurement of the actual activation energy of the rearrangement step, and is merely a reflection of the trend in barrier height based on the Bell-Evans-Polanyi principle.^{50,51}

This prediction is accurate in practice, with decreased conversions observed around 1.75 V vs. SCE for substrates attempted in our initial communication. It is also important to note that these calculations use $E_{p/2}$ values which are only approximations of the true thermodynamic value $E_{1/2}$. Attempts to obtain the $E_{1/2}$ values for the S-aryl carbamothioates were unsuccessful even at higher scan rates. As a result, great care should be taken when analyzing these calculations with $E_{p/2}$ that are close to this cutoff point. In accordance with our mechanistic conclusions that reaction conversion is kinetically controlled, dilution for some high potential substrates results in high conversions. Thus, in using this predictive tool it is important to consider low reaction concentrations for substrates that would have a product oxidation potential near or above the calculated threshold.

It is not possible to predict extent of conversion with this calculation for cases on the border of this value, however for values that deviate significantly it appears to be a powerful tool. Moreover, we've reported recently that redox potentials can be reasonably estimated using a simple

computational model, allowing a quick estimation to be used using these thermodynamic calculations.⁴¹

Despite the success of this model in predicting reactivity, it is important to note its shortcomings. Substrates bearing unsaturation conjugated with the arene in the ortho position do not appear to rearrange, despite possessing suitable $E_{p/2}$ values. The reason for this remains unclear but may be related to the formation of off-cycle intermediates as postulated for reactions containing olefins. The equilibrium for these intermediates may be more favorable given their formation would now constitute an intramolecular process. Reduction of these intermediates by the reduced catalyst would represent an increased rate of chain-termination for these substrates, shutting down reactivity.

2.12 Final Conclusions

Through a combination of spectroscopic and kinetic analyses we have elucidated key features of the cation-radical NKR. Fluorescence quenching experiments show that aryl carbamothioates are competent quenchers of excited state pyrylium species regardless of the electronic nature of the arene. This data, in combination with observed reactivity trends, suggests that this quenching event is an electron transfer event resulting in a carbamothioate cation-radical which features a significant degree of spin localization on the sulfur atom.

The reactivity of this cation-radical intermediate can best be characterized as an electrophilic thiyl radical. This radical undergoes reversible addition / elimination reactions with electron-rich olefins. A reversible adduct formation is also invoked for the observed substrate inhibition, whereby more dilute reactions give higher conversions. Hammett-type studies as well as thermodynamic calculations suggest that the rearrangement step for the cation-radical NKR can be thought of as an S_EAr process, with the arene acting as a nucleophile towards the thiyl radical

in an intramolecular process. This transition state features a large degree of charge and spin density buildup in the arene, explaining the large electronic dependence on reaction conversion.

A thermodynamic cycle based on known thermochemical parameters was constructed to predict when the cation-radical rearrangement is most favored. These calculations offer a reliable prediction of substrate reactivity in this system from an easily obtained thermochemical value: the oxidation potential of the *S*-aryl carbamothioate. This value can be obtained to a reasonable degree of accuracy via simple computational means.

We believe that the results reported here will aid the incorporation of the cation-radical NKR into standard use. The mechanistic trends allow for substrates to be more judiciously selected for this transformation. Moreover, a simple predictive tool has been devised to determine if a given substrate is suitable for this transformation possibly saving time and material when devising syntheses. More generally, we believe the development of a thermochemical cycle in cation-radical mediated transformations can aid in rationalizing reaction trends. We believe that similar cycles may be constructed for other transformations to obtain valuable information about reaction efficiencies.

REFERENCES

- (1) Chauhan, P.; Mahajan, S.; Enders, D. Organocatalytic Carbon–Sulfur Bond-Forming Reactions. *Chem. Rev.* **2014**, *114* (18), 8807–8864.
- (2) Liu, H.; Jiang, X. Transfer of Sulfur: From Simple to Diverse. *Chem. - Asian J.* **2013**, *8* (11), 2546–2563.
- (3) Fernández-Rodríguez, M. A.; Shen, Q.; Hartwig, J. F. A General and Long-Lived Catalyst for the Palladium-Catalyzed Coupling of Aryl Halides with Thiols. *J. Am. Chem. Soc.* **2006**, *128* (7), 2180–2181.
- (4) Newman, M. S.; Karnes, H. A. The Conversion of Phenols to Thiophenols via Dialkylthiocarbamates. *J. Org. Chem.* **1966**, *31* (12), 3980–3984.
- (5) Kwart, H.; Evans, E. R. The Vapor Phase Rearrangement of Thioncarbonates and Thioncarbarnates. *J. Org. Chem.* **1966**, *31* (2), 410–413.
- (6) Lloyd-Jones, G. C.; Moseley, J. D.; Renny, J. S. Mechanism and Application of the Newman-Kwart Rearrangement of O-Aryl Thiocarbarnates. *Synthesis* **2008**, 661–689.
- (7) Schönberg, A.; Schütz, O.; Bruckner, V.; Peter, J. Über thermolabile Thio-äther. (15. Mitteilung: Über organische Schwefelverbindungen). *Berichte Dtsch. Chem. Ges. B Ser.* **1929**, *62* (9), 2550–2562.
- (8) Relles, H.; Pizzolato, G. Steric Rate Enhancement in the Newman-Kwart Rearrangement. A Comparison with the Chapman Rearrangement. *J. Org. Chem.* **1968**, *33* (6), 2249–2253.
- (9) Kaji, A.; Araki, Y.; Miyazaki, K. Studies of the Thionyl Compound. *Bull. Chem. Soc. Jpn.* **1971**, 1393–1399.
- (10) Moseley, J. D.; Lenden, P. A High Temperature Investigation Using Microwave Synthesis for Electronically and Sterically Disfavoured Substrates of the Newman–Kwart Rearrangement. *Tetrahedron* **2007**, *63* (19), 4120–4125.
- (11) Moseley, J. D.; Sankey, R. F.; Tang, O. N.; Gilday, J. P. The Newman–Kwart Rearrangement Re-Evaluated by Microwave Synthesis. *Tetrahedron* **2006**, *62* (19), 4685–4689.
- (12) Harvey, J. N.; Jover, J.; Lloyd-Jones, G. C.; Moseley, J. D.; Murray, P.; Renny, J. S. The Newman-Kwart Rearrangement of O -Aryl Thiocarbarnates: Substantial Reduction in Reaction Temperatures through Palladium Catalysis. *Angew. Chem. Int. Ed.* **2009**, *48* (41), 7612–7615.
- (13) Prabhakar, S.; Kar, P.; Mirza, S. P.; Lakshmi, V. V. S.; Nagaiah, K.; Vairamani, M. Mass Spectral Study Of O- And S-Aryl Dimethylthiocarbarnates under Electron Impact

Conditions: Newman-Kwart Rearrangement in the Gas Phase. *Rapid Commun. Mass Spectrom.* **2001**, *15* (22), 2127–2134.

- (14) Daub, G. H.; Whaley, T. W. *J. Org. Chem.* **1978**, 4659.
- (15) Morse, P. D.; Nicewicz, D. A. Divergent Regioselectivity in Photoredox-Catalyzed Hydrofunctionalization Reactions of Unsaturated Amides and Thioamides. *Chem. Sci.* **2015**, *6* (1), 270–274.
- (16) Lakowicz, J. R. *Principles of Fluorescence Spectroscopy*, 3rd ed.; Springer: New York, 2006.
- (17) Aplin, J. T.; Bauld, N. L. Aryl Vinyl Sulfides as Probes for Electrophilic versus Electron Transfer Mechanisms. *J. Chem. Soc. Perkin Trans. 2* **1997**, No. 5, 853–855.
- (18) McCullough, J. J.; Yeroushalmi, S. Quenching of Fluorescence by Substituted Ethylenes. Substituent and Salt Effects as Criteria of Quenching Mechanism. *J. Chem. Soc. Chem. Commun.* **1983**, No. 6, 254–256.
- (19) Turro, N. J.; Scaiano, J. C.; Ramamurth, V. *Modern Molecular Photochemistry of Organic Molecules*; University Science Books: California, 2010.
- (20) Barham, J. P.; John, M. P.; Murphy, J. A. Contra-Thermodynamic Hydrogen Atom Abstraction in the Selective C–H Functionalization of Trialkylamine *N*-CH₃ Groups. *J. Am. Chem. Soc.* **2016**, *138* (47), 15482–15487.
- (21) Perkowski, A. J.; Cruz, C. L.; Nicewicz, D. A. Ambient-Temperature Newman–Kwart Rearrangement Mediated by Organic Photoredox Catalysis. *J. Am. Chem. Soc.* **2015**, *137* (50), 15684–15687.
- (22) Searle, R.; Williams, J. L. R.; DeMeyer, D. E.; Doty, J. C. *J. Chem. Soc., Chem. Commun.* **1967**, 1165.
- (23) Herkstroeter, W. G.; Hammond, G. S. *J. Am. Chem. Soc.* **1966**, *88*, 4769.
- (24) Kuriyama, Y.; Arai, T.; Sakuragi, H.; Tokumaru, K. Direct Observation of Cis-to-Trans Conversion of Oleh Radical Cations. Electron Transfer-Induced Isomerization of Stilbene Derivatives. *Chem. Phys. Lett.* **1990**, *173* (2), 4.
- (25) Majima, T.; Tojo, S.; Ishida, A.; Takamuku, S. *Cis – Trans* Isomerization and Oxidation of Radical Cations of Stilbene Derivatives. *J. Org. Chem.* **1996**, *61* (22), 7793–7800.
- (26) Riener, M.; Nicewicz, D. A. Synthesis of Cyclobutane Lignans via an Organic Single Electron Oxidant–electron Relay System. *Chem. Sci.* **2013**, *4* (6), 2625.
- (27) Romero, N. A.; Nicewicz, D. A. Mechanistic Insight into the Photoredox Catalysis of

- Anti-Markovnikov Alkene Hydrofunctionalization Reactions. *J. Am. Chem. Soc.* **2014**, *136* (49), 17024–17035.
- (28) Valega, T. M. Nuclear Magnetic Resonance Study of Some N, N-Dimethylcarbamates. *J. Org. Chem.* **1966**, *31* (4), 1150–1153.
- (29) Chatgililoglu, C.; Ferreri, C.; Guerra, M.; Samadi, A.; Bowry, V. W. The Reaction of Thiyl Radical with Methyl Linoleate: Completing the Picture. *J. Am. Chem. Soc.* **2017**, *139* (13), 4704–4714.
- (30) Sprinz, H.; Schwinn, J.; Naumov, S.; Brede, O. Mechanism of Thiyl Radical-Catalyzed Isomerization of Unsaturated Fatty Acid Residues in Homogeneous Solution and in Liposomes. *Biochim. Biophys. Acta BBA-Mol. Cell Biol. Lipids* **2000**, *1483* (1), 91–100.
- (31) Dénès, F.; Pichowicz, M.; Povie, G.; Renaud, P. Thiyl Radicals in Organic Synthesis. *Chem. Rev.* **2014**, *114* (5), 2587–2693.
- (32) Srivastava, V. P.; Yadav, A. K.; Yadav, L. D. S. Elettorsin Y Catalyzed Visible-Light Driven Aerobic Oxidative Cyclization of Thioamides to 1,2,4-Thiadiazoles. *N. Y.* **2013**, *6*.
- (33) Chang, H. S.; Yon, G. H.; Kim, Y. H. Facile Synthesis of 2-Substituted Aminobenzoxazole. One Pot Cyclodesulfurization of N-(2-Hydroxyphenyl)-N' Phenylthioureas with Superoxide Radical Anion. *Chem. Lett.* **1986**, 1291.
- (34) Kottisch, V.; Michaudel, Q.; Fors, B. P. Cationic Polymerization of Vinyl Ethers Controlled by Visible Light. *J. Am. Chem. Soc.* **2016**, *138* (48), 15535–15538.
- (35) Michaudel, Q.; Chauviré, T.; Kottisch, V.; Supej, M. J.; Stawiasz, K. J.; Shen, L.; Zipfel, W. R.; Abruña, H. D.; Freed, J. H.; Fors, B. P. Mechanistic Insight into the Photocontrolled Cationic Polymerization of Vinyl Ethers. *J. Am. Chem. Soc.* **2017**, *139* (43), 15530–15538.
- (36) Kottisch, V.; Michaudel, Q.; Fors, B. P. Photocontrolled Interconversion of Cationic and Radical Polymerizations. *J. Am. Chem. Soc.* **2017**, *139* (31), 10665–10668.
- (37) Barton, D. H. R.; Lacher, B.; Zard, S. Z. The Invention of New Radical Chain Reactions. *Tetrahedron* **1986**, *42* (8), 2325–2328.
- (38) Hammett, L. P. The Effect of Structure upon the Reactions of Organic Compounds. Benzene Derivatives. *J. Am. Chem. Soc.* **1937**, *59* (1), 96–103.
- (39) Hansch, C.; Leo, A.; Taft, R. W. A Survey of Hammett Substituent Constants and Resonance and Field Parameters. *Chem. Rev.* **1991**, *91* (2), 165–195.
- (40) Romero, N. A.; Margrey, K. A.; Tay, N. E.; Nicewicz, D. A. Site-Selective Arene C-H Amination via Photoredox Catalysis. *Science* **2015**, *349* (6254), 1326–1330.

- (41) Roth, H.; Romero, N.; Nicewicz, D. Experimental and Calculated Electrochemical Potentials of Common Organic Molecules for Applications to Single-Electron Redox Chemistry. *Synlett* **2015**, 27 (05), 714–723.
- (42) Sankararaman, S.; Haney, W. A.; Kochi, J. K. Aromatic Nitration with Ion Radical Pairs [ArH⁺,NO₂⁻] as Reactive Intermediates. Time-Resolved Studies of Charge-Transfer Activation of Dialkoxybenzenes. 15.
- (43) Cismesia, M. A.; Yoon, T. P. Characterizing Chain Processes in Visible Light Photoredox Catalysis. *Chem. Sci.* **2015**, 6 (10), 5426–5434.
- (44) Bordwell, F. G. Equilibrium Acidities in Dimethyl Sulfoxide Solution. *Acc. Chem. Res.* **1988**, 21 (12), 456–463.
- (45) Wayner, D. D. M.; Luszyk, E.; Page, D.; Ingold, K. U.; Mulder, P.; Laarhoven, L. J. J.; Aldrich, H. S. Effects of Solvation on the Enthalpies of Reaction of Tert-Butoxyl Radicals with Phenol and on the Calculated O-H Bond Strength in Phenol. *J. Am. Chem. Soc.* **1995**, 117 (34), 8737–8744.
- (46) Gardner, K. A.; Kuehnert, L. L.; Mayer, J. M. Hydrogen Atom Abstraction by Permanganate: Oxidations of Arylalkanes in Organic Solvents. *Inorg. Chem.* **1997**, 36 (10), 2069–2078.
- (47) Nelsen, S. F.; Ippoliti, J. T. The Deprotonation of Trialkylamine Cation Radicals by Amines. *J. Am. Chem. Soc.* **1986**, 108 (16), 4879–4881.
- (48) Dombrowski, G. W.; Dinnocenzo, J. P.; Zielinski, P. A.; Farid, S.; Wosinska, Z. M.; Gould, I. R. Efficient Unimolecular Deprotonation of Aniline Radical Cations. *J. Org. Chem.* **2005**, 70 (10), 3791–3800.
- (49) Jacobsen, H.; Donahue, J. P. Expanding the Scope of the Newman–Kwart Rearrangement — A Computational Assessment. *Can. J. Chem.* **2006**, 84 (11), 1567–1574.
- (50) Evans, M. G.; Polanyi, M. Some Applications of the Transition State Method to the Calculation of Reaction Velocities, Especially in Solution. *Trans. Faraday Soc.* **1935**, 31, 875.
- (51) Bell, R. P. The Theory of Reactions Involving Proton Transfers. *Proc. R. Soc. Lond.* **1936**, 154, 414.

CHAPTER 3: MECHANISTIC INVESTIGATIONS OF A PHOTOREDOX-MEDIATED ARENE C-H AMINATION

3.1 Introduction

The arene-amine linkage is one of the most prevalent scaffolds in pharmaceutical candidates. As a result, the ability to install this moiety selectively and under mild conditions has received considerable attention in recent years. Most notably, Buchwald-Hartwig^{1,2}, Ullman-type³, and Chan-lam couplings⁴, respectively catalyzed by Pd and Cu complexes, represent the most common methodologies for installing this molecular scaffold (**Figure 3.1**). As a reflection of the varied reactivity parameters, countless catalyst systems spanning a variety of pre-catalysts and ligand sets have been developed to achieve optimal reaction efficiency for a number of systems.

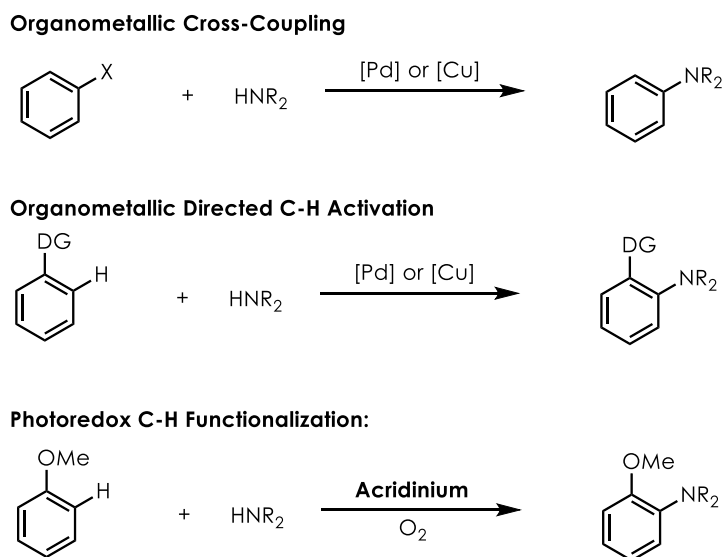


Figure 3.1. Methods for the installation of arene-amine linkage.

More direct methods of installing this linkage involve direct C-H activation of an arene system. These systems, while less developed, offer an attractive alternative to “traditional” coupling

strategies by removing the need for pre-functionalizing the arene coupling partner. This feature streamlines syntheses and offers the possibility of more atom economical methodologies. However, this reaction manifold features important obstacles in reaction development, namely the intrinsic inertness of aryl C-H bonds and difficulty in chemoselectively activating a single bond.

While many exciting developments in the field of organometallic arene C-H activation have been developed in recent years, there still exist significant hurdles. Advancements in the field have been achieved primarily through careful study of the kinetic dynamics of the initial C-H activation step. This step is commonly facilitated through the use of a directing group which pre-coordinates with the active catalyst to achieve C-H insertion. As a result, C-H activation systems typically feature extensive catalyst / ligand screening to optimize the reactivity active catalytic species. Insights gained from studying catalytically active complexes have been invaluable in advancing the potential of this field. However, the use of a directing group generally limits regioselectivity to positions ortho to the group. These groups also often require separate synthetic steps to “load” and remove and in some cases cannot be removed, severely limiting the generality of such methodologies.

As an alternative to organometallic C-H activation, many non-metallic methodologies have been developed. These typically proceed through oxidative pathways as a means of activating the arene towards nucleophilic addition^{5,6}. We recently disclosed⁷ the development of a photo-redox mediated aryl C-H functionalization manifold that has allowed for the direct functionalization of arenes with a number of nucleophiles using oxygen as terminal oxidant. This system generally features modest to excellent regioselectivity as well as good yields and offers orthogonal reactivity to known cross coupling reactivities. The use of an acridinium derived organic photoredox catalyst,

usually in combination with TEMPO as a co-catalyst, was found to be necessary to achieve usable reaction yields.

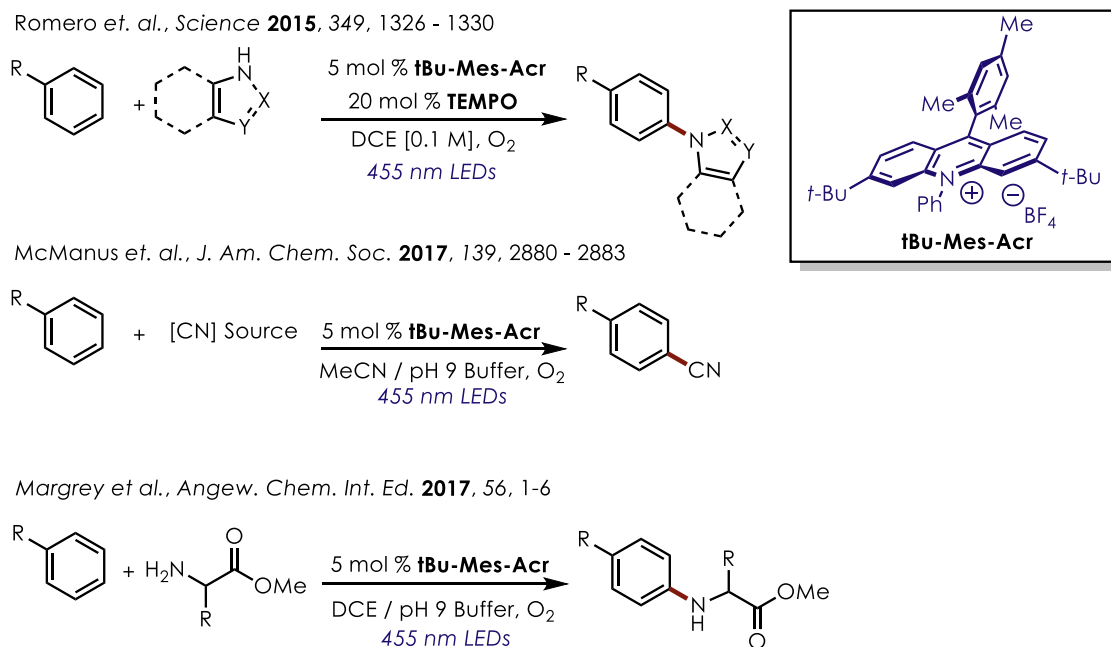


Figure 3.2. Photoredox-mediated arene C-H functionalization reactions developed in the Nicewicz group.

The initial report demonstrated an excellent substrate scope with a variety of electron-rich arenes and azole nucleophiles (**Figure 3.2 Top**). In all cases good to excellent selectivity for the para-substituted adduct was observed rendering this a synthetically useful transformation. Excellent yields could be obtained with irradiation of the reaction solutions with 24 h. The azole-arene products thus obtained are highly valuable intermediates in drug discovery. It was also shown that anilines could be synthesized using an ammonium salt as a nucleophilic partner, which represents an especially direct method for the synthesis of anilines (cross-coupling methodologies using ammonia, or ammonia equivalents, are underdeveloped in the literature).

In later reports it was found that this reaction manifold could be extended to a number of nucleophiles. Benzonitrile derivatives could be synthesized using the same general reaction conditions with TMSCN as a latent source of the cyanide anion, which was proposed to be slowly

liberated under the basic buffered conditions used.⁸ It was found that this transformation proceeded in excellent yields without the inclusion of TEMPO. Furthermore, primary amines were shown to be competent coupling partners to afford more functionalized aniline products.⁹

Intriguingly it was found that secondary amines were not suitable coupling partners under these conditions. It was initially proposed that this system could operate through a different mechanistic pathway from the previous cases. The amine substrate was shown to competitively quench the photocatalyst, affording the amine cation-radical intermediate, which could then be trapped by the arene substrate to eventually afford the desired product. This was shown to be the case with toluene and benzene which did not display quenching with the photocatalyst, though with arenes that do display quenching a mechanistic distinction could not be made. Most products obtained through this methodology displayed a slight preference for the ortho product, in contrast to the previous arene-azole C-H functionalization.

Due to the success of these systems in producing valuable synthetic targets we became interested in better understanding the general mechanism that we believed to be shared between the three systems. Previous work by Fukuzumi^{10,11} provided initial evidence that arene radical cations, when trapped by nucleophiles and in the presence of oxygen, could produce the oxidized adducts. More importantly, the proposed cyclohexadienyl radical intermediate has been shown to undergo aromatization in the presence of oxygen to produce hydroperoxyl radical.¹² However, numerous features regarding the reaction mechanism, as well as the influence of catalyst structure on reactivity, prompted us to pursue further studying the reaction mechanism. We believed that information obtained by such studies might inform our ongoing efforts towards extending this C-H functionalization manifold to other nucleophiles.

3.2 Initial Proposed Mechanism

The proposed reaction mechanism (**Figure 3.3**) for the arene-azole coupling involves photoexcitation of the catalyst to produce a strong oxidant, capable of removing an electron from the arene substrate and generating an arene cation-radical **1**. This intermediate undergoes nucleophilic trapping to afford the distonic cation-radical **2** which, following deprotonation, affords cyclohexadienyl radical **3**. In the presence of O₂, aromatization occurs via a formal oxidation process to afford the C-H functionalized product **5** and a peroxy radical¹⁰⁻¹⁴. Catalyst turnover is achieved by electron transfer between the reduced photoredox catalyst and oxygen (or the formed peroxy radical). It was found in most cases that the reaction displayed a preference for the formation of the para-substituted product. Initial optimization also suggested that oxygen is perhaps a privileged oxidant in this system

The inclusion of TEMPO was found to be necessary in the initial report to achieve high yields for most substrates. This was initially attributed to an improvement in the mass-balance for the reaction; without TEMPO substrates bearing activated alkyl C-H bonds would undergo oxidative functionalization. However, the possibility that TEMPO might aid in rearomatization of the cyclohexadienyl radical could not be excluded. It was also suspected that the photoredox catalyst might undergo degradative transformations¹⁵⁻¹⁷, via either nucleophilic or radical pathways, resulting in catalyst death. This was supported by the observation that an acridinium derivative bearing bulky tert-butyl groups on the acridinium core is the most effective catalyst in all reports thus far.

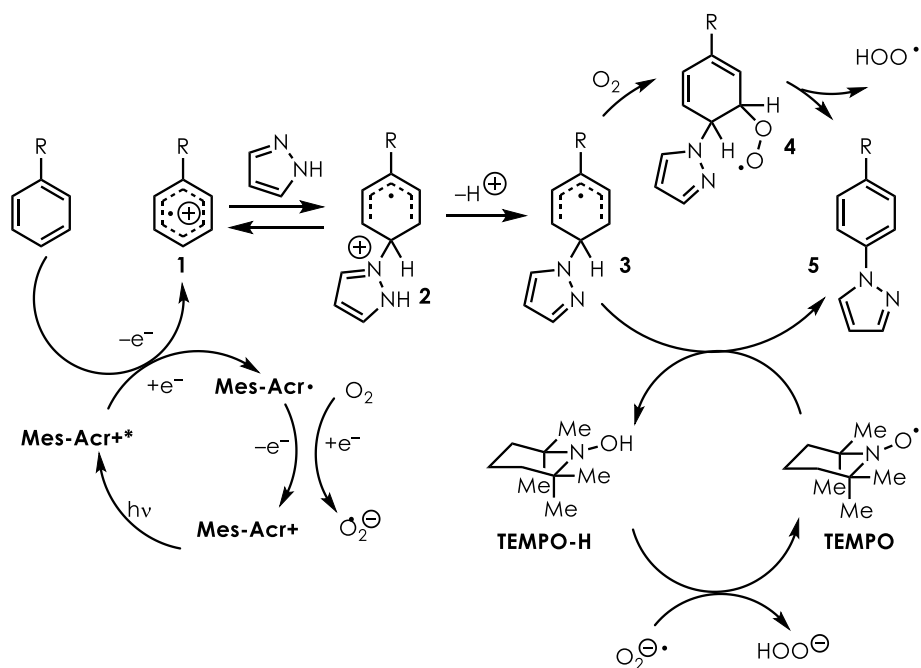


Figure 3.3. Working mechanistic proposal for acridinium-mediated arene C-H amination.

In light of these observations, and the desire to further develop this reaction manifold to other nucleophiles, we decided to undertake a mechanistic investigation of the first C-H amination system. Upon approaching this system a few key features, among others, were identified that we wished to better understand:

- 1) What is the role of TEMPO in the reaction?
- 2) What features of the acridinium catalyst are most important to achieving high reaction efficiency?
- 3) Can another oxidant be used in place of oxygen?
- 4) What is the origin of the para-selective nature of the reaction?

We proposed that we could answer these questions through a combination of absorption and emission spectroscopy techniques as well as a kinetic analysis of the various components of the reaction system.

3.3 Antioxidant Studies

3.3.1 Establishing the Presence of Peroxyl Radical Species

The optimization of the reaction with anisole originally found that without TEMPO the reaction afforded moderate yields (47%) of the material to the desired product. The remaining mass-balance of the starting material was determined to be primarily the oxidized formate adduct. Formation of this species was presumed to form via dioxygen trapping an α -oxy radical that could be formed through an initial HAT by the hydroperoxyl radical formed during the reaction. (**Figure 3.4**). Upon addition of TEMPO, this degradation was no longer observed and reaction yields were found to improve overall. Even for substrates that did not bear labile C-H bonds (e.g. diphenyl ether and biphenyl), the reaction was found to proceed to a greater extent upon the inclusion of TEMPO.

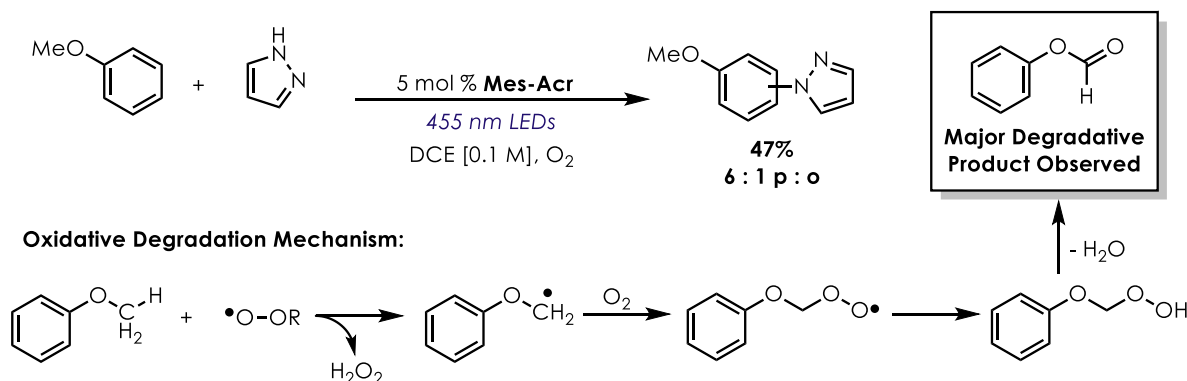


Figure 3.4. Observation of substrate decomposition during initial optimization of the reaction.

The improved mass-balance afforded by TEMPO could be explained by its ability to quench reactive oxygen species (ROS) that would be produced during the reaction. Various ROS could be produced during the reaction under the proposed mechanism, including superoxide¹⁸ (O₂⁻) and peroxy hydroperoxyl radical (HOO•). These species are known to abstract activated aliphatic C-H bonds, with hydroperoxyl radical predominately being thought of as the chain-carrying species

in hydrocarbon autooxidations¹⁹⁻²¹. While the mechanism(s) through which TEMPO quenches these ROS have been unclear until recently²²⁻²⁶ (vide infra), its use as an antioxidant in biological systems is well known. Thus, we first sought to determine if these ROS were generated during the reaction conditions.

The generation of superoxide was initially proposed to occur to allow for turnover of the acridinium catalyst, via oxidation of the acridine radical by O₂. However, examination of the reduction potentials of these species ($E_{1/2}(\text{Mes-Acr}^+/\text{Mes-Acr}\cdot) = -0.52 \text{ V vs. SCE}$; $E_{1/2}(\text{O}_2/\text{O}_2\cdot^-) = -0.75 \text{ vs SCE}$ ²⁷, both values in MeCN) suggests that such an electron transfer would be endergonic. Despite this, there exist reports of oxygen reduction in acridinium mediated systems where electron transfer would appear to be the only mechanism responsible for turnover of the acridinium species.^{10,17,28,29}

Consequently, we attempted to observe directly via UV-Vis spectroscopy, the oxidation of **tBu-Mes-Acr** \cdot by O₂. A solution of **tBu-Mes-Acr** \cdot in DCE was prepared via reduction of **tBu-Mes-Acr** by CoCp₂. The **tBu-Mes-Acr** \cdot , as has been shown previously³⁰, is stable in the absence of a suitable oxidant. Sparging of this solution with O₂ immediately resulted in the formation of **tBu-Mes-Acr** as confirmed by the complete reappearance of the absorbance bands centered around 425 nm (**Figure 3.5**). Indeed, this process is apparently rapid despite the apparent endergonicity of this process. Importantly, it appears that the acridinium moiety appears to be recovered intact during this process.

From these results, the existence of superoxide, a potent radical / nucleophilic oxygen source, during these reactions can be considered feasible. Moreover, based on literature precedent and the observation of reactivity in the absence of TEMPO, the formation of hydroperoxyl radical from the reaction of oxygen with the cyclohexadienyl radical can be reasonably assumed. Moreover,

protonation of superoxide by the distonic cation-radical intermediate **2** would also generate hydroperoxyl radical. As a result, there exist numerous pathways through which ROS, which may initiate substrate and catalyst degradation pathways, can be generated and that at any given point during the reaction there exists some concentration of each of these intermediates.

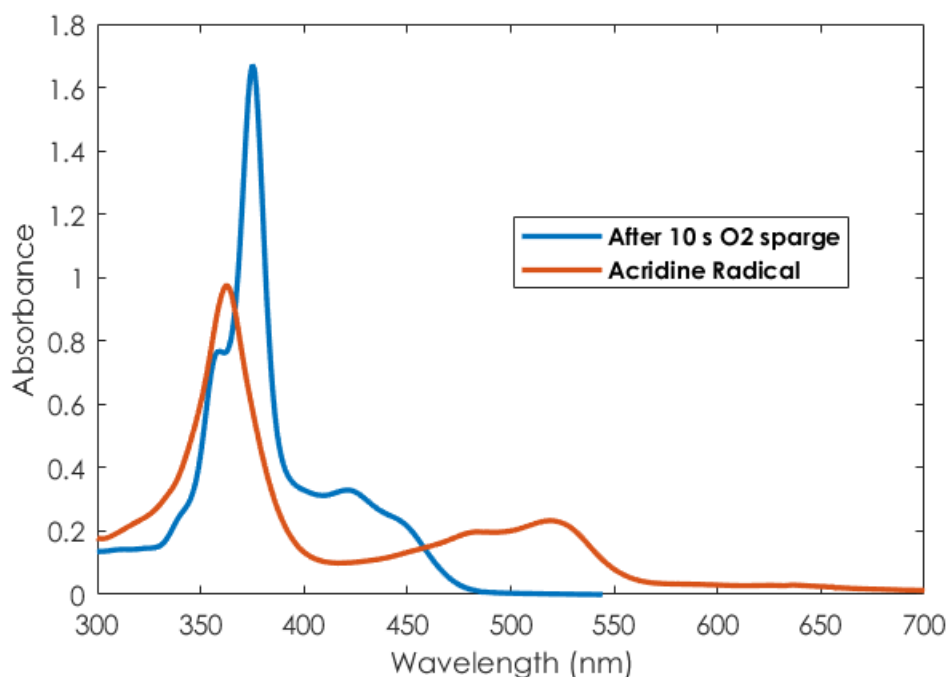
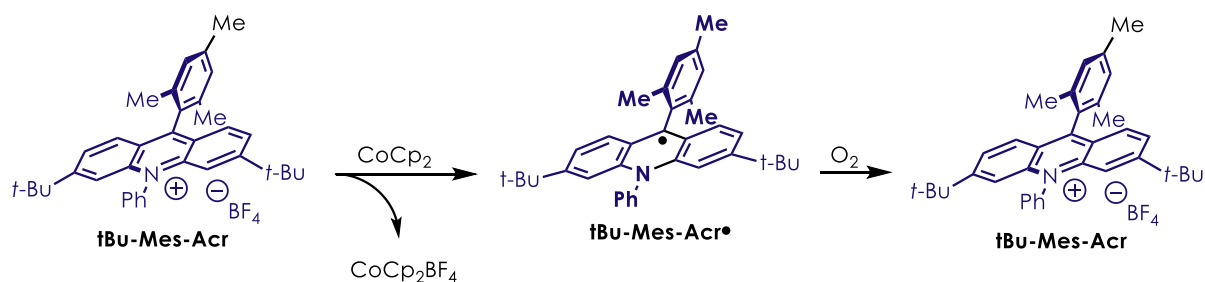


Figure 3.5. Spectroscopic evidence confirming turnover of acridine radical by oxygen. Data obtained by Nathan Romero.

3.3.2 Mechanisms of Peroxyl Radical Quenching by TEMPO

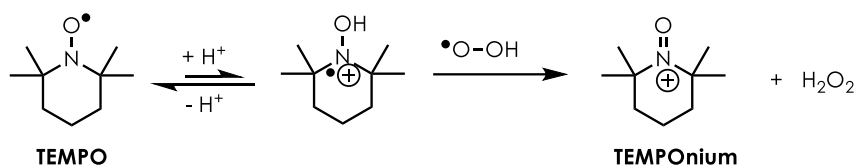
Given these results we believed it reasonable to assume that one major function of TEMPO during the arene C-H functionalization is to quench these ROS species. It has been shown that TEMPO can quench ROS through a number of mechanisms. Two mechanisms for its reactivity

with peroxy radicals have recently been elucidated (**Figure 3.6**). First, in the presence of a trace amount of acid, TEMPO can be protonated to produce TEMPO-H⁺, which undergoes a rapid disproportionation with peroxy radical to produce the oxoammonium TEMPO⁺ and hydrogen peroxide (**Figure 3.6A**)^{22,24}. This reaction operates at diffusion-controlled rates and is operable even when extremely small amounts of weak acids (e.g. acetic acid) are present in solution. In the second mechanism, TEMPO can react directly with hydroperoxyl radical in an HAT event which produces TEMPO-H and dioxygen (**Figure 3.6B**)²⁵. This reaction is driven thermodynamically by the favorable formation of the TEMPO-H bond (BDE 71 kcal / mol) from the weaker •OO-H bond (BDE 61 kcal / mol).

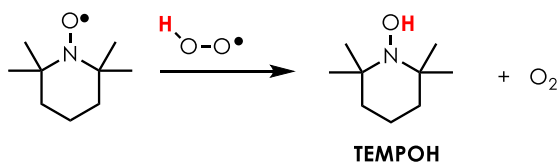
Under the reaction conditions we believe it reasonable to assume that both pathways may be operable. For the first mechanism, the trace acid required to form TEMPO-H⁺ could be generated from the formation of the distonic cation radical intermediate **2**. As has been shown by Pratt, only a small equilibrium concentration of TEMPO-H⁺ is required to effectively react with peroxy radicals as the process is essentially diffusion controlled. Moreover, the TEMPO⁺ generated from this pathway can conceivably be converted back to TEMPO by undergoing reduction by the reduced catalyst **tBu-Mes-Acr•**, which would also regenerate the active photocatalyst (**Figure 3.6C**).

The second mechanism can be assumed to be operative given that the generation of hydroperoxyl radical is proposed through the processes mentioned above. Moreover, TEMPO-H can be observed by GC-MS during the reaction supporting this mechanistic pathway. TEMPO can be regenerated under the reaction conditions through a number of HAT pathways.

A) Acid-promoted Reductive HAT of Hydroperoxyl Radical



B) Oxidative HAT of Hydroperoxyl Radical



C) Regeneration of tBu-Mes-Acr+ by TEMPO cation

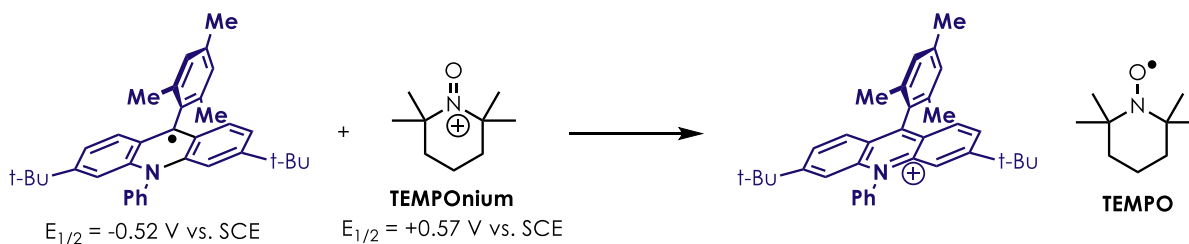


Figure 3.6. Reactivity of TEMPO and related species under aerobic photoredox conditions

Thermodynamically, HAT from TEMPO-H would be favorable to form either hydroperoxide anion from superoxide (BDFE $\text{-OO-H} = 81.6 \text{ kcal/mol}$) or hydrogen peroxide from hydroperoxyl radical (BDFE $\text{H-OOH} = 91.0 \text{ kcal/mol}$).²⁷ We believe that these pathways are responsible for the prevention of substrate decomposition upon inclusion of TEMPO.

We became interested in exploring if TEMPO played a role in the reaction beyond preventing substrate and catalyst degradation. Initially it was postulated that TEMPO might aid in the proposed rearomatization of the cyclohexadienyl radical intermediate. The rate of cyclohexadienyl trapping with oxygen is known to be diffusion controlled ($k \sim 10^9\text{-}10^{10} \text{ s}^{-1}$) in all solvents¹². Comparatively, the rate of TEMPO trapping of alkyl radicals is generally at least an order of magnitude slower³¹ ($k \sim 10^7\text{-}8 \text{ s}^{-1}$), however for cyclohexadienyl radical the rate has been reported to be $2.3 \times 10^8 \text{ M}^{-1} \text{ s}^{-1}$ in a 3 : 1 $\text{Me}_3\text{COOCMe}_3$: Benzene mixture. However, the rate for

trapping of carbon-centered radicals has been shown to be sensitive to solvent.³² For example, trapping of benzyl radical with TEMPO occurs at a rate of $\sim 1.7 * 10^8 \text{ M}^{-1} \text{ s}^{-1}$ in both benzene and ethyl acetate, however in DCM the rate falls by roughly a factor of 3 to $5.6 * 10^7 \text{ M}^{-1} \text{ s}^{-1}$. Given that the relative concentrations of O_2 and TEMPO under the arene C-H functionalization reaction conditions are relatively equal ($\sim 10 \text{ mM}$)¹², it seems unlikely that TEMPO would be kinetically relevant in the rearomatization step.

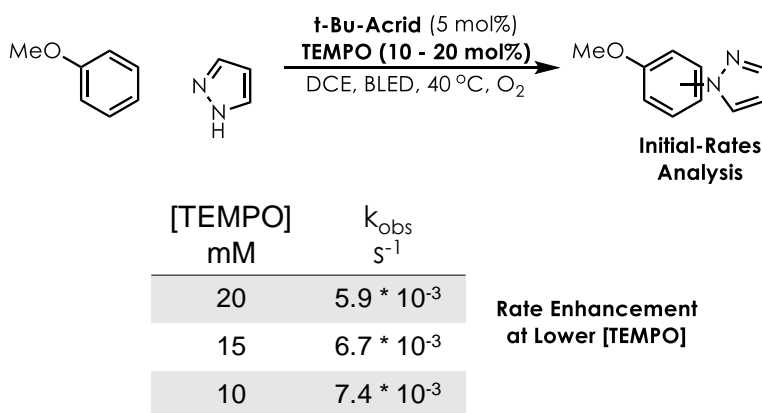


Figure 3.7. Initial rates analysis of TEMPO loading on rate of anisole - pyrazole photoredox coupling.

In light of this literature precedent we undertook a kinetic analysis of the reaction using the initial-rates method. Varying the concentration of TEMPO between 10 and 20 mol% showed an inverse relationship between k_{obs} and [TEMPO] (**Figure 3.7**). These data on their own would suggest that TEMPO is not responsible for an overall rate enhancement of the aryl C-H functionalization process. However, it is also important to note that TEMPO could be involved in unproductive pathways, like SET, with the active photocatalyst given its low reduction potential ($E_{1/2} = +0.57 \text{ V vs SCE in MeCN}$)³³ (**Figure 3.8**). Indeed, a Stern-Volmer quenching analysis showed very efficient, diffusion-controlled quenching ($k_q = 1.0 * 10^{10} \text{ M}^{-1} \text{ s}^{-1}$) of the excited state **Acr+**, suggesting that the observed inhibition of reactivity could in part be due to this unproductive

pathway. This quenching event, along with any downstream pathways, could make interpretation of the reaction kinetic results more difficult.

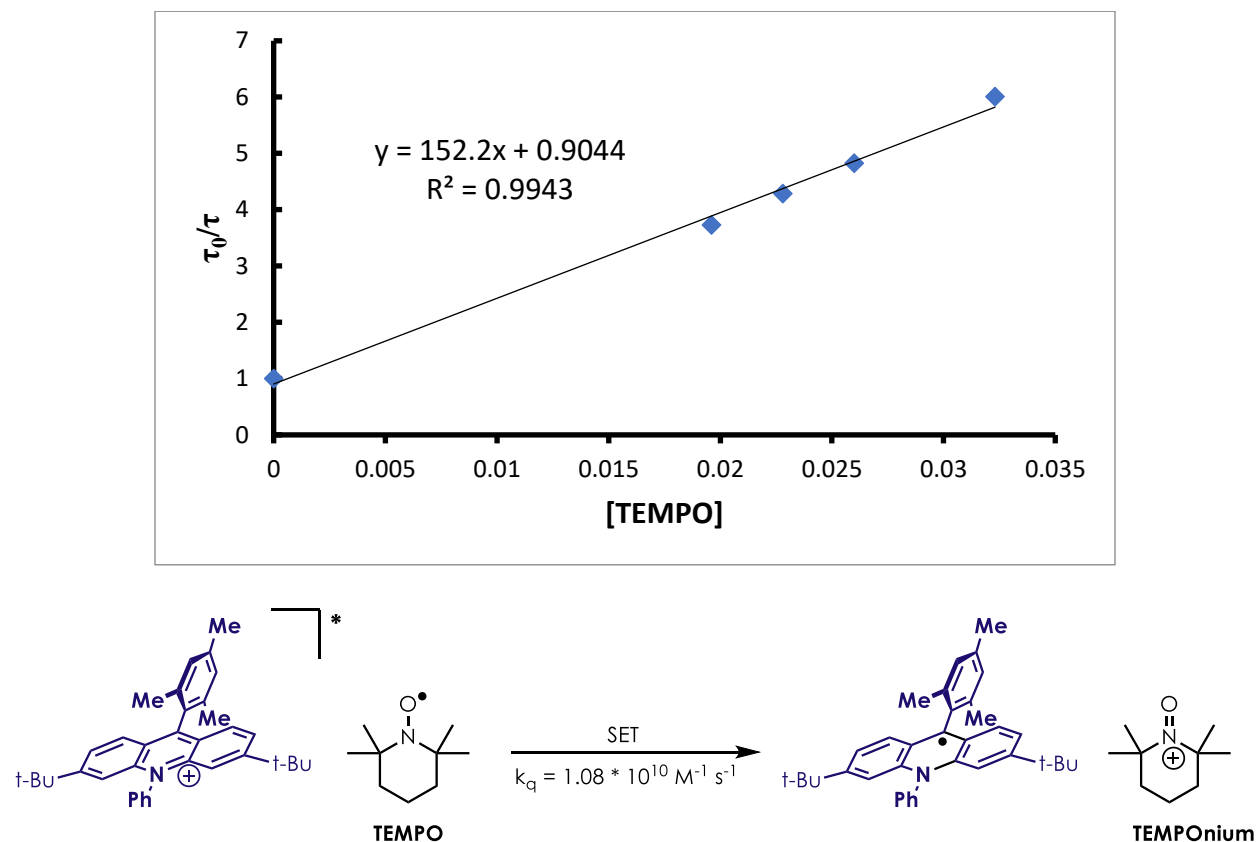


Figure 3.8. Stern-Volmer quenching analysis of TEMPO and proposed SET products.

3.3.3 Exploring Other Antioxidants

As a result of these data we decided that we could not rule out, with our kinetic data alone, a beneficial rearomatization step mediated by TEMPO. In order to provide further evidence towards this goal we envisioned that other peroxide scavenging compounds might also afford similar reactivity in our arene C-H functionalization system. We hypothesized that if a different antioxidant was added in place of TEMPO and did not alter the reaction dynamics, then it could be suggested that the proposed rearomatization by TEMPO is not kinetically relevant under these conditions. This conclusion could be further bolstered if the alternative antioxidants were neither nitroxide based nor converted to a nitroxide species during the reaction.

A number of compounds are commonly used as antioxidants in both biological and industrial applications. The quintessential biological antioxidants are those derived from tocopherol (Vitamin E) which features a sterically hindered phenol. The ROS quenching reactivity stems from the relatively weak O-H bond of these phenols (BDE ca. 77 kcal/mol), which serve to undergo HAT with peroxy radicals to quench these destructive species.^{34,35}

Antioxidants are commonly used industrially to preserve hydrocarbons-based oils used in combustion engines; at the high temperatures required for combustion, generation of peroxy radicals via HAT by ambient oxygen becomes a facile process. This initiation step is capable of starting a radical propagation chain reaction and as a result oxidative degradation of hydrocarbons at high temperatures is a major concern in these applications. For these applications, in general, amine-based antioxidants are preferred over phenolic-based additives.³⁶⁻³⁸ The amines are generally easier to handle, more amenable to mixing with materials, and possess similar rates of inhibition (generally referred to as k_{inh}) of ROS chain carrying species (for example, k_{inh} for diphenylamine is measured to be on the order of $10^4 \text{ M}^{-1} \text{ s}^{-1}$ while tocopherol is $10^4 \text{ M}^{-1} \text{ s}^{-1}$).

We selected a number of traditionally used antioxidants (BHT, Diphenylamine, 2,2,6,6 - Tetramethylpiperidine) as well as a recently developed derivative **3-CNPHenox** that shows excellent antioxidant ability (**Figure 3.9**). These additives have k_{inh} values³⁶⁻³⁸ ranging from $10^4 - 10^9 \text{ M}^{-1} \text{ s}^{-1}$, with TEMPO possessing an intermediate k_{inh} value of 10^4 as a point of reference. We began by assessing each additives effect on the reaction between anisole and pyrazole using **Acr+** as a catalyst and comparing the results to the optimized conditions with TEMPO. The phenol-based antioxidant BHT displayed a lower observed yield than that obtained with TEMPO, however, all of the amine-based antioxidants demonstrated comparable reactivity to the optimized conditions. This reactivity seemingly correlated with the higher k_{inh} values for the amine-derived

additives. This is supported by the lack of any observable oxidative degradation products in these reactions.

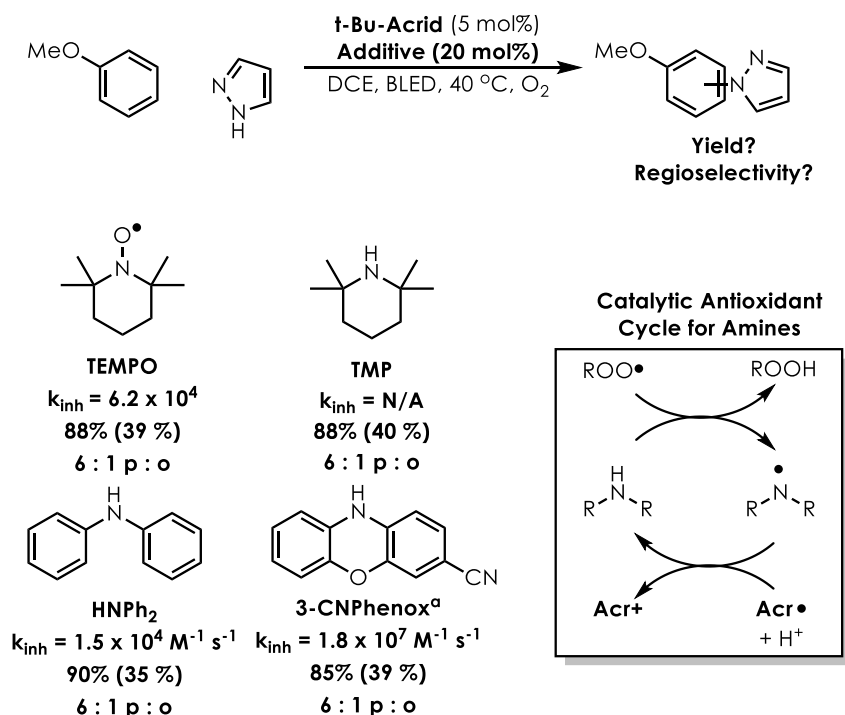


Figure 3.9. Investigations of alternative antioxidants for arene C-H functionalizations. Yields determined via NMR in reference to HMDSO internal standard. Paranthetical yields refer to reactions halted at 30 minutes reaction time. a) Additive loading was 1 mol%.

From these results we concluded that amine-derived antioxidants are most efficient in achieving high reactivity in the photoredox aryl C-H functionalization system. These results initially suggested that the presence of a nitroxide species is not strictly necessary for obtaining good reactivity in this system. In order to further investigate the effect of TEMPO and other additives we decided to assay these reactions at lower conversions. We believed that if the reaction conversions are similar between examples with TEMPO and with the other antioxidants then this would provide evidence that TEMPO is not involved in accelerating the rate of product formation.

Using the same additives we analyzed the reaction conversions after 30 minutes reaction time. Under the optimized conditions with TEMPO a 40% reaction yield could be observed (**Figure**

3.9). When the other amine-derived additives (**TMP**, **HNPh₂** and **3-CNPhenox**) were tested in this manner, similar yields could be observed; all reactions were found to have proceeded to around 40% yield as determined by NMR analysis. Importantly, it was noted during these reactions that the corresponding nitroxyl species for each amine-derived additive were not observed via NMR or GC-MS. This was especially surprising in the reaction using **TMP** as an additive, as the corresponding nitroxyl derivative is TEMPO! This suggests that the beneficial effect for these additives derives mainly from their ability to quench ROS via donation of a hydrogen atom. Presumably, the resulting radicals from this event could then undergo SET with the reduced catalyst and, after protonation, provide the regenerated additive.

These results, combined with the observed kinetic data, suggest that the major role of TEMPO in the arene C-H amination system is to solely quench ROS that accumulate during the reaction. While we cannot strictly rule-out the possibility that TEMPO might engage in HAT from the cyclohexadienyl radical it seems unlikely that such a step is relevant to achieving good reactivity. Perhaps most convincingly, the observation that arene C-H functionalization occurs with other nucleophiles in the absence of TEMPO lends further credence to this assertion. The ROS generated in other photoredox C-H functionalization systems could conceivably be quenched via different mechanisms due to the different reaction conditions. In general, these systems are run under biphasic conditions with a basic aqueous buffer. Any peroxide species generated during the reaction might be sequestered in the aqueous phase and eventually degraded due to the instability of peroxides under basic conditions.³⁹

3.4 Catalyst Degradation Studies

Having established the role of the TEMPO co-catalyst in the reaction system we turned our studies towards better understanding the stability of the acridinium-based catalysts under these

conditions. In the initial report it was noted that higher reaction yields were observed by modifying the acridinium catalyst to include more sterically bulky substituents around the acridinium core. The highest yields were observed when using the 3,6-di-*tert*-butyl-substituted acridinium catalyst (**Figure 2.10**). It was initially proposed that increasing the steric bulk of the substituents on the acridinium prevented decomposition of the catalyst.

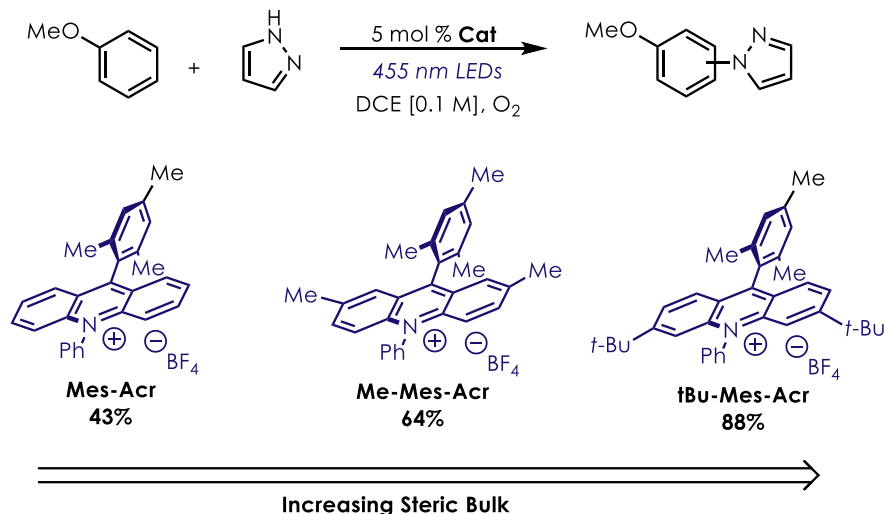


Figure 3.10. Dependence of substituent size on catalyst efficiency.

We became curious in characterizing the various decomposition pathways of the acridinium catalyst under these reaction conditions. Acridinium catalysts bearing mesityl substitution at the 9 position, so-called Fukuzumi catalysts, have been shown to undergo oxidative functionalization at the benzylic positions of the mesitylene moiety, ultimately furnishing the aldehyde adducts.¹⁵ These degradation pathways have been suggested to result in decreased activity in acridinium catalyzed systems. However, such a degradation pathway could still presumably be operative even in catalysts bearing substitution around the acridinium core.

Consequently, we instead considered that the catalyst might undergo oxidative functionalization of the acridinium core via nucleophilic addition (**Figure 3.11A**). Under the oxidative conditions of the reaction system it seemed plausible that the nucleophilic partner might

form an adduct with the electrophilic catalyst that could then undergo a formal oxidation to furnish a covalently-modified acridinium species. Possible species present in the reaction that could act as nucleophiles include the amine coupling partners as well as any various ROS generated during the reaction that could ultimately be a source of hydroxide.

It has been shown that the addition of electron-donating groups to the acridinium core can have a dramatic effect on the photophysical and electrochemical properties of acridinium dyes.^{40,41} We thus believed it likely that any acridinium species created through this pathway might become inactive catalysts. The beneficial inclusion of the bulky substituents could then be explained by preventing the initial nucleophilic capture event and decreasing the likelihood of catalyst modification.

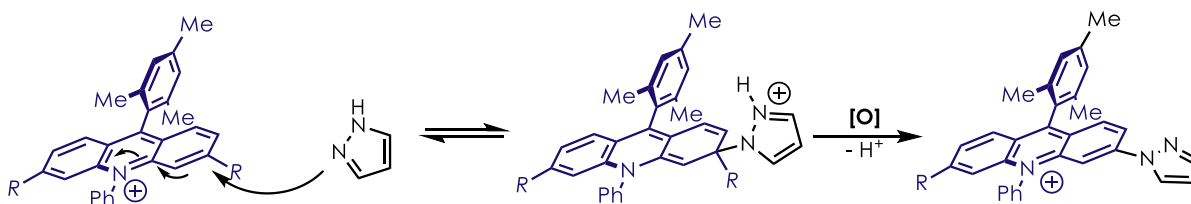


Figure 3.11. Proposed pathways for covalent catalyst modification.

We decided to study the stability of various acridinium catalysts in this reaction system through a combination of UV-Vis spectroscopy and LC-MS analysis. We envisioned that through monitoring the change in the absorbance spectra during the reaction could provide insight towards whether functionalization of the catalyst was occurring on the acridinium core or on the aryl ring at the 9-position. In general, dramatic changes in absorbance at longer wavelengths (>400 nm) of acridiniums are observed as substitution on the acridinium core increases. Additionally, substitution on the aryl ring of the 9-position can introduce new absorbance features in the visible (>400 nm) region of the spectrum.^{42,43} However, this effect is dramatically attenuated when this

ring possesses methyl groups in the 2 and 6 positions, as this modification locks the ring in an orthogonal angle to the acridinium core, preventing overlap of the π systems.

We hypothesized that if we observed large changes in the absorbance features at wavelengths >400 nm then the catalyst was being functionalized on the acridinium core. LC-MS analysis of these reaction solutions could then identify any possible acridinium derivatives that could then be synthesized and analyzed via the same methods for comparison.⁴⁴ Ultimately, we hoped to show that any species identified in this way could then be assessed in the arene C-H functionalization.

Beginning with the standard reaction conditions with the unsubstituted **Mes-NPA** catalyst we acquired UV-Vis data of the reaction over the course of 1 hour (**Figure 3.12**). Within 20 minutes an apparent bleaching of the reaction solution could be observed, suggesting that the π framework of the acridinium system was being disrupted. However, new absorbance features localized around 400 nm and 480 nm could be observed that appeared to grow in intensity as the reaction progressed. LC-MS analysis of these samples showed that within 20 minutes almost all of the initial **Mes-NPA** species could not be detected. Instead, a new species with $m/z = 440.212$ could be observed and was the only other major species detected that corresponded to an acridinium adduct.

This m/z corresponds to that of a pyrazole-acridinium adduct. Another species with a mass corresponding to functionalization of the catalyst by two equivalents of pyrazole could also be observed at late time points. Additional species corresponding to oxygenation of either the parent **Mes-NPA** or the pyrazole-adducts could also be observed, though in relatively smaller amounts. We also found that the same changes in UV-Vis and LC-MS data could be observed when anisole is removed from the reaction mixture, suggesting that this degradation pathway is operative irrespective of the overall transformation.

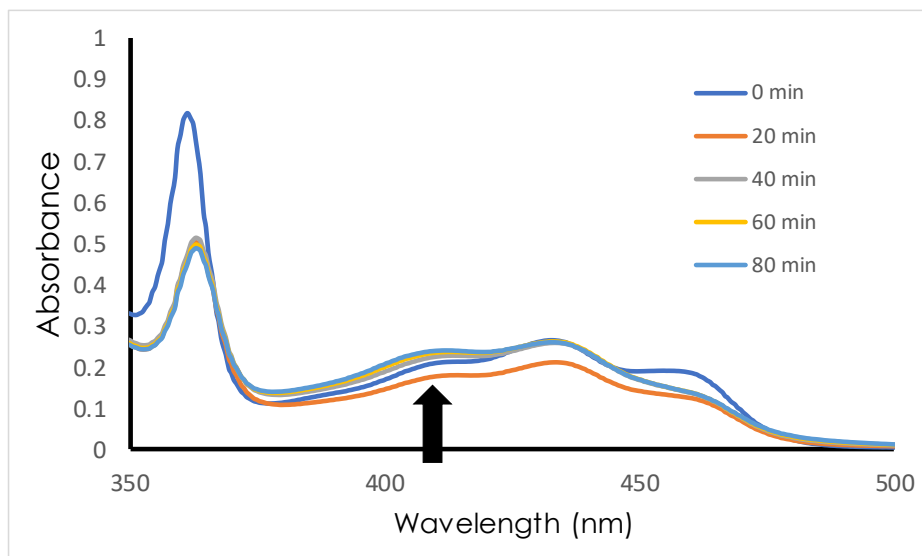
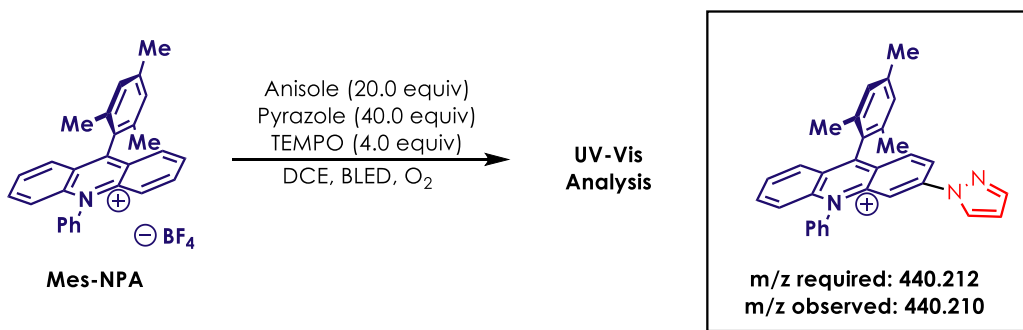
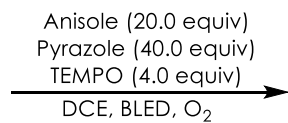
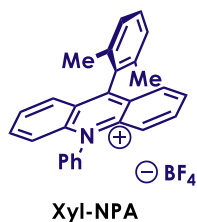


Figure 3.12. Analysis of reaction mixture via UV-Vis. Boxed structure refers to proposed acridinium degradation observed via LC-MS (ESI+).

We initially believed that this new species had undergone functionalization on either the acridinium core or the mesitylene ring. Functionalization of the mesitylene could occur at either the aryl (via the charge-transfer state) or benzylic C-H positions. To distinguish between these two possible sites of functionalization we decided to analyze the structurally similar 9-xylyl derivative **Xyl-NPA**. We have shown that substitution of the 9-mesityl group for a 9-xylyl group removes the charge-transfer character of the excited state acridinium.^{30,42} Thus, if functionalization is occurring



UV-Vis
Analysis

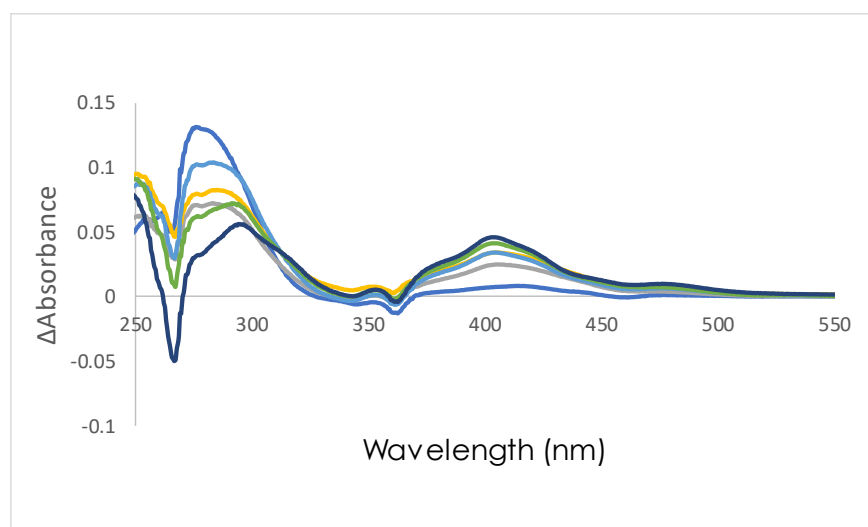
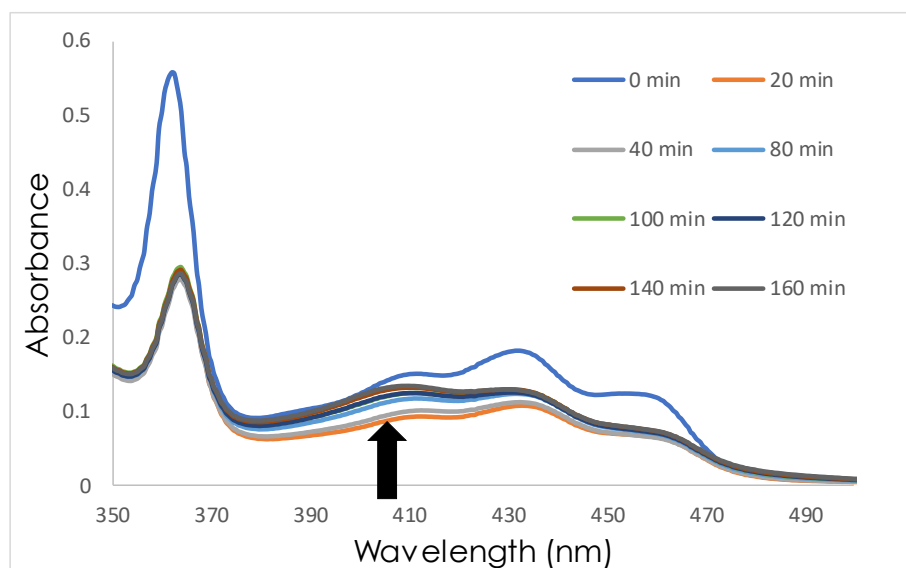
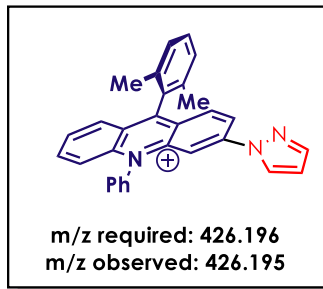


Figure 3.13. Analysis of reaction mixtures (top) via UV-Vis (middle). Delta Absorbance graph (bottom) generated by subtracting the spectrum obtained at 20 minutes from subsequent samples. Boxed structure refers to proposed acridinium degradation observed via LC-MS

through this state we would not expect to observe the same UV-Vis and LC-MS data as for the 9-mesityl derivative.

Monitoring the reaction solution with **Xyl-NPA** showed similar changes in the absorbance spectra as for **Mes-NPA**. A more drastic initial bleaching (ca. 50% of the overall absorbance at wavelengths >400 nm) could be observed followed by the growth of completely new absorbance features. The maxima of these new features, obtained by subtracting the spectra taken at 20 min from subsequent samples, were found to be centered around 400 and 480 nm as was observed for the mesityl derivative (**Figure 3.13 Bottom**). LC-MS data also supported the presence of a pyrazole adduct as the major acridinium species at all time points after 0 min.

Since **Xyl-NPA** does not possess a charge transfer species upon excitation we believe it is unlikely that functionalization is occurring at an aryl C-H position. This leaves either the acridinium core or benzylic C-H positions as likely positions for functionalization. However, substitution at the benzylic positions seems unlikely to affect the absorbance features in the visible region as this position is not conjugated with the acridinium π system. This leaves the acridinium core as the most likely site for functionalization, with the 3 and 6 positions being identified as the most electrophilic positions after considering possible structures that are most likely to be large resonance contributors.

In support of this hypothesis the acridinium derivatives bearing *tert*-butyl groups at the 3 and 6 positions (**tBu-Mes-NPA**) do not display a significant change in the absorbance features at wavelengths >400 nm (**Figure 3.14**). Despite this, a pyrazole adduct can still be observed to form which we tentatively attribute to functionalization on the arene ring at the 9 position of these catalysts, though work is ongoing to confirm the identity of this species.

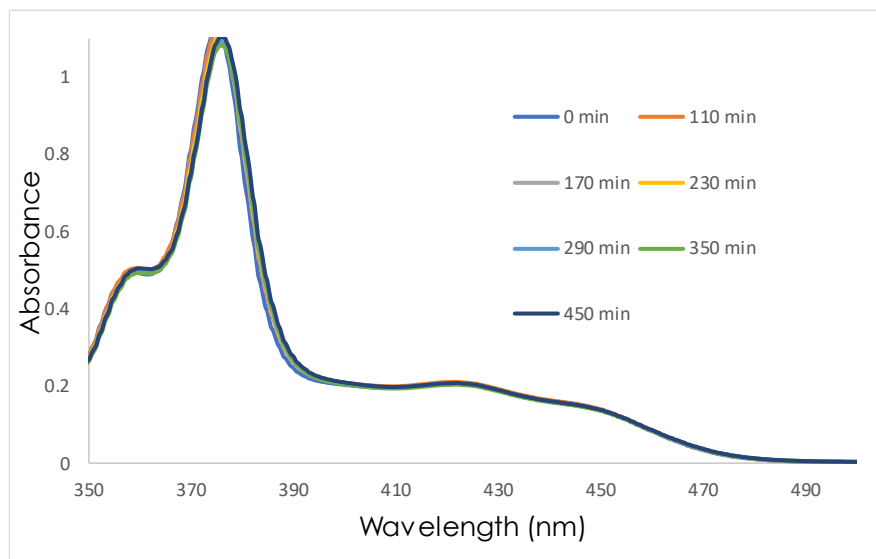
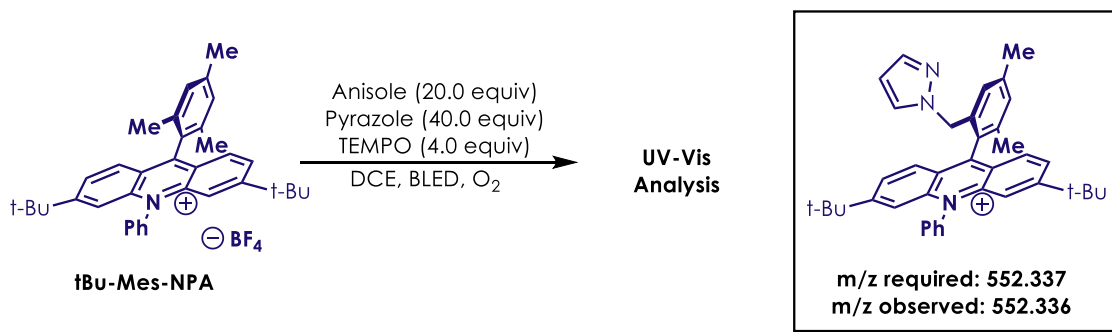


Figure 3.14. Analysis of reaction mixtures via UV-Vis (middle). Boxed structure refers to proposed acridinium degradation observed via LC-MS (ESI+).

We then independently synthesized the 3-pyrazoyl acridinium derivative **3-Pyrazoyl-Xyl-NPA** in an attempt to confirm the structures of the major species observed via UV-Vis and LCMS. The UV-Vis spectra (**Figure 3.15**) show absorbance maxima at more red-shifted wavelengths that match those observed from the reaction mixture. The pyrazole species also possesses significantly higher ϵ values, suggesting that it would preferentially absorb light if it was present in the reaction mixture. However, the retention times of these species observed via LC-MS do not match those of the acridinium species observed to form during the reactions.

To account for this observation two options seem plausible. First, the mono-pyrazole adduct may correspond to functionalization of the benzylic positions and the observed changes in the

absorption spectra can be attributed to further functionalizations of this species. For example, after functionalization of the benzylic position, the acridinium core might undergo functionalization at the 3 position and result in the apparent UV-Vis changes. This would agree with the observation that a large amount of mono-pyrazole adduct is seen at 20 min despite an apparent bleaching in the UV-Vis. Alternatively, it is possible that the mono-pyrazole adduct corresponds to functionalization on the acridinium ring at a different position. Work is ongoing to synthesize these other isomers and compare their properties to the absorption and LC-MS spectra obtained from the reaction mixtures.

We were curious to characterize the activity of the pyrazoyl-substituted acridinium in the reaction. We reasoned that if the synthesized derivatives displayed reduced activity this would further support this pathway as a route for catalyst deactivation. Indeed, the synthesized pyrazoyl acridiniums show reduced activity as a catalyst for the desired transformation. Moreover, LC-MS analysis of these reactions shows that these catalysts undergo further degradation. Surprisingly, a hydroxylated species (**3-OH-Xyl-NPA**) corresponding to substitution of the pyrazole moiety for an alcohol could be observed. That the pyrazoyl-acridinium is unstable under the reaction conditions could suggest that it is formed transiently in reactions and is consumed, potentially complicating its identification in reaction mixtures. Moreover, this species may ultimately be responsible for the loss of catalytic activity. Overall, we believe these results provide good initial evidence towards our overall hypothesis that functionalization of the acridinium catalyst by nucleophiles leads to lowered activities in this system.

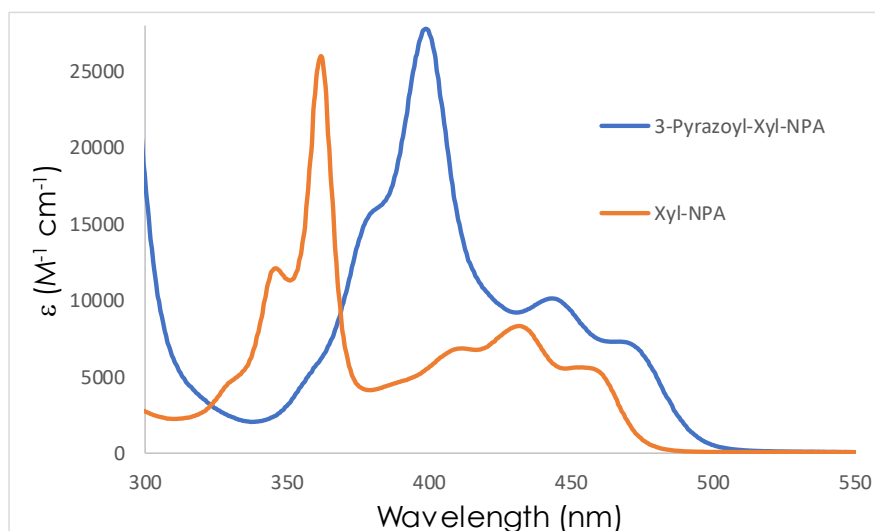
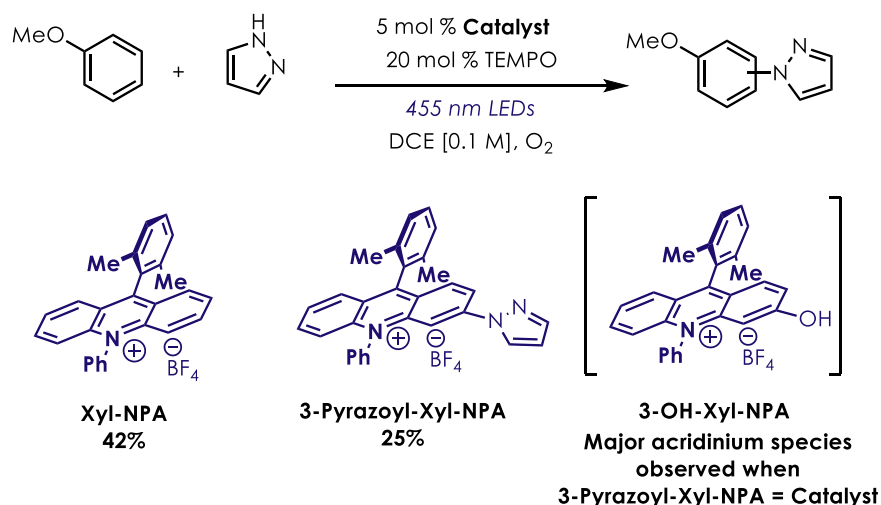


Figure 3.15. Comparison of the absorptivity of the acridiniums shown.

3.5 Ground State or Excited State Decomposition?

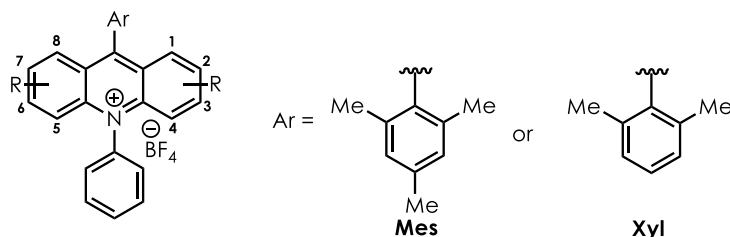
In the previous section we demonstrated that acridinium catalysts that do not possess bulky substitution on the core undergo a significant degree of functionalization under the reaction conditions. Consequently, we were curious if this reactivity was driven through photochemical processes or thermal processes. We envisioned that the acridinium core might be sufficiently electrophilic to undergo nucleophilic addition in its ground state.

We subjected the catalysts **Mes-Acr** and **Xyl-Acr** to the reaction conditions in the absence of any irradiation source. In both cases we observed no major changes in the absorption profiles as

well as the lack of any functionalization by LC-MS analysis. Moreover, we conducted these experiments at both room temperature and slightly elevated temperatures as the LEDs used for irradiation generate heat during use (reaction temperatures are generally around 40 °C) and obtained the same results. Finally, in order to probe the existence of a sigma-adduct that existed in equilibrium with the free **Xyl-Acr** species we conducted a UV-Vis experiment wherein the absorbance of **Xyl-Acr** is monitored as varying amounts of pyrazole are added to the solution. The results of this shows a linear bleaching of the acridinium absorbance that is consistent with the expected decrease in absorbance from dilution. From these studies we concluded that under the reaction conditions there is no background reactivity between the nucleophile and the acridinium catalyst.

Having obtained these results we thus considered that any adduct formation might proceed through a photochemical pathway. In order to probe the feasibility of such a pathway we turned to fluorescence quenching studies (*i.e.* Stern-Volmer quenching)⁴⁵. It was found that pyrazole exhibits significant quenching ($k_q = 1.5 - 3.0 * 10^9 \text{ s}^{-1}$) of the excited states of **Mes-Xyl** and **Xyl-Acr**. While this quenching could be rationalized as a SET event this seemed unlikely given the reduction potential for pyrazole oxidation ($E_{p/2} = 2.20 \text{ V vs SCE}$) and the apparent magnitude of the quenching constant. The thermodynamics for electron transfer between these catalysts and pyrazole should only be weakly exergonic at best and thus it would be expected that only a small degree ($k_q \sim 10^8$ has been observed for acridinium quenching of similar thermodynamic properties).³⁰ Extremely weak quenching ($1.6 - 2.6 * 10^8 \text{ s}^{-1}$) was observed between pyrazole and the 3,6-tert-butyl derivatives.

Table 3.1 Stern-Volmer quenching data of a combination of catalysts and quenchers. All electrochemical potentials are reported as V vs. SCE.



R	Ar	$E_{1/2}^*$	Pyrazole k_q ($E_{p/2} = 2.21$ V)	Anisole k_q ($E_{p/2} = 1.81$ V)	m-Xylene k_q ($E_{p/2} = 2.22$ V)
H	Mes	2.20	$3.0 * 10^9$	$6.7 * 10^9$	0
H	Xyl	2.20	$1.4 * 10^9$	$9.3 * 10^9$	-
2,7-di(Me)	Mes	2.09	$5.5 * 10^8$	$6.0 * 10^9$	0
3,6-di(t-Bu)	Mes	2.15	$2.6 * 10^8$	$2.1 * 10^9$	-
3,6-di(t-Bu)	Xyl	2.15	$1.6 * 10^8$	$4.0 * 10^9$	$1.0 * 10^8$

In order to test the feasibility of electron transfer between pyrazole and the various acridinium species we decided to determine k_q for an arene that has a similar $E_{p/2}$ for one electron oxidation. We reasoned that if this arene displays a similar k_q then a SET event could be considered feasible. We identified *m*-xylene as a suitable arene ($E_{p/2} = 2.22$ V vs. SCE)⁴⁶ and found that it displayed no quenching with the unsubstituted and methylated catalysts and extremely inefficient quenching with the bulkier tert-butyl acridinium. Furthermore, we also found that anisole ($E_{p/2} = 1.90$ V vs. SCE) quenches these catalysts efficiently, in one case near the diffusion limit ($k_q = 3.0 - 9.3 * 10^9$ s⁻¹).

From the above data it appears that in all cases quenching of excited state **Acr**⁺ derivatives is sensitive to the structure of the chromophore. In general, increasing steric bulk of the chromophore decreases the efficiency of quenching and results in lower values of k_q for both substrates tested for the 3,6-tert-butyl derivatives. However, this reduction in quenching is more pronounced for pyrazole than anisole as the quenching rates decrease by an order of magnitude for pyrazole as

opposed to a factor of ~3 for anisole. While the tert-butyl derivatives possess lower $E^*_{1/2}$ values it would be expected that if electron-transfer is the primary result of the quenching event that the k_q values should vary to a similar degree for these substrates.⁴⁷ Additionally, we found that *m*-xylene, which possesses a reduction potential similar to that of pyrazole, does not quench the unsubstituted catalysts at all.

As a more pronounced change in k_q is seen for pyrazole than for anisole it is likely that the quenching event proceeds, in some part, through a different mechanism of quenching. This is further supported by the comparison of quenching rates between pyrazole and *m*-xylene. One alternative mechanism for quenching is that for pyrazole, which is a potent nucleophile, quenching proceeds through a nucleophilic capture process.⁴⁸ Examples of nucleophilic capture on excited nitroarenes is known to occur and have been shown to lead to functionalization of arenes in a manner similar to S_NAr transformations.⁴⁹

Thus, analyzing the quenching data under this mechanistic hypothesis would provide a pathway for formation of a pyrazole-acridinium sigma adduct that could then lead to the functionalized derivatives suggested in the previous section. Moreover, the decrease in quenching observed for pyrazole between the unsubstituted and 3,6-tert-butyl acridiniums can be explained through steric shielding of the excited acridinium from nucleophilic capture. This decrease is also consistent with the relative size of the substituents, as the 2,7-methyl acridinium displays an intermediate pyrazole k_q between the two extremes.

From this data we conclude that the addition of bulky substituents on the acridinium core decreases the amount of quenching by nucleophilic species. Minimizing this interaction accomplishes two goals. First, this quenching event is not a productive pathway for the overall arene C-H functionalization transformation. Eliminating this process increases the efficiency of

the reaction. Second, this quenching event is responsible for the eventual formation of modified catalyst structures which can be implicated in catalyst deactivation.

We became interested in applying these new concepts to the catalyst degradation studies we performed. While these results did not definitively identify a pyrazole-adduct at the 3-position, substitution at this position does cause a dramatic decrease in the quenching rate that appears to ultimately be responsible for catalyst functionalization. This suggests that the sigma-adduct that forms following quenching does so at either the 3-position or one of the nearby sites (the 2 or 4 positions). This is supported by the decreased rate of quenching observed for the 2,7-methyl-acridinium species.

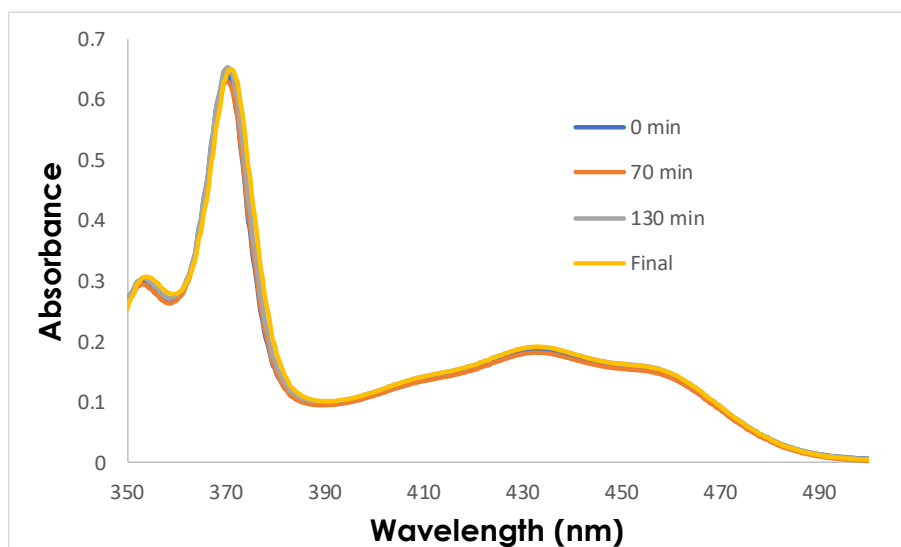
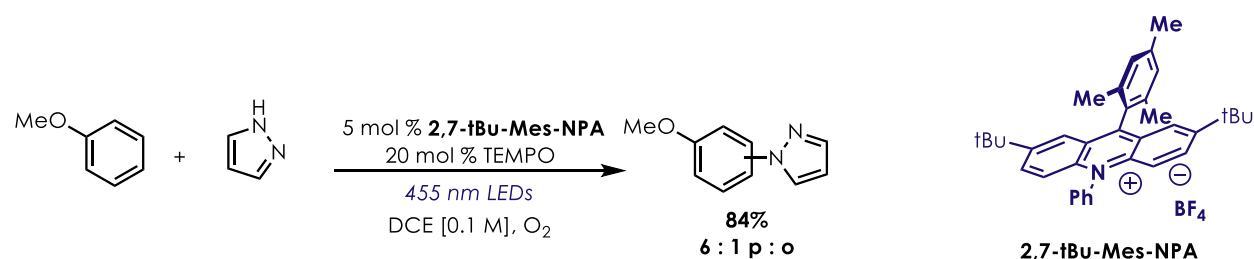


Figure 3.16. Reaction efficiency and catalyst stability observed using 2,7-tBu-Mes-NPA.

We also synthesized the 2,7-tert-butyl acridinium derivative (**2,7-tBu-Mes-NPA**) and found that pyrazole quenches the excited state to a lesser degree than for 3,6-tert-butyl acridinium ($k_q(2,7-$

tert-Butyl) = $1.7 * 10^8 \text{ s}^{-1}$ and $k_q(3,6\text{-tert-Butyl}) = 2.6 * 10^8 \text{ s}^{-1}$), suggesting that the steric shielding effect can be beneficial at multiple positions. This catalyst was found to perform comparably to the 3,6-substituted isomer and features an enhanced excited state lifetime. It was also found to possess similar stability under the reaction conditions (**Figure 3.16**). As a result, it appears that sufficiently bulky groups installed at either the 2,7 or 3,6 positions can afford similar levels of stability.

While we were unable to make a definitive identification of the various acridinium degradation products we believe the results of these studies have provided important insights into catalyst design. It was shown that the inclusion of sterically bulky substituents at the 3 and 6 positions of the acridinium shields the catalyst from nucleophilic addition. Importantly, we have determined that nucleophiles add to the acridinium core through a photochemical pathway. Decreasing the likelihood of this process serves to decrease unproductive catalyst quenching as well as prevent oxidative functionalization of the acridinium chromophore. Moreover, it was demonstrated that the addition of electron-donating groups at the 3 position of the chromophore degrades catalytic activity. We hope that these results will be beneficial in the design, and judicious use, of acridinium photocatalysts for future applications.

3.6 TEMPO_{ium}: Alternative Reaction Pathways

As noted in a previous section, it was found that TEMPO quenches the excited state catalyst at a diffusion-controlled rate ($k_q \sim 10^{10} \text{ s}^{-1}$). Through this presumed PET process, we assumed that the formation of the oxoammonium salt (TEMPO_{ium}) during the reaction would be feasible. We especially were curious on exploring the possible intermediacy of TEMPO_{ium} in the conditions that were first reported for alkylated benzenoids like mesitylene. In the initial report it was found that substrates such as mesitylene and xylene were not compatible with the aerobic conditions used

for most other arenes. These substrates were observed to undergo significant benzylic oxidation, furnishing an aldehyde adduct, in the presence of oxygen even when TEMPO was included. Consequently, it was found that degassing the solutions with N₂ and including a stoichiometric amount of TEMPO allowed for the suppression of this undesired product.

It was proposed that this change in TEMPO stoichiometry, in light of the observed kinetic deceleration under aerobic conditions, would result in a slower overall reaction. This was initially tested using anisole as a substrate under these anaerobic conditions. An initial rates analysis of this reaction showed that the reaction rate was significantly retarded by almost an order of magnitude ($k_{\text{obs}} \sim 10^{-4}$ with 1.0 equiv. TEMPO vs 10^{-3} with 0.2 equiv. TEMPO), underscoring the observation that the competitive quenching of TEMPO could be deleterious to reaction efficiency. We also were curious if this effect was exacerbated by the production of TEMPO⁺.

The inclusion of a catalytic amount of TEMPO⁺BF₄, in place of TEMPO, under aerobic conditions was found to have no meaningful impact on reaction yield. Similarly, under anaerobic conditions, substituting TEMPO⁺BF₄ for TEMPO afforded equal levels of reactivity between mesitylene and pyrazole even though TEMPO⁺BF₄ does not possess great solubility in DCE. However, during these experiments it was noted that upon the addition of the arene substrate to the reaction solutions containing TEMPO⁺BF₄ a dramatic color change could be observed. For both anisole and mesitylene, the initially yellow solutions darkened to a deep red color.

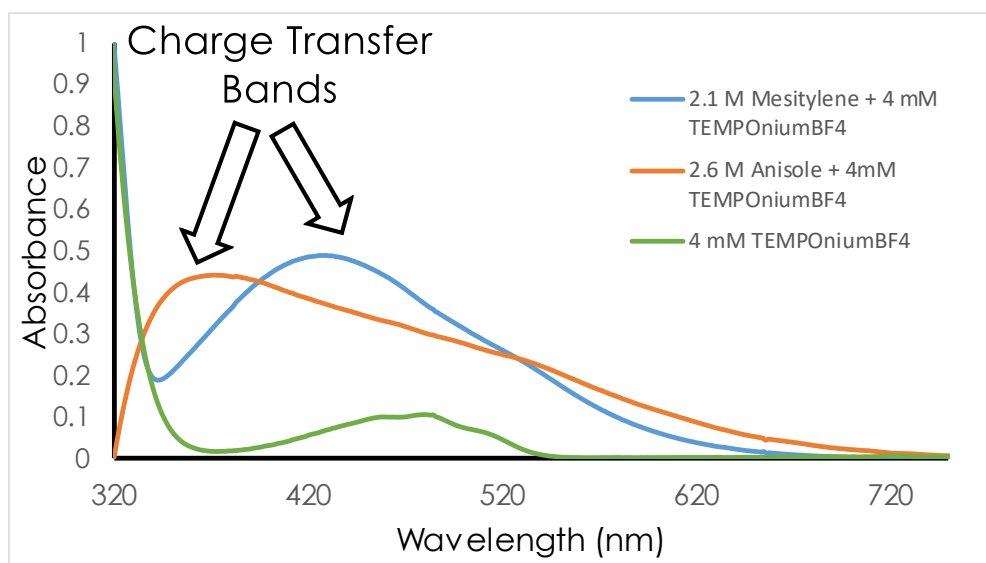
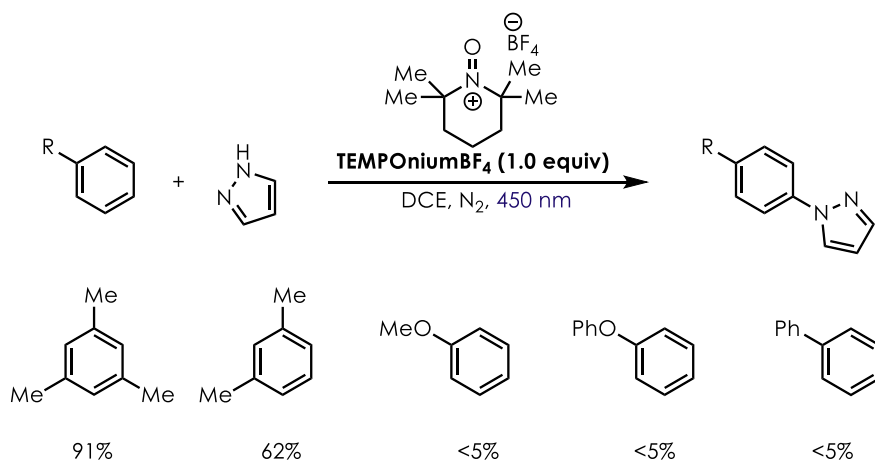


Figure 3.17. Reactivity of TEMPOOniumBF₄ with various arenes (upper). UV-Vis spectra showing the formation of the charge-transfer bands upon mixing of TEMPOOniumBF₄ and arene (lower).

The observation of a color change upon mixing is usually indicative of the formation of a charge-transfer complex between two species.^{50–53} It was found that this color change could be observed when only the TEMPOOniumBF₄ and arene substrate were mixed in solution. The formation of a charge-transfer complex could have important implications in the proposed reaction mechanism. It has been shown that when charge-transfer complexes are irradiated electron transfer between the donor and the acceptor species can occur to give the fully oxidized and reduced species, respectively⁵⁰. In the complex formed between TEMPOOnium and arenes, this would result

in the formation of the arene (donor) radical cation and TEMPO (acceptor). This would allow for the reaction to proceed without the need for a strongly oxidizing photocatalyst such as **Mes-Acr**. During the course of our investigations examples of charge transfer complexes between olefins and TEMPO⁺ were reported to be implicated in various transformations.⁵⁴ Additionally, a DDQ-catalyzed arene functionalization was reported that features charge transfer processes.⁵⁵

Surprisingly, quantitative conversion was observed in the reaction between mesitylene and pyrazole in the presence of a stoichiometric amount of TEMPO⁺ and without any added **Mes-Acr** (**Figure 3.17**). This observation prompted us to consider if the formation of TEMPO⁺ was in fact beneficial to the reaction for all arenes and if two different mechanisms could be operating. We found that the corresponding reaction of anisole and pyrazole with only a stoichiometric amount of TEMPO⁺ did not afford more than 5% conversion. Moreover, no reactivity could be observed for a number of other substrates.

As m-xylene does not exhibit significant quenching of the **Mes-Acr**⁺ catalyst (vide supra) it is instead proposed that this reaction proceeds first through oxidation of TEMPO to form TEMPO⁺. A charge-transfer complex with m-xylene then forms which, upon absorption of a photon, produces the necessary arene cation-radical. Subsequent steps as in the aerobic functionalization mechanism furnishes the product. Importantly, the observation that the reaction proceeds with only TEMPO, and without O₂, provides strong evidence that TEMPO is capable of rearomatizing the cyclohexadienyl radical intermediate. As noted in previous sections when oxygen is present this mechanistic pathway is superfluous. Turnover of the catalyst can be achieved via reduction of TEMPO⁺ that is formed from the disproportionation of TEMPO as acid is formed during the course of the reaction. Moreover, given the relative quenching efficiencies of mesitylene and TEMPO we cannot rule out this pathway.

To date, the only arene substrates observed to undergo C-H functionalization with pyrazole are alkylated benzenoids such as mesitylene and m-xylene. Further studies detailing the various charge transfer interactions as well as further screening of this reaction system can be found in the subsequent chapter. Importantly, these results provide critical details about the arene C-H amination in the presence of stoichiometric TEMPO.

3.7 Development of New Anaerobic Conditions

Having established that the developed anaerobic conditions display reduced reactivity for the majority of substrates, and also allows for alternative mechanistic pathways, we became interested in developing alternative conditions. We believed that if we could develop conditions that could reduce the required loading of TEMPO to catalytic levels then increased reaction yields could be achieved.

In order to achieve this a suitable terminal oxidant would be needed to replace oxygen and TEMPO in the aerobic and anaerobic conditions, respectively. Identifying conditions that did not rely on the use of oxygen as a terminal oxidant were desirable as superoxide and peroxy radical species, generated during the reaction, contribute to substrate and catalyst degradation. Moreover, the use of oxygen presents practical challenges upon scaling up these reactions due to the difficulties in maintaining a constant supply of the gaseous reagent as well as its flammability. Thus, a soluble oxidant that could be added as a liquid or solid to the reaction mixture represents an ideal solution to this problem.

In the initial report it was shown that common alternative oxidants, such as persulfates or benzophenone derivatives, were ineffective in the reaction, affording significantly worse yields in comparison to O₂. However, after beginning our studies of the reaction mechanism we began to consider the possibility that hydrogen peroxide, formed during the reaction through a number of

mechanisms, might be capable of acting as the terminal oxidant. The redox values for H_2O_2 and **Mes-Acr•** suggest that turnover of the catalyst should be feasible.

We found that substituting the O_2 atmosphere with a stoichiometric amount of hydrogen peroxide, supplied as a solid in the form of urea – hydrogen peroxide, afforded similar levels of reactivity.

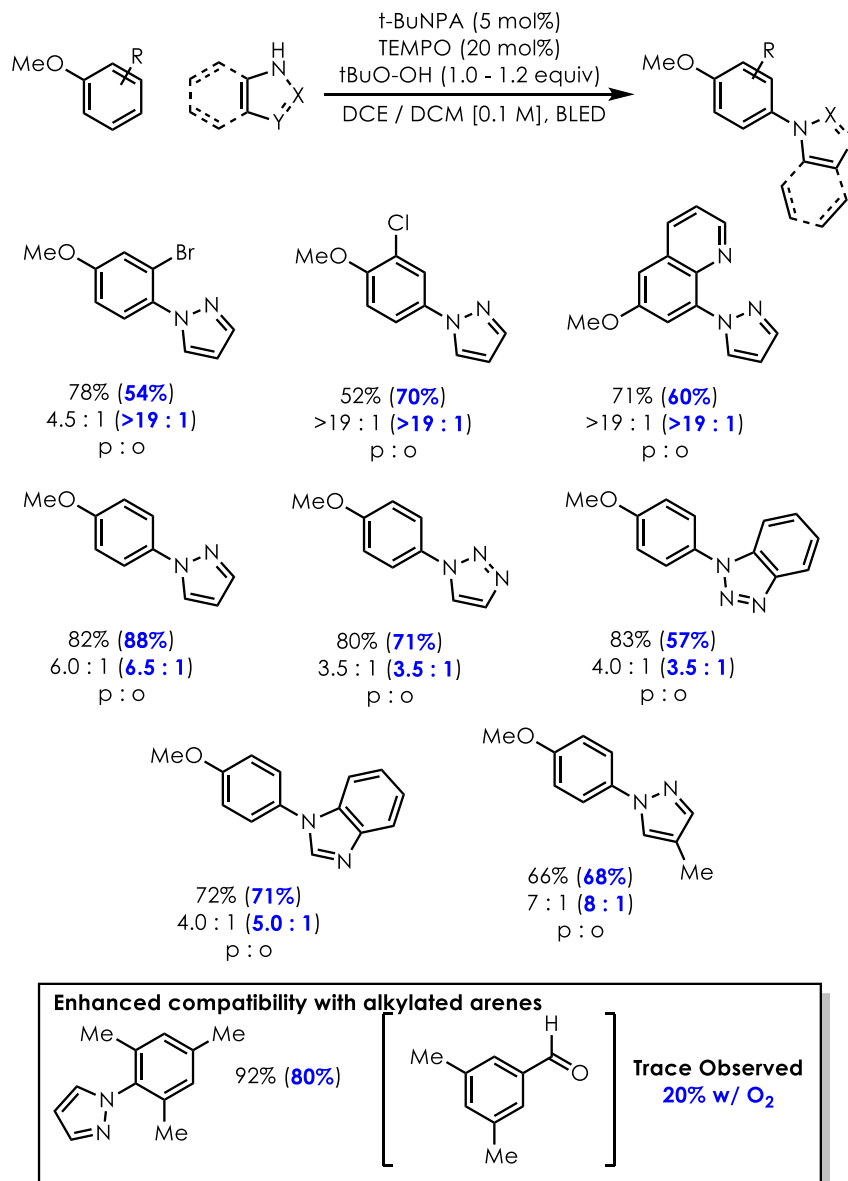


Figure 3.18. Demonstration of scope for "second-generation" anaerobic conditions using tert-butyl hydroperoxide as terminal oxidant. Paranthetical yields refer to results obtained using standard aerobic conditions.

However, urea – hydrogen peroxide is poorly solubility in DCE and as a result a more soluble peroxide source was investigated and tert-butyl hydroperoxide was found to perform equally well and is available as a stable solution that can be easily added to reaction solutions.

After identifying these new anaerobic conditions, a preliminary assessment of its efficacy in relation to the original aerobic conditions were undertaken. Four arene targets as well as four azole nucleophiles were evaluated under these new conditions and the yields were compared to those obtained under O₂ (**Figure 3.18**). It was found that in all cases reactivity using H₂O₂ was comparable to that under O₂. Additionally, it was found that mesitylene underwent appreciable amination under these conditions without any detectable benzylic oxidation product which was a major pathway for degradation under aerobic conditions. This result highlights the amenability of these new conditions for sensitive substrates that would previously have been utilized under the more inefficient “first-generation” anaerobic conditions. Moreover, it also suggests that the degradation of alkylated arenes is initiated via superoxide as these conditions preclude the formation of this species.

Importantly, the regioselectivity was found to be the same as well suggesting that changing the terminal oxidant does not alter the reaction mechanism. Moreover, this provides further evidence that TEMPO is capable of undergoing HAT with the cyclohexadienyl radical and that this step does not alter the regioselectivity of the reaction. This was further probed by omitting the TEMPO and only including an equivalent of H₂O₂. The reaction was found to proceed in a significantly diminished yield (15%) of the desired product as well as the observation of multiple degradation species, including phenyl formate. Additionally, the product was obtained as a 2:1 mixture of p : o isomers, underscoring the need for either O₂ or TEMPO as a rearomatizing agent.

3.8 Elucidating the Origin of Regioselectivity

As highlighted in the previous section the regioselectivity of the reaction is highly dependent on the presence of O₂ or TEMPO. Our next steps in investigating the aryl C-H amination system were focused on investigating what factors influenced the observed regioselectivity. We became interested in identifying the product determining step of the reaction as a means of possibly altering the reaction selectivity. This would be desirable synthetically as it might allow for a synthetic route to obtain good yields of either para or ortho isomers by simply changing the reaction conditions. In order to probe this proposal, we decided to determine the rate-determining and product-determining step(s) of the reaction. We proposed that we could determine both of these factors through a combination of kinetic isotope effect studies.

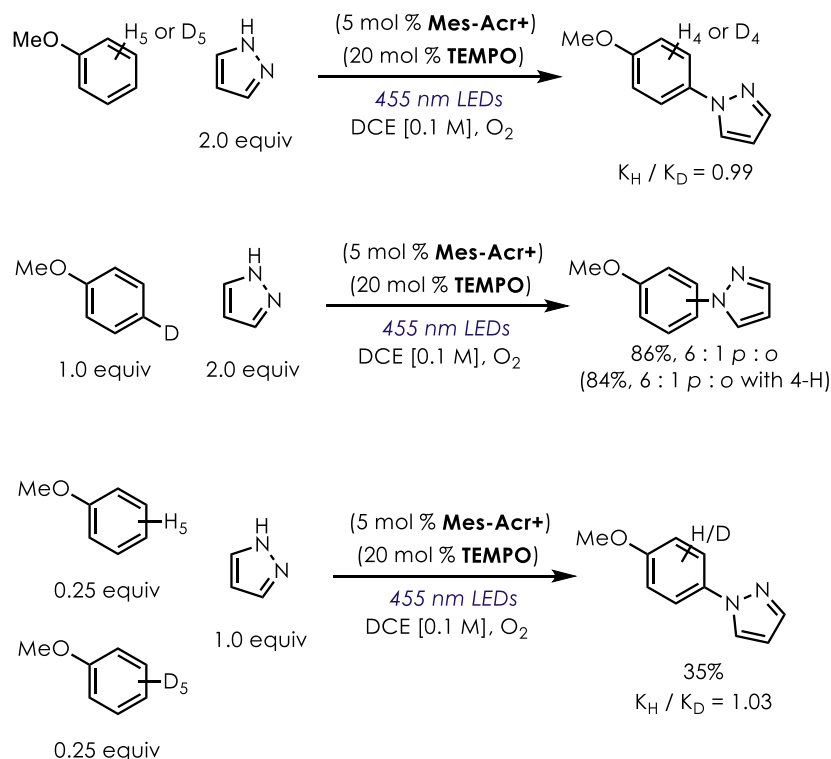


Figure 3.19. Top: Parallel kinetic isotope experiment revealing no observable KIE. Middle: Intramolecular kinetic isotope experiment. Bottom: Intermolecular competition KIE experiment.

To begin our kinetic isotope effect investigations, we obtained the d₅-anisole derivative and performed a parallel rates KIE experiment with H₅-anisole in order to determine if the rearomatization step is rate determining. We reasoned that if rearomatization (via any mechanism that involves cleavage of the 2/6 or 4-position protons) were rate-limiting then a normal, primary KIE should be observed. An initial rates analysis using both of these substrates in parallel reactions yielded $k_H/k_D = 0.99$, suggesting that the rearomatization is not rate determining (**Figure 3.19**). It also seemed unlikely, given this result, that this step is product-determining as the reaction has been shown to be irreversible.

In order to elucidate the product-determining step we employed both intra- and intermolecular KIE studies. We proposed that when using 4-d-anisole as a substrate a different ratio of isomers should be observed if the rearomatization step is product-determining. Furthermore, this would suggest that the elementary steps prior to rearomatization are reversible and that an equilibrium exists between the pro-para and pro-ortho cyclohexadienyl radical intermediates. It was found that the reaction with 4-d-anisole resulted in the formation of the pyrazole adduct with the same isomer distribution as the protio-variant (**Figure 3.19**). In addition to this, an intermolecular competition experiment was performed with protio and pentadeutero anisole. Analyzing the mixture at 35% conversion revealed a $k_H/k_D = 1.03$ (**Figure 3.19**). These data combined suggest that the rearomatization step is neither rate-determining nor product-determining.

Having ruled out rearomatization as the product-determining step we began to consider what factors would influence regioselectivity. In parallel with our work investigating the mechanism of the transformation our lab has showed that the generally para-selective reactions can be explained by a greater charge density at the para position for the cation-radical species.⁵⁷ These values were

determined computationally and displays excellent agreement with the selectivity observed for the majority of substrates.

These data suggested that the selectivity is derived from a kinetically controlled addition of the amine nucleophile. Under this assumption it would be presumed that the initial nucleophilic capture step is irreversible. However, previous work in our lab on a related photoredox catalyzed system, the anti-markovnikov addition of alcohols to alkene cation-radicals, suggested that the deprotonation step of the distonic cation-radical intermediate might exert a rate-limiting influence.³⁰ Taking this into consideration we became curious if the deprotonation of the distonic cation-radical might have an influence on the rate or product-determining step. We were curious in studying if a similar effect was at play in the aryl functionalization system.

We began studying the effect of acid on the regioselectivity of the transformation by including an equivalent of pyrazolium tetrafluoroborate (**Figure 3.20**) in the reaction conditions. We reasoned that the addition of this species represents a reasonable approximation for the actual build-up of acid during the reaction. Since the pyrazole nucleophile is used in excess under the reaction conditions, the inclusion of this salt represents an artificial buffering of the solution.

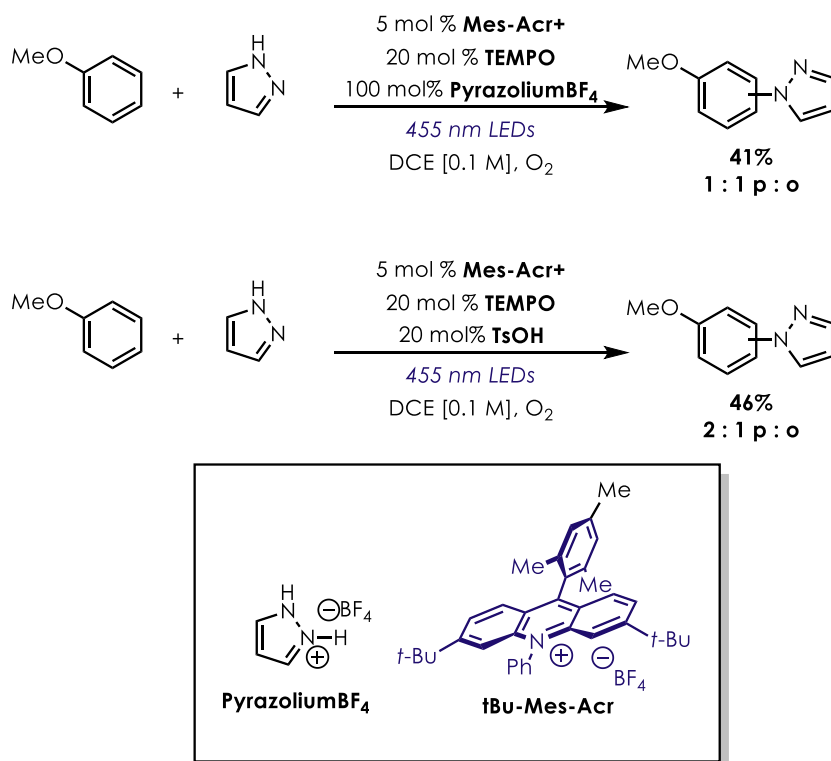


Figure 3.20. Exploring the effect of solution acidity on regioselectivity in addition of pyrazole to anisole.

It was found that under these acidic conditions that the regioselectivity of the reaction was diminished significantly. The pyrazole adduct was observed to form in an almost nonselective fashion (1 : 1 p : o) albeit in a decreased combined yield (41%). Excitingly, this result confirmed our hypothesis that the deprotonation step exerts product-determining influence on the reaction.

We became curious if this effect could be enhanced by using a different acid. Adding a more acidic additive like TsOH did not afford a noticeable difference in the selectivity. Moreover, it was found that upon the addition of TsOH that a decrease in yield was observed that could be attributed to substrate decomposition. The mass balance of the reaction became significantly worse and phenyl formate, among other unidentified byproducts, could be observed. These degradation products could be formed via HAT by the radicals formed via oxidation of the conjugate base.

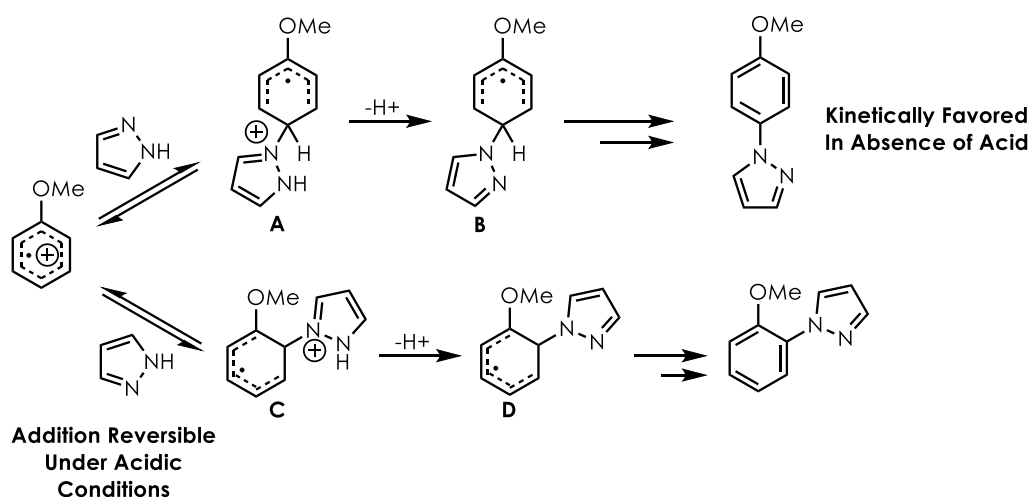


Figure 3.21. Outline of the elementary steps responsible for regioselectivity and the influence of acid on the equilibria.

We concluded that it was unlikely that this effect could be further enhanced to favor selective formation of the ortho product. Given these results we considered that the product-determining step is the deprotonation of the distonic cation-radical intermediates **A** or **C** (**Figure 3.21**). The regioselectivity of the initial nucleophilic addition to the arene cation-radical is determined by the charge-density of each position in the ring. In the absence of exogenous acid, the subsequent deprotonation is sufficiently rapid that there is not a significant degree of equilibration between the two regioisomeric distonic cation-radical intermediates. With added acid, however, the deprotonation is slow and the two nucleophile adducts can interconvert. Importantly, the essentially non-selective product distribution observed under these conditions suggests that the difference in energy between the two distonic cation-radicals is negligible. Thus, under the normal conditions the product distribution is kinetically controlled while under acidic conditions it is under thermodynamic control.

3.9 Clarifying the Mechanism

In the previous sections we detailed our efforts to elucidate the various factors that influence the photoredox arene C-H amination system (**Figure 3.22**). Through kinetic analysis we have

established that TEMPO is not kinetically relevant in the product-forming process. Instead, TEMPO is operating in a purely anti-oxidant role to quench both hydroperoxyl radicals and superoxide formed during the reaction. This was also confirmed by comparing reaction efficiencies using other effective antioxidants.

Through kinetic isotope effect studies, we determined that the rearomatization of the cyclohexadienyl radical does not have rate-determining or product-determining influence. We found that the regioselectivity of the transformation can be altered by adding acid to the reaction mixture, suggesting that the product-determining step is the deprotonation of the distonic cation-radical intermediate. By extension, we determined that the regioselectivity of the transformation without acid is kinetically controlled by the initial nucleophilic addition which itself is guided by the charge distribution of the arene cation-radical.

We also determined that the structure of the acridinium catalyst has a dramatic effect on reaction efficiency. Through a combination of spectroscopic and LC-MS investigations we found that bulky alkyl groups on the acridinium core prevent deleterious quenching interactions between the excited state catalyst and nucleophiles. Moreover, these groups also prevent covalent modification of the catalyst through oxidative functionalization with nucleophiles. We also found that bulkier groups on the catalyst also have a deleterious effect on productive quenching events with the arene substrates. These results suggest that the choice of catalyst for a given transformation could be guided by balancing these two effects.

Working Mechanistic Proposal:

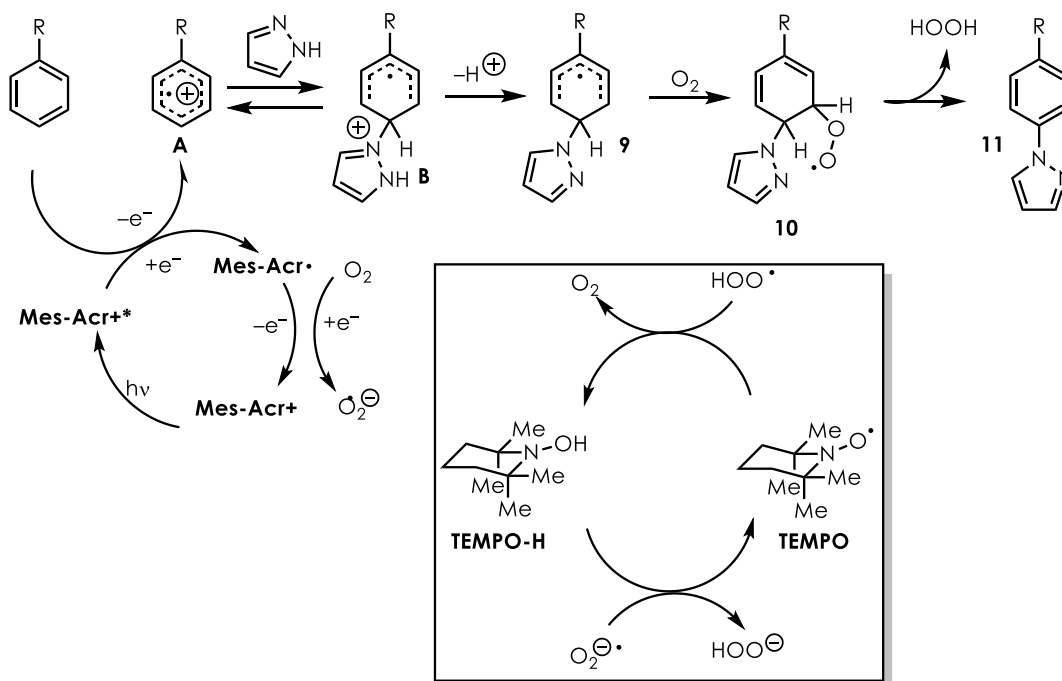


Figure 3.22. Revised mechanism for the photoredox arene C-H amination system and the catalytic effect of TEMPO.

Additionally, the very low quantum yield of the reaction ($\phi = 0.03$) suggests that more effort should be directed towards maximizing this value. One possible source of this inefficiency could be from unproductive back-electron transfer from **Mes-Acr•** to the cation-radical **A** to regenerate the catalyst and substrate. Efforts to minimize this process could focus on developing catalysts that undergo PET through a triplet manifold. Under this pathway, back-electron transfer becomes a spin-forbidden process and would become slower allowing the downstream, productive product-forming pathways to become more dominant.

3.10 Conclusions

In this chapter we reported our efforts towards better understanding the relevant reaction dynamics of a photoredox-mediate arene C-H amination system. We demonstrated that a variety of spectroscopic and kinetic analyses of this system can be used to discern important reaction

details. We believe that the results from these studies can be applied to other photoredox arene C-H functionalizations. More generally, the investigations into catalyst degradation can inform the design of more effective acridinium catalysts that can be used in other photoredox reaction manifolds.

REFERENCES

- (1) Wolfe, J. P.; Wagaw, S.; Marcoux, J.-F.; Buchwald, S. L. Rational Development of Practical Catalysts for Aromatic Carbon–Nitrogen Bond Formation. *Acc. Chem. Res.* **1998**, *31* (12), 805–818.
- (2) Hartwig, J. F. Carbon–Heteroatom Bond-Forming Reductive Eliminations of Amines, Ethers, and Sulfides. *Acc. Chem. Res.* **1998**, *31* (12), 852–860.
- (3) Sambiago, C.; Marsden, S. P.; Blacker, A. J.; McGowan, P. C. Copper Catalysed Ullmann Type Chemistry: From Mechanistic Aspects to Modern Development. *Chem Soc Rev* **2014**, *43* (10), 3525–3550.
- (4) Qiao, J. X.; Lam, P. Y. S. Recent Advances in Chan-Lam Coupling Reaction: Copper Promoted C-Heteroatom Bond Cross-Coupling Reactions with Boronic Acids and Derivatives. In *Boronic Acids*; Hall, D. G., Ed.; Wiley-VCH Verlag GmbH & Co. KGaA: Weinheim, Germany, 2011; pp 315–361.
- (5) Yoshimura, A.; Zhdankin, V. V. Advances in Synthetic Applications of Hypervalent Iodine Compounds. *Chem. Rev.* **2016**, *116* (5), 3328–3435.
- (6) Sun, C.-L.; Shi, Z.-J. Transition-Metal-Free Coupling Reactions. *Chem. Rev.* **2014**, *114* (18), 9219–9280.
- (7) Romero, N. A.; Margrey, K. A.; Tay, N. E.; Nicewicz, D. A. Site-Selective Arene C-H Amination via Photoredox Catalysis. *Science* **2015**, *349* (6254), 1326–1330.
- (8) McManus, J. B.; Nicewicz, D. A. Direct C–H Cyanation of Arenes via Organic Photoredox Catalysis. *J. Am. Chem. Soc.* **2017**, *139* (8), 2880–2883.
- (9) Margrey, K. A.; Levens, A.; Nicewicz, D. A. Direct Aryl C–H Amination with Primary Amines Using Organic Photoredox Catalysis. *Angew. Chem. Int. Ed.* **2017**, *56* (49), 15644–15648.
- (10) Ohkubo, K.; Mizushima, K.; Iwata, R.; Fukuzumi, S. Selective Photocatalytic Aerobic Bromination with Hydrogen Bromide via an Electron-Transfer State of 9-Mesityl-10-Methylacridinium Ion. *Chem. Sci.* **2011**, *2* (4), 715.
- (11) Ohkubo, K.; Fujimoto, A.; Fukuzumi, S. Photocatalytic Monofluorination of Benzene by Fluoride via Photoinduced Electron Transfer with 3-Cyano-1-Methylquinolinium. *J. Phys. Chem. A* **2013**, *117* (41), 10719–10725.
- (12) Maillard, B.; Ingold, K. U.; Scaiano, J. C. Rate Constants for the Reactions of Free Radicals with Oxygen in Solution. *J. Am. Chem. Soc.* **1983**, *105* (15), 5095–5099.
- (13) Pan, X.-M.; Schuchmann, M. N.; von Sonntag, C. Oxidation of Benzene by the OH

- Radical. A Product and Pulse Radiolysis Study in Oxygenated Aqueous Solution. *J. Chem. Soc. Perkin Trans. 2* **1993**, No. 3, 289.
- (14) Fang, X.; Pan, X.; Rahmann, A.; Schuchmann, H.-P.; von Sonntag, C. Reversibility in the Reaction of Cyclohexadienyl Radicals with Oxygen in Aqueous Solution. *Chem. - Eur. J.* **1995**, *1* (7), 423–429.
- (15) Benniston, A. C.; Elliott, K. J.; Harrington, R. W.; Clegg, W. On the Photochemical Stability of the 9-Mesityl-10-Methylacridinium Cation. *Eur. J. Org. Chem.* **2009**, *2009* (2), 253–258.
- (16) Hering, T.; Slanina, T.; Hancock, A.; Wille, U.; König, B. Visible Light Photooxidation of Nitrate: The Dawn of a Nocturnal Radical. *Chem. Commun.* **2015**, *51* (30), 6568–6571.
- (17) Yamada, Y.; Maeda, K.; Ohkubo, K.; Karlin, K. D.; Fukuzumi, S. Improvement of Durability of an Organic Photocatalyst in P-Xylene Oxygenation by Addition of a Cu(II) Complex. *Phys. Chem. Chem. Phys.* **2012**, *14* (27), 9654.
- (18) Hayyan, M.; Hashim, M. A.; AlNashef, I. M. Superoxide Ion: Generation and Chemical Implications. *Chem. Rev.* **2016**, *116* (5), 3029–3085.
- (19) Frank, C. E. Hydrocarbon Autoxidation. *Chem. Rev.* **1950**, *46* (1), 155–169.
- (20) Ingold, K. U. Inhibition of the Autoxidation of Organic Substances in the Liquid Phase. *Chem. Rev.* **1961**, *61* (6), 563–589.
- (21) Poon, J.-F.; Pratt, D. A. Recent Insights on Hydrogen Atom Transfer in the Inhibition of Hydrocarbon Autoxidation. *Acc. Chem. Res.* **2018**.
- (22) Amorati, R.; Pedulli, G. F.; Pratt, D. A.; Valgimigli, L. TEMPO Reacts with Oxygen Centered Radicals under Acidic Conditions. *Chem. Commun.* **2010**, *46* (28), 5139.
- (23) Griesser, M.; Shah, R.; Van Kessel, A. T.; Zilka, O.; Haidasz, E. A.; Pratt, D. A. The Catalytic Reaction of Nitroxides with Peroxyl Radicals and Its Relevance to Their Cytoprotective Properties. *J. Am. Chem. Soc.* **2018**, *140* (10), 3798–3808.
- (24) Haidasz, E. A.; Meng, D.; Amorati, R.; Baschieri, A.; Ingold, K. U.; Valgimigli, L.; Pratt, D. A. Acid Is Key to the Radical-Trapping Antioxidant Activity of Nitroxides. *J. Am. Chem. Soc.* **2016**, *138* (16), 5290–5298.
- (25) Harrison, K. A.; Haidasz, E. A.; Griesser, M.; Pratt, D. A. Inhibition of Hydrocarbon Autoxidation by Nitroxide-Catalyzed Cross-Dismutation of Hydroperoxyl and Alkylperoxyl Radicals. *Chem. Sci.* **2018**, *9* (28), 6068–6079.
- (26) Valgimigli, L.; Amorati, R.; Petrucci, S.; Pedulli, G. F.; Hu, D.; Hanthorn, J. J.; Pratt, D. A. Unexpected Acid Catalysis in Reactions of Peroxyl Radicals with Phenols. *Angew.*

- Chem. Int. Ed.* **2009**, *48* (44), 8348–8351.
- (27) Warren, J. J.; Tronic, T. A.; Mayer, J. M. Thermochemistry of Proton-Coupled Electron Transfer Reagents and Its Implications. *Chem. Rev.* **2010**, *110* (12), 6961–7001.
- (28) Ohkubo, K.; Mizushima, K.; Iwata, R.; Souma, K.; Suzuki, N.; Fukuzumi, S. Simultaneous Production of P-Tolualdehyde and Hydrogen Peroxide in Photocatalytic Oxygenation of p-Xylene and Reduction of Oxygen with 9-Mesityl-10-Methylacridinium Ion Derivatives. *Chem Commun* **2010**, *46* (4), 601–603.
- (29) Ohkubo, K.; Fujimoto, A.; Fukuzumi, S. Photocatalytic Monofluorination of Benzene by Fluoride via Photoinduced Electron Transfer with 3-Cyano-1-Methylquinolinium. *J. Phys. Chem. A* **2013**, *117* (41), 10719–10725.
- (30) Romero, N. A.; Nicewicz, D. A. Mechanistic Insight into the Photoredox Catalysis of Anti-Markovnikov Alkene Hydrofunctionalization Reactions. *J. Am. Chem. Soc.* **2014**, *136* (49), 17024–17035.
- (31) Arends, I. W. C. E.; Mulder, P.; Clark, K. B.; Wayner, D. D. M. Rate Constants for Termination and TEMPO Trapping of Some Resonance Stabilized Hydroaromatic Radicals in the Liquid Phase. *J. Phys. Chem.* **1995**, *99* (20), 8182–8189.
- (32) Beckwith, A. L. J.; Bowry, V. W.; Ingold, K. U. Kinetics of Nitroxide Radical Trapping. 1. Solvent Effects. *J. Am. Chem. Soc.* **1992**, *114* (13), 4983–4992.
- (33) Marx, L.; Schöllhorn, B. Intramolecular Charge Effects in the Electrochemical Oxidation of Aminoxyl Radicals. *New J. Chem.* **2006**, *30* (3), 430.
- (34) Nam, T.; Rector, C. L.; Kim, H.; Sonnen, A. F.-P.; Meyer, R.; Nau, W. M.; Atkinson, J.; Rintoul, J.; Pratt, D. A.; Porter, N. A. Tetrahydro-1,8-Naphthyridinol Analogues of α Tocopherol as Antioxidants in Lipid Membranes and Low-Density Lipoproteins. *J. Am. Chem. Soc.* **2007**, *129* (33), 10211–10219.
- (35) Angeli, J. P. F.; Shah, R.; Pratt, D. A.; Conrad, M. Ferroptosis Inhibition: Mechanisms and Opportunities. *Trends Pharmacol. Sci.* **2017**, *38* (5), 489–498.
- (36) Farmer, L. A.; Haidasz, E. A.; Griesser, M.; Pratt, D. A. Phenoxazine: A Privileged Scaffold for Radical-Trapping Antioxidants. *J. Org. Chem.* **2017**, *82* (19), 10523–10536.
- (37) Hanthorn, J. J.; Valgimigli, L.; Pratt, D. A. Incorporation of Ring Nitrogens into Diphenylamine Antioxidants: Striking a Balance between Reactivity and Stability. *J. Am. Chem. Soc.* **2012**, *134* (20), 8306–8309.
- (38) Shah, R.; Haidasz, E. A.; Valgimigli, L.; Pratt, D. A. Unprecedented Inhibition of Hydrocarbon Autoxidation by Diarylamine Radical-Trapping Antioxidants. *J. Am. Chem. Soc.* **2015**, *137* (7), 2440–2443.

- (39) Nicoll, W. D.; Smith, A. F. Stability of Dilute Alkaline Solutions of Hydrogen Peroxide. *Ind. Eng. Chem.* **1955**, *47* (12), 2548–2554.
- (40) Joshi-Pangu, A.; Lévesque, F.; Roth, H. G.; Oliver, S. F.; Campeau, L.-C.; Nicewicz, D.; DiRocco, D. A. Acridinium-Based Photocatalysts: A Sustainable Option in Photoredox Catalysis. *J. Org. Chem.* **2016**, *81* (16), 7244–7249.
- (41) Fischer, C.; Sparr, C. Synthesis of 1,5-Bifunctional Organolithium Reagents by a Double Directed Ortho -Metalation: Direct Transformation of Esters into 1,8-Dimethoxy Acridinium Salts. *Tetrahedron* **2018**.
- (42) Jones, G.; Farahat, M. S.; Greenfield, S. R.; Gosztola, D. J.; Wasielewski, M. R. Ultrafast Photoinduced Charge-Shift Reactions in Electron Donor-Acceptor 9-Arylacridinium Ions. *Chem. Phys. Lett.* **1994**, *229* (1–2), 40–46.
- (43) Jonker, S. A.; Ariese, F.; Verhoeven, J. W. Cation Complexation with Functionalized 9 Arylacridinium Ions: Possible Applications in the Development of Cation-Selective Optical Probes. *Recl. Trav. Chim. Pays-Bas* **2010**, *108* (3), 109–115.
- (44) Devery III, J. J.; Douglas, J. J.; Nguyen, J. D.; Cole, K. P.; Flowers II, R. A.; Stephenson, C. R. J. Ligand Functionalization as a Deactivation Pathway in a Fac-Ir(Ppy)₃-Mediated Radical Addition. *Chem. Sci.* **2015**, *6* (1), 537–541.
- (45) Lakowicz, J. R. *Principles of Fluorescence Spectroscopy*, 3rd ed.; Springer: New York, 2006.
- (46) Roth, H.; Romero, N.; Nicewicz, D. Experimental and Calculated Electrochemical Potentials of Common Organic Molecules for Applications to Single-Electron Redox Chemistry. *Synlett* **2015**, *27* (05), 714–723.
- (47) Turro, N. J.; Scaiano, J. C.; Ramamurth, V. *Modern Molecular Photochemistry of Organic Molecules*; University Science Books: California, 2010.
- (48) Valentino, M. R.; Boyd, M. K. Quenching Behavior of Singlet Excited 9-Arylxanthylum Cations. *J. Org. Chem.* **1993**, *58* (21), 5826–5831.
- (49) Cornelisse, J.; Havinga, E. Photosubstitution Reactions of Aromatic Compounds. 36.
- (50) Rosokha, S. V.; Kochi, J. K. Fresh Look at Electron-Transfer Mechanisms via the Donor/Acceptor Bindings in the Critical Encounter Complex. *Acc. Chem. Res.* **2008**, *41* (5), 641–653.
- (51) Bockman, T. M.; Karpinski, Z. J.; Sankararaman, S.; Kochi, J. K. Time-Resolved Charge Transfer Spectroscopy of Aromatic Electron Donor-Acceptor Complexes with Nitrosonium. Inner-Sphere Mechanism for Electron Transfer in the Isoergonic Region. *J. Am. Chem. Soc.* **1992**, *114* (6), 1970–1985.

- (52) Hubig, S. M.; Rathore, R.; Kochi, J. K. Steric Control of Electron Transfer. Changeover from Outer-Sphere to Inner-Sphere Mechanisms in Arene/Quinone Redox Pairs. *J. Am. Chem. Soc.* **1999**, *121* (4), 617–626.
- (53) Sankararaman, S.; Haney, W. A.; Kochi, J. K. Aromatic Nitration with Ion Radical Pairs [ArH⁺,NO₂⁻] as Reactive Intermediates. Time-Resolved Studies of Charge-Transfer Activation of Dialkoxybenzenes. 15.
- (54) Liu, J.-L.; Zhu, Z.-F.; Liu, F. Oxycyanation of Vinyl Ethers with 2,2,6,6-Tetramethyl- *N*-Oxopiperidinium Enabled by Electron Donor–Acceptor Complex. *Org. Lett.* **2018**, *20* (3), 720–723.
- (55) Das, S.; Natarajan, P.; König, B. Teaching Old Compounds New Tricks: DDQ Photocatalyzed C–H Amination of Arenes with Carbamates, Urea, and N-Heterocycles. *Chem. - Eur. J.* **2017**, *23* (72), 18161–18165.
- (56) Simmons, E. M.; Hartwig, J. F. On the Interpretation of Deuterium Kinetic Isotope Effects in C–H Bond Functionalizations by Transition-Metal Complexes. *Angew. Chem. Int. Ed.* **2012**, *51* (13), 3066–3072.
- (57) Margrey, K. A.; McManus, J. B.; Bonazzi, S.; Zecri, F.; Nicewicz, D. A. Predictive Model for Site-Selective Aryl and Heteroaryl C–H Functionalization via Organic Photoredox Catalysis. *J. Am. Chem. Soc.* **2017**, *139* (32), 11288–11299.

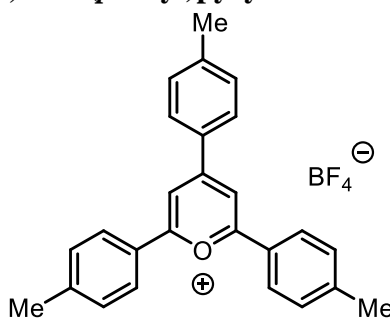
APPENDIX A: SUPPORTING INFORMATION FOR “DEVELOPMENT OF A PHOTOREDOX-MEDIATED NEWMAN-KWART REARRANGEMENT”

A.1 General Information

Methods and Materials: Proton and carbon magnetic resonance spectra (^1H NMR and ^{13}C NMR) were recorded on a Bruker AVANCE III 600 CryoProbe (^1H NMR at 400 MHz, 600 MHz and ^{13}C NMR at 100, 150 MHz) spectrometer with solvent resonance as the internal standard (^1H NMR: CDCl_3 at 7.26 ppm; ^{13}C NMR: CDCl_3 at 77.0 ppm). ^1H NMR data are reported as follows: chemical shift, multiplicity (s = singlet, d = doublet, t = triplet, dd = doublet of doublets, dt = doublet of triplets, td = triplet of doublets, m = multiplet, br = broad singlet, bm = broad multiplet), coupling constants (Hz), and integration. Infrared (IR) spectra were obtained using a Jasco 260 Plus Fourier transform infrared spectrometer. High Resolution Mass Spectra (HRMS) were obtained using a Thermo LTqFT mass spectrometer with electrospray ionization in positive or negative mode. Flash chromatography was performed using SiliaFlash P60 silica gel (40-63 μm) purchased from Silicycle. All solvents were dried by passage over activated alumina columns immediately prior to use unless otherwise noted. Irradiation of photochemical reactions was carried out using three 15W PAR38 blue LED floodlamp purchased from EagleLight (Carlsbad, CA) with an output centered at a wavelength of approximately 450 nm. The reactions were carried out in 2 dram borosilicate glass vials (purchased from Fisher Scientific, catalogue # 03-339-22D) sealed with polypropylene caps equipped with Teflon coated septa (purchased through VWR international, Microliter Product # 15-0060K), or in 16mm x 150mm glass culture tubes sealed with rubber septa if reaction volume was greater than 7 mL. All reagents were purchased from Sigma-Aldrich corporation or Fisher Scientific corporation and were used without additional purification unless otherwise noted.

A.2. Synthesis and Characterization of Catalyst and Substrates

Preparation of 2,4,6-Tri(*p*-tolyl)pyrylium Tetrafluoroborate Salt



2,4,6-tri(*p*-tolyl)pyrylium tetrafluoroborate

1

2,4,6-Tri(*p*-tolyl)pyrylium tetrafluoroborate (**1**) was synthesized according to literature procedures in an isolated yield of 2.5 g (31% yield relative to starting *p*-tolualdehyde). The product was recrystallized from hot acetic acid. Residual acetic acid was removed by taking up the resulting crystals in a minimum amount of dichloromethane (~200 mL), and precipitating the material from

diethyl ether (~800 mL). The resulting precipitate was collected via filtration and dried under high vacuum. The analytical data matched that reported in the literature.¹

¹H NMR (600 MHz, CDCl₃): δ 8.43 (s, 2H), 8.27 – 8.22 (m, 4H), 8.22 – 8.16 (m, 2H), 7.55 – 7.48 (m, 4H), 7.23 – 7.17 (m, 2H), 2.48 (s, 6H), 2.15 (s, 3H); **¹³C NMR** (150 MHz, CDCl₃): δ 169.40, 164.46, 147.10, 147.09, 131.13, 131.01, 130.04, 129.09, 128.42, 125.76, 112.77, 22.03, 21.72.

Synthesis of *O*-aryl dimethylcarbamothioate substrates

Method A (adapted from literature procedure²)

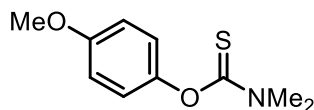
A 100 mL round-bottom flask was equipped with a Teflon coated stir bar and flame dried and allowed to cool under N₂ atmosphere. The flask was then charged with dimethylthiocarbamoyl chloride (1.5 equiv) and anhydrous dimethylformamide (DMF) to create a 0.75 M solution of the chloride. The phenol and 1,4 Diazabicyclo[2.2.2]-octane (DABCO, 1.5 equiv) were added sequentially and the solution was sealed, placed under an atmosphere of N₂ and allowed to stir at ambient temperature for 16 hours. Then, the flask was placed in a 0 °C bath and the resulting suspension was diluted with 25 mL water. Workup and purification was then achieved in one of two ways.

- I) If addition of water resulted in formation of a precipitate, the precipitate could be collected *via* vacuum filtration and washed with water affording the crude phenyl-*O*-dimethyl carbamothioate. The crude product could be recrystallized from either ethanol (EtOH) or EtOH/water solvent systems to afford the pure carbamothioate product.
- II) If addition of water did not result in formation of a precipitate, then the solution was transferred to a separatory funnel and extracted with ethyl acetate (3x). The combined organics were then washed 4-5 times with a saturated brine solution, dried over Na₂SO₄ and concentrated under reduced pressure. The resulting residue was then purified by column chromatography using a hexanes/ethyl acetate eluent. In some cases, residual phenol starting material co-eluted with the product carbamothioate. The phenol could be removed by dissolving the sample in Et₂O and washing (3x) with a 0.3 M NaOH solution. The organic layer could then be concentrated under reduced pressure to afford the pure carbamothioate.

Method B (adapted from literature procedure³)

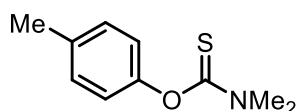
A clean, dry, 100 mL round-bottom flask (rbf) equipped with a teflon coated stir bar was purged with nitrogen and then charged with 1.06 g (26.4 mmol, 1.2 equiv.) of sodium hydride (60% dispersion in mineral oil). A syringe was then used to wash the sodium hydride with petroleum ether (20 to 30 mL of petroleum ether in four to six portions) to remove the mineral oil. Then, 10 mL of anhydrous DMF was added to the rbf via syringe under positive nitrogen pressure and allowed to stir. Then, the relevant phenol (22 mmol, 1.0 equiv.), dissolved in 12 mL of anhydrous DMF, was added dropwise to the sodium hydride suspension. Addition was carried

out slowly over the course of 3 to 5 minutes. After addition was complete, 3.26 g (26.4 mmol, 1.2 equiv.) of dimethylthiocarbamoyl chloride was added in a single portion. The rbf was then heated in an oil bath to 80 °C with stirring for one to three hours. The rbf was allowed to cool to room temperature, and then transferred to a 1 L separatory funnel containing 200 mL of diethyl ether. The rbf was rinsed with approximately 50 mL of diethyl ether and 50 mL of deionized water. The organic layer was then washed with three 100 mL portions of water, followed by four 50 mL portions of water. The diethyl ether was transferred to a 500 mL Erlenmeyer flask and dried using anhydrous magnesium sulfate, filtered via filter paper, and the solvent removed under reduced pressure, giving either a yellow oil or, sometimes, a yellowish-white solid. All oils were purified by flash chromatography using hexanes/ethyl acetate as eluent. Some solids were amenable to purification via recrystallization from ethanol or ethanol/water, though most were also purified via flash chromatography.



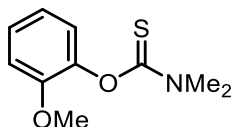
Analytical data for ***O*-(4-methoxyphenyl) dimethylcarbamothioate (2a)**: Synthesized by **Method B** from 4-methoxyphenol. Purified via recrystallization from 19:1 hexanes/diethyl ether to give 12.6 g (60% yield) of a white crystalline solid. Analytical data were in agreement with previous literature reports.⁴

¹H NMR (600 MHz, CDCl₃): δ 7.01 – 6.94 (m, 2H), 6.93 – 6.87 (m, 2H), 3.81 (s, 3H), 3.46 (s, 3H), 3.34 (s, 3H); ¹³C NMR (150 MHz, CDCl₃): δ 188.5, 157.4, 147.7, 123.6, 114.3, 55.7, 43.6, 38.8



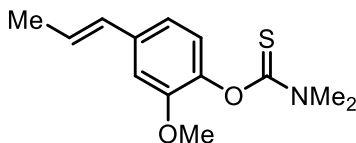
***O*-(4-methylphenyl) dimethylcarbamothioate (2b)**: Synthesized by **Method A** from 4-methylphenol (p-Cresol) in 31% yield. Analytical data were in agreement with previous literature reports.⁴

¹H NMR (600 MHz, CDCl₃): δ 7.21 – 7.16 (m, 2H), 6.97 – 6.92 (m, 2H), 3.46 (s, 3H), 3.34 (s, 3H), 2.36 (s, 3H); ¹³C NMR (150 MHz, CDCl₃): δ 188.2, 151.9, 135.7, 129.9, 122.5, 43.4, 38.8, 21.1



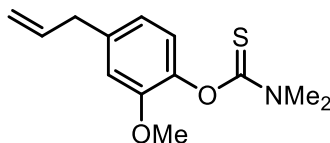
***O*-(2-methoxyphenyl) dimethylcarbamothioate (2d)**: Synthesized by **Method A** from 2-Methoxyphenol (Guaiacol) in 43% yield. Analytical data were in agreement with previous literature reports.⁵

¹H NMR (600 MHz, CDCl₃): δ 7.23 (ddd, *J* = 8.2, 7.4, 1.7 Hz, 1H), 7.04 (dd, *J* = 7.7, 1.7 Hz, 1H), 7.00 – 6.95 (m, 2H), 3.83 (s, 3H), 3.47 (s, 3H), 3.36 (s, 3H); **¹³C NMR** (150 MHz, CDCl₃): δ 188.0, 151.7, 143.0, 127.1, 124.2, 120.7, 112.7, 56.1, 43.5, 38.9



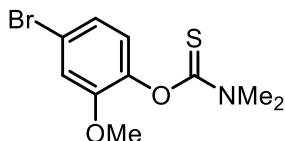
O-(2-methoxy-4-propenylphenyl) dimethylcarbamothioate (2e): Synthesized by **Method A** from (E)-2-methoxy-4-(prop-1-en-1-yl)phenol (Isoeugenol) in 74% yield. Isolated as a >19:1 mix of *E* : *Z* isomers. NMR shifts are reported for the *E* isomer unless otherwise noted.

¹H NMR (600 MHz, CDCl₃): δ 6.98 – 6.88 (m, 3H), 6.37 (dq, *J* = 15.6, 1.7 Hz, 1H), 6.19 (dq, *J* = 15.7, 6.6 Hz, 1H), 3.83 (s, 3H), 3.46 (s, 3H), 3.35 (s, 3H), 1.87 (dd, *J* = 6.6, 1.7 Hz, 3H); **¹³C NMR** (150 MHz, CDCl₃): δ 188.1, 151.5, 141.8, 137.1, 130.7, 129.6 (*Z*), 127.1 (*Z*), 126.1, 123.9, 123.7 (*Z*), 121.2 (*Z*), 118.3, 113.3 (*Z*), 109.9, 56.0, 43.5, 38.9, 18.6; **IR** (thin film): 2936, 1598, 1536, 1506, 1464, 1394, 1289, 1263, 1205, 1134, 1033 cm⁻¹; **HRMS** (+ESI): *m/z* calculated for [M+H]⁺: 252.1058; found: 252.1051



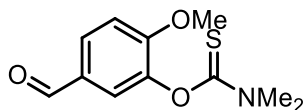
O-(4-allyl-2-methoxyphenyl) dimethylcarbamothioate (2f): Synthesized by **Method A** from 4-allyl-2-methoxyphenol (Eugenol) in 63% yield.

¹H NMR (600 MHz, CDCl₃): δ 6.95 (d, *J* = 8.6 Hz, 1H), 6.79 (d, *J* = 6.7 Hz, 2H), 6.03 – 5.93 (m, 1H), 5.14 – 5.07 (m, 2H), 3.81 (s, 3H), 3.46 (s, 3H), 3.40 (d, *J* = 6.7 Hz, 2H), 3.35 (s, 3H); **¹³C NMR** (150 MHz, CDCl₃): δ 188.1, 151.3, 141.2, 139.0, 137.1, 123.7, 120.6, 116.3, 113.0, 56.0, 43.5, 40.2, 38.8; **IR** (thin film): 2937, 1638, 1603, 1508, 1463, 1394, 1288, 1204, 1133, 1033 cm⁻¹; **HRMS** (+ESI): *m/z* calculated for [M+H]⁺: 252.1058; found: 252.1050



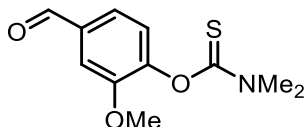
O-(4-bromo-2-methoxyphenyl) dimethylcarbamothioate (2g): Synthesized by **Method A** from 4-bromo-2-methoxyphenol in 47% yield.

¹H NMR (600 MHz, CDCl₃): δ 7.09 (d, *J* = 7.1 Hz, 2H), 6.93 – 6.88 (m, 1H), 3.82 (s, 3H), 3.45 (s, 3H), 3.34 (s, 3H); **¹³C NMR** (150 MHz, CDCl₃): δ 187.4, 152.3, 142.1, 125.4, 123.6, 119.6, 116.2, 56.3, 43.6, 38.9; **IR** (thin film): 2939, 1540, 1495, 1395, 1287, 1259, 1200, 1175, 1119, 1024, 863 cm⁻¹; **HRMS** (+ESI): *m/z* calculated for [M+H]⁺: 289.9850; found: 289.9843



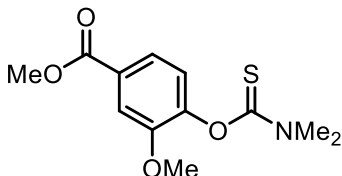
O-(3-formyl-2-methoxyphenyl) dimethylcarbamothioate (2h): Synthesized by **Method A** from 3-hydroxy-4-methoxybenzaldehyde (Isovanillin) in 75% yield.

¹H NMR (600 MHz, CDCl₃): δ 9.88 (s, 1H), 7.79 (d, *J* = 8.4 Hz, 1H), 7.57 (s, 1H), 7.08 (d, *J* = 8.3 Hz, 1H), 3.91 (s, 3H), 3.46 (s, 3H), 3.37 (s, 3H); **¹³C NMR** (150 MHz, CDCl₃): δ 190.3, 187.2, 156.9, 143.3, 130.0, 129.8, 125.0, 112.3, 56.4, 43.6, 38.9; **IR** (thin film): 2939, 1687, 1605, 1509, 1438, 1395, 1287, 1195, 1132, 1008 cm⁻¹; **HRMS** (+ESI): *m/z* calculated for [M+H]⁺: 240.0694; found: 240.0687



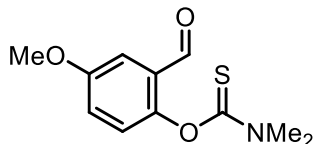
***O*-(4-formyl-2-methoxyphenyl) dimethylcarbamothioate (2i)**: Synthesized by **Method A** from 4-hydroxy-3-methoxybenzaldehyde (Vanillin) in 76% yield.

¹H NMR (600 MHz, CDCl₃): δ 9.96 (s, 1H), 7.51 (m, 2H), 7.23 (d, *J* = 8.4 Hz, 1H), 3.90 (s, 3H), 3.47 (s, 3H), 3.38 (s, 3H); **¹³C NMR** (150 MHz, CDCl₃): δ 191.2, 186.9, 152.5, 147.8, 135.2, 124.8, 124.7, 111.0, 56.2, 43.5, 39.0; **IR** (thin film): 1690, 1536, 1506, 1377, 1288, 1205, 1158, 1024 cm⁻¹; **HRMS** (+ESI): *m/z* calculated for [M+H]⁺: 240.0694; found: 240.0688



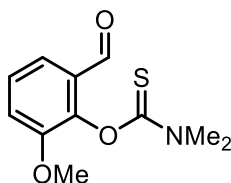
methyl 4-((dimethylcarbamothioyl)oxy)-3-methoxybenzoate (2j): Synthesized by **Method A** from methyl 4-hydroxy-3-methoxybenzoate (methyl vanillate) in 34% yield.

¹H NMR (600 MHz, CDCl₃): δ 7.69 (d, *J* = 8.2 Hz, 1H), 7.66 (s, 1H), 7.10 (d, *J* = 8.2 Hz, 1H), 3.91 (s, 3H), 3.88 (s, 3H), 3.46 (s, 3H), 3.37 (s, 3H); **¹³C NMR** (150 MHz, CDCl₃): δ 187.1, 166.5, 151.6, 146.6, 128.8, 124.1, 122.5, 113.7, 56.2, 52.4, 43.5, 38.9; **IR** (thin film): 2748, 1720, 1604, 1536, 1507, 1433, 1396, 1291, 1244, 1201, 1175, 1120, 1030 cm⁻¹; **HRMS** (+ESI): *m/z* calculated for [M+H]⁺: 270.0800; found: 270.0794



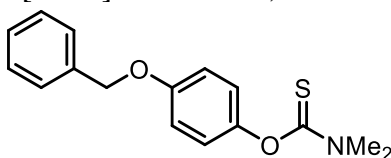
***O*-(2-formyl-4-methoxyphenyl) dimethylcarbamothioate (2k)**: Synthesized by **Method A**, with heating at 60 °C, from 2-hydroxy-5-methoxybenzaldehyde in 35% yield. Analytical data were in agreement with previous literature reports.⁶

¹H NMR (600 MHz, CDCl₃): δ 10.02 (s, 1H), 7.38 (d, *J* = 3.2 Hz, 1H), 7.17 (dd, *J* = 8.9, 3.2 Hz, 1H), 7.04 (d, *J* = 8.9 Hz, 1H), 3.86 (s, 3H), 3.47 (s, 3H), 3.42 (s, 3H); **¹³C NMR** (150 MHz, CDCl₃): δ 188.3, 187.9, 157.7, 149.7, 129.6, 125.5, 122.1, 111.4, 55.9, 43.6, 39.0



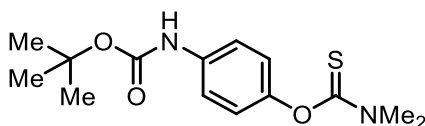
O-(2-formyl-6-methoxyphenyl) dimethylcarbamothioate (2l): Synthesized by **Method A**, with heating at 60 °C, from 2-hydroxy-3-methoxybenzaldehyde in 35% yield. Analytical data were in agreement with previous literature reports.⁶

¹H NMR (600 MHz, CDCl₃): δ 10.09 (d, *J* = 0.7 Hz, 1H), 7.50 (dd, *J* = 7.8, 1.5 Hz, 1H), 7.34 (td, *J* = 8.0, 0.7 Hz, 1H), 7.21 (dd, *J* = 8.2, 1.5 Hz, 1H), 3.87 (s, 3H), 3.48 (s, 3H), 3.43 (s, 3H)
¹³C NMR (150 MHz, CDCl₃): δ 188.97, 188.95, 187.3, 152.1, 145.1, 130.4, 126.8, 120.1, 117.9, 56.5, 43.7, 39.1 **IR** (thin film): 1697, 1584, 1541, 1483, 1394, 1274, 1250, 1179, 1116 cm⁻¹;
HRMS (+ESI): *m/z* calculated for [M+H]⁺: 240.0694; found: 240.0685



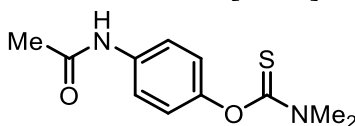
O-(4-benzyloxyphenyl) dimethylcarbamothioate (2m): Synthesized by **Method A** from 4-(Benzyloxy)phenol in 67% yield.

¹H NMR (600 MHz, CDCl₃): δ 7.45 – 7.42 (m, 1H), 7.42 – 7.36 (m, 1H), 7.33 (t, *J* = 7.3 Hz, 1H), 6.98 (s, 2H), 5.05 (s, 1H), 3.46 (s, 2H), 3.34 (s, 2H); **¹³C NMR** (150 MHz, CDCl₃): δ 188.4, 156.6, 147.9, 136.9, 128.7, 128.1, 127.7, 123.6, 115.1, 70.4, 43.6, 38.8; **IR** (thin film): 2936, 2360, 1534, 1502, 1393, 1287, 1195, 1132, 1008 cm⁻¹; **LRMS** (+ESI): *m/z* calculated for [M+H]⁺: 288.1058; found: 288.1049



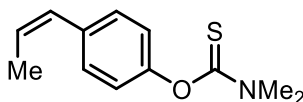
tert-butyl(4-((dimethylcarbamothioyl)oxy)phenyl)carbamate (2n): Synthesized by **Method B** from tert-butyl (4-hydroxyphenyl)carbamate. Purified by recrystallization from ethanol/water (~9:1) to give 2.52 g (84% yield) of a white crystalline solid.

¹H NMR (600 MHz, CDCl₃): δ 7.38 (d, *J* = 7.9 Hz, 2H), 6.98 (d, *J* = 8.9 Hz, 2H), 6.47 (s, 1H), 3.45 (s, 3H), 3.33 (s, 3H), 1.51 (s, 9H); **¹³C NMR** (150 MHz, CDCl₃): δ 170.5, 135.9, 134.5, 129.3, 129.0, 71.5, 41.8, 21.3, 21.0, 19.4 ; **IR** (thin film): 2360, 1642, 1529, 1393, 1287, 1204, 1159, 1053 cm⁻¹; **HRMS** (+ESI): *m/z* calculated for [M+H]⁺: 297.1273; found: 297.1266



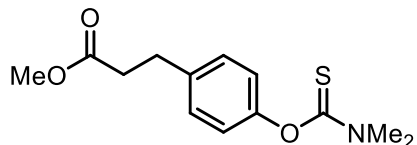
O-(4-acetamidophenyl) dimethylcarbamothioate (2o): Synthesized by **Method A** from N-(4-hydroxyphenyl)acetamide (Acetaminophen) in 62% yield.

¹H NMR (600 MHz, CDCl₃): δ 7.51 (d, *J* = 8.8 Hz, 2H), 7.21 (br, 1H) 7.01 (d, *J* = 8.8 Hz, 2H), 3.45 (s, 3H), 3.34 (s, 3H), 2.17 (s, 3H); **¹³C NMR** (150 MHz, CDCl₃): 188.0, 168.3, 150.2, 135.8, 123.2, 120.7, 43.4, 38.9, 24.7; **IR** (thin film): 1667, 1536, 1504, 1395, 1286, 1201 cm⁻¹;
HRMS (+ESI): *m/z* calculated for [M+H]⁺: 239.0854; found: 239.0848



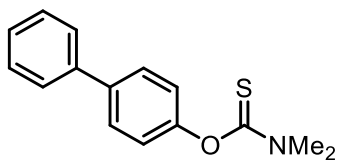
***O*-(4-propenylphenyl) dimethylcarbamothioate (2p):** Synthesized by **Method A** from 4-(prop-1-en-1-yl)phenol as a 9 : 1 mixture of *Z* : *E* isomers. 4-(prop-1-en-1-yl)phenol was prepared according to a published literature procedure. The analytical data matched that reported in the literature.⁷

¹H NMR (600 MHz, CDCl₃): δ 7.32 (d, *J* = 8.4 Hz, 1H), 7.03 (d, *J* = 8.5 Hz, 1H), 6.41 (d, *J* = 11.6 Hz, 1H), 5.90 – 5.72 (m, 1H), 3.46 (s, 2H), 3.35 (s, 2H), 1.91 (d, *J* = 7.2 Hz, 1H); ¹³C NMR (150 MHz, CDCl₃): δ 187.9, 187.8, 152.8, 152.4, 135.9, 135.4, 130.2, 129.8, 129.6, 129.4, 129.1, 127.0, 126.5, 126.0, 122.8, 122.4, 43.3, 38.84, 18.6, 14.7; **IR** (thin film): 2938, 1643, 1531, 1504, 1393, 1286, 1208, 1168, 1130, 1014, 845 cm⁻¹; **HRMS** (+ESI): *m/z* calculated for [M+H]⁺: 222.0952; found: 222.0946



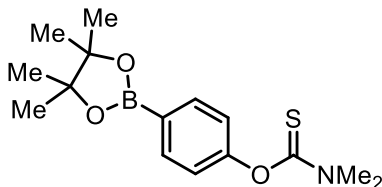
methyl 3-(4-((dimethylcarbamothioyl)oxy)phenyl)propanoate (2q): Synthesized by **Method A** with heating at 60 °C from methyl 3-(4-hydroxyphenyl)propanoate in 76% yield. 3-(4-hydroxyphenyl)propanoate was prepared according to a published literature procedure. The analytical data matched that reported in the literature.⁸

¹H NMR (600 MHz, CDCl₃): δ 7.22 (d, *J* = 8.4 Hz, 1H), 6.98 (d, *J* = 8.4 Hz, 1H), 3.67 (s, 2H), 3.45 (s, 2H), 3.33 (s, 2H), 2.96 (t, *J* = 7.9 Hz, 1H), 2.81 – 2.61 (m, 1H); ¹³C NMR (150 MHz, CDCl₃): δ 187.9, 173.4, 152.5, 138.2, 129.1, 122.8, 51.8, 43.4, 38.8, 35.6, 30.5; **IR** (thin film): 2938, 1737, 1537, 1506, 1395, 1288, 1213, 1170, 1017 cm⁻¹; **HRMS** (+ESI): *m/z* calculated for [M+H]⁺: 268.1007; found: 268.0998



***O*-([1,1'-biphenyl]-4-yl) dimethylcarbamothioate (2r):** Synthesized by **Method A** from 4-phenylphenol in 73% yield.

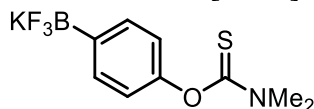
¹H NMR (600 MHz, CDCl₃): δ 7.64 – 7.54 (m, 4H), 7.43 (dd, *J* = 8.4, 7.1 Hz, 2H), 7.37 – 7.31 (m, 1H), 7.16 – 7.12 (m, 2H), 3.48 (d, *J* = 1.1 Hz, 3H), 3.37 (d, *J* = 1.0 Hz, 3H); ¹³C NMR (150 MHz, CDCl₃): δ 187.8, 153.5, 140.4, 139.0, 128.8, 127.4, 127.4, 127.2, 123.1, 43.4, 38.9; **IR** (thin film): 1646, 1509, 1484, 1394, 1287, 1209, 1132, 1007, 765 cm⁻¹; **HRMS** (+ESI): *m/z* calculated for [M+H]⁺: 258.0952; found: 258.0944



***O*-(4-(4,4,5,5-tetramethyl-1,3,2-dioxaborolan-2-yl)phenyl) dimethylcarbamothioate (2w):** Synthesized by **Method B** from 4-(4,4,5,5-tetramethyl-1,3,2-dioxaborolan-2-yl)phenol in a 43% yield.

¹H NMR (600 MHz, CDCl₃): δ 7.88 – 7.82 (m, 2H), 7.10 – 7.04 (m, 2H), 3.45 (s, 3H), 3.35 (s, 3H), 1.33 (s, 12H); ¹³C NMR (150 MHz, CDCl₃): δ 187.61, 156.46, 135.98, 122.19, 83.87,

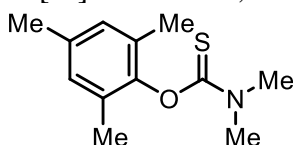
43.25, 38.78, 24.88; **IR** (thin film): 2977, 1600, 1536, 1397, 1358, 1323, 1286, 1206, 1141, 1085, 1016 cm^{-1} ; **HRMS** (+ESI): m/z calculated for $[\text{M}+\text{H}]^+$: 308.1492; found: 308.1482



O-(4-(trifluoro- λ^4 -boranyl)phenyl) dimethylcarbamothioate, potassium salt (2s):

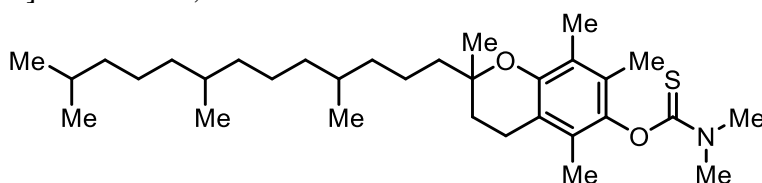
Synthesized by an adapted procedure⁹ from O-(4-(4,4,5,5-tetramethyl-1,3,2-dioxaborolan-2-yl)phenyl) dimethylcarbamothioate (**2w**). To a 20 mL scintillation vial was added 1.0 g of **2w**, 1.0g KHF_2 (4.0 equiv), 2 mL H_2O and 13 mL MeOH. The vial was equipped with a Teflon coated stir bar, sealed and allowed to stir at r.t. overnight. After, the solution was concentrated and the resulting residue washed with acetone (10 mL x 3). Each wash was collected and filtered through a cotton plug and the combined organics were then concentrated. The solid was then dissolved in 5 mL acetone and then Et_2O was added until further addition yielded no additional precipitate. The white precipitate was collected by vacuum filtration and dried to afford **2s** as a white powder (560 mg, 59%).

¹H NMR (600 MHz, DMSO-d_6): 7.29 (d, $J = 8.1$ Hz, 2H), 6.73 (d, $J = 7.8$ Hz, 2H), 3.34 (s, 3H), 3.28 (s, 3H); **¹³C NMR** (150 MHz, DMSO-d_6): δ 187.1, 151.8, 131.7, 120.2, 42.7, 38.3; **¹⁹F NMR** (376 MHz, DMSO-d_6): δ -138 **IR** (thin film): 1543, 1501, 1395, 1284, 1211, 1149, 983 cm^{-1} ; **HRMS** (-ESI): m/z calculated for $[\text{M}]^-$: 248.0528; found: 248.0531



O-(2,4,6-trimethylphenyl) dimethylcarbamothioate (2t): Synthesized by **Method B** from 2,4,6-trimethylphenol in six batches. Each batch was purified by flash chromatography (19:1 hexanes/ethyl acetate) on average giving 4.30 g (86% yield) of a white crystalline solid.

¹H NMR (600 MHz, CDCl_3): δ 6.88 (s, 2H), 3.48 (s, 3H), 3.37 (s, 3H), 2.28 (s, 3H), 2.13 (s, 6H); **¹³C NMR** (150 MHz, CDCl_3): δ 186.65, 149.0, 135.4, 130.4, 129.3, 43.4, 38.5, 21.0, 16.6; **IR** (thin film): 2924, 2856, 1529, 1482, 1393, 1288, 1196, 1141 cm^{-1} ; **HRMS** (+ESI): m/z calculated for $[\text{M}+\text{H}]^+$: 224.1109; found: 224.1102

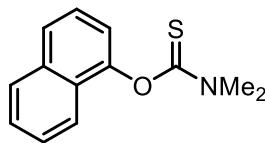


(\pm)-O-(2,5,7,8-tetramethyl-2-(4,8,12-trimethyltridecyl)chroman-6-yl)

dimethylcarbamothioate (2u): Synthesized by **Method B** from (\pm)-alpha tocopherol. Purified by flash chromatography (19:1 hexanes/ethyl acetate) giving 4.79 g (94% yield) of a viscous, clear, slightly yellow oil.

¹H NMR (600 MHz, CDCl_3): δ 3.49 (s, 3H), 3.37 (s, 3H), 3.37 (s, 3H), 2.60-2.52 (m, 2H), 2.11 (d, 3H), 2.03 (s, 3H), 1.99 (d, 3H), 1.90-1.68 (m, 2H), 1.65-1.00 (m, 23H), 0.90-0.80 (m, 12H); **¹³C NMR** (150 MHz, CDCl_3): δ 187.41, 149.36, 149.28, 143.69, 143.64, 127.40, 125.68, 125.66, 122.91, 122.83, 117.18, 117.11, 74.97, 43.28, 41.39, 41.36, 39.34, 39.06, 38.95, 38.33, 37.53, 37.48, 37.44, 37.42, 37.40, 37.37, 37.35, 37.33, 37.28,

37.27, 37.24, 34.64, 34.51, 32.78, 32.76, 32.75, 32.72, 32.69, 32.66, 32.64, 32.63, 31.58, 31.15, 31.08, 30.66, 30.63, 27.96, 26.89, 25.25, 24.81, 24.80, 24.76, 24.75, 24.44, 24.41, 23.13, 23.10, 22.72, 22.65, 22.62, 21.10, 21.08, 21.06, 20.97, 20.95, 20.69, 20.59, 20.55, 19.75, 19.73, 19.69, 19.68, 19.66, 19.63, 19.61, 19.59, 19.57, 14.13, 13.18, 12.33, 11.91, 11.90. **IR** (thin film): 2924, 2856, 1529, 1482, 1393, 1288, 1196, 1141 cm^{-1} ; **HRMS** (+ESI): m/z calculated for $[\text{M}+\text{H}]^+$: 518.4031; found: 518.4016



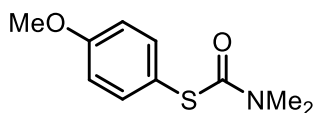
O-(1-naphthyl) dimethylcarbamothioate (2v): Synthesized by **Method A** from 1-Naphthol. Purified by flash chromatography (19:1 hexanes/ethyl acetate) to give 4.10 g (68% yield) of a white crystalline solid.

^1H NMR (600 MHz, CDCl_3): δ 7.91 – 7.85 (m, 1H), 7.83 – 7.79 (m, 1H), 7.79 – 7.74 (m, 1H), 7.54 – 7.45 (m, 3H), 7.22 (dd, $J = 7.5, 1.0$ Hz, 1H), 3.53 (s, 3H), 3.51 (s, 3H); **^{13}C NMR** (150 MHz, CDCl_3): δ 188.0, 150.0, 134.6, 128.2, 127.5, 126.5, 126.4, 126.2, 125.4, 121.6, 119.6, 43.5, 38.9; **IR** (thin film): 2930, 1598, 1531, 1389, 1286, 1256, 1130, 1013, 799 cm^{-1} ; **HRMS** (+ESI): m/z calculated for $[\text{M}+\text{H}]^+$: 232.0796; found: 232.0788

A.3 Methods and Analytical Data for Rearranged Products

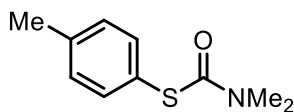
Example Method for Cation Radical Accelerate Newman-Kwart Rearrangement

A 2 dram vial equipped with a Teflon coated stir bar was charged with 2.1 mg (0.0047 mmol, 0.01 equiv.) of 2,4,6-tri(p-tolyl)pyrylium tetrafluoroborate and 100 mg (0.47 mmol, 1.0 equiv.) of *O*-(4-methoxyphenyl) dimethylcarbamothioate. The vial was sealed with a Teflon coated septum cap. Next, 1.0 mL of anhydrous acetonitrile (0.5 M with respect to substrate) was added to the vial via syringe. The solution was then sparged with nitrogen gas for 15 minutes (the needle piercings of the septum were covered with a small piece of electrical tape after sparging to minimize solvent loss). The vials were placed on a stir plate and irradiated for 24 hrs. After irradiation, the reaction volume was reduced under vacuum, and the residual solution was loaded onto a silica plug (5 to 7 mL of silica) and eluted with 19:1 (9:1 for more polar products) hexanes/ethyl acetate.



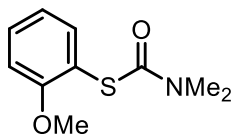
S-(4-methoxyphenyl) dimethylcarbamothioate (3a): Isolated in 95% yield (95 mg), representing an average of two reactions. Analytical data were in agreement with previous literature reports.⁴

¹H NMR (600 MHz, CDCl₃): δ 7.39 (d, *J* = 8.4 Hz, 2H), 6.91 (d, *J* = 8.4 Hz, 2H), 3.81 (s, 3H), 3.09 (br, 3H), 3.01 (br, 3H); ¹³C NMR (150 MHz, CDCl₃): δ 167.8, 160.6, 137.4, 119.5, 114.7, 55.4, 37.0



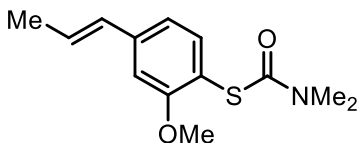
S-(4-methylphenyl) dimethylcarbamothioate (3b): Isolated in 79% yield (79 mg), representing an average of two reactions. Analytical data were in agreement with previous literature reports.⁴

¹H NMR (600 MHz, CDCl₃): δ 7.37 (d, *J* = 8.1 Hz, 2H), 7.19 (d, *J* = 8.0 Hz, 2H), 3.09 (br, 3H), 3.01 (br, 3H), 2.36 (s, 3H); ¹³C NMR (150 MHz, CDCl₃): δ 167.4, 139.5, 135.8, 129.9, 125.2, 37.0, 21.4



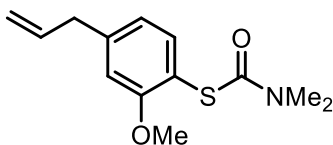
S-(2-methoxyphenyl) dimethylcarbamothioate (3d): Isolated in 93% yield (93 mg), representing an average of two reactions. Analytical data were in agreement with previous literature reports.⁵

¹H NMR (600 MHz, CDCl₃): δ 7.46 (d, *J* = 7.5 Hz, 1H), 7.40 (t, *J* = 7.8 Hz, 1H), 7.04 – 6.93 (m, 2H), 3.88 (s, 3H), 3.14 (br, 3H), 3.01 (br, 3H); **¹³C NMR** (150 MHz, CDCl₃): δ 166.4, 160.2, 138.2, 131.6, 121.1, 116.7, 111.5, 56.2, 37.1, 37.0



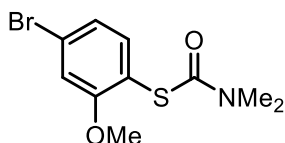
S-(2-methoxy-4-propenylphenyl) dimethylcarbamothioate (3e): Isolated in 99% yield (99 mg), representing an average of two reactions.

¹H NMR (600 MHz, CDCl₃): δ 7.36 (d, *J* = 7.9 Hz, 1H), 6.94 (d, *J* = 9.4 Hz, 1H), 6.89 (s, 1H), 6.39 (d, *J* = 17.0 Hz, 1H), 6.35 – 6.23 (m, 1H), 3.88 (s, 3H), 3.13 (br, 3H), 3.00 (br, 3H), 1.89 (d, *J* = 8.0 Hz, 3H); **¹³C NMR** (150 MHz, CDCl₃): δ 166.6, 160.2, 141.6, 138.2, 130.8, 127.5, 118.8, 114.7, 108.9, 56.1, 37.1, 18.7; **IR** (thin film): 2935, 1667, 1592, 1560, 1463, 1404, 1360, 1289, 1251, 1172, 1096, 1066, 1030 cm⁻¹; **HRMS** (+ESI): *m/z* calculated for [M+H]⁺: 252.1058; found: 252.1050



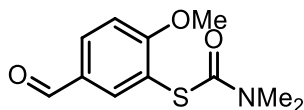
S-(4-allyl-2-methoxyphenyl) dimethylcarbamothioate (3f): Isolated in 97% yield (97 mg), representing an average of two reactions.

¹H NMR (600 MHz, CDCl₃): δ 7.36 (d, *J* = 7.7 Hz, 1H), 6.81 (d, *J* = 7.8 Hz, 1H), 6.78 (s, 1H), 6.03 – 5.88 (m, 1H), 5.16 – 5.03 (m, 2H), 3.86 (s, 3H), 3.40 (d, *J* = 6.7 Hz, 2H), 3.13 (br, 3H), 3.00 (br, 3H); **¹³C NMR** (150 MHz, CDCl₃): δ 166.6, 160.2, 144.2, 138.1, 136.8, 121.4, 116.5, 114.1, 111.9, 56.2, 40.5, 37.0; **IR** (thin film): 2921, 1668, 1595, 1568, 1463, 1405, 1361, 1255, 1169, 1097, 1065, 1032, 909 cm⁻¹; **HRMS** (+ESI): *m/z* calculated for [M+H]⁺: 252.1058; found: 252.1050



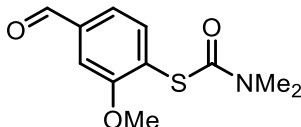
S-(4-bromo-2-methoxyphenyl) dimethylcarbamothioate (3g): Isolated in 96% yield (96 mg), representing an average of two reactions.

¹H NMR (600 MHz, CDCl₃): δ 7.31 (d, *J* = 8.1 Hz, 1H), 7.11 (dd, *J* = 8.1, 1.9 Hz, 1H), 7.08 (d, *J* = 1.9 Hz, 1H), 3.86 (s, 3H), 3.12 (br, 3H), 3.00 (br, 3H); **¹³C NMR** (150 MHz, CDCl₃): δ 165.7, 160.6, 139.0, 125.3, 124.2, 116.1, 115.2, 56.5, 37.1; **IR** (thin film): 1663, 1576, 1479, 1374, 1254, 1087, 908 cm⁻¹; **HRMS** (+ESI): *m/z* calculated for [M+H]⁺: 289.9850; found: 289.9842



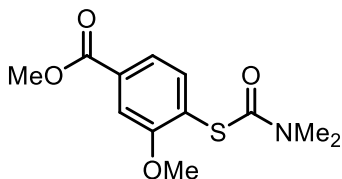
S-(3-formyl-2-methoxyphenyl) dimethylcarbamothioate (3h): Isolated in 94% yield (94 mg), representing an average of two reactions.

¹H NMR (600 MHz, CDCl₃): δ 9.99 (s, 1H) 7.70-7.69 (d, 1H), 7.47-7.46 (d, 1H) 7.45 (s, *J* = 6.6 Hz, *J* = 13.6 Hz, 1H) 3.95 (s, 3H) 3.15 (br, 3H) 3.02 (br, 3H); **¹³C NMR** (150 MHz, CDCl₃): δ 190.2, 187.3, 156.9, 143.3, 129.9, 129.9, 125.0, 112.3, 56.4, 43.6, 38.9; **IR** (thin film): 2978.5, 2927.4, 2858.9, 1736.6, 1515.8, 1452.1, 1372.1, 1243.9 cm⁻¹; **HRMS** (+ESI): *m/z* calculated for [M+H]⁺: 240.0694; found: 240.0687



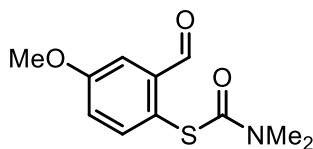
S-(4-formyl-2-methoxyphenyl) dimethylcarbamothioate (3i): Isolated in 95% yield (95 mg), representing an average of two reactions.

¹H NMR (600 MHz, CDCl₃): δ 9.99 (s, 1H), 7.69 (d, *J* = 7.7 Hz, 1H), 7.46 (d, *J* = 9.1 Hz, 1H), 7.45 (s, 1H), 3.95 (s, 3H), 3.15 (br, 3H), 3.02 (br, 3H); **¹³C NMR** (150 MHz, CDCl₃): δ 191.80, 191.78, 165.0, 160.3, 138.6, 138.2, 125.1, 123.8, 109.5, 56.5, 37.2, 37.1; **IR** (thin film): 2922, 1693, 1661, 1570, 1484, 1406, 1373, 1290, 1255, 1175, 1096, 1060, 1028, 905 cm⁻¹; **HRMS** (+ESI): *m/z* calculated for [M+H]⁺: 240.0694; found: 240.0687



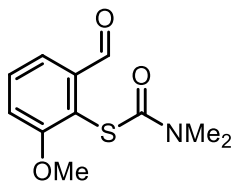
methyl 4-((dimethylcarbamoyl)thio)-3-methoxybenzoate (3j): Isolated in 95% yield (95 mg), representing an average of two reactions.

¹H NMR (600 MHz, CDCl₃): δ 7.64 (dd, *J* = 7.9, 1.6 Hz, 1H), 7.61 (d, *J* = 1.2 Hz, 1H), 7.55 (d, *J* = 7.9 Hz, 1H), 3.93 (s, 3H), 3.92 (s, 3H), 3.14 (br, 3H) 3.01 (br, 3H); **¹³C NMR** (150 MHz, CDCl₃): δ 166.7, 165.3, 159.8, 137.7, 132.8, 122.8, 122.0, 112.1, 56.4, 52.5, 37.1; **IR** (thin film): 1720, 1671, 1399, 1290, 1235, 1097 cm⁻¹; **HRMS** (+ESI): *m/z* calculated for [M+H]⁺: 270.0800; found: 270.0792



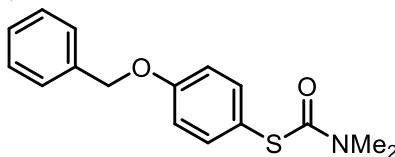
S-(2-formyl-4-methoxyphenyl) dimethylcarbamothioate (3k): Isolated in 56% yield (56 mg), representing an average of two reactions. Analytical data were in agreement with previous literature reports.⁶

¹H NMR (600 MHz, CDCl₃): δ 10.33 (s, 1H), 7.54 (d, *J* = 3.0 Hz, 1H), 7.46 (d, *J* = 8.5 Hz, 1H), 7.13 (dd, *J* = 8.5, 3.0 Hz, 1H), 3.88 (s, 3H), 3.16 (br, 3H) 3.02 (br, 3H); **¹³C NMR** (150 MHz, CDCl₃): δ 191.5, 191.4, 166.0, 161.2, 139.0, 123.5, 121.3, 112.0, 55.8, 37.1



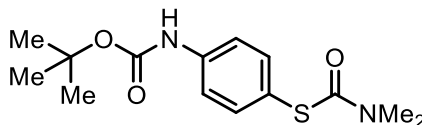
S-(2-formyl-6-methoxyphenyl) dimethylcarbamothioate (3l): Isolated in 98% yield (98 mg), representing an average of two reactions.

¹H NMR (600 MHz, CDCl₃): δ 10.46 (d, *J* = 0.8 Hz, 1H), 7.63 (dd, *J* = 7.7, 1.3 Hz, 1H), 7.53 (ddd, *J* = 8.5, 7.7, 0.8 Hz, 1H), 7.19 (dd, *J* = 8.3, 1.3 Hz, 1H), 3.92 (s, 3H), 3.22 (s, 3H), 3.02 (s, 3H); **¹³C NMR** (150 MHz, CDCl₃): δ 191.9, 191.8, 164.9, 160.2, 139.2, 131.2, 120.7, 120.6, 116.3, 56.7, 37.4, 37.3 **IR** (thin film): 1668, 1574, 1271, 1097 cm⁻¹; **HRMS** (+ESI): *m/z* calculated for [M+H]⁺: 240.0694; found: 240.0686



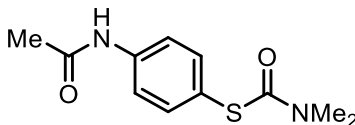
S-(4-benzyloxyphenyl) dimethylcarbamothioate (3m): Isolated in 93% yield (93 mg), representing an average of two reactions.

¹H NMR (600 MHz, CDCl₃): δ 7.45 – 7.36 (m, 6H), 7.33 (t, *J* = 7.2 Hz, 1H), 6.98 (d, *J* = 8.8 Hz, 2H), 5.07 (s, 2H), 3.09 (br, 3H), 3.01 (br, 3H); **¹³C NMR** (150 MHz, CDCl₃): δ 167.7, 159.8, 137.4, 136.7, 128.7, 128.2, 127.6, 119.8, 115.6, 70.2, 37.0; **IR** (thin film): 2924, 1667, 1591, 1572, 1493, 1455, 1403, 1363, 1284, 1242, 1175, 1105, 1089, 1003 cm⁻¹; **HRMS** (+ESI): *m/z* calculated for [M+H]⁺: 288.1058; found: 288.1048



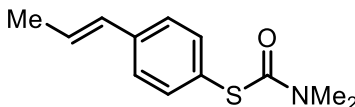
tert-butyl(4-((dimethylcarbamothioyl)thio)phenyl)carbamate (3n): Isolated in 97% yield (97 mg), representing an average of two reactions.

¹H NMR (600 MHz, CDCl₃): δ 7.38 (s, 4H), 6.58 (s, 1H), 3.05 (d, *J* = 41.8 Hz, 6H), 1.51 (s, 9H); **¹³C NMR** (150 MHz, CDCl₃): δ 167.5, 152.5, 139.6, 136.7, 121.9, 118.7, 80.9, 37.0, 28.4; **IR** (thin film): 2976, 1725, 1650, 1591, 1525, 1399, 1366, 1311, 1235, 1159, 1093 cm⁻¹; **HRMS** (+ESI): *m/z* calculated for [M+H]⁺: 297.1273; found: 297.1265



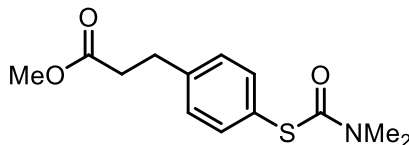
S-(4-acetamidophenyl) dimethylcarbamothioate (3o): Isolated in 88% yield (88 mg), representing an average of two reactions.

¹H NMR (600 MHz, CDCl₃): δ 7.87 (s, 1H), 7.40 (d, *J* = 8.4 Hz, 2H), 7.34 (d, *J* = 8.4 Hz, 2H), 3.12 (br, 3H), 3.04 (br, 3H), 2.09 (s, 3H); **¹³C NMR** (150 MHz, CDCl₃): δ 168.5, 168.1, 168.0, 158.0, 139.5, 136.5, 122.6, 120.3, 120.3, 37.1, 24.6; **IR** (thin film): 2924, 1644, 1589, 1530, 1399, 1371, 1317, 1248, 1085, 1003 cm⁻¹; **HRMS** (+ESI): *m/z* calculated for [M+H]⁺: 239.0854; found: 239.0846



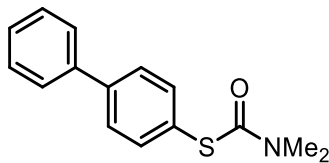
S-(4-propenylphenyl) dimethylcarbamothioate (3p): Isolated in 98% yield (98 mg) as a >19:1 mixture of *E* to *Z* isomers, representing an average of two reactions.

¹H NMR (600 MHz, CDCl₃): δ 7.40 (d, *J* = 8.3 Hz, 2H), 7.32 (d, *J* = 8.2 Hz, 2H), 6.39 (d, *J* = 15.8 Hz, 1H), 6.32 – 6.23 (m, 1H), 3.09 (br, 3H), 3.02 (br, 3H) 1.89 (d, *J* = 6.6 Hz, 3H); **¹³C NMR** (150 MHz, CDCl₃): δ 167.2, 139.0, 135.9, 130.5, 127.3, 126.6, 37.0, 18.7; **IR** (thin film): 3019, 2934, 1650, 1448, 1402, 1362, 1257, 1088, 961 cm⁻¹; **HRMS** (+ESI): *m/z* calculated for [M+H]⁺: 222.0952; found: 222.0945



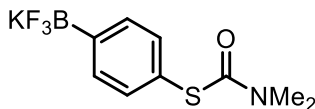
methyl 3-(4-((dimethylcarbamothioyl)thio)phenyl)propanoate (3q): Isolated in 91% yield (91 mg), representing an average of two reactions.

¹H NMR (600 MHz, CDCl₃): δ 7.40 (d, *J* = 8.1 Hz, 1H), 7.22 (d, *J* = 8.1 Hz, 1H), 3.67 (s, 2H), 3.09 (br, 3H), 3.01 (br, 3H), 2.96 (t, *J* = 7.9 Hz, 1H), 2.66 – 2.60 (m, 1H); **¹³C NMR** (150 MHz, CDCl₃): δ 173.3, 167.2, 141.9, 136.0, 129.1, 126.4, 51.8, 37.0, 35.5, 30.7; **IR** (thin film): 2949, 1737, 1671, 1399, 1290, 1235, 1097 cm⁻¹; **HRMS** (+ESI): *m/z* calculated for [M+H]⁺: 268.1007; found: 268.0998



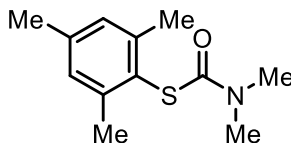
S-([1,1'-biphenyl]-4-yl) dimethylcarbamothioate (3r): Isolated in 96% yield (96 mg), representing an average of two reactions.

¹H NMR (600 MHz, CDCl₃): δ 7.63 – 7.53 (m, 6H), 7.44 (t, *J* = 7.7 Hz, 2H), 7.36 (t, *J* = 7.4 Hz, 1H), 3.12 (br, 3H) 3.04 (br, 3H); **¹³C NMR** (150 MHz, CDCl₃): δ 167.0, 142.2, 140.5, 136.1, 128.9, 127.8, 127.73, 127.3, 123.1, 37.0; **IR** (thin film): 1670, 1478, 1364, 1256, 1040 cm⁻¹; **HRMS** (+ESI): *m/z* calculated for [M+H]⁺: 258.0952; found: 258.0943



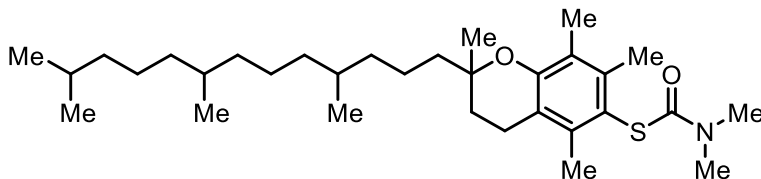
S-(4-(trifluoro-λ⁴-boranyl)phenyl) dimethylcarbamothioate, potassium salt (3s): Isolated in 80% yield (80 mg), representing an average of two reactions. Product was isolated by diluting the reaction mixture with acetone and then precipitating the product by addition of Et₂O.

¹H NMR (600 MHz, DMSO-d₆): 7.33 (d, *J* = 7.7 Hz, 1H), 7.14 (d, *J* = 7.6 Hz, 1H), 3.02 (br, 3H) 2.90 (br, 3H); **¹³C NMR** (150 MHz, DMSO-d₆): δ 166.3, 134.1, 132.3, 124.4, 36.8, 31.1; ; **¹⁹F NMR** (376 MHz, DMSO-d₆): δ -139 **IR** (thin film): 1669, 1366, 1202, 1089, 965 cm⁻¹; **HRMS** (-ESI): *m/z* calculated for [M]⁻: 248.0528; found: 248.0532



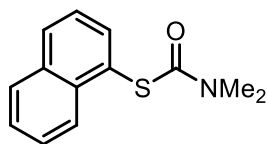
S-(2,4,6-trimethylphenyl) dimethylcarbamothioate (3t): Isolated in 79% yield (79 mg), representing an average of two reactions.

¹H NMR (600 MHz, CDCl₃): δ 6.96 (s, 2H), 3.16 (br, 3H), 3.08 (br, 3H) 2.37 (s, 6H), 2.27 (s, 3H); **¹³C NMR** (150 MHz, CDCl₃): δ 166.4, 143.5, 139.6, 129.2, 124.7, 36.9, 22.0, 21.29; **IR** (thin film): 2921, 1667, 1601, 1458, 1359, 1259, 1096, 1056, 907 cm⁻¹; **HRMS** (+ESI): *m/z* calculated for [M+H]⁺: 224.1109; found: 224.1101



(±)-S-(2,5,7,8-tetramethyl-2-(4,8,12-trimethyltridecyl)chroman-6-yl) dimethylcarbamothioate (3u): Isolated in 99% yield (99 mg), representing an average of two reactions.

¹H NMR (600 MHz, CDCl₃): δ 3.17 (brs, 3H), 3.00 (brs, 3H), 2.62 (t, 2H, *J* = 6 Hz), 2.37 (s, 3H), 2.34 (s, 3H), 2.12 (s, 3H), 1.85-1.70 (m, 2H), 1.62-1.47 (m, 4H), 1.45-1.00 (m, 23H), 0.90-0.80 (m, 12H); **¹³C NMR** (150 MHz, CDCl₃): δ 167.51, 153.04, 140.21, 139.51, 123.23, 117.79, 117.64, 75.38, 40.14, 39.35, 37.51, 37.49, 37.44, 37.42, 37.39, 37.37, 37.35, 37.33, 37.26, 37.03, 36.79, 32.78, 32.76, 32.71, 32.68, 31.12, 31.07, 27.97, 24.81, 24.80, 24.45, 24.44, 23.99, 22.73, 22.63, 21.38, 21.05, 21.03, 19.74, 19.68, 19.65, 19.61, 19.58, 18.72, 17.85, 12.59. **IR** (thin film): 2923, 2866, 1669, 1563, 1461, 1359, 1306, 1260, 1157, 1097 cm⁻¹; **HRMS** (+ESI): *m/z* calculated for [M+H]⁺: 518.4031; found: 518.4020

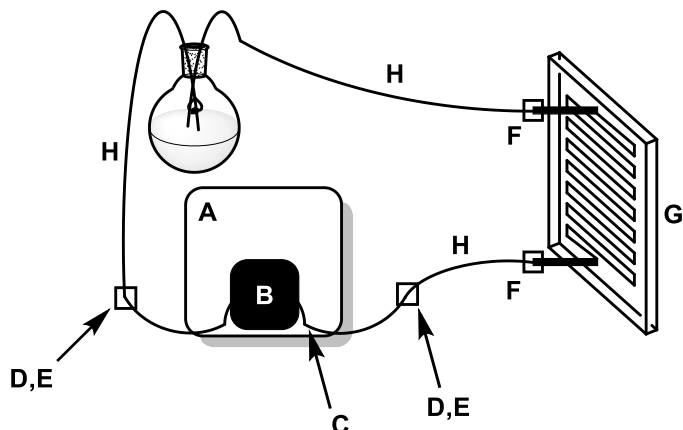


S-(1-naphthyl) dimethylcarbamothioate (3v): Isolated in 94% yield (94 mg), representing an average of two reactions.

¹H NMR (600 MHz, CDCl₃): δ 8.32 (d, *J* = 8.5 Hz, 1H), 7.94 (d, *J* = 8.2 Hz, 1H), 7.87 (d, *J* = 8.1 Hz, 1H), 7.78 (d, *J* = 7.1 Hz, 1H), 7.57 (t, *J* = 7.6 Hz, 1H), 7.54 – 7.46 (m, 2H), 3.24 (br, 3H), 3.02 (br, 3H); **¹³C NMR** (150 MHz, CDCl₃): δ 166.6, 136.2, 135.3, 134.2, 130.9, 128.6, 127.1, 126.3, 126.2, 125.8, 125.6, 37.1; **IR** (thin film): 1668, 1503, 1360, 1257, 1093, 798 cm⁻¹; **HRMS** (+ESI): *m/z* calculated for [M+H]⁺: 232.0796; found: 232.0788

A.4 Large Scale Flow Synthesis: *S*-(2,4,6-trimethylphenyl)dimethylcarbamothioate

Figure S1. Diagram of Flow Chemical Apparatus



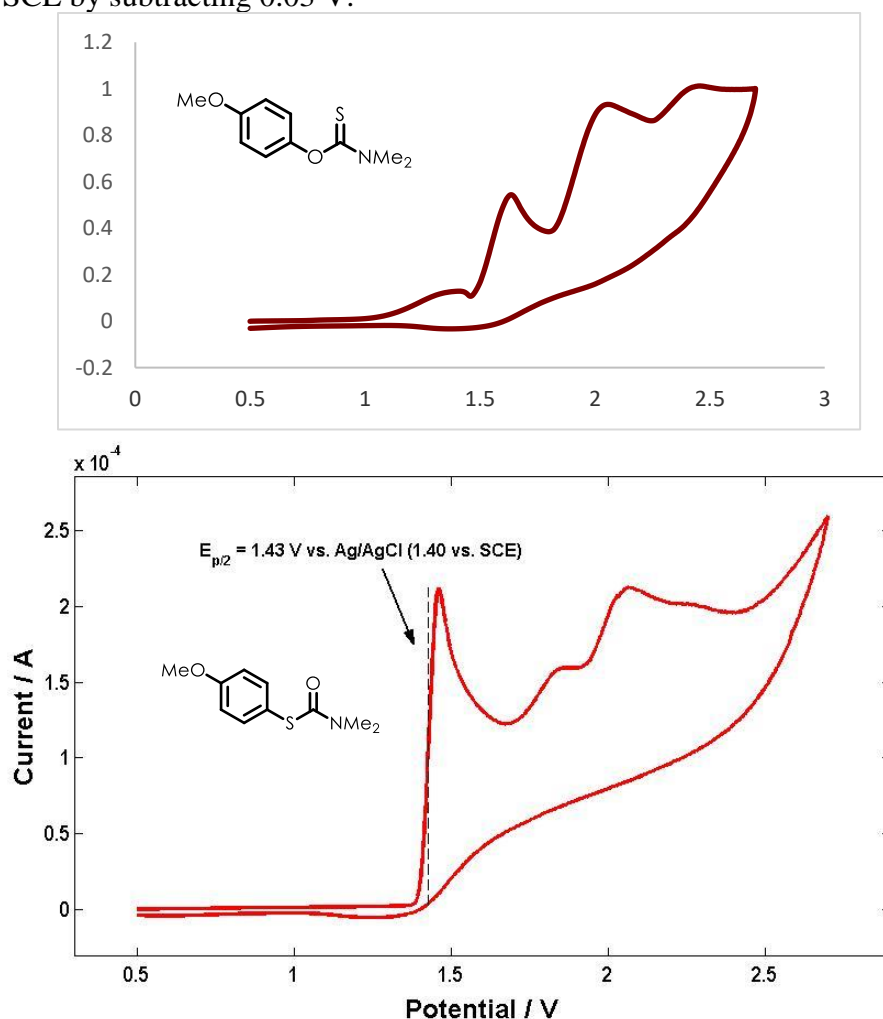
- A.** Masterflex L/S Variable-Speed Drive (Cole-Parmer # EW-07528-30)
- B.** Masterflex L/S Rigid PTFE-Tubing Pump Head (Cole-Parmer # EW-77390-00)
- C.** MASTERFLEX PTFE-TUBING 4MM O.D. (COLE-PARMER # EW-77390-50)
- D.** 4MM PTFE MALE NPT COMPRESSION ADAPTER (COLE-PARMER # WU-31321-62)
- E.** 1/8" O.D. TO 1/8" PTFE FEMALE NPT COMPRESSION ADAPTER (COLE-PARMER # EW-31320-50)
- F.** 1/4-28 FLANGELESS FITTING/FERRULE FOR 1/8" O.D. TUBING (SIGMA-ALDRICH SUPELCO # 58686)
- G.** Microreactor (Little Things Factory GmbH # XXL-ST-02)
- H.** PTFE TUBING 1/16" I.D., 1/8" O.D. (COLE-PARMER # WU-06605-27)

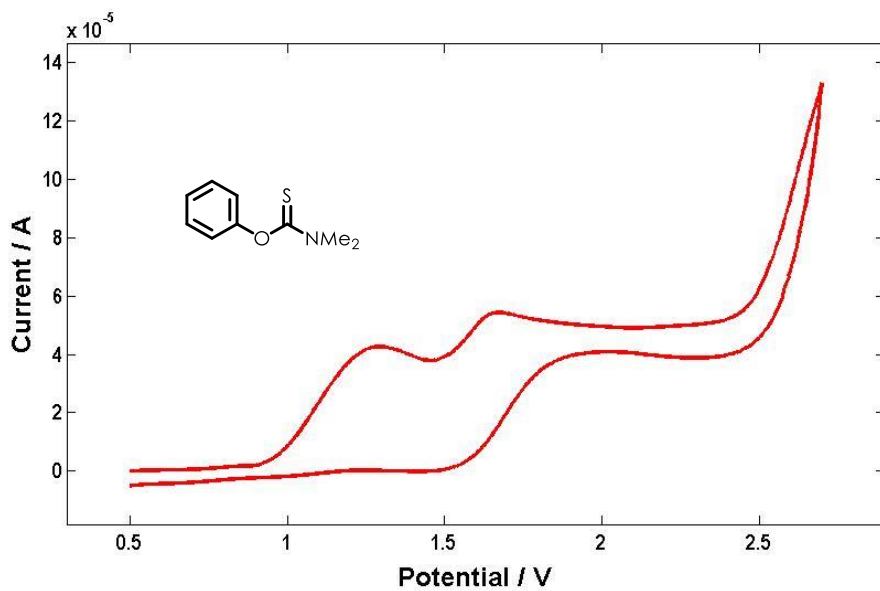
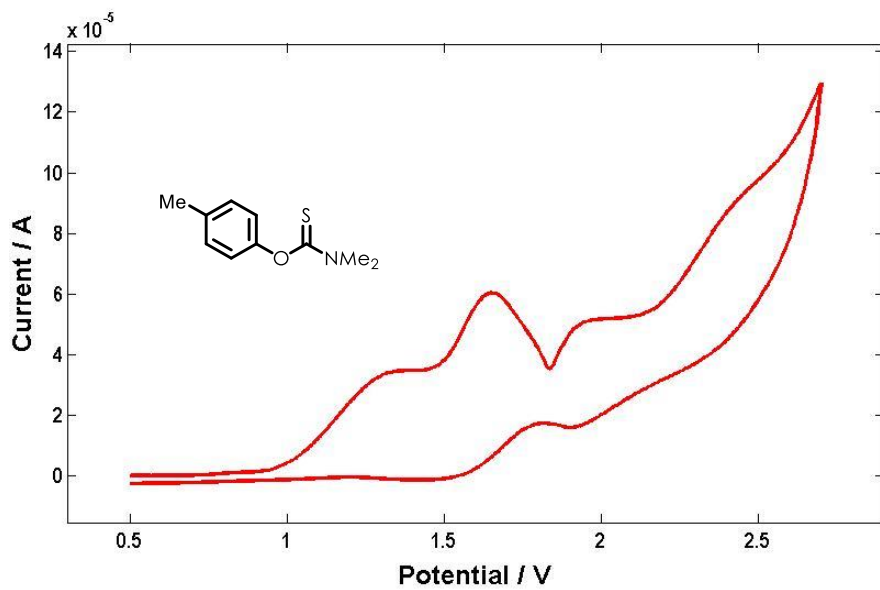
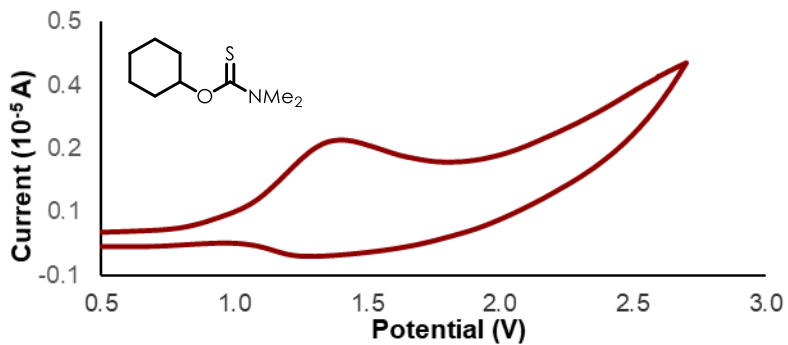
CHAPTER 1:

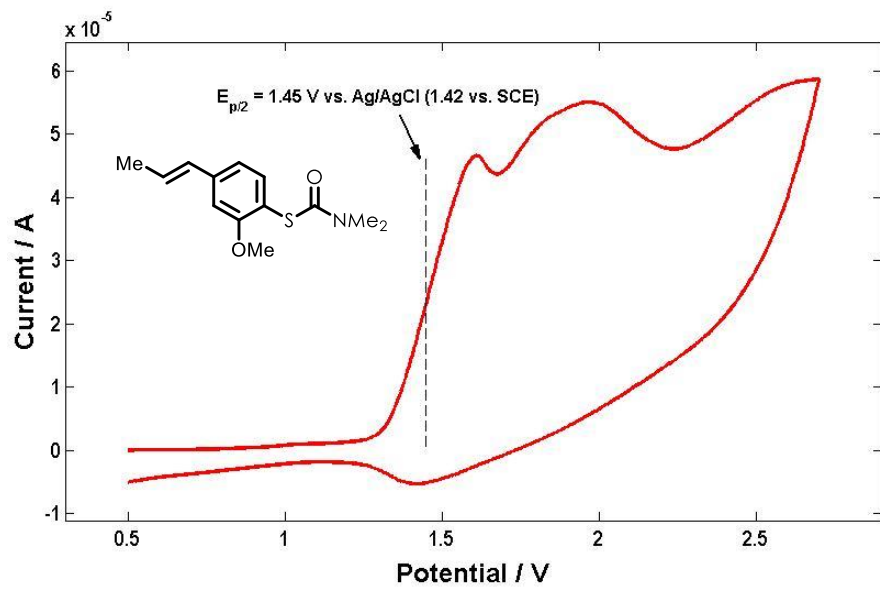
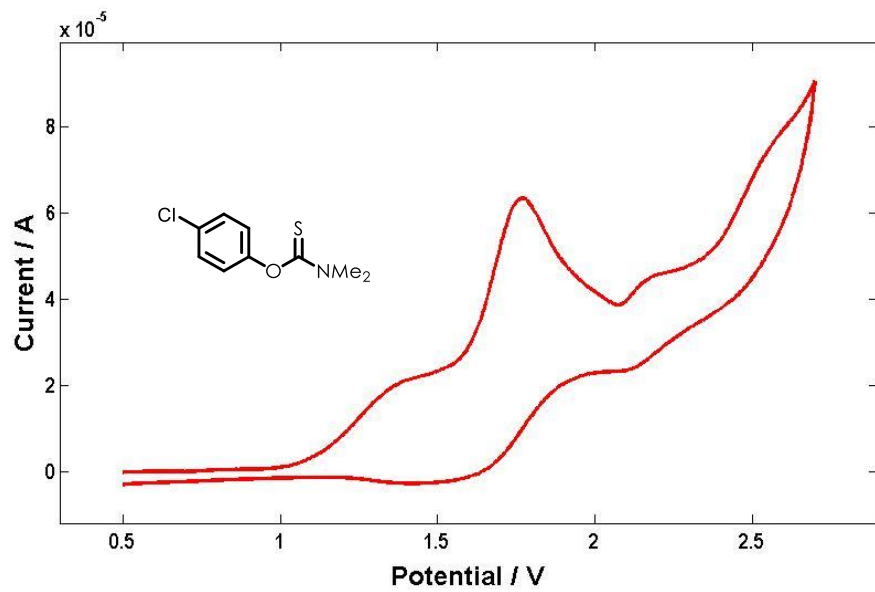
A 1 L rbf was charged with 21.5 grams of *O*-(2,4,6-trimethylphenyl)dimethylcarbamothioate (96.4 mmol), followed by 0.38 g of triphenylpyrylium tetrafluoroborate (0.96 mmol, 0.01 equivalents). Next, a teflon coated stir bar was added, followed by 800 mL of acetonitrile. Two 15W PAR38 blue LED floodlamps were positioned on either side of the microreactor (G). The 1 L rbf was clamped in place over a stir plate and moderate stirring was begun. The rbf was fitted with a rubber stopper with two holes drilled through it. Into one hole was placed the PTFE tubing inlet. This tubing was placed several inches below the surface of the solution. Into the second hole was placed the PTFE tubing outlet. This was placed above the surface of the solution to allow visual verification of circulation. The Masterflex L/S Variable-Speed Drive was set to 60 rpm, the occlusion bed of the pump head was adjusted as per the manufacturer's instructions, and the blue LED floodlamps were switched on. The reaction was sampled every 10 to 12 hours and analyzed via ¹H NMR to determine reaction progress. After 82 hours, all starting material was determined to have been consumed. The solvent was removed under vacuum and the resulting yellow solid was purified via silica gel chromatography (600 mL silica gel, 19:1 to 9:1 to 4:1 petroleum ether/ethyl acetate). After chromatography, 19.7 g (88.2 mmol, 91% yield) of a yellowish white crystalline solid was obtained. The solid was confirmed to be the desired product, *S*-(2,4,6-trimethylphenyl) dimethylcarbamothioate.

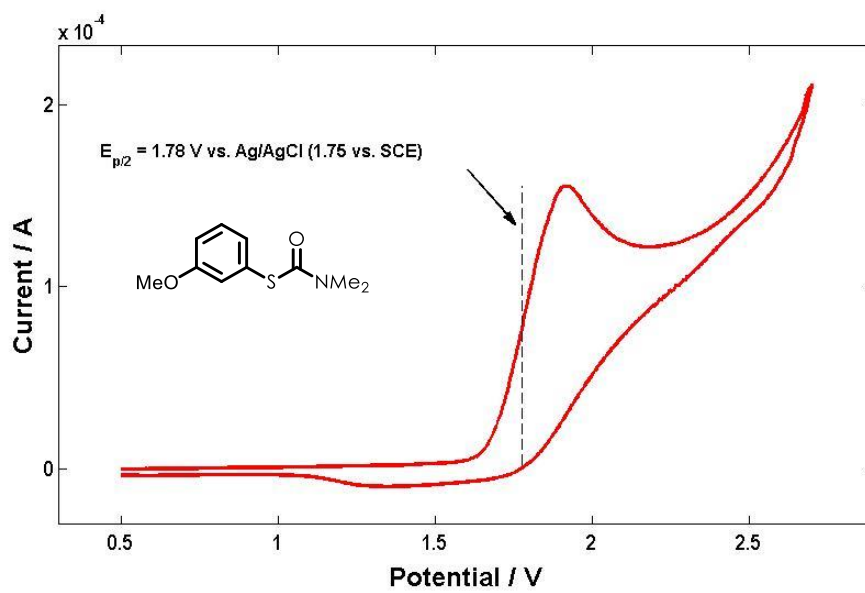
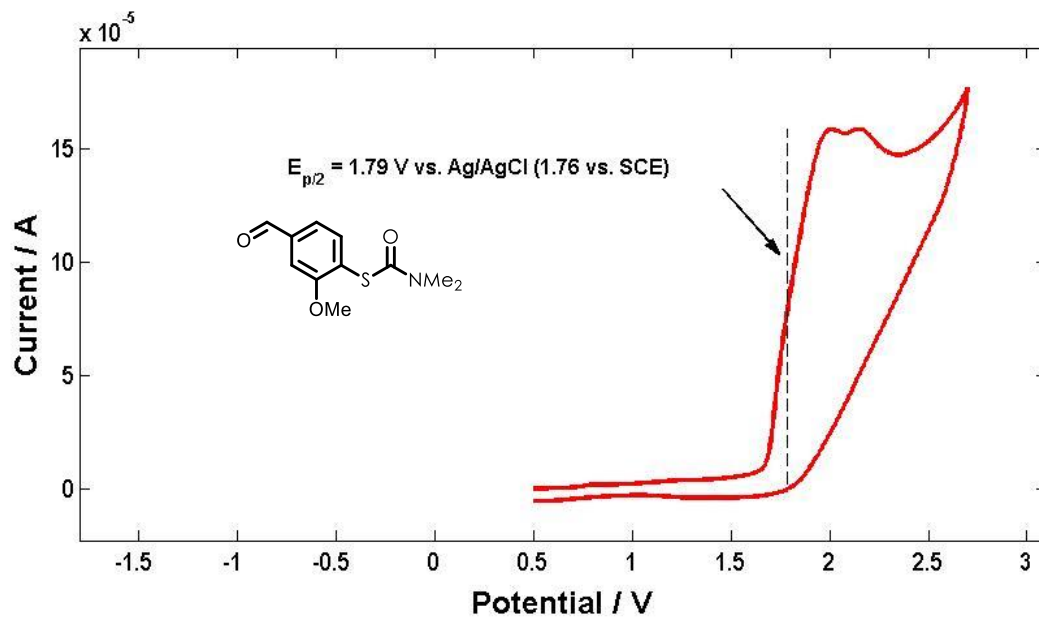
A.5 Measurement of Redox Potentials via Cyclic Voltammetry

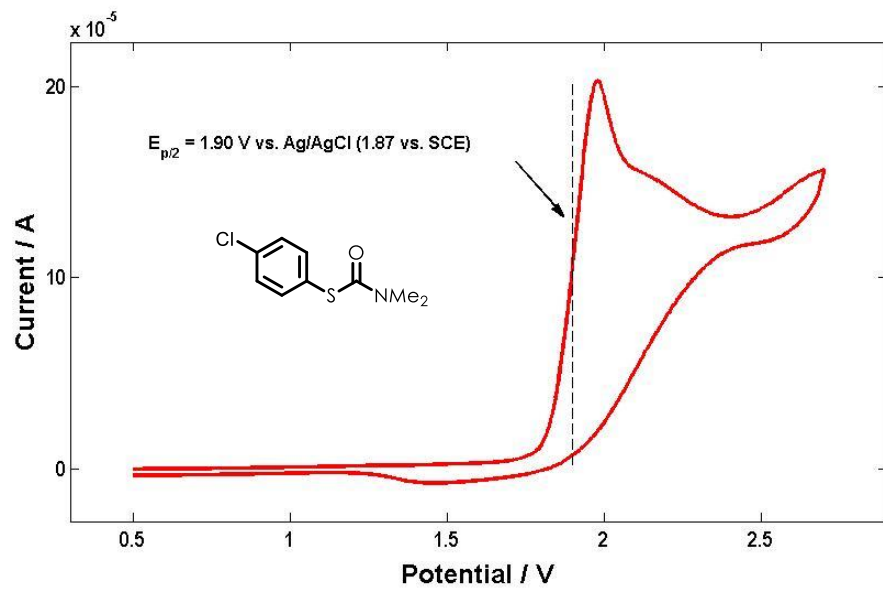
Electrochemical potentials were obtained by collecting cyclic voltammograms with a Pine WaveNow Potentiostat. Samples were prepared with 0.05 mmol of substrate in 5 mL of 0.1 M tetra-*n*-butylammonium hexafluorophosphate in dry, degassed acetonitrile. Measurements employed a glassy carbon working electrode, platinum wire counter electrode, 3.5 M NaCl silver-silver chloride reference electrode, and a scan rate of 100 mV/s. Reductions were measured by scanning potentials in the negative direction and oxidations in the positive direction; the glassy carbon electrode was polished between each scan. Data was analyzed using MATLAB by subtracting a background current prior to identifying the maximum current (C_p) and determining the potential ($E_{p/2}$) at half this value ($C_{p/2}$). The obtained value was referenced to Ag/AgCl and converted to SCE by subtracting 0.03 V.











A.6. Photophysical measurements

Time-resolved and steady state emission spectra were recorded using an Edinburgh FLS920 spectrometer. Unless otherwise specified, measurements were taken under ambient conditions. For collection of steady state fluorescence spectra, the excitation wavelength was set to 420 nm, and a 435 nm low pass optical filter was used to remove extraneous wavelengths from the excitation light. All spectra (1 nm step size, 5 nm bandwidth) are fully corrected for the spectral response of the instrument. Time resolved emission measurements (including Stern-Volmer quenching studies) were made by the time-correlate single photon counting (TCSPC) capability of the same instrument (FLS920) with pulsed excitation light (444.2 nm, typical pulse width = 95 ps) generated by a Edinburgh EPL-445 ps pulsed laser diode operating at a repetition rate of 20 MHz for **1**. The maximum emission channel count rate was less than 5% of the laser count channel rate, and each data set collected 5000 counts on the maximum channel.

The fluorescence lifetime was determined by reconvolution fit to the instrument response function using the Edinburgh FS900 software. In all cases, after reconvolution, fluorescence was found to satisfactorily fit a monoexponential function of the form:

$$I_t = I_0 e^{-t/\tau}$$

A.6.1. Stern-Volmer Quenching Experiments

Stern-Volmer experiments were conducted with detection at 515 nm. A solution of **1** (5.0 μM) was prepared and 2.4 - 2.5 mL was added to 4 mL (nominal volume) quartz cuvette and sealed with a septum screw cap. The lifetime of **1** was recorded in the absence of quencher as outlined in the general procedure and found to be 4.40 ns. Generally, a 0.5 M solution of the quencher was prepared and then added to the solution of **1** in 10 μL increments (in all cases up to at least 50 μL of quencher solution was added to achieve a final [Quencher] of ~ 10 mM)

Stern-Volmer analysis was conducted according to the following relationship:

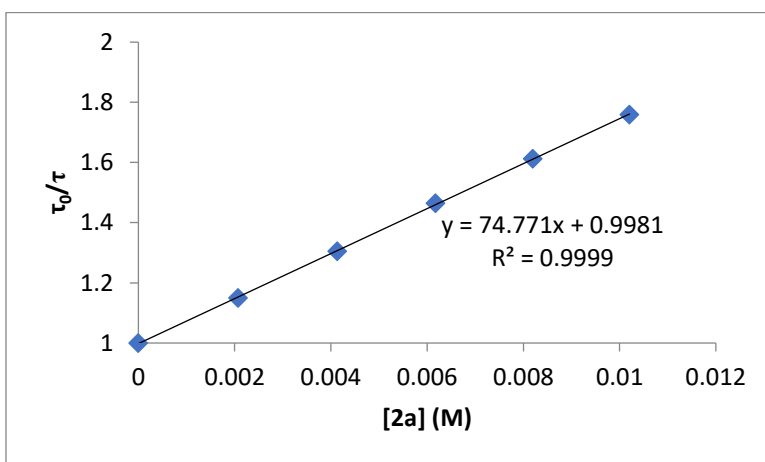
Equation A.1

$$\frac{\tau_0}{\tau} = 1 + K_{SV} = 1 + k_q\tau_0[\text{Quencher}]$$

where τ_0 and τ are the fluorescence lifetime in the absence and presence of quencher Q , K_{SV} is the Stern-Volmer constant, k_q is the bimolecular quenching constant, and $[\text{Quencher}]$ is the concentration of quencher.

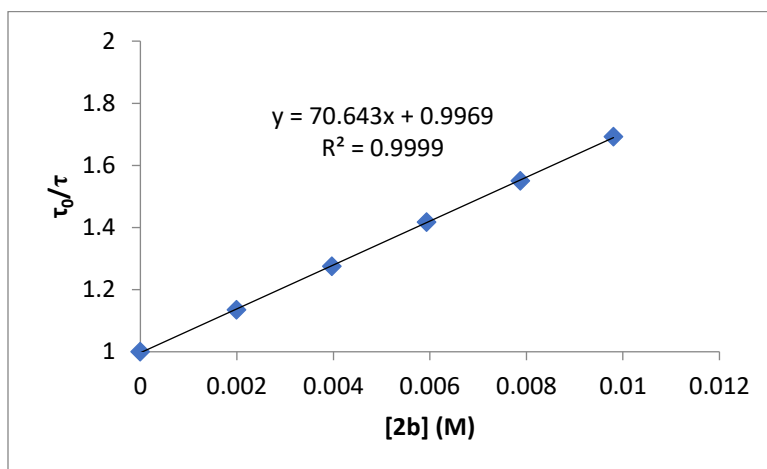
[2a] (mM)	τ (ns)
0	4.45
2.08	3.87
4.13	3.41
6.17	3.04
8.20	2.76
10.2	2.53

$K_{SV} = 74.8 \text{ M}^{-1}$; $k_q = 1.68 \times 10^9 \text{ M}^{-1} \text{ s}^{-1}$



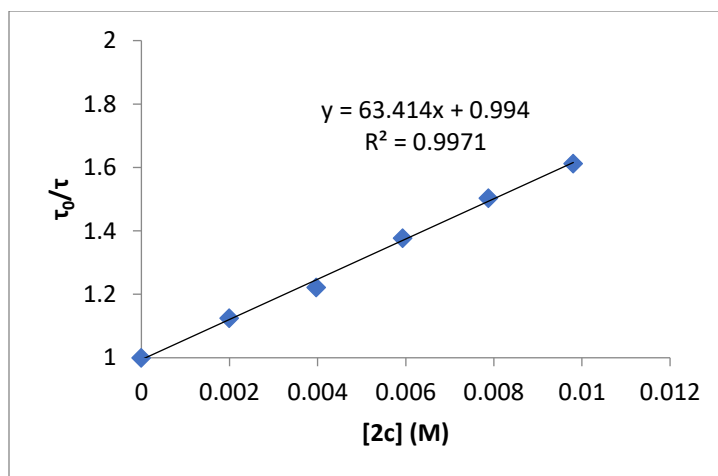
[2b] (mM)	τ (ns)
0	4.45
2.00	3.92
3.97	3.49
5.92	3.14
7.87	2.87
9.80	2.63

$$K_{SV} = 70.7 \text{ M}^{-1}; k_q = 1.59 \times 10^9 \text{ M}^{-1} \text{ s}^{-1}$$



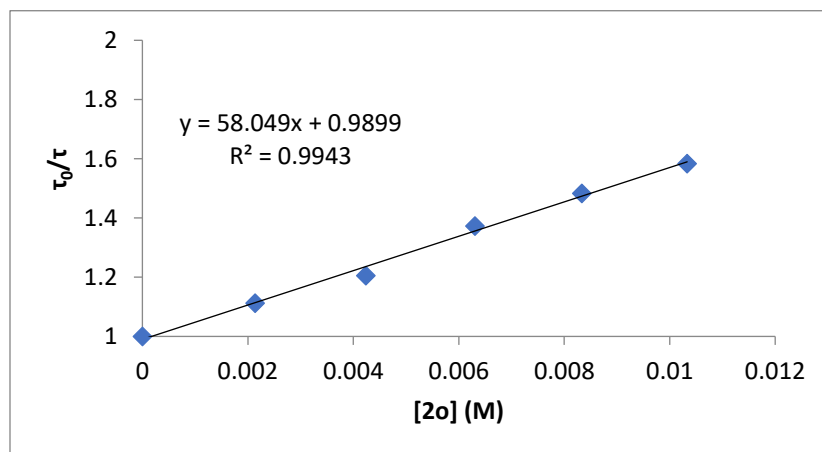
[2c] (mM)	τ (ns)
0	4.24
2.00	3.77
3.97	3.47
5.92	3.08
7.87	2.82
9.80	2.63

$$K_{SV} = 73.8 \text{ M}^{-1}; k_q = 1.50 \times 10^9 \text{ M}^{-1} \text{ s}^{-1}$$



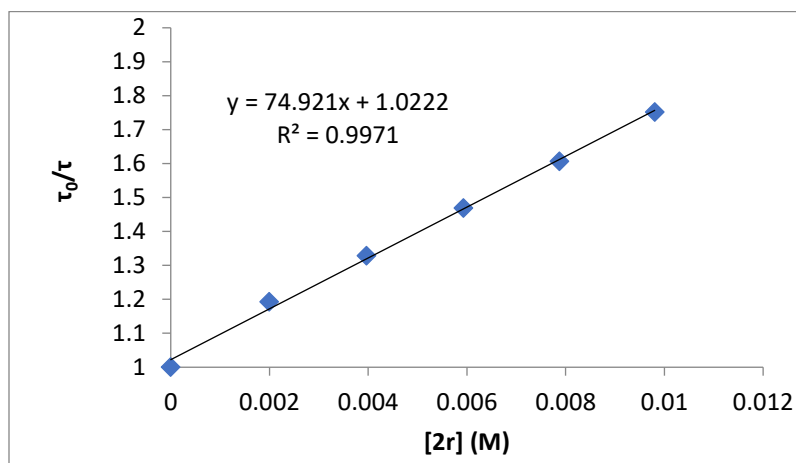
$[2o]$ (mM)	τ (ns)
0	4.45
2.14	4.00
4.23	3.69
6.30	3.24
8.33	3.00
10.3	2.81

$K_{SV} = 58.0 \text{ M}^{-1}$; $k_q = 1.30 \times 10^9 \text{ M}^{-1} \text{ s}^{-1}$



[2r] (mM)	τ (ns)
0	4.45
2.00	3.73
4.00	3.35
5.93	3.03
7.87	2.77
9.80	2.54

$K_{SV} = 74.9 \text{ M}^{-1}$; $k_q = 1.68 \times 10^9 \text{ M}^{-1} \text{ s}^{-1}$



[4j] (mM)	τ (ns)
0	4.43
2.00	3.91
4.00	3.51
5.96	3.03
7.94	2.77
9.90	2.54

$K_{SV} = 76.7 \text{ M}^{-1}$; $k_q = 1.72 \times 10^9 \text{ M}^{-1} \text{ s}^{-1}$

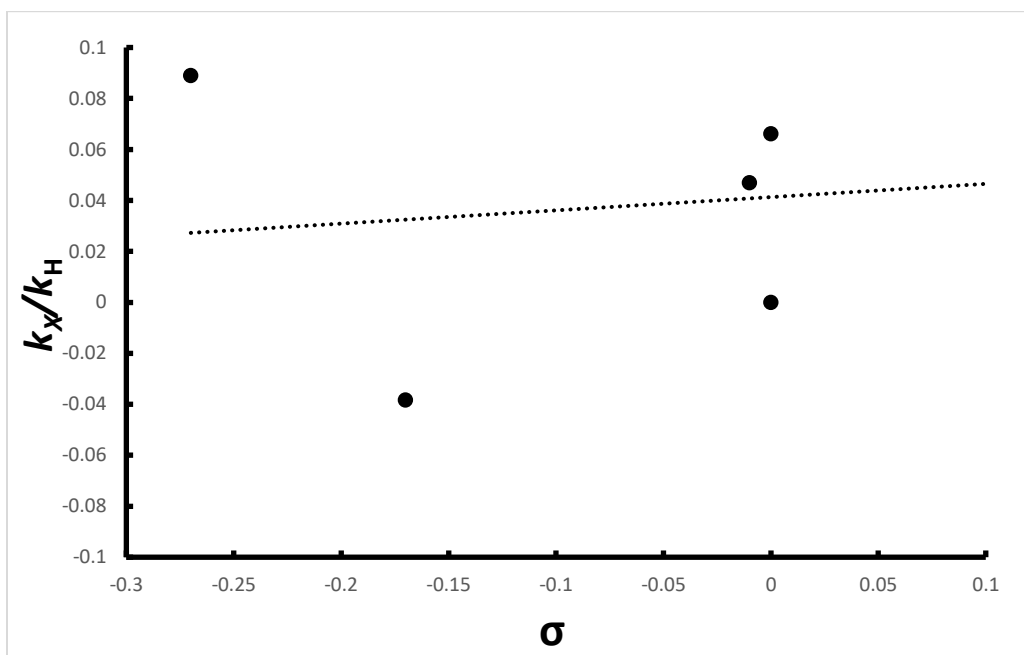
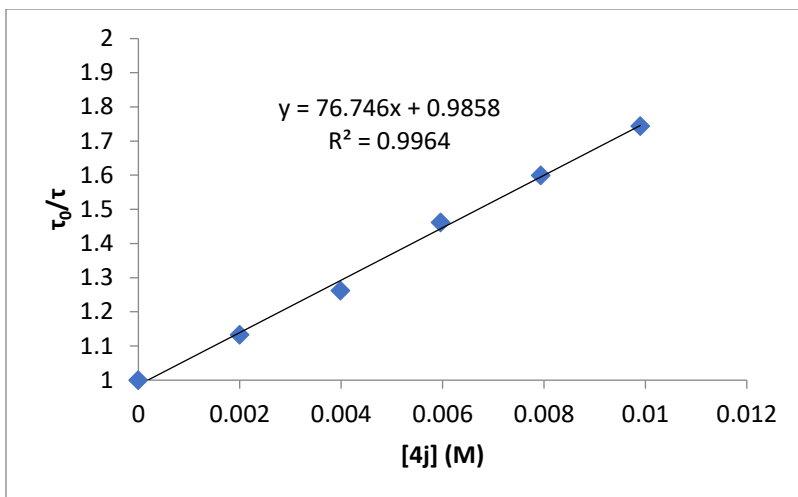
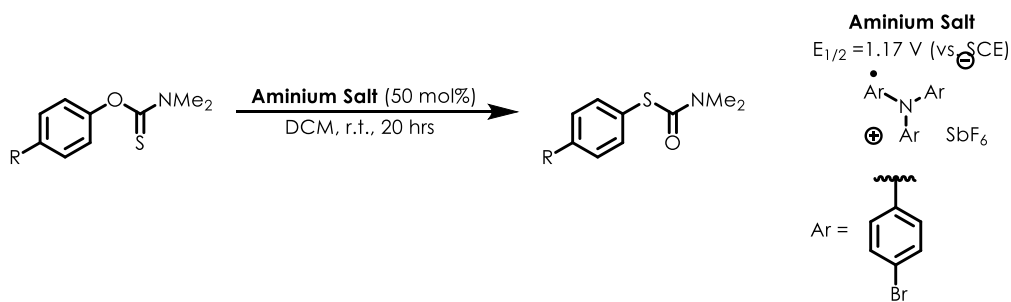


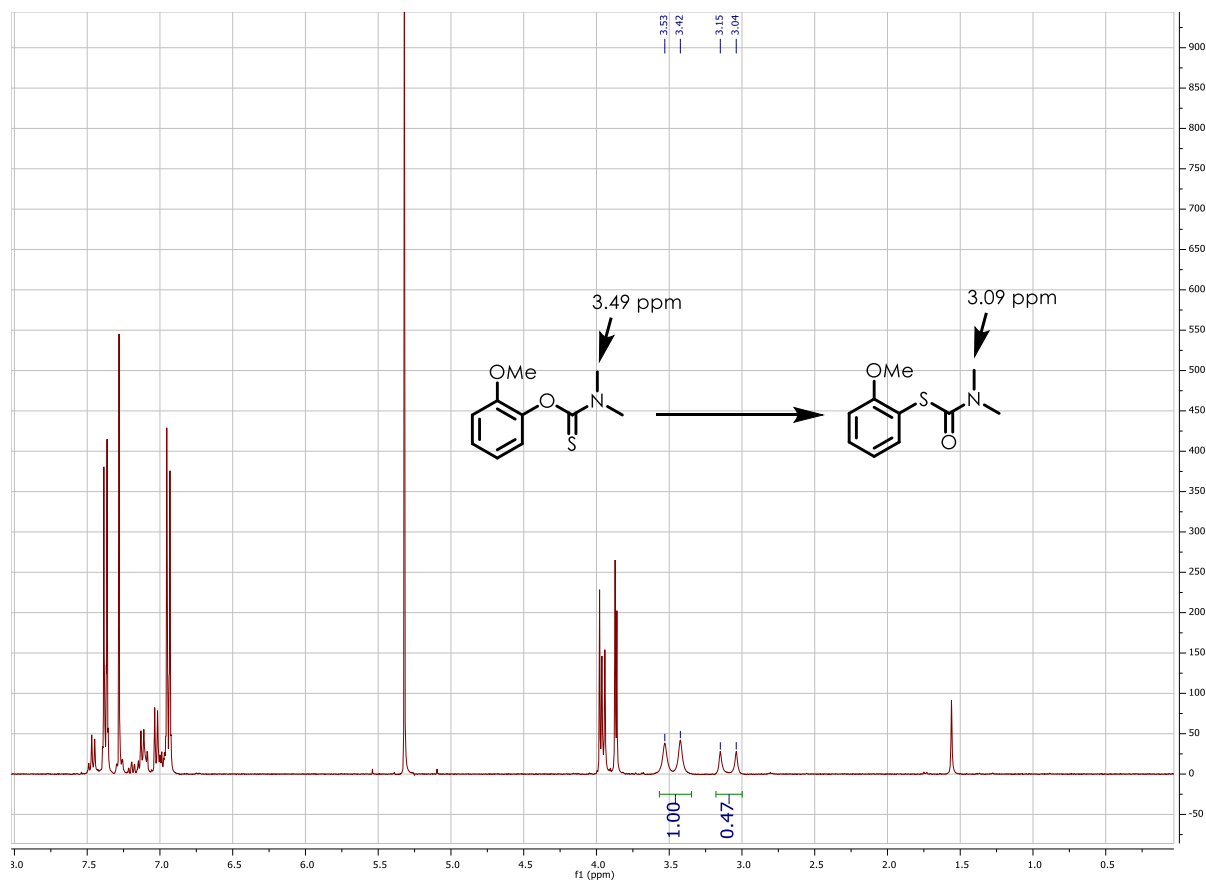
Figure A.1. Hammett Plot of stern-volmer quenching data.

A.7. Aminium Cation-Radical Reactions



General Procedure:

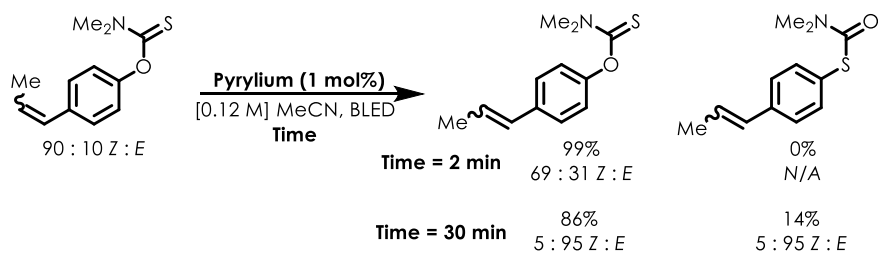
A flame dried 2 dram vial was charged with the carbamothioate, suspended in 2 mL DCM and the vial sealed with a septum-lined screw cap. The deep blue suspension was sparged with N_2 for 5 minutes and then the carbamothioate (dissolved in 2 mL DCM) was added through the septum and the solution allowed to stir overnight, during which time the blue color faded and an orange-red color developed. After stirring, the solution was concentrated and the conversion was determined by crude NMR, comparing the integration of the starting material to the rearranged product.



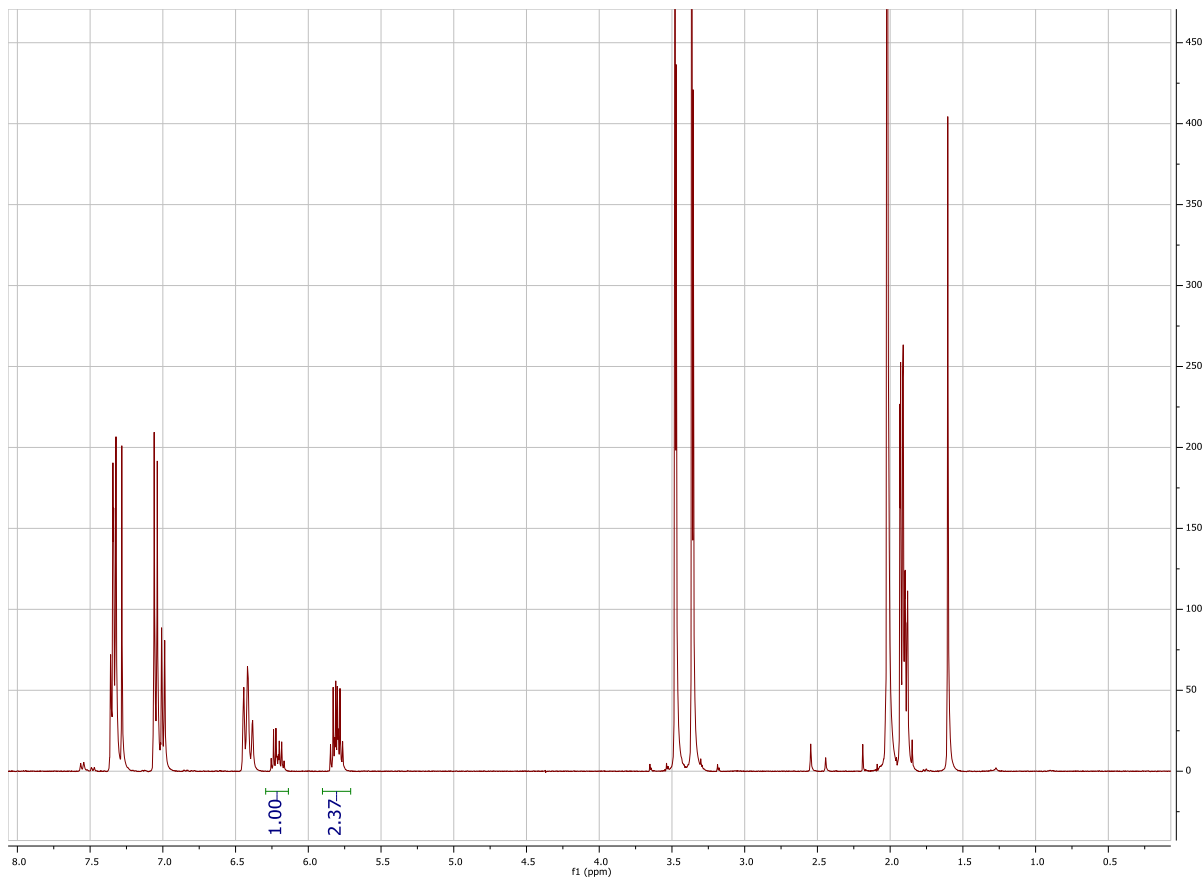
A.8. Olefin Isomerization Studies

General Procedure:

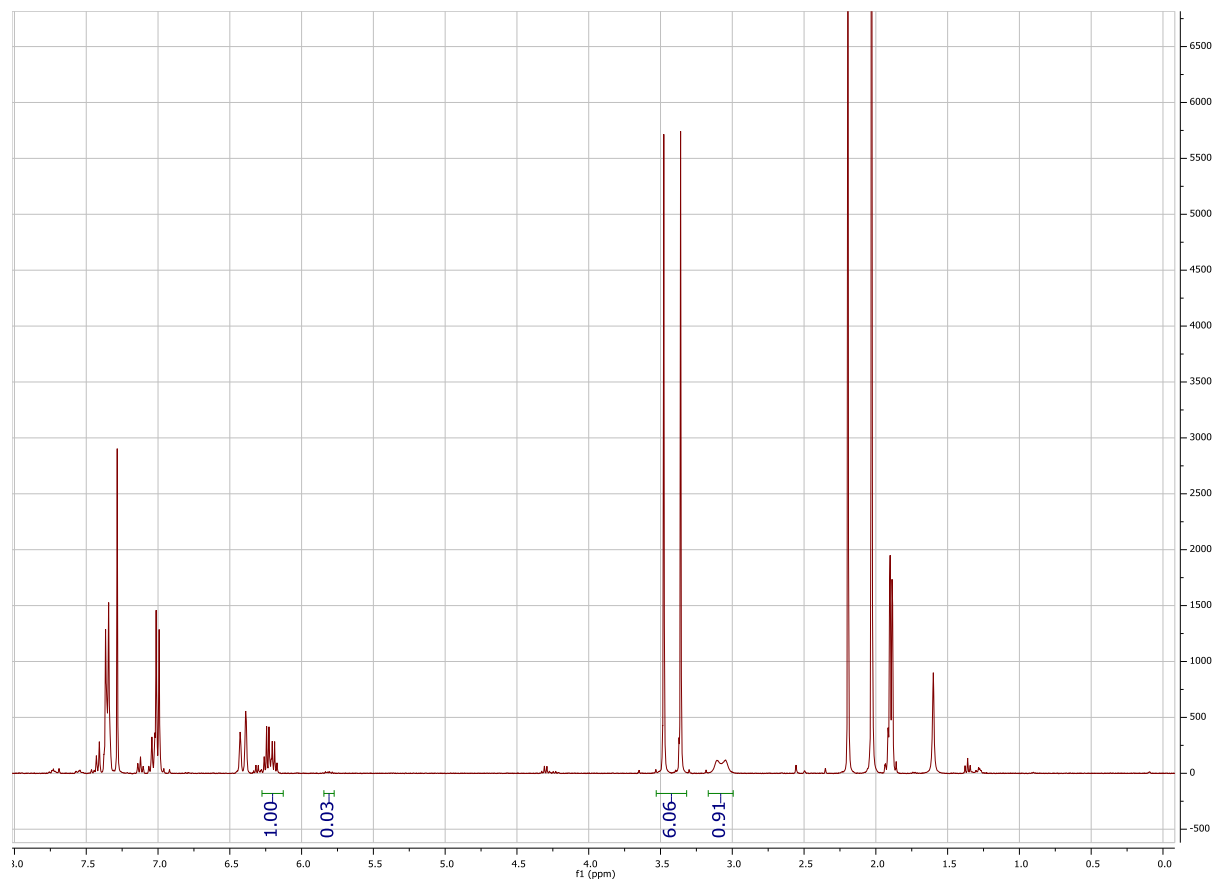
A flame dried 2 dram vial was charged with the substrate(s) (0.5 mmol), **1** (1 mol%) and additive, if applicable, and dissolved in MeCN. The resulting solution was then sparged for 5 minutes and the vial cap sealed with Teflon tape and placed under irradiation for the stated duration. For analysis the samples were then concentrated, after irradiating for the stated time, and then dissolved in CDCl₃ and analyzed by ¹H NMR. Yields were obtained by taking the ratio of the starting material *O*-aryl carbamothioate (more downfield, sharp doublet) and the product *S*-aryl carbamothioate (more upfield, broader doublet). The olefin isomer ratios were obtained by taking the integrated ratio of the β-Proton of the *E*-isomer (more downfield resonance, ~6.2 ppm) and the *Z*-isomer (more upfield resonance, ~5.8 ppm).

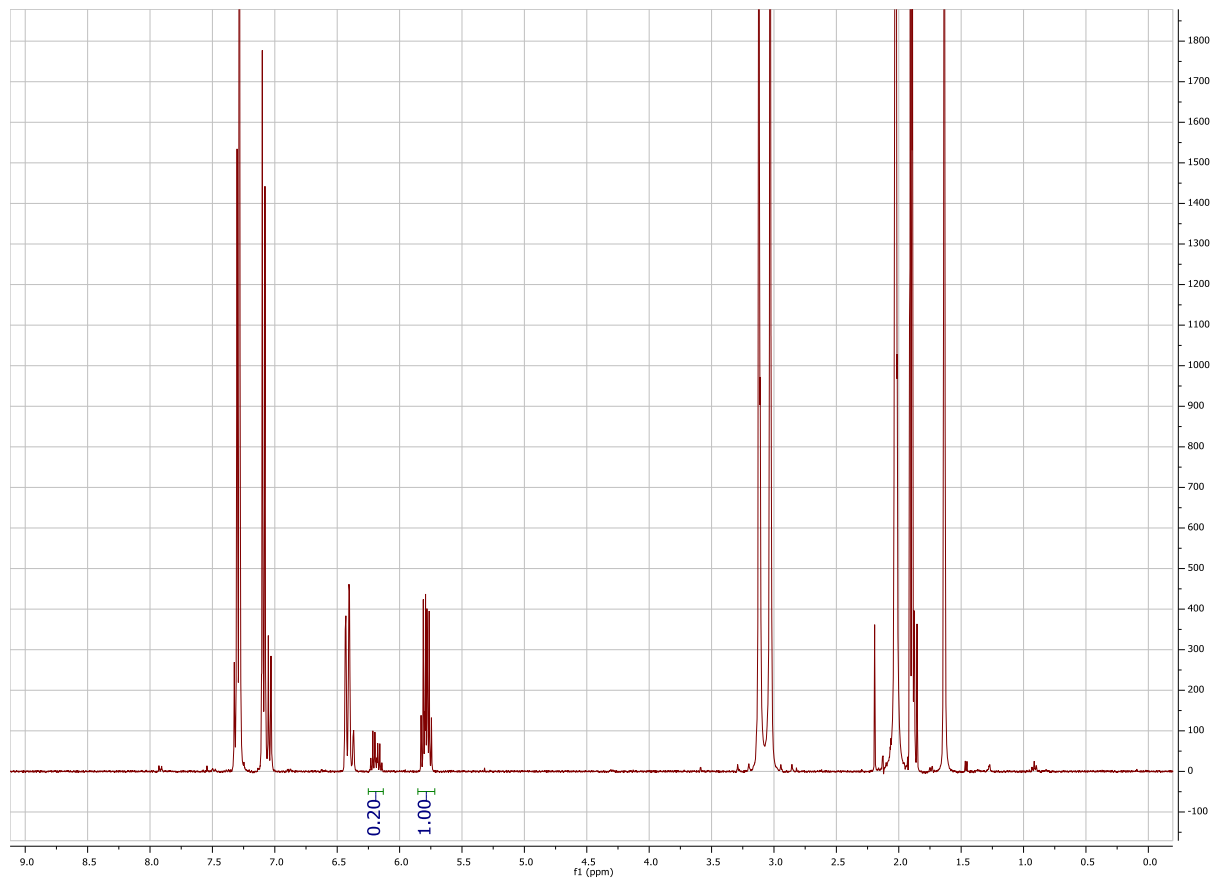
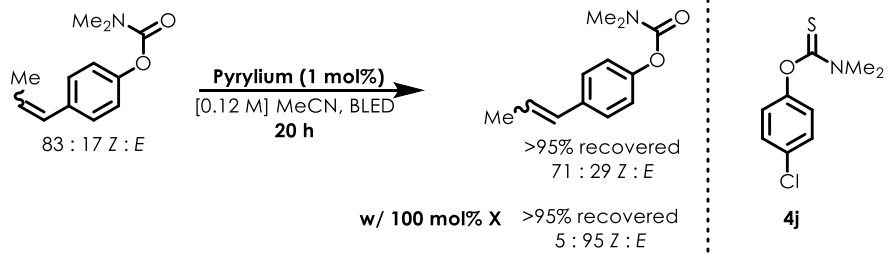


2 minutes:

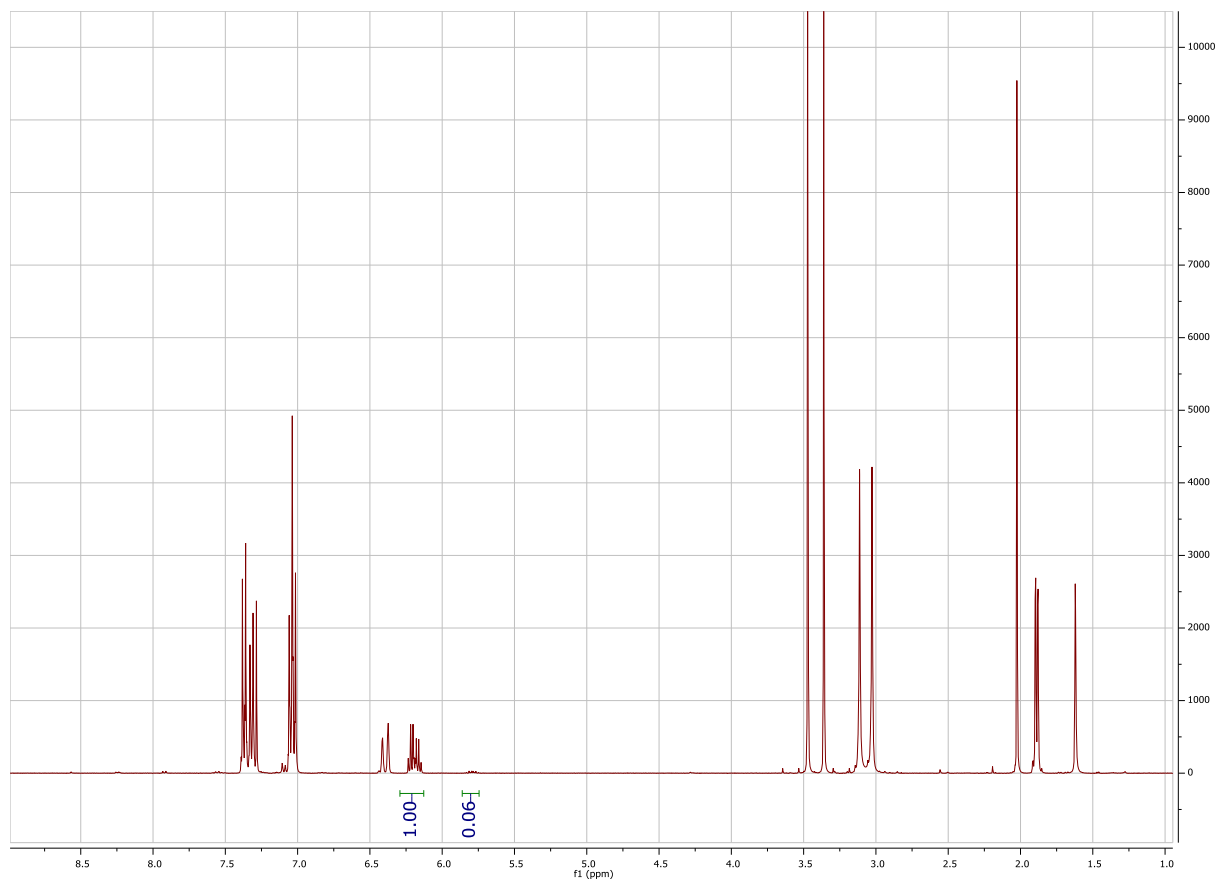


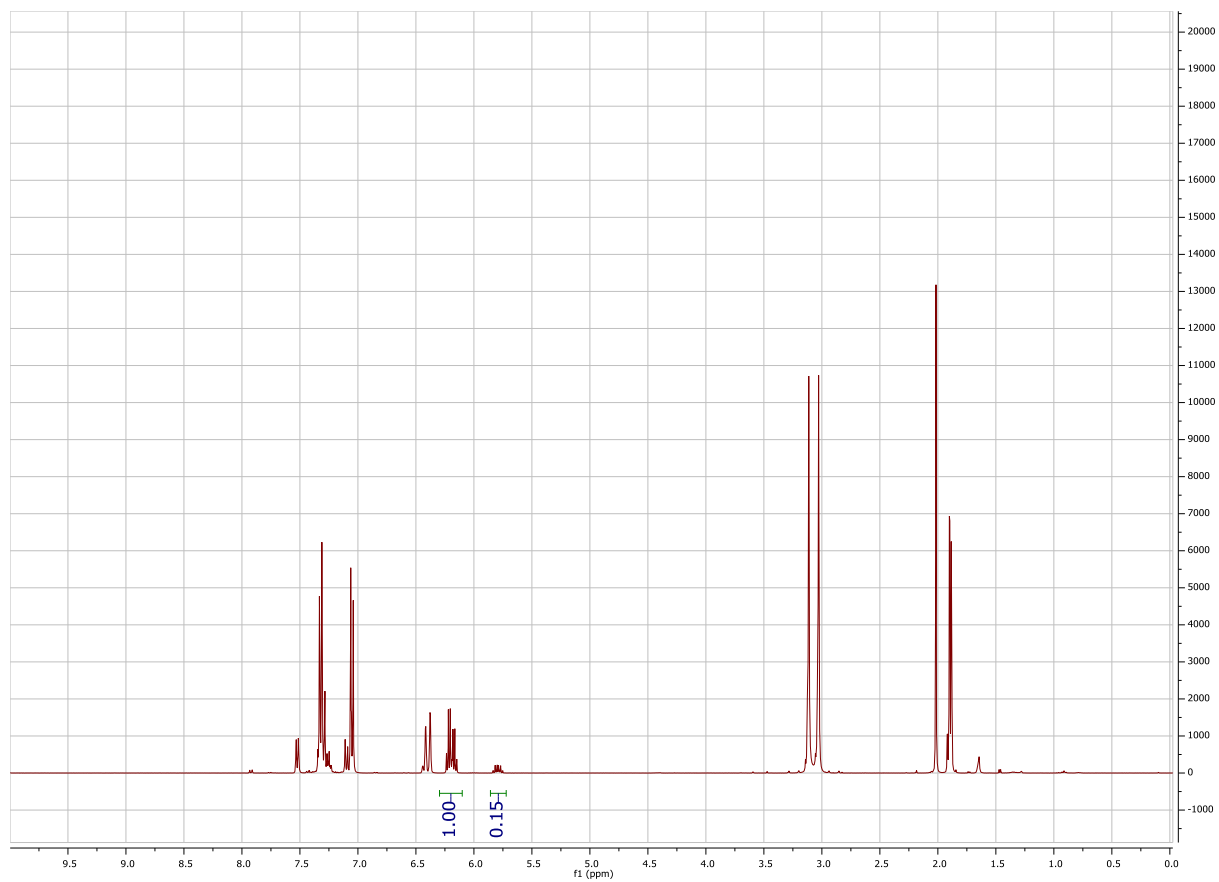
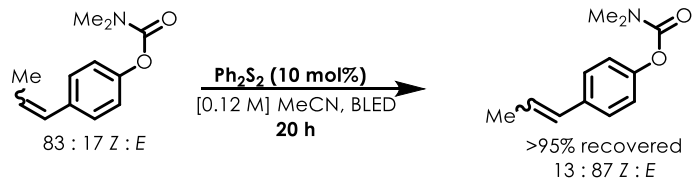
30 minutes

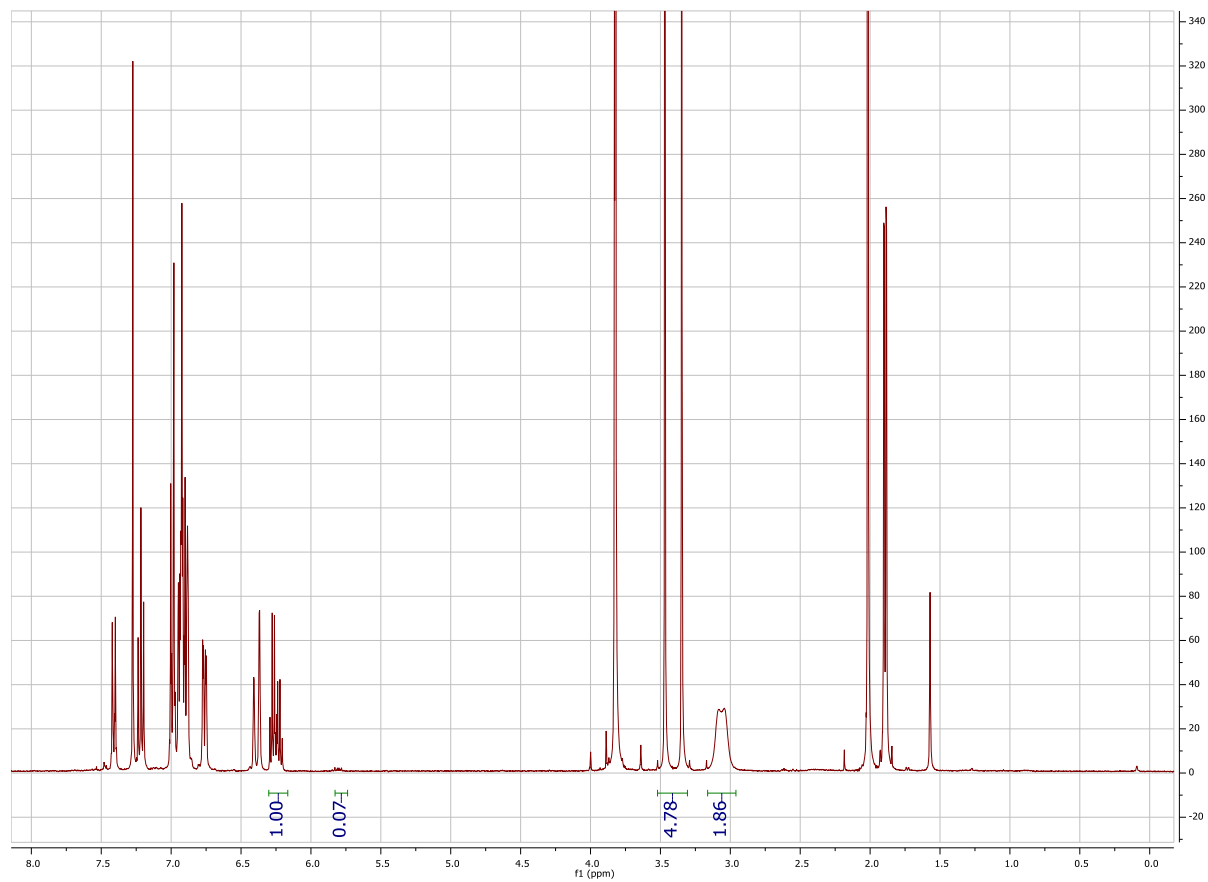
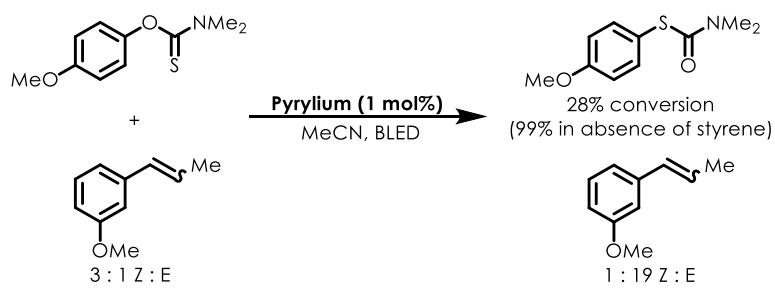




w/ 4j



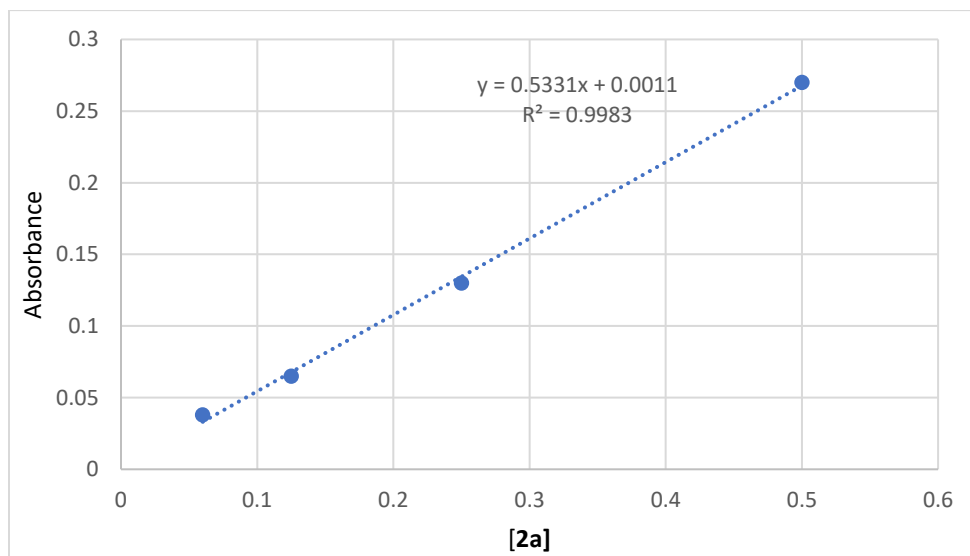


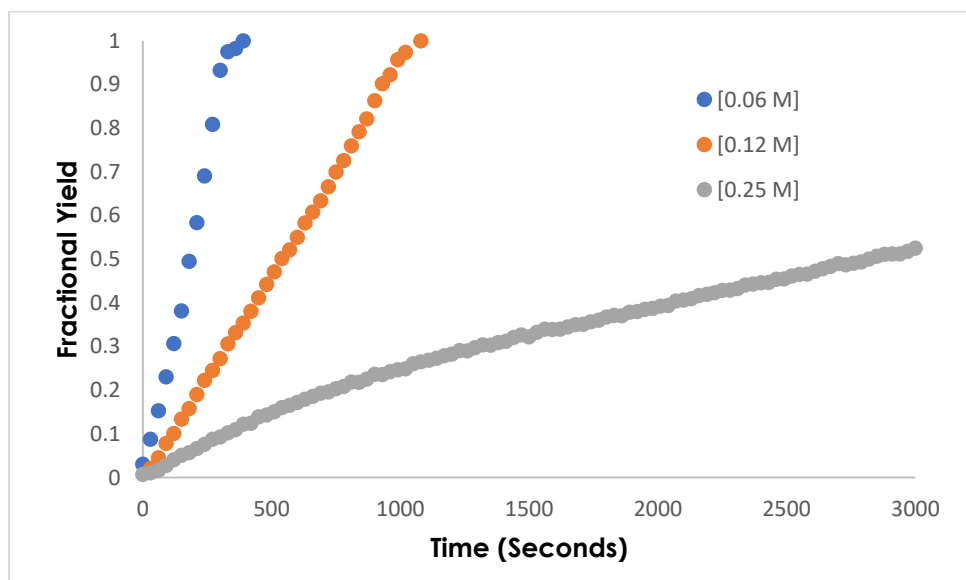
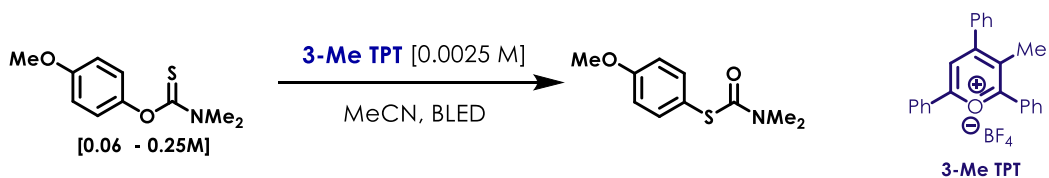
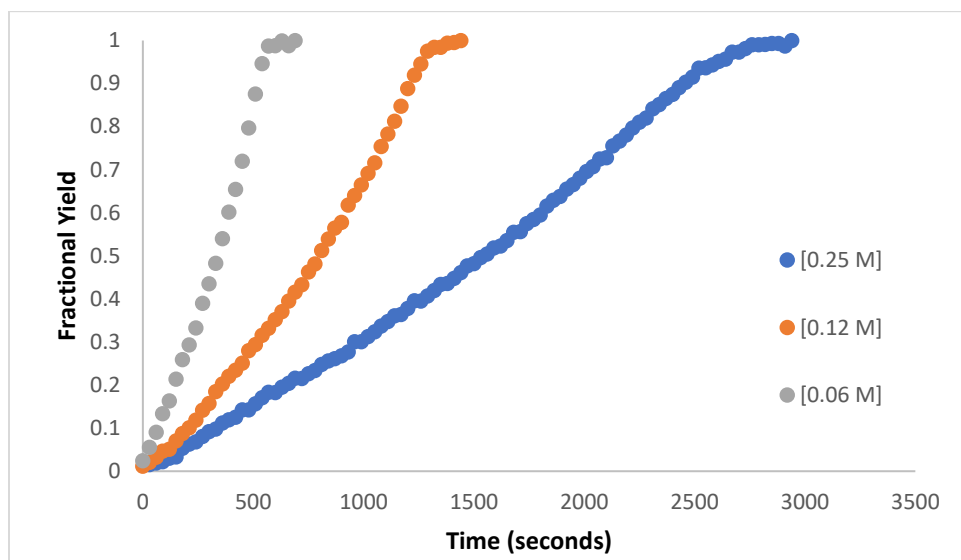
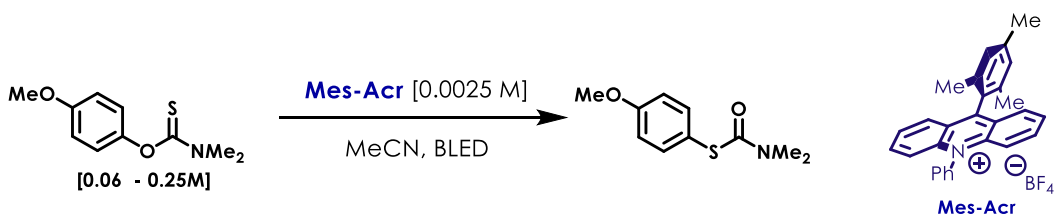


A.9. Reaction Monitoring using *in situ* IR Spectroscopy

In-situ monitoring of the reaction was performed using a Mettler-Toledo ReactIR™ 15 instrument equipped with a 6.3 mm AgX Sicamp Fiber Conduit. Plots were generated from absorbance at 1670 cm^{-1} (corresponding to $\pi_{\text{C-O}}$ stretching frequency of the rearranged product) over the course of the reaction. The reactions were setup in flame dried Schlenk tubes and irradiated with two 15W PAR38 blue LED floodlamps purchased from EagleLight (Carlsbad, CA). The solvent was subtracted from the reaction spectra using the software provided with the instrument.

In order to convert the obtained absorbance values to concentration a “response factor” for the stretch at 1670 cm^{-1} was constructed by taking absorbance readings of known concentrations of the carbamothioates (0.06 – 0.5 M). A linear dependence of absorbance on the concentration was observed and the slope of a linear fit to this data was then used to convert the temporal data obtained during experiments to concentration.





REFERENCES

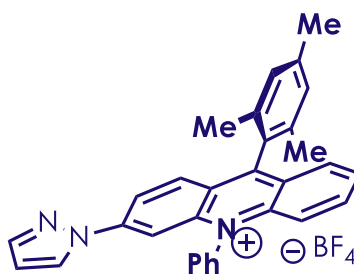
- (1) Martiny, M.; Steckhan, E.; Esch, T. *Chem. Ber.* **1993**, *126*, 1671.
- (2) Zhao, Y.; Xie, Y.; Xia, C.; Huang, H. *Adv. Synth. Catal.* **2014**, *356*, 2471.
- (3) Newman, M. S.; Karnes, H. A. *J. Org. Chem.* **1966**, *31*, 3980.
- (4) Harvey, J. N.; Jover, J.; Lloyd-Jones, G. C.; Moseley, J. D.; Murray, P.; Renny, J. S. *Angew. Chem. Int. Ed.* **2009**, *48*, 7612.
- (5) Moseley, J. D.; Sankey, R. F.; Tang, O. N.; Gilday, J. P. *Tetrahedron* **2006**, *62*, 4685.
- (6) Romagnoli, R.; Baraldi, P. G.; Carrion, M. D.; Cruz-Lopez, O.; Tolomeo, M.; Grimaudo, S.; Cristina, A. D.; Pipitone, M. R.; Balzarini, J.; Brancale, A.; Hamel, E. *Bioorg. Med. Chem.* **2010**, *18*, 5114.
- (7) Chen, P.-Y.; Wu, Y.-H.; Hsu, M.-H.; Wang, T.-P.; Wang, E.-C. *Tetrahedron* **2013**, *69*, 653.
- (8) Rauniyar, V.; Hall, D. G. *J. Org. Chem.* **2009**, *74*, 4236.
- (9) Molander, G.A.; Cavalcanti, L. N.; Garcia-Garcia, C. *J. Org. Chem.* **2013**, *78*, 6427

APPENDIX B: SUPPORTING INFORMATION FOR “MECHANISTIC INVESTIGATIONS OF A PHOTOREDOX-MEDIATED ARENE C-H AMINATION”

B.1 General Information

Methods and Materials: Proton and carbon magnetic resonance spectra (^1H NMR and ^{13}C NMR) were recorded on a Bruker AVANCE III 600 CryoProbe (^1H NMR at 400 MHz, 600 MHz and ^{13}C NMR at 100, 150 MHz) spectrometer with solvent resonance as the internal standard (^1H NMR: CDCl_3 at 7.26 ppm; ^{13}C NMR: CDCl_3 at 77.0 ppm). ^1H NMR data are reported as follows: chemical shift, multiplicity (s = singlet, d = doublet, t = triplet, dd = doublet of doublets, dt = doublet of triplets, td = triplet of doublets, m = multiplet, br = broad singlet, bm = broad multiplet), coupling constants (Hz), and integration. Infrared (IR) spectra were obtained using a Jasco 260 Plus Fourier transform infrared spectrometer. High Resolution Mass Spectra (HRMS) were obtained using a Thermo LTqFT mass spectrometer with electrospray ionization in positive or negative mode. Flash chromatography was performed using SiliaFlash P60 silica gel (40-63 μm) purchased from Silicycle. All solvents were dried by passage over activated alumina columns immediately prior to use unless otherwise noted. Irradiation of photochemical reactions was carried out using three 15W PAR38 blue LED floodlamp purchased from EagleLight (Carlsbad, CA) with an output centered at a wavelength of approximately 450 nm. The reactions were carried out in 2 dram borosilicate glass vials (purchased from Fisher Scientific, catalogue # 03-339-22D) sealed with polypropylene caps equipped with Teflon coated septa (purchased through VWR international, Microliter Product # 15-0060K), or in 16mm x 150mm glass culture tubes sealed with rubber septa if reaction volume was greater than 7 mL. All reagents were purchased from Sigma-Aldrich corporation or Fisher Scientific corporation and were used without additional purification unless otherwise noted.

B.2. Synthesis and Characterization of Catalysts and Substrates



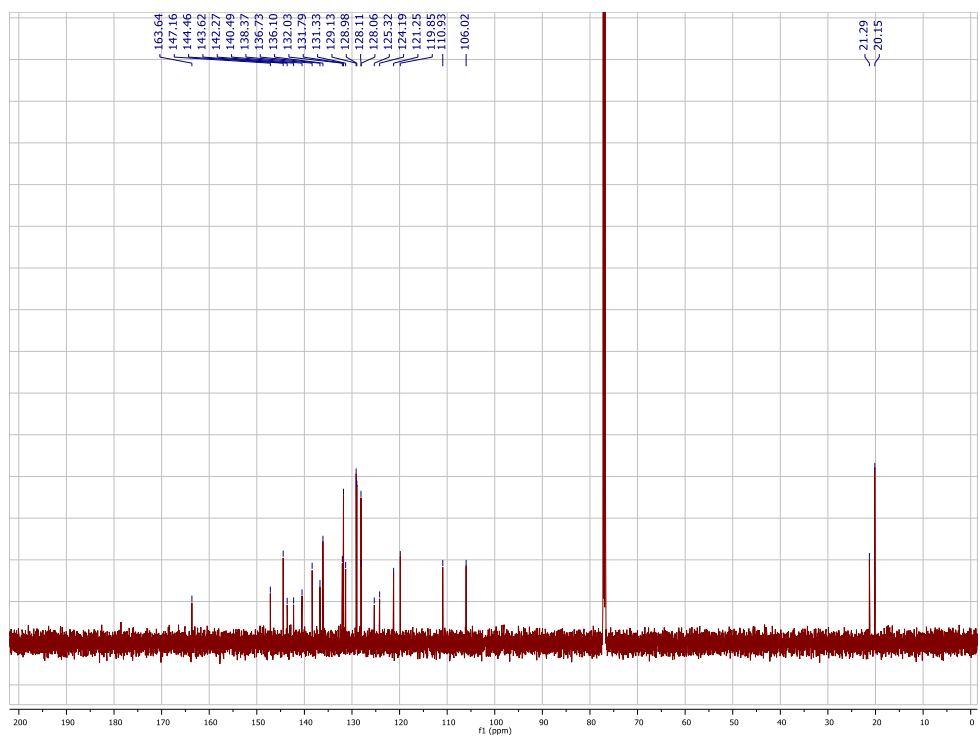
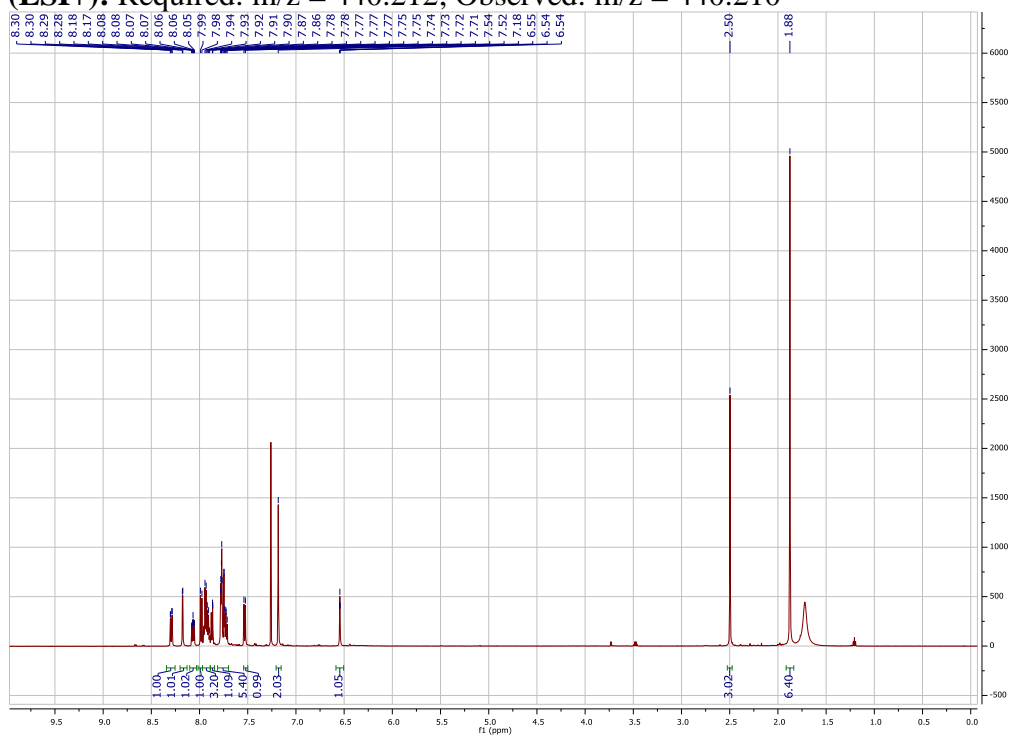
3-Pyrazoyl-Mes-NPA

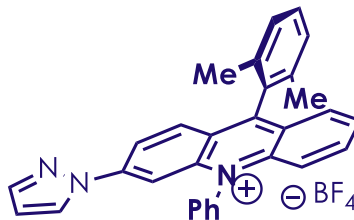
9-mesityl-10-phenyl-3-(1H-pyrazol-1-yl)acridin-10-ium tetrafluoroborate: Synthesized following a similar synthetic procedure for acridiniums from our lab.¹

^1H NMR (600 MHz, CDCl_3) δ 8.29 (dd, $J = 9.4, 1.9$ Hz, 1H), 8.18 (d, $J = 2.7$ Hz, 1H), 8.07 (ddd, $J = 8.7, 6.7, 1.4$ Hz, 1H), 7.98 (d, $J = 9.3$ Hz, 1H), 7.93 (dd, $J = 13.9, 7.2$ Hz, 3H), 7.86 (d, $J = 1.4$ Hz, 1H), 7.81 – 7.69 (m, 5H), 7.53 (d, $J = 9.0$ Hz, 1H), 7.18 (s, 2H), 6.54 (t, $J = 2.1$ Hz, 1H), 2.50 (s, 3H), 1.88 (s, 6H)

^{13}C NMR (150 MHz, CDCl_3): 163.6, 147.1, 144.4, 143.6, 142.2, 140.4, 138.3, 136.7, 136.1, 132.0, 131.7, 131.3, 129.1, 128.9, 128.1, 128.0, 125.3, 124.1, 121.2, 119.8, 110.9, 106.0, 21.2, 20.1

HRMS (ESI+): Required: $m/z = 440.212$; Observed: $m/z = 440.210$





3-Pyrazoyl-Xyl-NPA

9-(2,6-dimethylphenyl)-10-phenyl-3-(1H-pyrazol-1-yl)acridin-10-ium tetrafluoroborate:

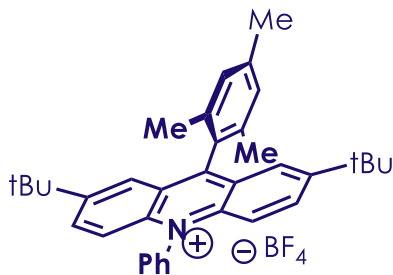
Synthesized following a similar synthetic procedure for acridiniums from our lab.¹

¹H NMR (600 MHz, Chloroform-*d*) δ 8.29 (dd, $J = 9.4, 2.0$ Hz, 1H), 8.16 (d, $J = 2.7$ Hz, 1H), 8.07 (ddd, $J = 9.1, 6.7, 1.5$ Hz, 1H), 7.98 – 7.88 (m, 4H), 7.84 (dd, $J = 8.6, 1.4$ Hz, 1H), 7.81 – 7.77 (m, 3H), 7.75 (d, $J = 1.7$ Hz, 1H), 7.74 – 7.70 (m, 1H), 7.59 – 7.48 (m, 2H), 7.37 (d, $J = 7.7$ Hz, 2H), 6.54 (dd, $J = 2.7, 1.6$ Hz, 1H), 1.92 (s, 6H)

¹³C NMR (150 MHz, CDCl₃): δ 162.9, 147.1, 144.4, 143.7, 142.3, 138.3, 136.7, 136.3, 132.0, 131.9, 131.7, 131.1, 128.8, 128.8, 128.3, 128.1, 128.1, 125.0, 123.9, 121.3, 119.9, 110.9, 106.0, 20.2

HRMS (ESI+): Required: $m/z = 426.195$; Observed: $m/z = 426.197$

$E_{1/2}^* = E_{1/2} + E_{0,0} = -0.430$ V vs. SCE + 2.57 eV = 2.14 V vs. SCE



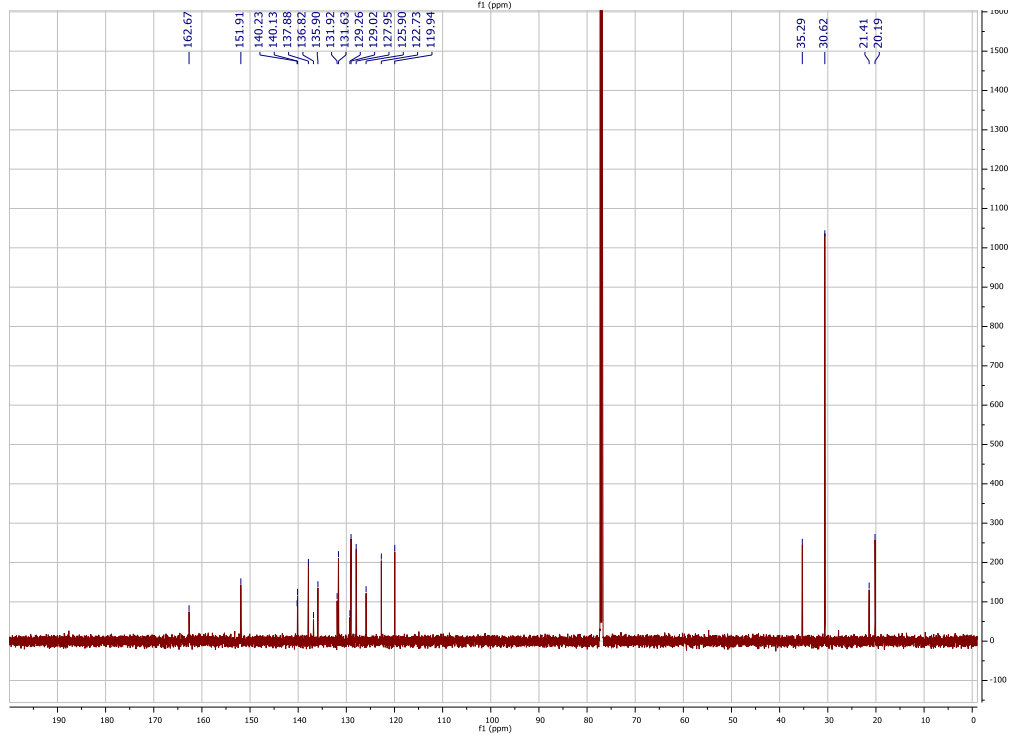
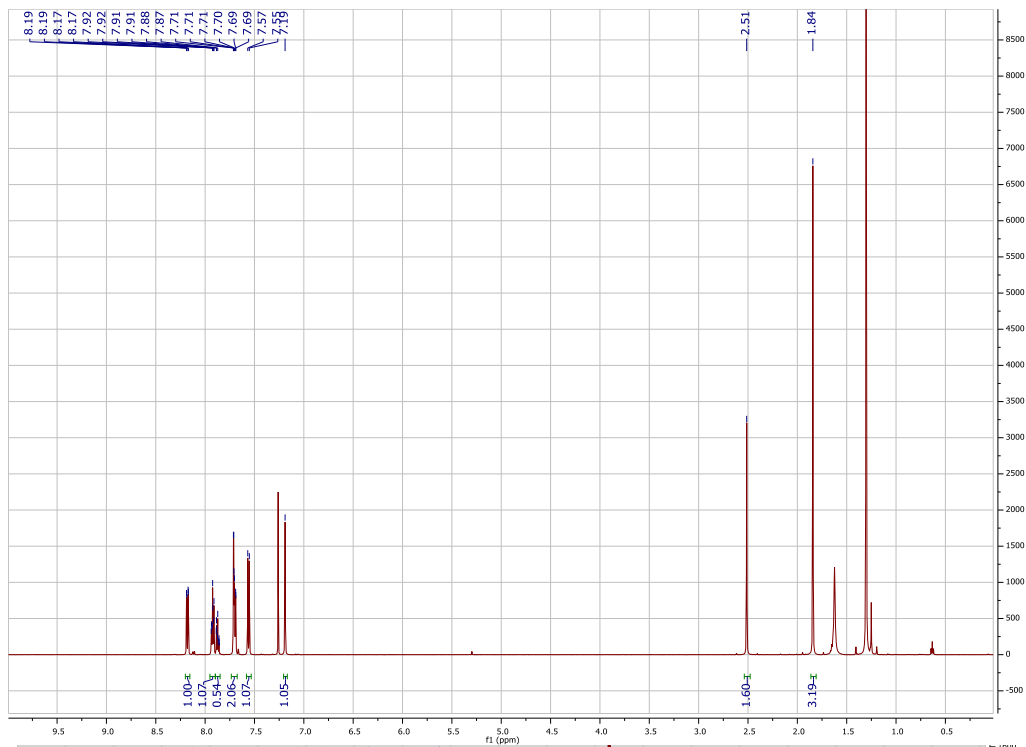
2,7-*t*Bu-Mes-NPA

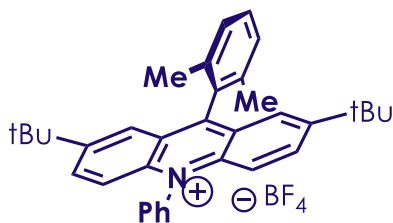
2,7-di-tert-butyl-9-mesityl-10-phenylacridin-10-ium tetrafluoroborate: Synthesized following a similar synthetic procedure for acridiniums from our lab.¹

¹H NMR (600 MHz, Chloroform-*d*) δ 8.18 (dd, $J = 9.5, 2.2$ Hz, 1H), 7.92 (td, $J = 7.5, 6.6, 1.4$ Hz, 1H), 7.89 – 7.84 (m, 1H), 7.71 (d, $J = 2.1$ Hz, 1H), 7.71 – 7.68 (m, 1H), 7.56 (d, $J = 9.5$ Hz, 1H), 7.19 (s, 1H), 2.51 (s, 1H), 1.84 (s, 3H)

¹³C NMR (150 MHz, CDCl₃): δ 162.6, 151.9, 140.2, 140.1, 137.8, 136.8, 135.9, 131.9, 131.6, 129.2, 129.0, 127.9, 125.9, 122.7, 119.9, 35.2, 30.6, 21.4, 20.1

$E^*_{1/2} = E_{1/2} + E_{0,0} = -0.55$ V vs. SCE + 2.65 eV = 2.10 V vs. SCE



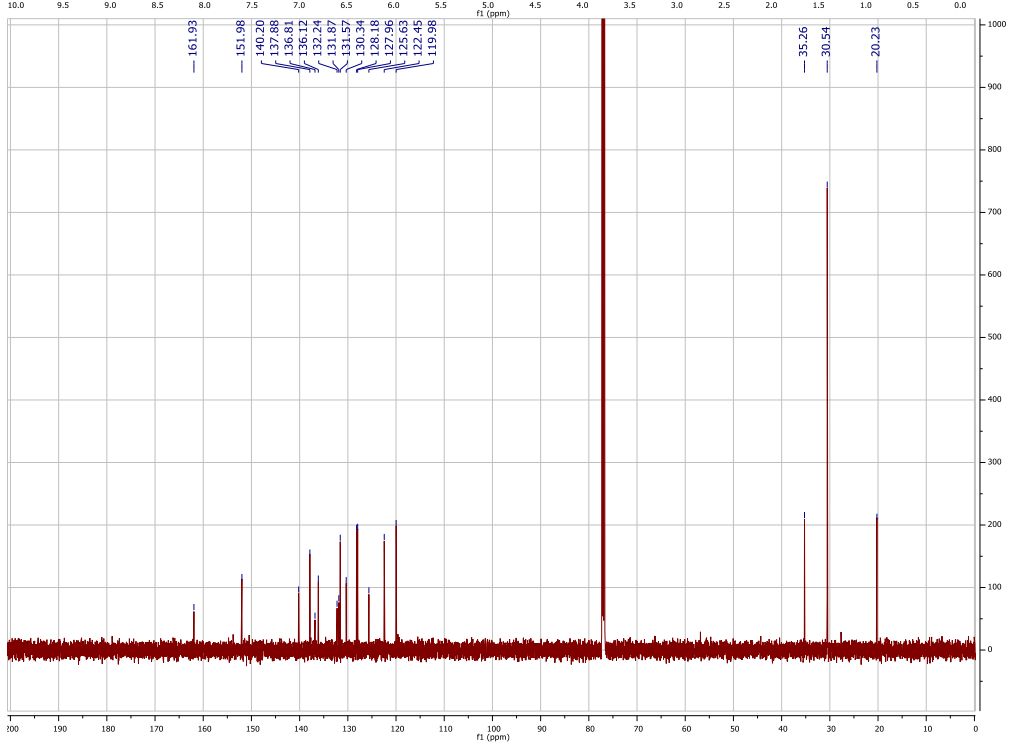
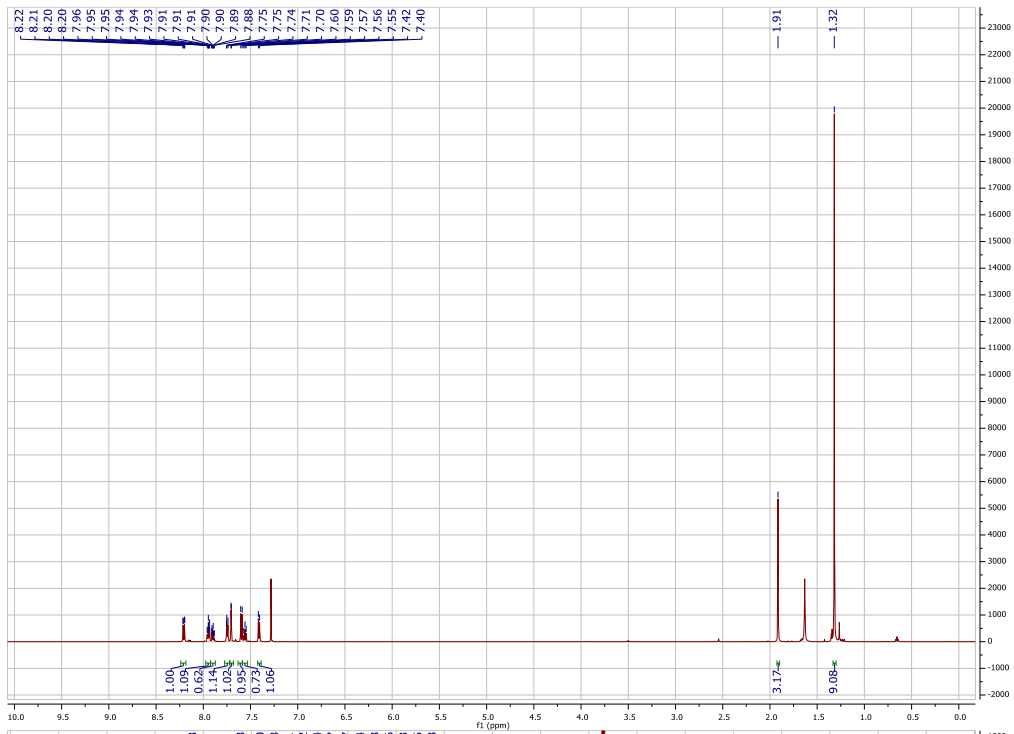


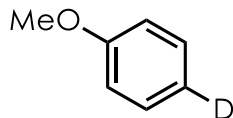
2,7-*t*Bu-Xyl-NPA

2,7-di-tert-butyl-9-mesityl-10-phenylacridin-10-ium tetrafluoroborate: Synthesized following a similar synthetic procedure for acridiniums from our lab.¹

¹H NMR (400 MHz, Chloroform-*d*) δ 8.20 (dd, $J = 9.5, 2.2$ Hz, 1H), 7.93 (dt, $J = 13.9, 7.0$ Hz, 2H), 7.79 – 7.73 (m, 1H), 7.71 (d, $J = 2.1$ Hz, 1H), 7.57 (dd, $J = 20.1, 8.5$ Hz, 2H), 7.41 (d, $J = 7.7$ Hz, 1H), 1.92 (s, 3H).

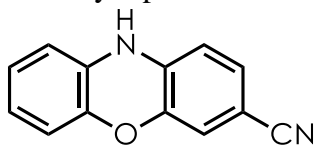
¹³C NMR (150 MHz, CDCl₃): δ 161.9, 151.9, 140.2, 137.8, 136.8, 136.1, 132.2, 131.8, 131.5, 130.3, 128.1, 127.9, 125.6, 122.4, 119.9, 35.2, 30.54, 20.2





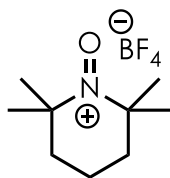
4-d-Anisole

anisole-4-d: Synthesized following a literature procedure from 4-Br-Anisole. Spectroscopic data were in agreement with what was previously reported.



3-CNPhenox

10H-phenoxazine-3-carbonitrile: Synthesized following a literature procedure.² Spectroscopic data were in agreement with what was previously reported.

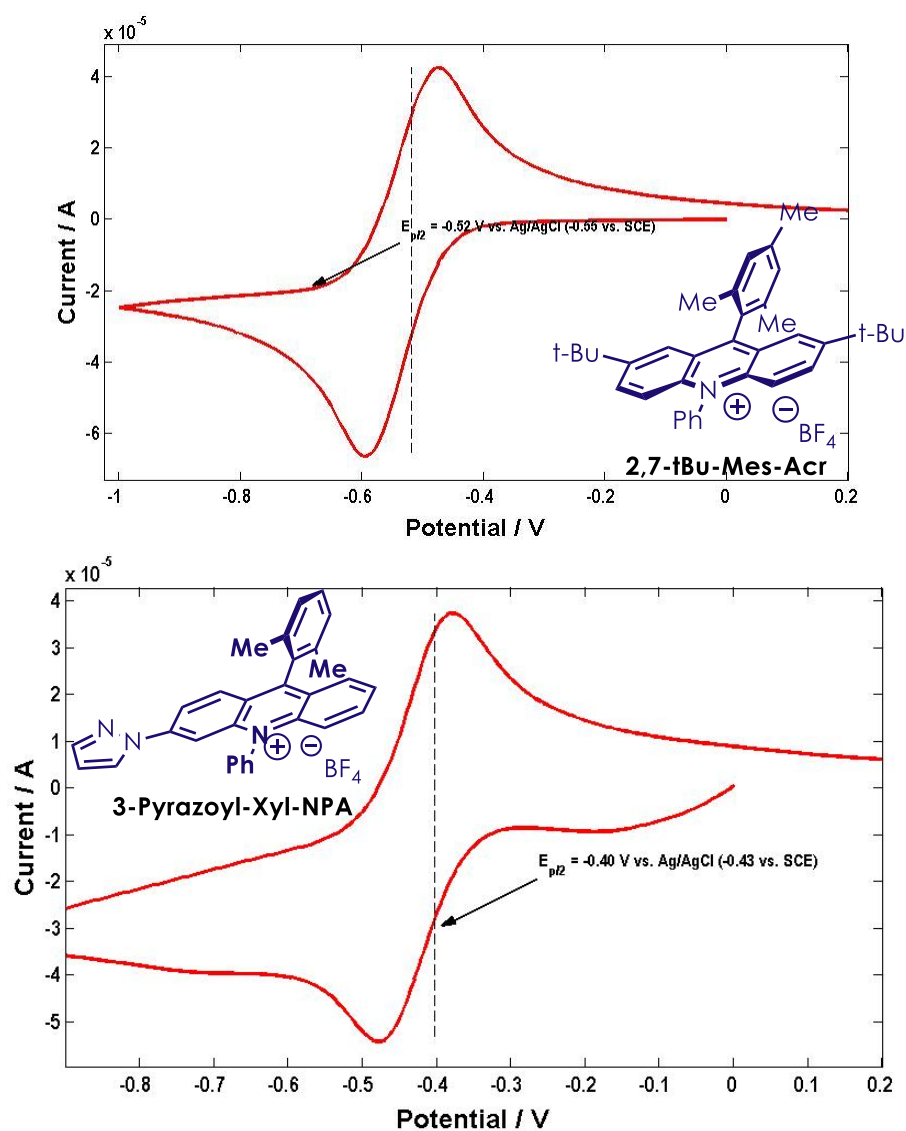


TEMPOoniumBF₄

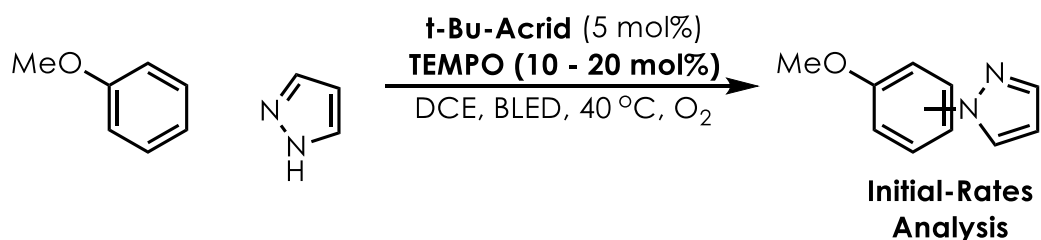
2,2,6,6-tetramethyl-1-oxopiperidin-1-ium: Synthesized following a literature procedure.³ Spectroscopic data were in agreement with what was previously reported.

B.3 Measurement of Redox Potentials via Cyclic Voltammetry

Electrochemical potentials were obtained by collecting cyclic voltammograms with a Pine WaveNow Potentiostat. Samples were prepared with 0.05 mmol of substrate in 5 mL of 0.1 M tetra-*n*-butylammonium hexafluorophosphate in dry, degassed acetonitrile. Measurements employed a glassy carbon working electrode, platinum wire counter electrode, 3.5 M NaCl silver-silver chloride reference electrode, and a scan rate of 100 mV/s. Reductions were measured by scanning potentials in the negative direction and oxidations in the positive direction; the glassy carbon electrode was polished between each scan. Data was analyzed using MATLAB by subtracting a background current prior to identifying the maximum current (C_p) and determining the potential ($E_{p/2}$) at half this value ($C_{p/2}$). The obtained value was referenced to Ag/AgCl and converted to SCE by subtracting 0.03 V.



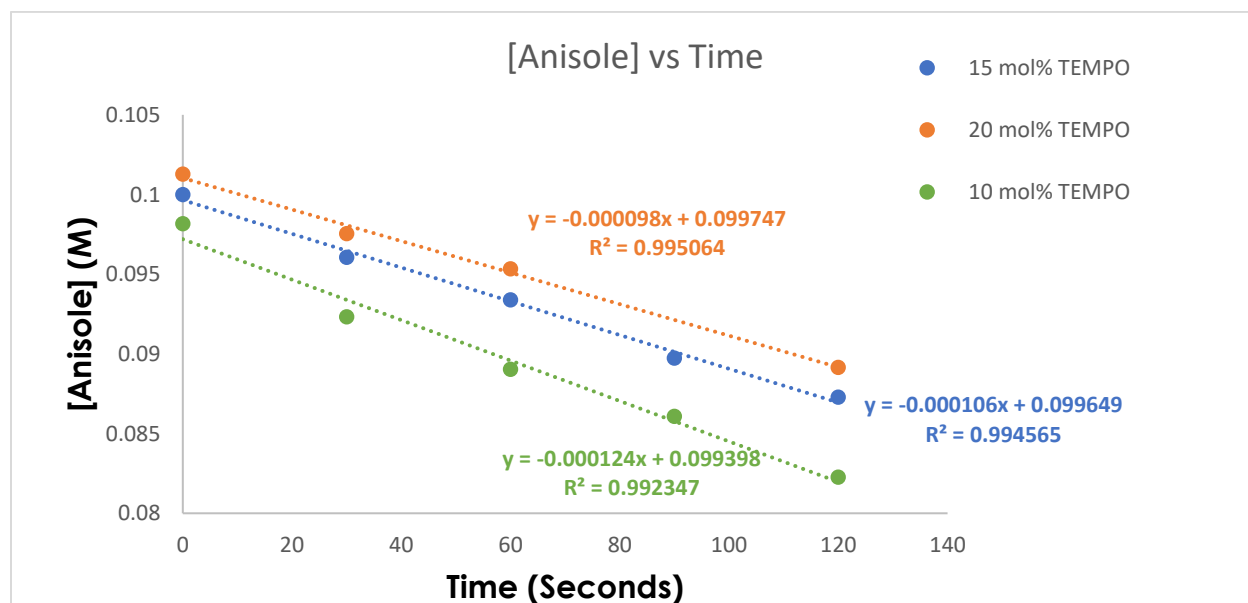
B.4. Initial-Rates Kinetic Analyses



General Procedure:

Stock solutions in DCE of the following concentrations were prepared: Anisole (1.0 molar), Pyrazole (1.0 molar), TEMPO (1.0 molar), 1,3-dichlorobenzene (internal standard, 1.0 molar). For each experiment, the solutions were prepared in a 2 dram vial (using 100 – 500 μ L microliter syringes to ensure accuracy and reproducibility) on a 0.30 mmol scale respective to Anisole and sealed with a septum screw-cap. The reagents were added from stock solutions such that the total volume was 3.0 mL DCE and the concentrations of reagents were as follows: Anisole [0.1 M], Pyrazole [0.2 M], TEMPO [0.01 – 0.02 M] and internal standard [0.1 M]. The catalyst was added as a solid (9.0 mg, 0.015 mmol). The solution was then sparged for 5 minutes with an O₂ balloon and afterwards left under 1 atm O₂ (balloon).

The irradiation setup was allowed to equilibrate to 40 °C for 5 minutes prior to the insertion of the samples and 50 μ L aliquots were removed at the given timepoints. The aliquots were diluted ~50x with diethyl ether and then analyzed via GC-MS. The anisole concentrations were determined based on the relative integrations of the anisole and the internal standard.



20 mol% TEMPO:

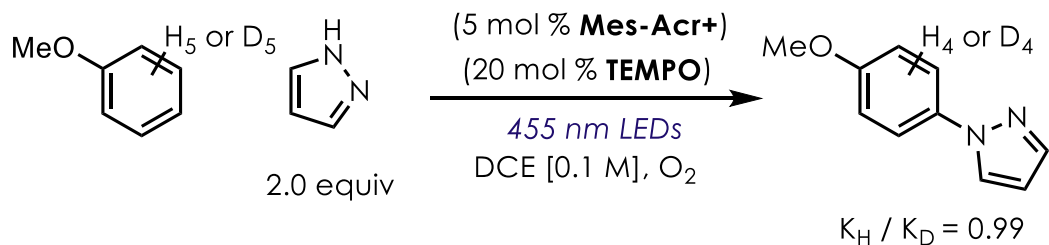
Time (Seconds)	[Anisole] (M)
0	0.101
30	0.098
60	0.095
120	0.089

15 mol% TEMPO:

Time (Seconds)	[Anisole] (M)
0	0.099
30	0.096
60	0.093
90	0.090
120	0.087

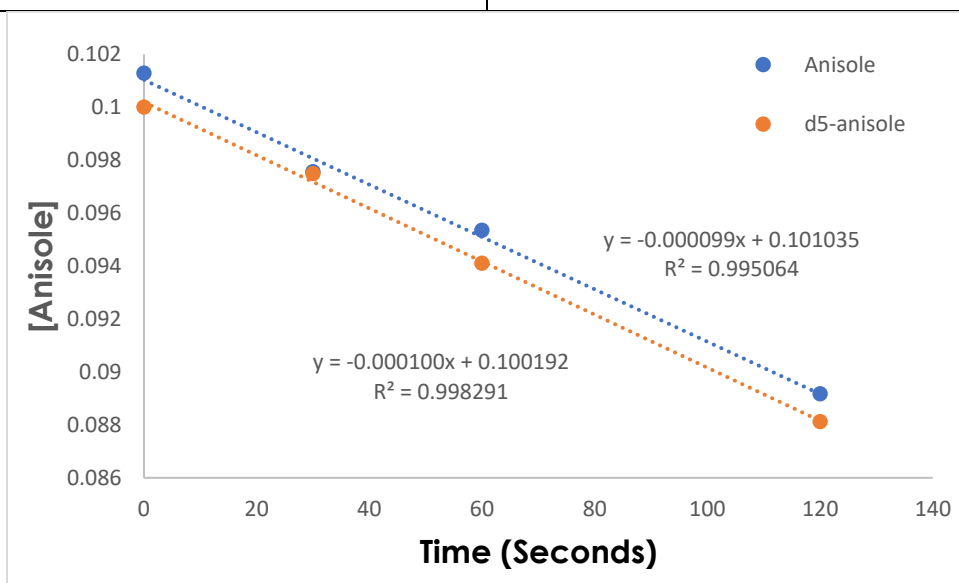
10 mol% TEMPO:

Time (Seconds)	[Anisole] (M)
0	0.098
30	0.092
60	0.089
90	0.086
120	0.082



w/ d₅-Anisole:

Time (Seconds)	[Anisole] (M)
0	0.100
30	0.097
60	0.094
120	0.082



$$k_H / k_D = 0.000099 / 0.000100 = 0.99$$

B.5. Photophysical measurements

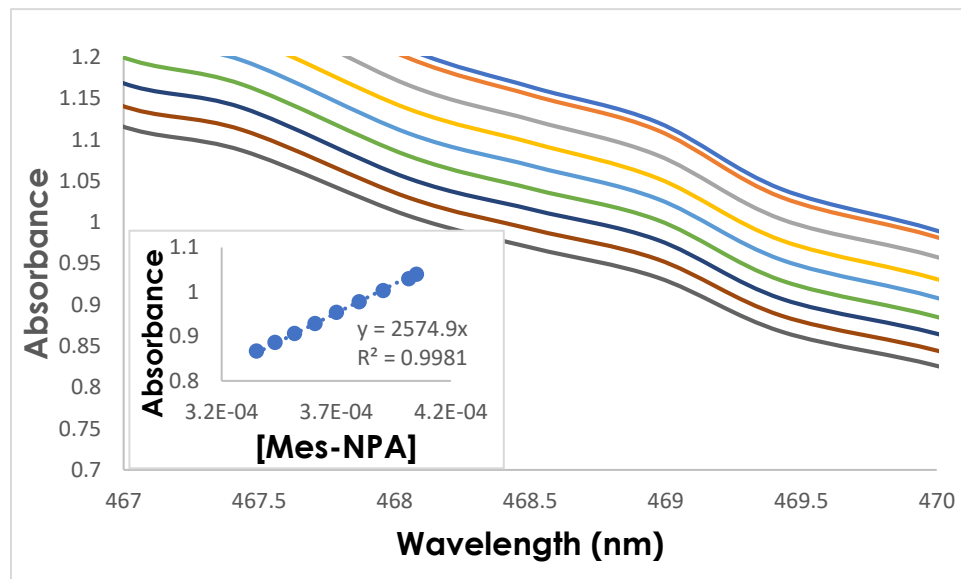
UV-Vis spectra were recorded on a Cary 50 Bio UV-Vis Spectrophotometer. Time-resolved and steady state emission spectra were recorded using an Edinburgh FLS920 spectrometer. Unless otherwise specified, measurements were taken under ambient conditions. For collection of steady state fluorescence spectra, the excitation wavelength was set to 420 nm, and a 435 nm low pass optical filter was used to remove extraneous wavelengths from the excitation light. All spectra (1 nm step size, 5 nm bandwidth) are fully corrected for the spectral response of the instrument. Time resolved emission measurements (including Stern-Volmer quenching studies) were made by the time-correlate single photon counting (TCSPC) capability of the same instrument (FLS920) with pulsed excitation light (444.2 nm, typical pulse width = 95 ps) generated by a Edinburgh EPL-445 ps pulsed laser diode operating at a repetition rate of 2-20 MHz. The maximum emission channel count rate was less than 5% of the laser count channel rate, and each data set collected 5000 counts on the maximum channel.

The fluorescence lifetime was determined by reconvolution fit to the instrument response function using the Edinburgh FS900 software. In all cases, after reconvolution, fluorescence was found to satisfactorily fit a monoexponential function of the form:

$$I_t = I_0 e^{-t/\tau}$$

B.6. Ground-state Pyrazole – Acridinium Complex Investigation:

A 405 μM solution of **Mes-NPA** (3.5 mL) was charged in a 4 mL (nominal volume) cuvette and a UV-Vis spectrum obtained. To the cuvette was added varying amounts of a 1.0 M pyrazole solution and a spectrum was obtained after each addition (with shaking to mix the solution). The concentration of this solution was such that monitoring the absorbance maximum (~ 425 nm) was not accurate due to the high absorbance at this value (>2.5 M). The concentration was monitored at 469.4 nm as the absorbance observed in this concentration range is within the linear response regime of the instrument (~ 1.0 Abs). The linear decrease in concentration upon addition of pyrazole solution is in line with what would be observed for dilution ($\epsilon_{469.4} = 2567 \text{ M}^{-1} \text{ cm}^{-1}$). If a complex was forming between pyrazole and **Mes-NPA** it would be expected that this equilibrium would remove more **Mes-NPA** from solution, lowering the effective concentration and resulting in downward curvature of the plot.



B.7. Stern-Volmer Quenching Experiments

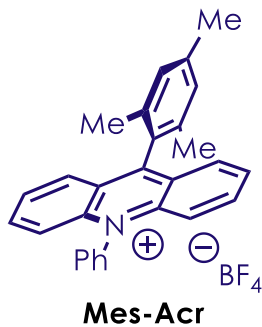
Stern-Volmer experiments were conducted with detection at 515 nm. A solution of the appropriate **acridinium** (16.0 μM) was prepared and 2.4 - 2.5 mL was added to 4 mL (nominal volume) quartz cuvette and sealed with a septum screw cap. The lifetime in the absence of quencher was noted. Generally, a 0.5 M solution of the quencher was prepared and then added to the solution of **acridinium** in 10 μL increments (in all cases up to at least 50 μL of quencher solution was added to achieve a final [Quencher] of ~ 10 mM).

Stern-Volmer analysis was conducted according to the following relationship:

Equation A.1

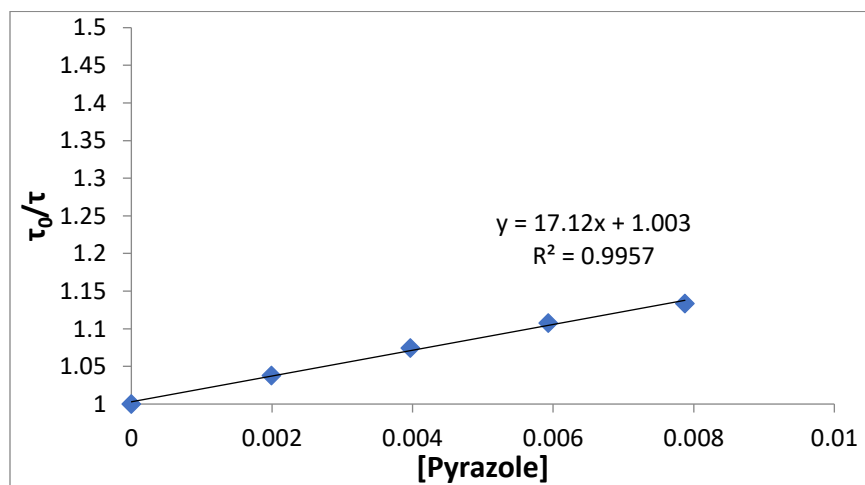
$$\frac{\tau_0}{\tau} = 1 + K_{SV} = 1 + k_q\tau_0[\textit{Quencher}]$$

where τ_0 and τ are the fluorescence lifetime in the absence and presence of quencher Q , K_{SV} is the Stern-Volmer constant, k_q is the bimolecular quenching constant, and [Quencher] is the concentration of quencher.



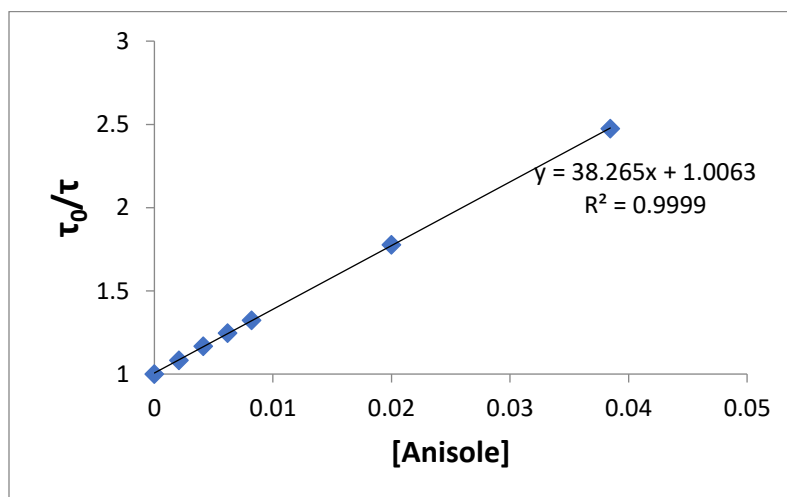
[Pyrazole] (mM)	τ (ns)
0	5.77
1.99	5.56
3.96	5.37
5.92	5.21
7.87	5.09

$K_{SV} = 17.1 \text{ M}^{-1}$; $k_q = 2.97 \times 10^9 \text{ M}^{-1} \text{ s}^{-1}$



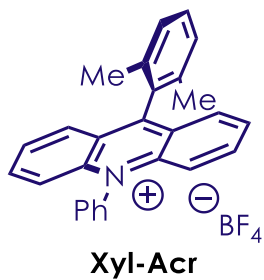
[Anisole] (mM)	τ (ns)
0	5.74
2.08	5.30
4.13	4.92
6.17	4.61
8.20	4.34
20.0	3.23

$K_{SV} = 38.2 \text{ M}^{-1}$; $k_q = 6.65 \times 10^9 \text{ M}^{-1} \text{ s}^{-1}$



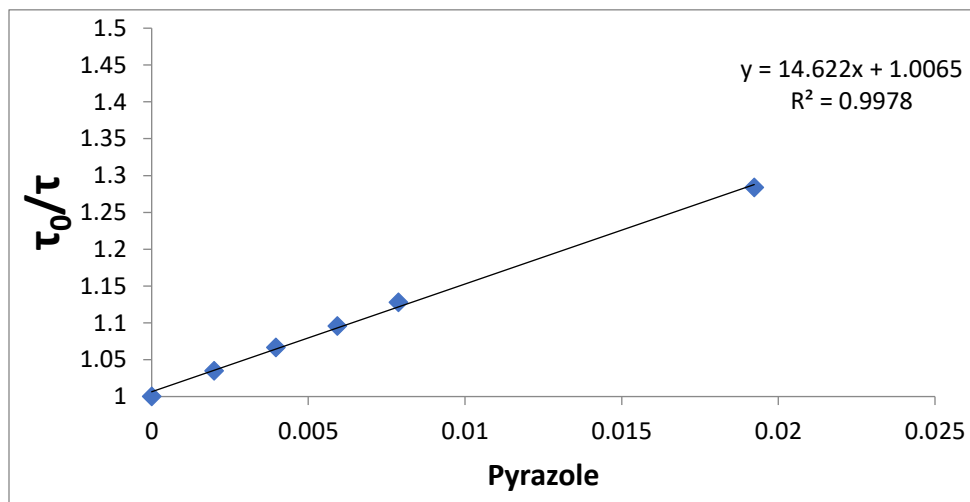
[m-Xylene] (mM)	τ (ns)
0	5.83
1.99	5.80
3.96	5.80
5.92	5.81
7.87	5.79

$K_{SV} = \text{N/A}$; $k_q = \text{N/A}$



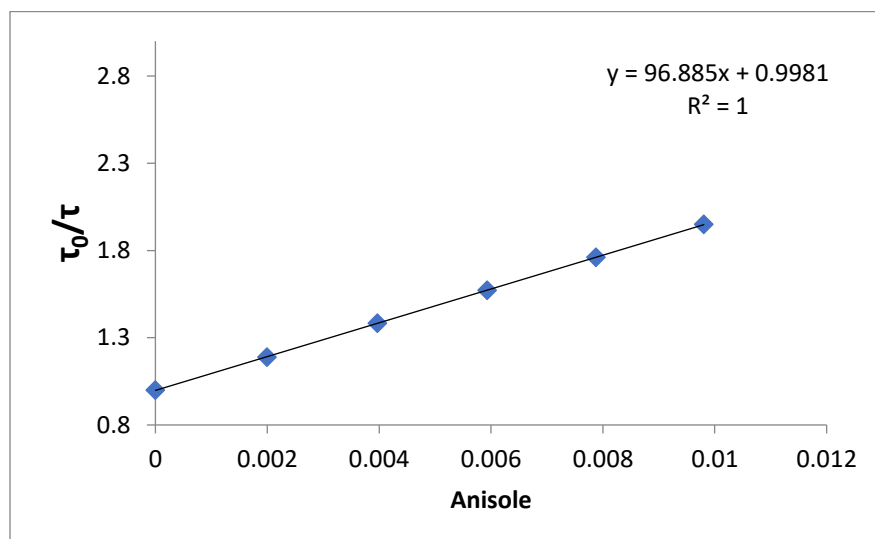
[Pyrazole] (mM)	τ (ns)
0	10.40
2.00	10.05
3.97	9.75
5.92	9.49
7.87	9.22
19.2	8.10

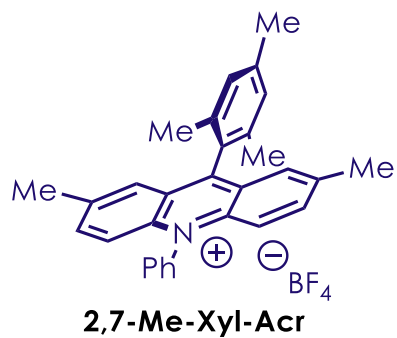
$K_{SV} = 14.6 \text{ M}^{-1}$; $k_q = 1.41 \times 10^9 \text{ M}^{-1} \text{ s}^{-1}$



[Anisole] (mM)	τ (ns)
0	10.37
2.14	8.72
4.23	7.50
6.30	6.60
8.33	5.89
9.8	5.32

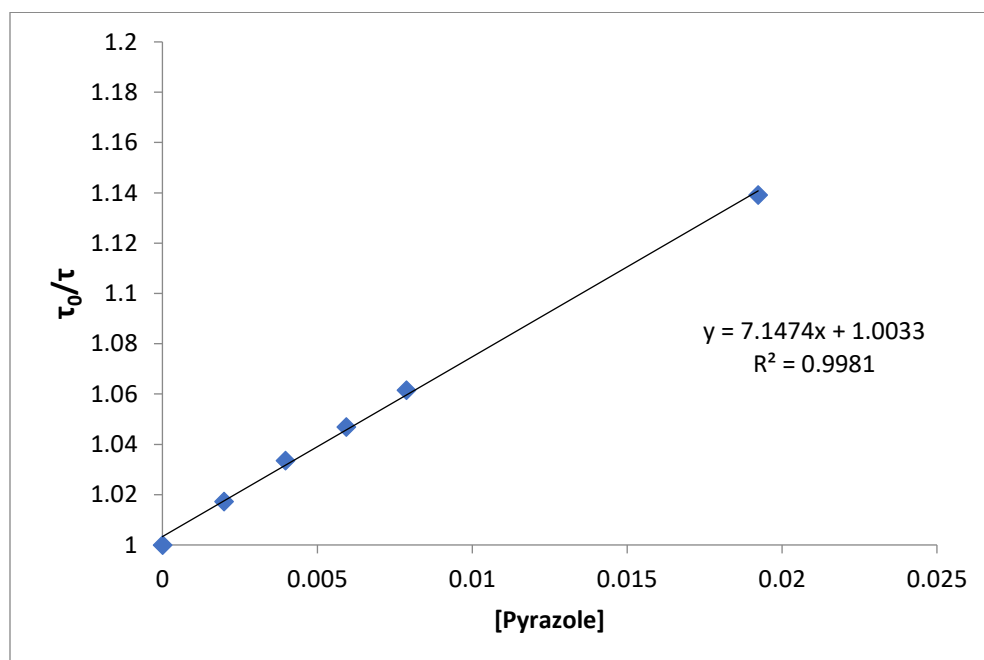
$K_{SV} = 96.9 \text{ M}^{-1}$; $k_q = 9.30 \times 10^9 \text{ M}^{-1} \text{ s}^{-1}$





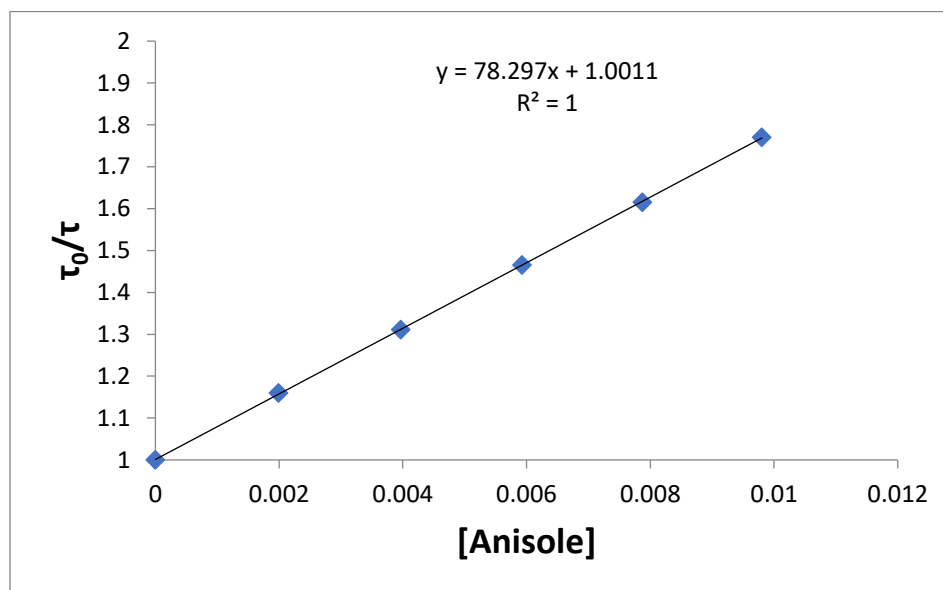
[Pyrazole] (mM)	τ (ns)
0	12.93
2.00	12.71
4.00	12.51
5.93	12.35
7.87	12.18
19.2	11.35

$K_{SV} = 7.1 \text{ M}^{-1}$; $k_q = 5.5 \times 10^8 \text{ M}^{-1} \text{ s}^{-1}$



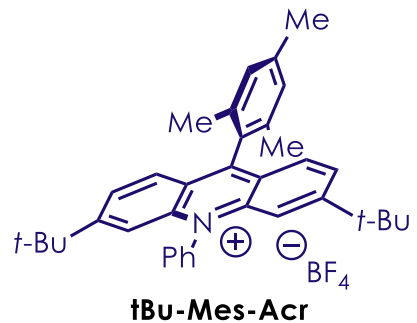
[Anisole] (mM)	τ (ns)
0	12.94
2.00	11.16
4.00	9.87
5.96	8.83
7.94	8.01
9.80	7.31

$K_{SV} = 78.3 \text{ M}^{-1}$; $k_q = 6.00 \times 10^9 \text{ M}^{-1} \text{ s}^{-1}$



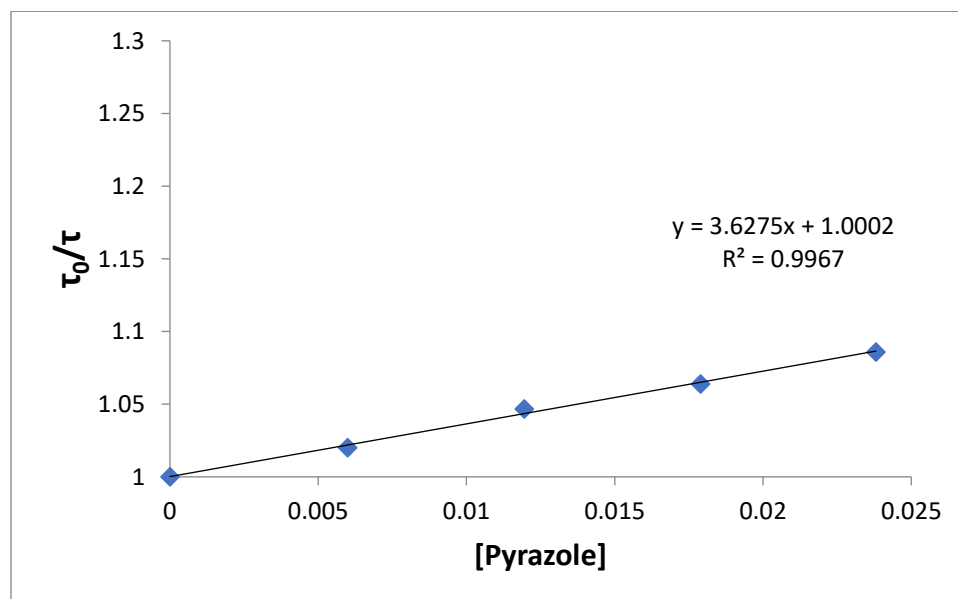
[m-Xylene] (mM)	τ (ns)
0	13.16
2.00	13.13
4.00	13.09
5.96	13.08
7.94	13.08
9.80	13.08

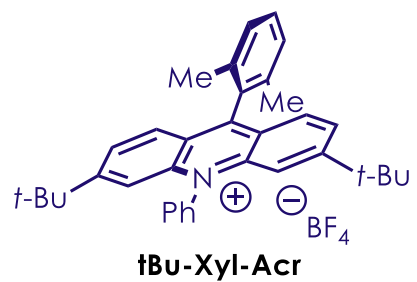
$K_{SV} = \text{N/A}$; $k_q = \text{N/A}$



[Pyrazole] (mM)	τ (ns)
0	13.63
5.99	13.36
12.0	13.02
17.9	12.81
23.8	12.55

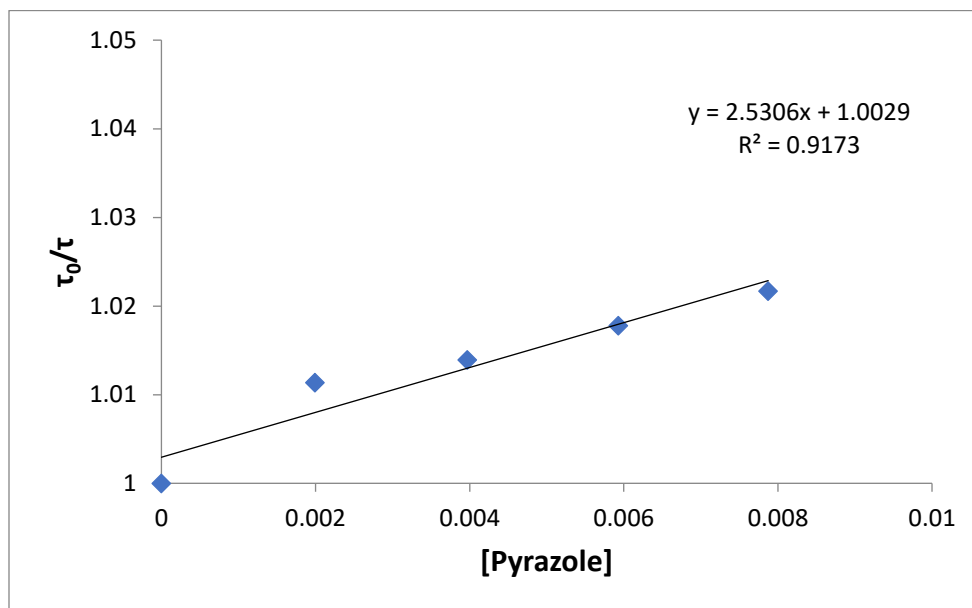
$K_{sv} = 3.6 \text{ M}^{-1}$; $k_q = 2.6 \times 10^8 \text{ M}^{-1} \text{ s}^{-1}$





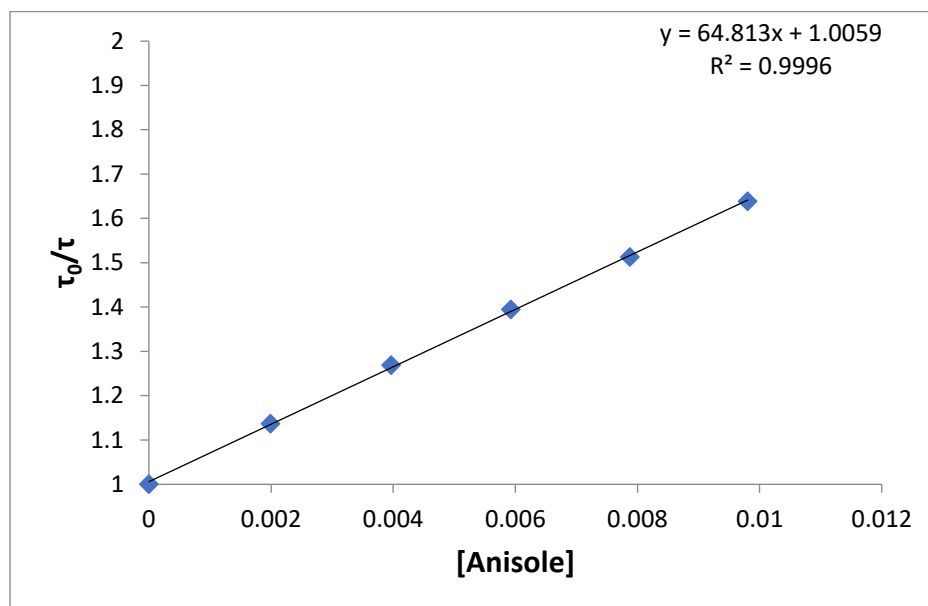
[Pyrazole] (mM)	τ (ns)
0	16.03
2.00	15.85
4.00	15.81
5.96	15.75
7.94	15.69

$K_{SV} = 2.5 \text{ M}^{-1}$; $k_q = 1.6 \times 10^8 \text{ M}^{-1} \text{ s}^{-1}$



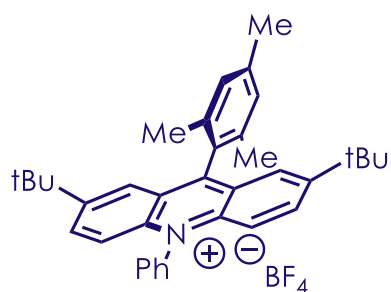
[Anisole] (mM)	τ (ns)
0	16.19
2.00	14.24
4.00	12.76
5.96	11.61
7.94	10.70
9.80	9.88

$K_{SV} = 64.8 \text{ M}^{-1}$; $k_q = 4.0 \times 10^9 \text{ M}^{-1} \text{ s}^{-1}$



[m-Xylene] (mM)	τ (ns)
0	16.34
2.00	16.21
4.00	16.18
5.96	16.14
7.94	16.12
9.80	16.10

$K_{SV} = 1.3 \text{ M}^{-1}$; $k_q = 1.0 \times 10^8 \text{ M}^{-1} \text{ s}^{-1}$



2,7-tBu-Mes-Acr

[Pyrazole] (mM)	τ (ns)
0	15.82
2.00	15.66
4.00	15.56
5.96	15.43
7.94	15.40
9.80	15.32

$K_{SV} = 2.7 \text{ M}^{-1}$; $k_q = 1.7 \times 10^8 \text{ M}^{-1} \text{ s}^{-1}$

B.8. Monitoring Reaction Mixtures via UV-Vis and LC-HRMS

General Procedure:

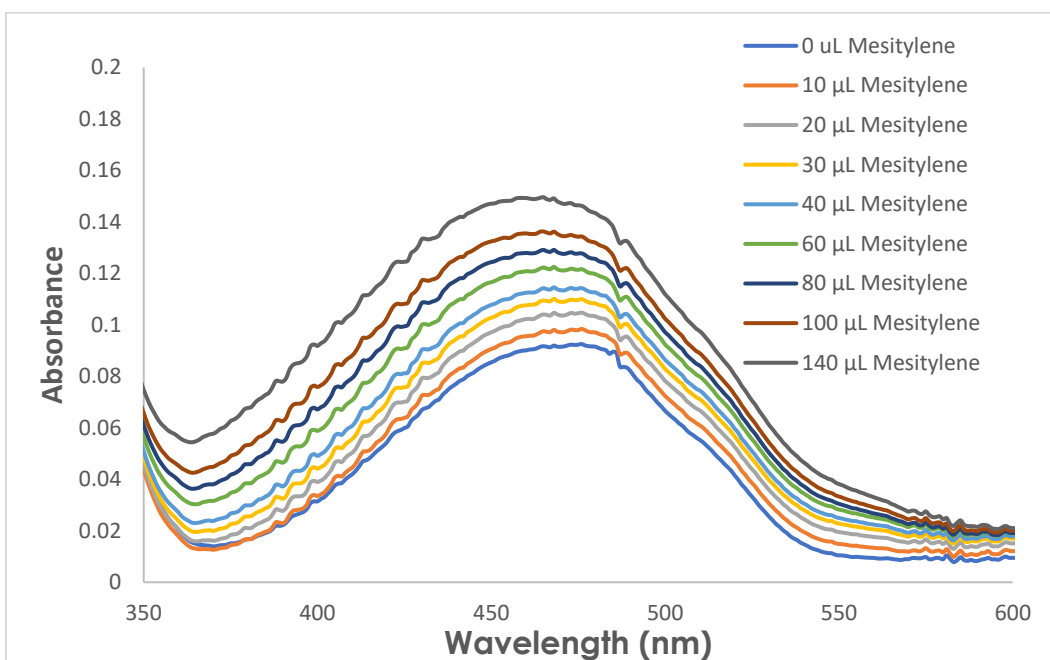
A 2 dram vial was charged with anisole (0.3 mmol, 1.0 equiv), pyrazole (0.6 mmol, 2.0 equiv), **catalyst** (0.015 mmol, 5 mol%), and TEMPO (0.06 mmol, 0.2 mmol) and DCE (3 mL) and then sealed with a septum cap. The solution was then sparged with a balloon of O₂ for 5 minutes.

Afterwards the vial was placed under irradiation while under an atmosphere of O₂ (balloon) and stirred. At the indicated time points, 30 μL aliquots were removed through the septum cap and diluted to 5 mL in DCE using a volumetric flask. The solution was then transferred to a cuvette and a UV-Vis spectrum was recorded. The solutions were also analyzed either by HRMS (ESI) direct inject or LC-HRMS (ESI).

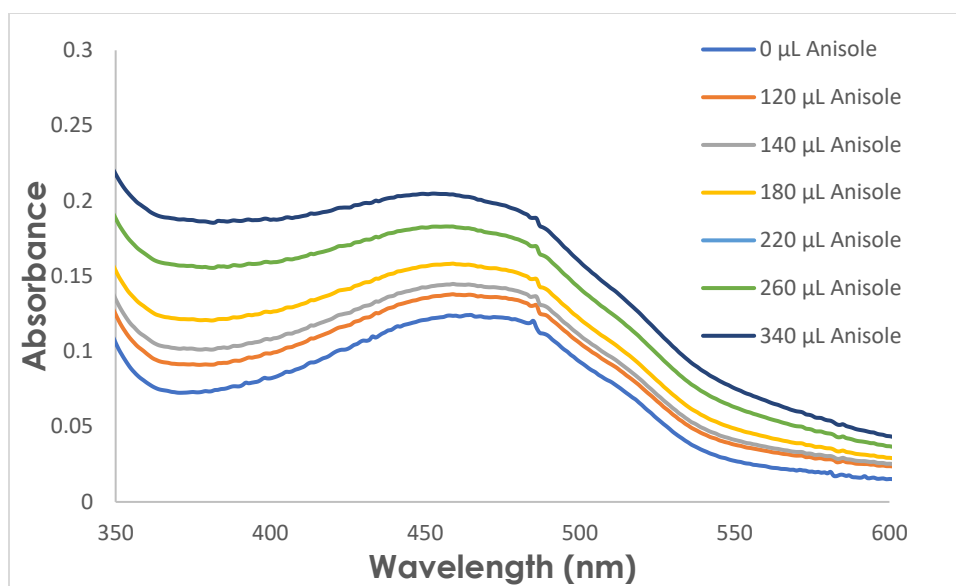
B.9. Observation of TEMPO⁺BF₄⁻ Charge Transfer by UV-Vis

To visualize the charge transfer bands between mesitylene and anisole, a 4 mM TEMPO⁺BF₄⁻ solution was prepared in MeCN and 3.0 mL was charged to a quartz cuvette. Arene was then added as a neat liquid in varying amounts and UV-Vis spectra were collected after each addition. The traces to identify λ_{max} of the resulting charge transfer bands (Δ Absorbance plots) were created by subtracting the spectrum of TEMPO⁺BF₄⁻ in the absence of quencher from each spectrum.

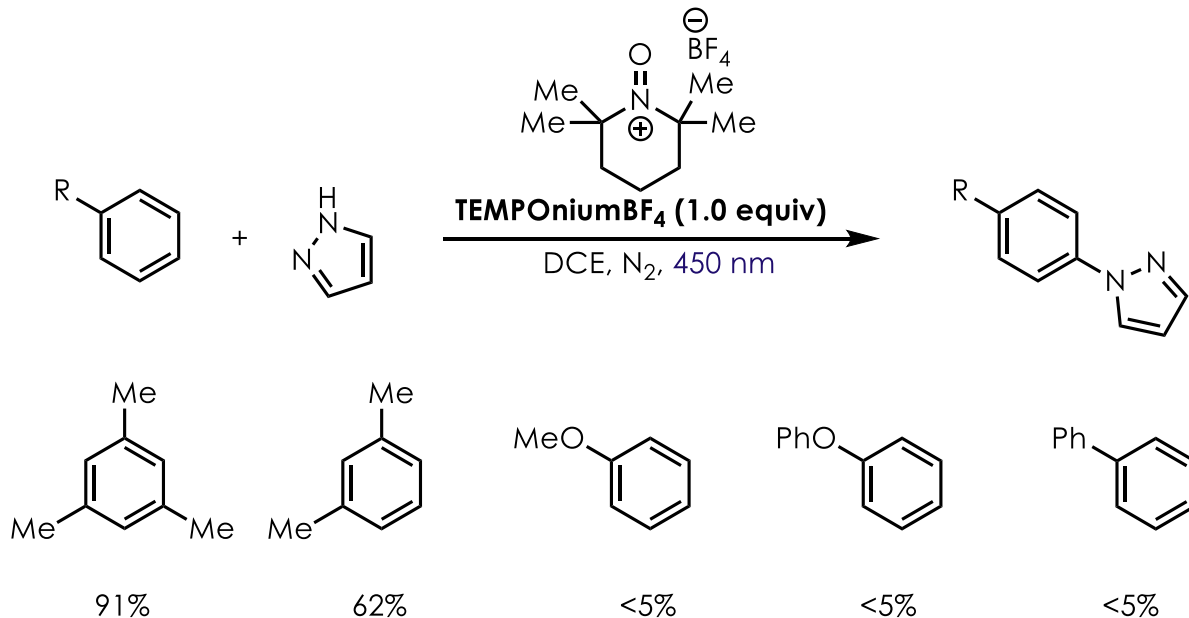
TEMPO⁺BF₄⁻ and Mesitylene



TEMPO⁺BF₄⁻ and Anisole



B.10. TEMPO⁺BF₄⁻ mediated arene C-H amination

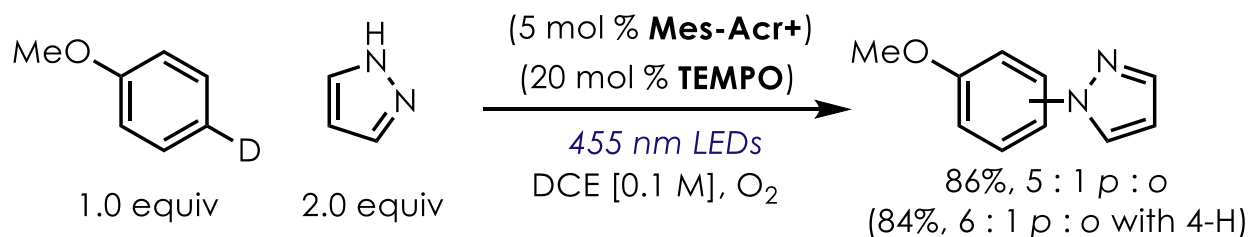


General Procedure: To a flame dried 2 dram vial was charged the arene (0.4 mmol), pyrazole (0.2 mmol) and **TEMPO⁺BF₄⁻** (0.2 mmol) and DCE (2.0 mL, [0.1 M] with respect to pyrazole). The suspension was sparged with N₂ for 5 minutes and then the septum sealed with electrical tape and the vial was irradiated for 20 h. After irradiation, the solutions were concentrated under pressure and the residue was dissolved in ~1.0 mL CDCl₃ and 0.051 mmol (10 μL) Hexamethyldisiloxane (HMDSO) was added as an internal standard. An NMR spectrum was obtained and the yield was determined from the ratio of product peaks to internal standard.

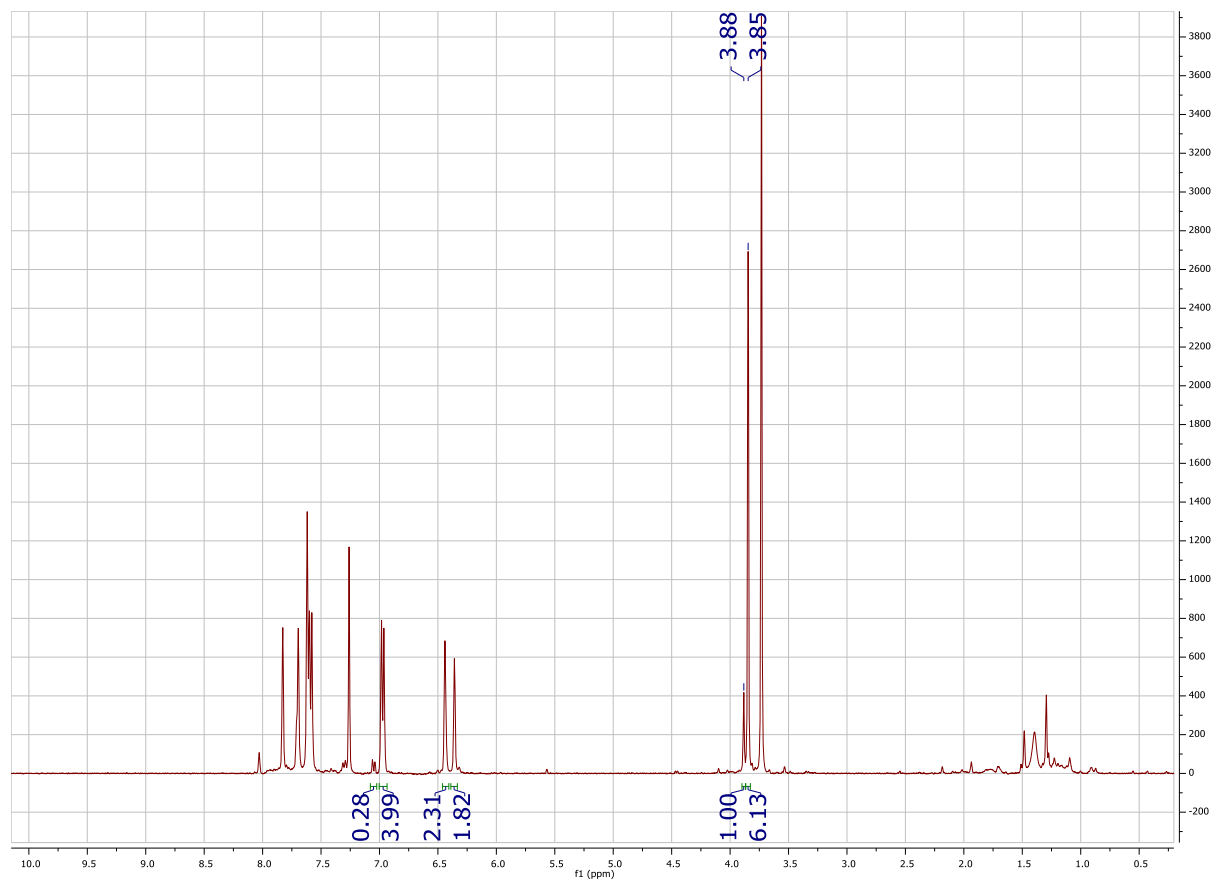
B.11. Development of New Anaerobic Conditions

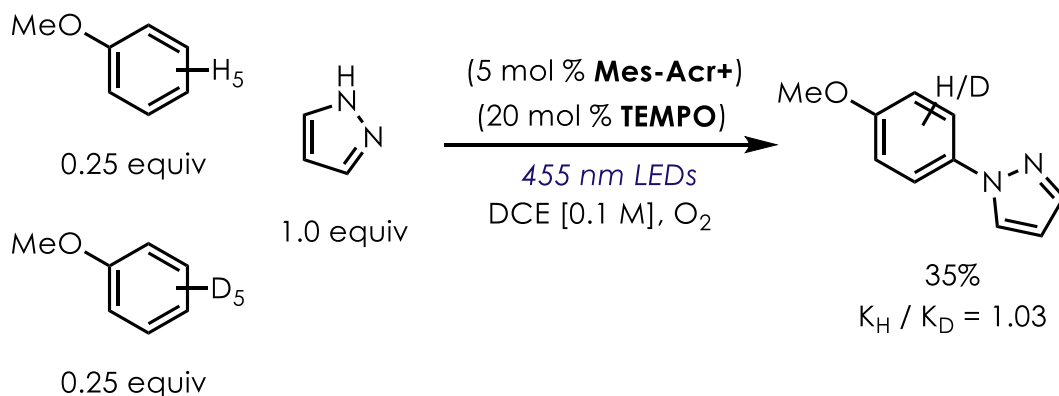
A 2 dram vial was charged with arene (0.3 mmol, 1.0 equiv), pyrazole (0.6 mmol, 2.0 equiv), **catalyst** (0.015 mmol, 5 mol%), and TEMPO (0.06 mmol, 0.2 mmol), and tert-butyl hydroperoxide (0.30 mmol, provided as a 5.0 M solution in decene) and DCE (3 mL) and sealed with a septum cap. **For mesitylene the mesitylene and pyrazole stoichiometry was reversed.** The solution was then sparged with a balloon of N₂ for 5 minutes and then sealed with electrical tape and irradiated for 20 h. After, the solutions were removed from irradiation, concentrated under pressure, and the residues dissolved in ~1 mL CDCl₃ and 0.051 mmol (10 μL) Hexamethydisiloxane internal standard was added. An NMR sample was prepared from this solution and the yield determined by the relative integrations of the product peaks and internal standard.

B.12. KIE Experiments

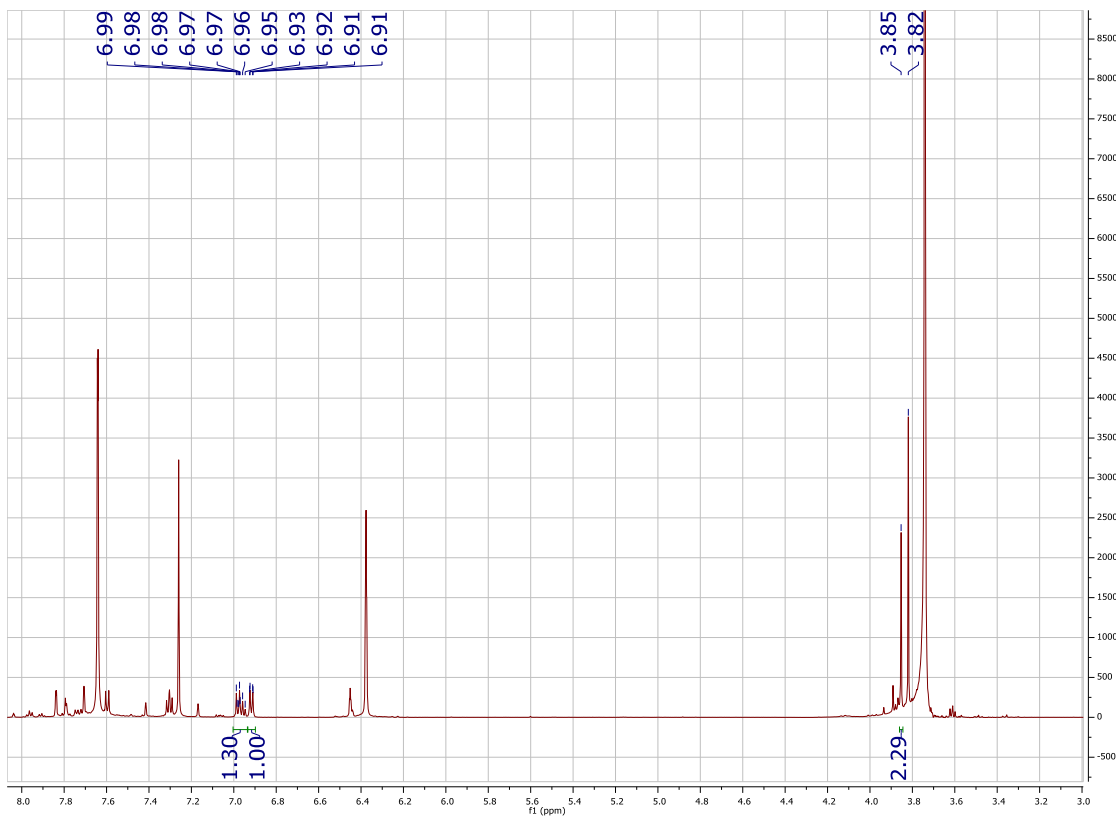
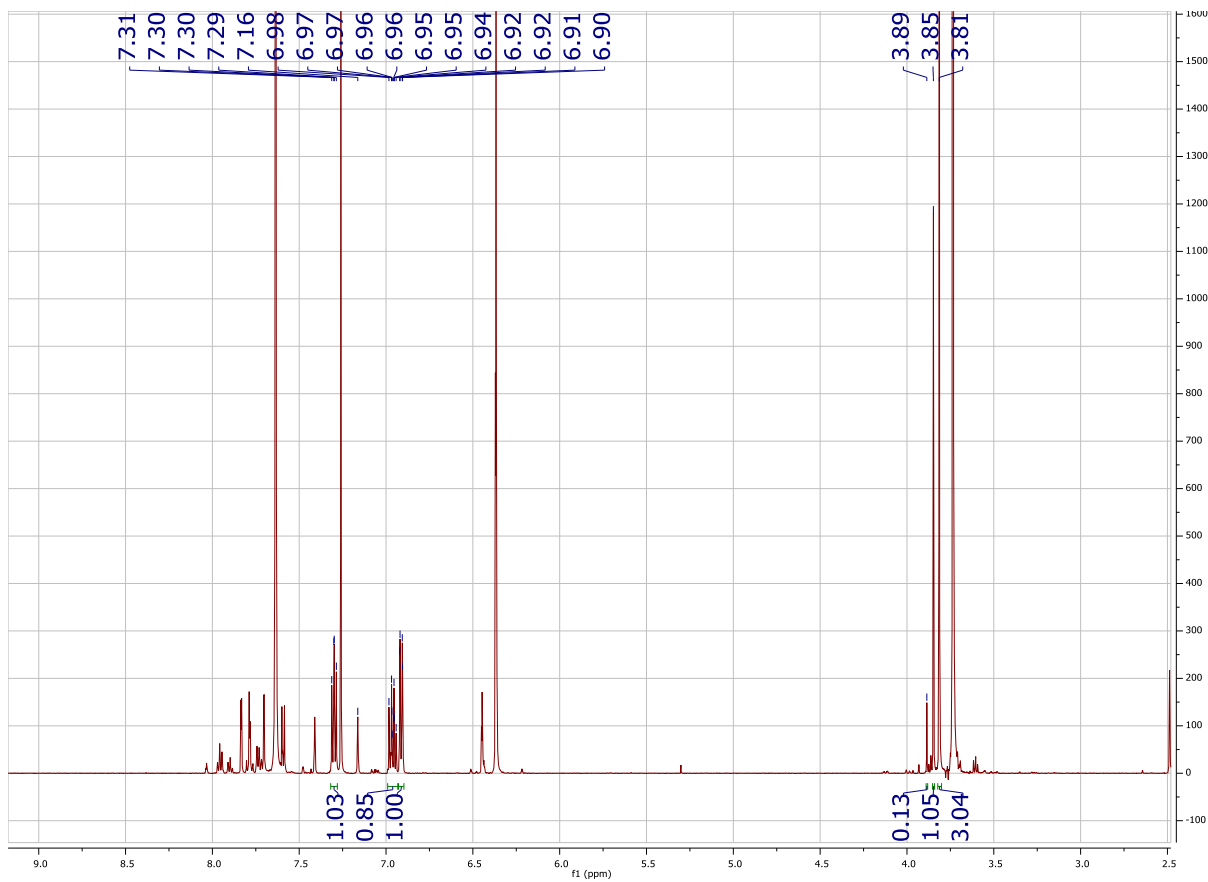


A 2 dram vial was charged with 4-d-anisole (0.3 mmol, 1.0 equiv), pyrazole (0.6 mmol, 2.0 equiv), **tBu-Mes-NPA** (0.015 mmol, 5 mol%), **TEMPO** (0.06 mmol, 0.2 mmol) and the indicated amount of acid and dissolved in DCE (3 mL) and then sealed with a septum cap. The solution was then sparged with a balloon of O₂ for 5 minutes. Afterwards the vial was placed under irradiation while under an atmosphere of O₂ (balloon) and stirred for 20 h. Afterwards, the solutions were concentrated under pressure and then the residues dissolved in ~1 mL CDCl₃ and 0.051 mmol HMDSO was added as an internal standard. From this solution an NMR sample was prepared and the yields were determined from the relative integrations of product to internal standard peaks. The regioselectivities were determined by the ratio of the OCH₃ peaks for the ortho product (3.89 ppm) to the para product (3.85 ppm)



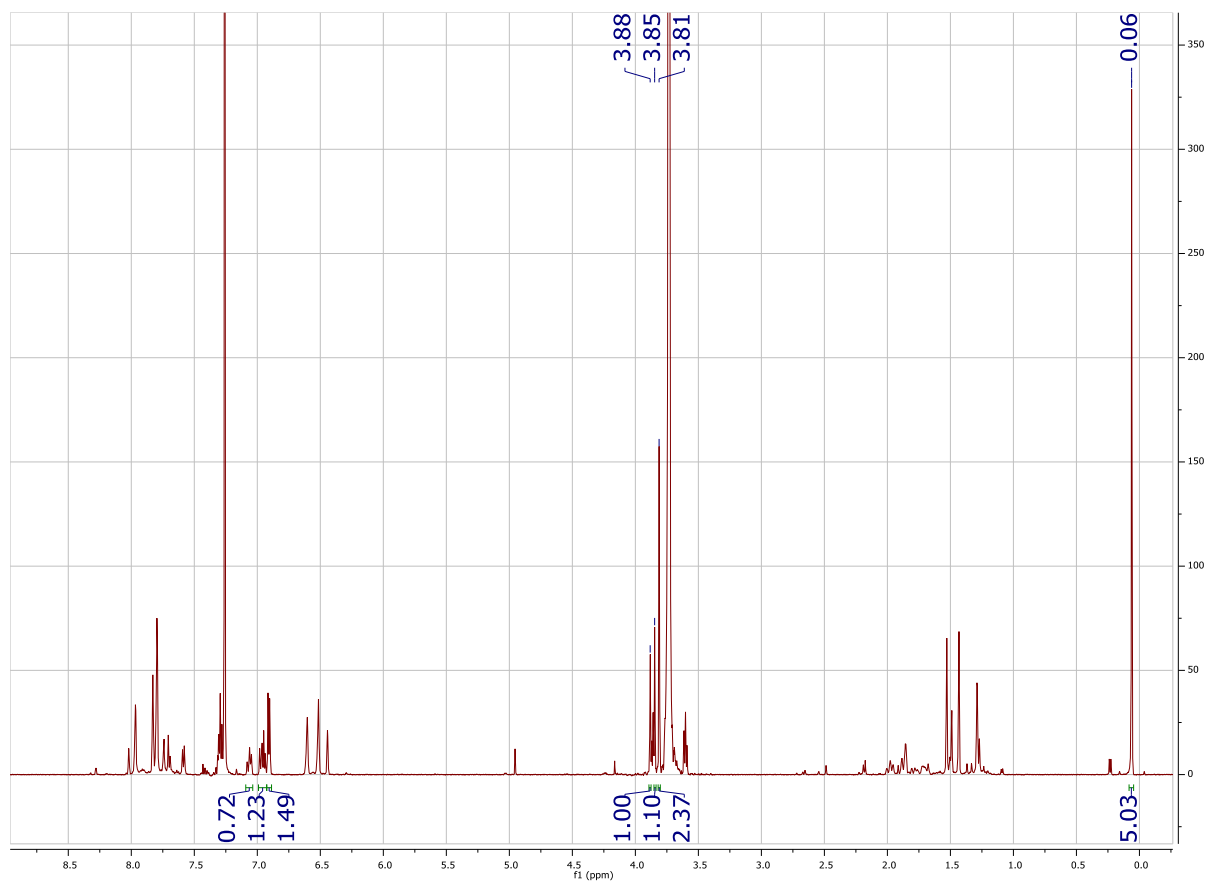
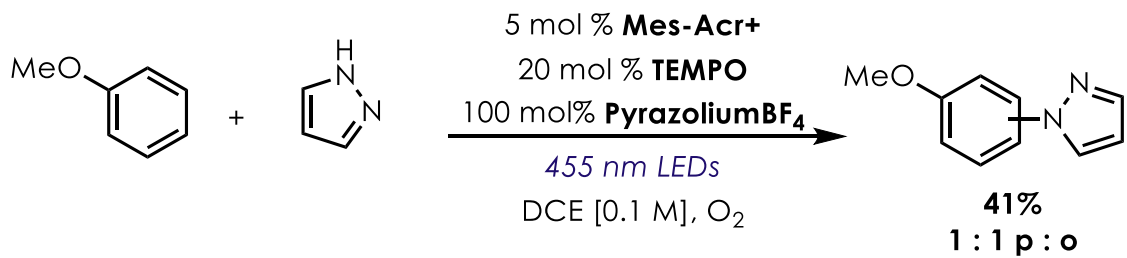


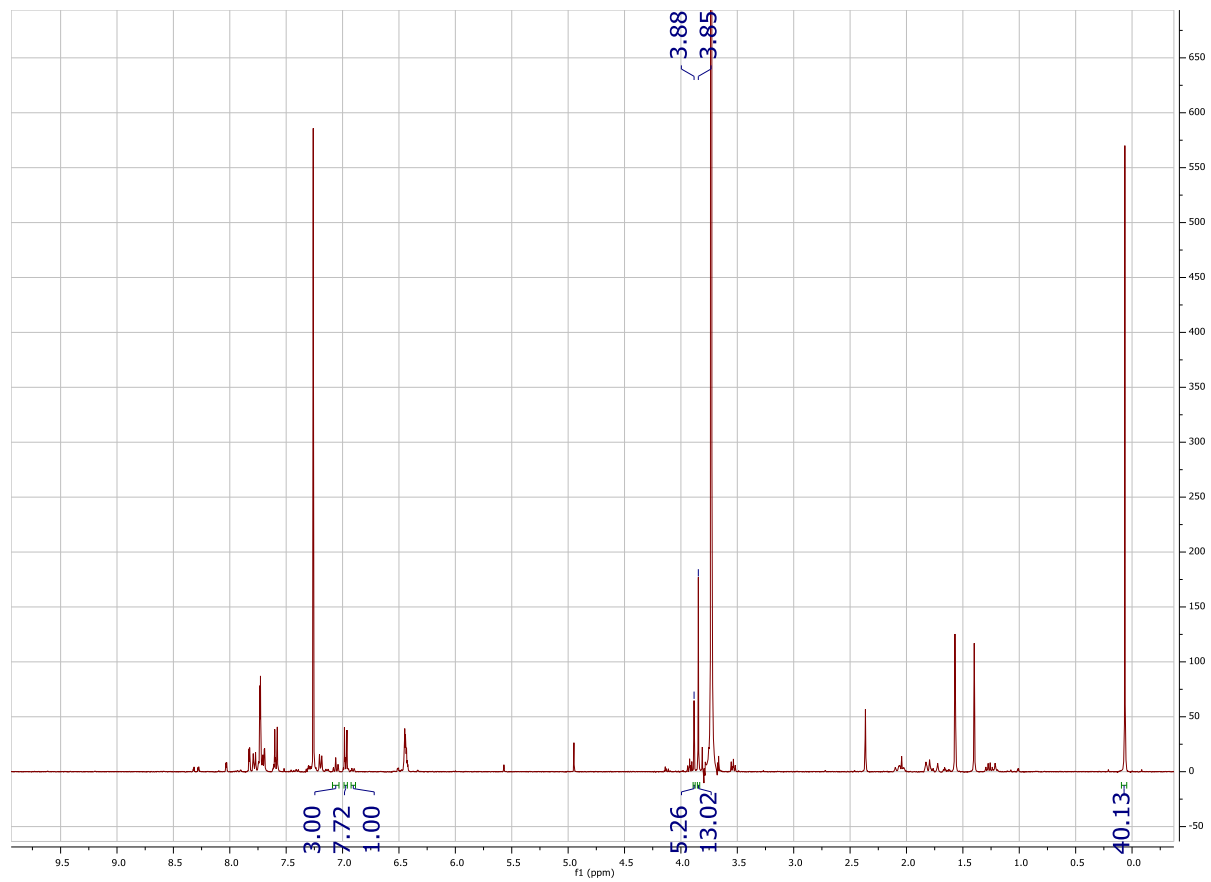
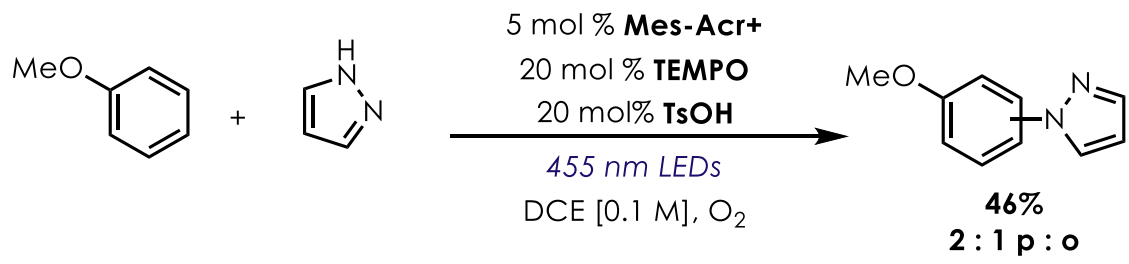
A 2 dram vial was charged with anisole (0.15 mmol), d_5 -anisole (0.15 mmol), pyrazole (0.6 mmol, 2.0 equiv), **tBu-Mes-NPA** (0.015 mmol, 5 mol%), TEMPO (0.06 mmol, 0.2 mmol) and the indicated amount of acid and dissolved in DCE (3 mL) and then sealed with a septum cap. The solution was then sparged with a balloon of O_2 for 5 minutes. Afterwards the vial was placed under irradiation while under an atmosphere of O_2 (balloon) and stirred for 15 minutes (corresponding to 35% conversion). Afterwards, the solutions were concentrated under pressure and then the residues dissolved in ~1 mL $CDCl_3$. From this solution an NMR sample was prepared and obtained (1H 600 MHz) and the K_H/K_D was determined from the relative integrations for protio and deuterio species. Comparing the integrations for the protio-anisole ortho protons (6.91 ppm, integration = 1.00) and the multiplet that contains the para- H_4 -product protons (6.95 ppm, integration = 0.85, 0.50 from para-proton from protio-anisole, 0.35 from 2 protons from para- H_4 -product). The para-product OCH_3 peak located at 3.85 ppm integrates to 1.05. Based on the relative integrations determined for para- H_4 -product, 0.525 of this integral should correspond to OCH_3 for the protio-product. Thus, 0.525 of the integral remains for the deuterio-product. $k_H / k_D = 1.00$ and second trial affords 1.05, for an average of 1.03.



B.13. Acid Studies

A 2 dram vial was charged with anisole (0.3 mmol, 1.0 equiv), pyrazole (0.6 mmol, 2.0 equiv), **tBu-Mes-NPA** (0.015 mmol, 5 mol%), TEMPO (0.06 mmol, 0.2 mmol) and the indicated amount of acid and dissolved in DCE (3 mL) and then sealed with a septum cap. The solution was then sparged with a balloon of O₂ for 5 minutes. Afterwards the vial was placed under irradiation while under an atmosphere of O₂ (balloon) and stirred for 20 h. Afterwards, the solutions were concentrated under pressure and then the residues dissolved in ~1 mL CDCl₃ and 0.051 mmol HMDSO was added as an internal standard. From this solution an NMR sample was prepared and the yields were determined from the relative integrations of product to internal standard peaks. The regioselectivities were determined by the ratio of the OCH₃ peaks for the ortho (3.89 ppm) and para (3.85 ppm).





REFERENCES

- (1) Romero, N. A.; Nicewicz, D. A. Mechanistic Insight into the Photoredox Catalysis of Anti-Markovnikov Alkene Hydrofunctionalization Reactions. *J. Am. Chem. Soc.* **2014**, *136* (49), 17024–17035.
- (2) Farmer, L. A.; Haidasz, E. A.; Griesser, M.; Pratt, D. A. Phenoxazine: A Privileged Scaffold for Radical-Trapping Antioxidants. *J. Org. Chem.* **2017**, *82* (19), 10523–10536.
- (3) Vogler, T.; Studer, A. Rhodium-Catalyzed Oxidative Homocoupling of Boronic Acids. *Adv. Synth. Catal.* **2008**, *350* (13), 1963–1967.